From Earth to exoplanets: Quantifying atmospheric biosignatures and biogeochemical controls on habitability

Joshua E. Krissansen-Totton

A dissertation

submitted in partial fulfillment of the

requirements for the degree of

Doctor of Philosophy

University of Washington

2019

Reading Committee:

David C. Catling, Chair

Roger Buick

Victoria Meadows

Program Authorized to Offer Degree:

Department of Earth and Space Sciences

University of Washington

University of Washington

Abstract

From Earth to exoplanets: Quantifying atmospheric biosignatures and biogeochemical controls on habitability

Joshua E. Krissansen-Totton

Chair of the Supervisory Committee:

David C. Catling, Ph.D.

Department of Earth and Space Sciences

It will soon be possible to determine the atmospheric composition of potentially habitable planets around other stars via astronomical observations. This raises the exciting possibility of detecting life remotely from its waste gases. But knowing what gases to look for and ruling out non-biological processes may be difficult. Fortunately, Earth is an invaluable natural laboratory for understanding biosignatures and habitability more broadly, as illustrated by this thesis.

The first three chapters of this thesis explore chemical disequilibrium as a possible exoplanet biosignature. A rigorous calculation of the disequilibrium in Earth's atmosphere-ocean system is presented. Earth's disequilibrium is larger than that of any other Solar System body, and is dominated by the coexistence of N_2, O_2, and liquid water. This combination is a more compelling biosignature than O_2 alone because it would not persist without continuous replenishment of O_2. Next, disequilibrium calculations were applied to the early, anoxic Earth (4.0-2.5 Ga). It is found that CH_4 and CO_2 were out of equilibrium in the Archean. This disequilibrium combination is biogenic because it would not persist without continuous replenishment of CH_4 from life. Moreover, this CH_4+CO_2 biosignature is potentially ubiquitous and detectable with the upcoming James Webb Space Telescope.

An assessment of planetary habitability is important contextual information for interpreting any purported biosignature detection. The next two chapters of this thesis investigate how the carbon cycle has maintained habitable conditions on Earth. It is widely believed that the continental weathering thermostat buffered Earth's climate against a secular solar luminosity increase over Earth history. But exactly how this feedback works, and the role of seafloor weathering—a complimentary climate buffer—is unknown. An inverse carbon cycle model is applied to the last 100 Ma and by fitting proxy data for pCO_2, ocean chemistry, and temperature, Earth's climate sensitivity and the dependence of silicate weathering on temperature are constrained. Next, the carbon cycle model is applied to all of Earth history to answer long-debated questions about the conditions on the early Earth. The Archean Earth was likely temperate (<40°C) with a slightly acidic to neutral ocean pH, contrary to the hot Archean climates or alkaline oceans that have previously been proposed.

Taken as a whole, this thesis elucidates the processes that have maintained habitable surface conditions on Earth and uses this understanding to constrain surface conditions on the early Earth. Additionally, the development of a theory of disequilibrium biosignatures provides novel prospects for exoplanet life detection that could be realized with next generation telescopes.

Table of Contents

List of Figures

List of Tables

Acknowledgements

This thesis was made possible by the support of many faculty, graduate students, departmental staff, friends, and family.

First, I would like to thank my advisor David Catling for his scientific mentorship. I have been fortunate to have benefited from David's extensive knowledge of planetary science, wealth of creative ideas, and insights into academia. I would not have had the confidence to tackle the diverse topics in this thesis without his guidance. I would also like to thank my thesis committee Roger Buick and Victoria Meadows for their direction and encouragement over the years. Both Roger and Vikki have been valuable collaborators and made important contributions to the research described in this thesis. I would also like to thank Patrick Irwin for his assistance during my time at the University of Oxford, without which Chapter 4 would not have been possible.

Part of the reason why I came to the University of Washington was its interdisciplinary Astrobiology Program. During my time at UW the astrobiology program has provided me with many unique, intellectually stimulating opportunities and has formed an integral part of my identity as a graduate student. I thank the director Victoria Meadows, the steering committee, and the astrobiology student community for building and maintaining this wonderful program.

I would like to thank my support network both inside and outside of graduate school for their friendship and empathy. Many people have shown me kindness over the years, but I would especially like to thank Candace Abrahamson, Elena Amador, Chloe Hart, Matthew Koehler, Van-Anh La, Ashwin Karnik, Jana Meixnerová, Jillian Schleicher, Steven Sholes, Meg Smith, Debi Talukdar, and Julia Weed for supporting me through setbacks, illness, and existential crises.

Finally, I would like to thank my family for their unconditional love and support. There's 11,265 km between Seattle and my home in New Zealand, and the physical separation hasn't always been easy. I would like to thank my brother Eben for his enthusiastic interest and encouragement. I would like to thank my parents Alan and Rosemary for nurturing my curiosity, encouraging my interest in science, and supporting me through my schooling. None of this would have been possible without them.

Chapter 1 - Introduction

"Maybe you see that God created only this single world and that God did not create humans besides you. Well, I swear by God that God created thousands and thousands of worlds and thousands and thousands of humankind." – Imam Muhammad al-Baqir (676–733).

In many respects, Earth occupies an unremarkable place in the cosmos. Similarly sized, rocky planets are abundant (Burke et al. 2015), and Earth orbits a typical main sequence star (Scalo 1986). The solar system is one of many multi-planet systems (Ballard & Johnson 2016) in our galaxy of ~10^{11} stars, which, in turn, is merely one of the ~10^{12} galaxies in the observable universe (Conselice et al. 2016). But an important question about our position in the cosmos is unanswered, namely what is life's place in the universe? This is the central question asked by the interdisciplinary subject of astrobiology: is life a commonplace planetary phenomenon? Or is Earth anomalous—perhaps even unique—by virtue of its prolific and diverse biosphere? The answer to this question will have ramifications that transcend science (Davies 1995).

Technology will soon exist to enable the search for life on planets around other stars. Several telescopes capable of measuring the atmospheric composition of potentially habitable exoplanets are under construction or in the planning phases (Fischer et al. 2018; Gaudi et al. 2018; Greene et al. 2016; Rodler & López-Morales 2014; Snellen et al. 2013). Existing telescopes routinely measure the atmospheric composition of large gaseous exoplanets (Sing et al. 2016) and are on the threshold of doing the same for smaller, rocky planets (de Wit et al. 2016; De Wit et al. 2018; Delrez et al. 2018). With upcoming instruments, it will be possible to interrogate the atmospheres of terrestrial exoplanets for the telltale waste products of biology.

These upcoming observations present daunting challenges, however. How do we determine with confidence whether a distant exoplanet hosts life based merely on atmospheric composition and limited contextual information? Even within our own solar system, where *in situ* analyses are possible, there is a rich diversity of worlds, and the processes that affect the composition of planetary atmospheres are complex and not completely understood (Catling & Kasting 2017). Without the possibility of *in situ* analyses, interpreting and understanding the great variety of worlds that exist around other stars will be difficult.

Thesis Outline

Distinguishing living from lifeless worlds is the subject of the first half of this thesis. **Chapter 2** investigates this using atmospheric chemical disequilibrium as an exoplanet biosignature. This idea originated during the early days of space exploration when scientists were focused on life detection in the solar system context. The essential idea, first proposed by Lovelock (1965) and Lederberg (1965), was that waste gases produced by life may alter the atmospheric composition of planets in a way that is remotely detectable.

Specifically, Lovelock (1965) proposed that the coexistence of two or more chemically incompatible species, such as oxygen and methane, could be indicative of continuous biological replenishment. The idea of chemical disequilibrium as a biosignature is commonly cited but rarely quantified, and so Chapter 2 presents a quantitative metric for thermodynamic disequilibrium based on available Gibbs free energy. The metric is applied to the solar system planets to evaluate its usefulness for exoplanet life detection. It is found that Earth possesses by far the largest disequilibrium of all the solar system planets due to the presence of life, specifically due to the coexistence of biogenic oxygen, nitrogen, and liquid water. This combination of gases is a more compelling biosignature than oxygen alone.

Oxygen is the posterchild for biosignature gases: it is difficult to produce in large quantities without life, and oxygen is readily detectable with the right instrument (Meadows 2017). In some respects, the oxygen+nitrogen+water disequilibrium biosignature proposed in Chapter 2 is a variation on oxygen as a biosignature. However, whether oxygen biosignatures are likely to be common elsewhere is an open question. Oxygenic photosynthesis is a complex metabolism that only evolved once on Earth, and we know from Earth's geologic record that modern levels of atmospheric oxygen are atypical (Knoll 2008; Lane 2002; Lyons et al. 2014). **Chapter 3** explores alternative biosignatures. We examine the disequilibrium in Earth's atmosphere over its history and find that on the anoxic, Archean Earth (4.0-2.5 Ga) there was a large disequilibrium between methane and carbon dioxide. This disequilibrium combination was attributable to life because atmospheric methane replenishment was largely biogenic. Moreover, out-of-equilibrium methane could be a ubiquitous and readily detectable exoplanet biosignature in anoxic exoplanet atmospheres.

Chapter 4 explores the subject of biosignature detectability more closely. This chapter investigates whether the anoxic methane plus carbon dioxide biosignature combination described in Chapter 3 would be detectable on planets in the nearby TRAPPIST-1 system with the upcoming James Webb Space Telescope (JWST). The answer is a tentative yes, pending uncertainties in on-orbit performance and stellar noise. Furthermore, this methane plus carbon dioxide biosignature is considerably easier to detect than modern Earth-like oxygen biosignatures with JWST.

The second half of this thesis addresses the broader question of what makes a planet habitable to begin with. Understanding planetary habitability is a prerequisite for interpreting purported biosignature gas detections. A necessary condition for habitability is the availability of liquid water (Pohorille & Pratt 2012). For all practical purposes, an exoplanet is habitable if it possesses *surface* liquid water (subsurface oceans are unlikely to support biospheres that could be detectable across interstellar distances). A multitude of factors control whether rocky planets may develop and maintain liquid water oceans (Meadows & Barnes 2018), but surface temperature is arguably the most important determinant. This is the basis for the habitable

zone concept (Kasting et al. 1993b; Kopparapu et al. 2013): planets too close to their host star will lose their oceans to vaporization and hydrogen escape, whereas planets too distant will become permanently frozen.

Within these broad insolation limits, the surface climate of potentially habitable terrestrial planets is believed to be controlled by the cycling of carbon between the atmosphere, ocean, and the interior (Abbot et al. 2012; Foley 2015; Rushby et al. 2018; Walker et al. 1981). This is because carbon dioxide is a strong greenhouse gas, and so its atmospheric abundance determines surface temperature. On long timescales, the amount of carbon dioxide in the air is controlled by outgassing and weathering processes.

Earth's carbon cycle serves as the basis of our understanding for these processes. **Chapter 5** examines the operation of Earth's carbon cycle over the last 100 million years, a timespan for which geological data is relatively abundant. A model of the carbon cycle is developed, proxy data are used to constrain the model, and in doing so quantifies how Earth's carbon cycle operates.

In **Chapter 6**, this data-driven understanding is applied to modeling the evolution of Earth's climate from 4 Ga to the present. One key motivation for this work is to help answer longstanding questions about the conditions on the early Earth. There is considerable debate as to whether the Archean Earth was glaciated (de Wit & Furnes 2016), temperate (Hren et al. 2009), or suited only to thermophiles (Knauth & Lowe 2003). Similarly, there is uncertainty over the Archean ocean pH, with estimates varying from quite acidic (Halevy & Bachan 2017) to highly alkaline (Kempe & Degens 1985). Constraining such conditions on the early Earth is important for understanding the early evolution of life.

The quantification of what were previously qualitative concepts is a common thread throughout this thesis. The idea of using chemical disequilibrium as a biosignature is not new, but prior to the studies described here, there were limited attempts to rigorously quantify it. By developing the underlying theory, describing quantitative disequilibrium metrics, and exploring their detectability a more complete picture of the utility of this biosignature is provided, and from this analysis emerged novel disequilibrium gas combinations. Similarly, the weathering feedbacks in Earth's carbon cycle have been described and modeled previously. But in Chapter 5 we apply rigorous inverse methods to constrain the strength of these feedbacks using proxy data from the geologic record. Our data-constrained model of the carbon cycle is then extended to the entirety of Earth history to address long-standing quantitative questions about conditions on the early Earth. In the future, evaluating whether an exoplanet hosts life will be a difficult and controversial debate, and quantitative approaches such as those described in this thesis are helpful for couching uncertainties and hopefully avoiding the human tendency to see what we want to see.

Chapter 2 - Quantifying disequilibrium biosignatures

"It is a cliché of science fiction for the captain of a space craft when approaching a new planetary system to call his exobiological officer and ask "do any of those planets bear life?". The operation by this officer of a remote sensing device soon provides a confident answer, yes or no. One purpose of this paper is to consider the possible basis of such a device." – James Lovelock, 1975

Life detection via remote sensing is fraught with challenges and human biases. The history of planetary science is full of examples of scientists misinterpreting observations as evidence for inhabitance. The cloud-obscured surface of Venus was commonly imagined to be covered with swampy forests (Arrhenius 1918). As late as the 1950s, scientists—perhaps influenced by popular images of Venus as a clement abode for life—argued Venus possessed a vast surface ocean (Menzel & Whipple 1955). Late 19th century observations of Mars famously convinced many (e.g. Schiaparelli 1899) that Mars' surface was crisscrossed by engineered canals. These were later shown to be optical illusions (Webb 1957). To this day, debate rages over purported detections of variable martian methane, which, if present, constitute a possible sign of inhabitation or geological activity (Giuranna et al. 2019; Korablev et al. 2019; Zahnle et al. 2011).

These cautionary tales are especially relevant for terrestrial exoplanet observations where the information gleaned from observations will, at least initially, be extremely limited and require interpretation. Ultimately, a commonly agreed-upon quantitative framework for biosignature detection will be needed (e.g. Catling et al. 2018) to minimize the chance of misinterpretations. One possible approach to quantifying exoplanet biosignatures is using atmospheric chemical disequilibrium as an objective, generalizable sign of life. This chapter presents a method for quantifying disequilibrium in planetary atmospheres and applies it to the solar system planets to test its utility as a biosignature.

Portions of this chapter were originally published in collaboration with David S. Bergsman and David C. Catling in the journal Astrobiology (Krissansen-Totton et al. (2016), On detecting biospheres from chemical thermodynamic disequilibrium in planetary atmospheres, Astrobiology, 16, 39-67.)

Abstract

Atmospheric chemical disequilibrium has been proposed as a method for detecting extraterrestrial biospheres from exoplanet observations. Chemical disequilibrium is potentially a generalized biosignature since it makes no assumptions about particular biogenic gases or metabolisms. Here, we present the first rigorous calculations of the thermodynamic chemical disequilibrium in Solar System atmospheres, in which we quantify the available Gibbs energy: the Gibbs free energy of an observed atmosphere minus that of atmospheric gases reacted to equilibrium. The purely gas phase disequilibrium in Earth's atmosphere is mostly attributable to O_2 and CH_4. The available Gibbs energy is not unusual compared to other Solar System atmospheres and smaller than that of Mars. However, Earth's fluid envelope contains an ocean, allowing gases to react with water and requiring a multiphase calculation with aqueous species. The disequilibrium in Earth's atmosphere-ocean system (in joules per mole of atmosphere) ranges from ~20 to 2×10^6 times larger than the disequilibria of other atmospheres in the Solar System, where Mars is second to Earth. Only on Earth is the chemical disequilibrium energy comparable to the thermal energy per mole of atmosphere (excluding comparison to Titan with lakes, where quantification is precluded because the mean lake composition is unknown). Earth's disequilibrium is biogenic, mainly caused by the coexistence of N_2, O_2 and liquid water instead of more stable nitrate. In comparison, the O_2-CH_4 disequilibrium is minor, although kinetics requires a large CH_4 flux into the atmosphere. We identify abiotic processes that cause disequilibrium in the other atmospheres. Our metric requires minimal assumptions and could potentially be calculated using observations of exoplanet atmospheres. However, further work is needed to establish whether thermodynamic disequilibrium is a practical exoplanet biosignature, requiring an assessment of false positives, noisy observations, and other detection challenges. Our Matlab code and databases for these calculations are available, open source.

Introduction

The most interesting question about exoplanets is whether any of them host life. In recent years, significant progress has been made in the detection and characterization of the atmospheres of Jupiter and Neptune-sized exoplanets (Barman 2007; Charbonneau et al. 2002; Deming et al. 2013; Fraine et al. 2014; Pont et al. 2008; Vidal-Madjar et al. 2003). With the upcoming launch of NASA's James Webb Space Telescope and the construction of larger ground-based telescopes such as the European Extremely Large Telescope, it may be possible to constrain the atmospheric composition of terrestrial planets in the near future (Belu et al. 2011; Deming et al. 2009; Hedelt et al. 2013; Misra et al. 2014; Rauer et al. 2011; Rodler & López-Morales 2014; Snellen et al. 2013). Whether or not the presence of an exoplanet biosphere could be inferred remotely from these atmospheric observations needs to be carefully considered.

Life detection using remote sensing was first proposed in the 1960s and 1970s in the context of Solar System exploration (Lederberg 1965). The realization that life on Earth has profoundly influenced the geochemical environment, and in particular the composition of the atmosphere and oceans, led naturally to the suggestion that alien biospheres may be detectable remotely via their influence on atmospheric composition (Lovelock 1965; Lovelock 1975; Lovelock & Margulis 1974). More specifically, chemical disequilibrium in planetary atmospheres, such as the co-existence of two long-term incompatible species like oxygen and methane, was proposed as a possible sign of life (Hitchcock & Lovelock 1967; Lovelock 1965). It is now understood that all the bulk gases except for the inert gases in Earth's atmosphere are modulated by biology (Catling & Kasting 2007), and so it is reasonable to expect exoplanet atmospheres to be similarly perturbed away from chemical equilibrium by biogenic gas fluxes.

Chemical disequilibrium as a biosignature is appealing because unlike searching for biogenic gases specific to particular metabolisms, the chemical disequilibrium approach makes no assumptions about the underlying biochemistry. Instead, it is a generalized life-detection metric that rests only on the assumption that distinct metabolisms in a biosphere will produce waste gases that, with sufficient fluxes, will alter atmospheric composition and result in disequilibrium.

In the modern literature on exoplanets and astrobiology, atmospheric chemical disequilibrium is often cited as a possible means of life detection (Cockell et al. 2009; Kasting et al. 2009; Léger 2000; Sagan et al. 1993; Seager 2014; Seager & Bains 2015; Seager & Deming 2010), and sometimes criticized (Schwartzman & Volk 2004; Seager & Bains 2015). However, this idea is not quantified, except in rare and specific instances. For example, Simoncini et al. (2013) used kinetic arguments and non-equilibrium thermodynamics to infer the minimum power driving atmospheric disequilibrium for Earth and Mars, and Seager et al. (2013) applied kinetic arguments to deduce biomass estimates for biosignature gas detections. Kleidon (2012) reviewed the mechanisms for free energy generation on the Earth and the possible effects of increasing human consumption of free energy, whilst Ulanowicz and Hannon (1987) argued that surfaces dominated by biology such as tropical rainforests are more dissipative than desert surfaces, and that this difference in entropy production might be accessible to remote sensing. Estrada (2012) introduced a novel but perhaps non-intuitive atmospheric disequilibrium metric based on examining the directionality of the network of chemical reactions in an atmosphere. Estrada's method highlights species injected into an atmosphere, but many of them for Earth are anthropogenic, such as halocarbons.

Thermodynamic disequilibrium in planetary atmospheres and its quantification for biosignature detection on exoplanets has not been examined for several decades. Lippincott et al. (1967) and Lovelock (1975) made early attempts to calculate thermodynamic disequilibrium for the Solar System planets, but knowledge of the actual atmospheric composition of Solar System planets, computational methods, and

thermodynamic data for chemical equilibrium calculations have since greatly improved. Additionally, Lovelock (1975), who is the only author to report the magnitude of disequilibrium in Earth's atmosphere-ocean system, did not provide the details of his method. However, we infer that he probably used analytic calculations and assumed that key redox couples reacted to completion (see results section). This method does not give the correct answer for the thermodynamic equilibrium of the Earth atmosphere-ocean system because completion is not necessarily the same as the equilibrium state.

Another important issue is that all atmospheres are in disequilibrium to some extent because they receive a free energy flux from sunlight and, more generally, could obtain additional free energy from release of volcanic gases, tidal energy, or internal heat. Indeed there are already ostensible detections of thermodynamic disequilibrium in the atmospheres of transiting, Jovian-like exoplanets (e.g. Knutson et al. (2012); Moses et al. (2011); Stevenson et al. (2010), although see Line and Yung (2013) for an alternative view). Consequently, inferring life from atmospheric thermodynamic disequilibrium is a question of degree. In order to understand the issue properly, accurate quantification is necessary. Thus, part of the purpose in this work is to examine the abiotic disequilibria in Solar System atmospheres and compare with the Earth.

Here, we present a rigorous methodology and calculation of thermodynamic disequilibrium in the atmospheres of Solar System planets and Saturn's largest moon, Titan, using Gibbs free energy. We quantify chemical disequilibrium in atmospheres as the difference between the Gibbs energy of observed atmospheric constituents and the Gibbs free energy of the same atmosphere if all its constituents were reacted to equilibrium under prevailing conditions of temperature and pressure. For Earth, the purely gas phase calculation does not capture the disequilibrium in the atmosphere-ocean system, and so we present a method for quantifying the atmosphere-ocean disequilibrium using multiphase Gibbs energy minimization. We do not consider kinetic disequilibrium in our analysis, which will be the topic of future work. Finally, we discuss whether using thermodynamic disequilibrium as a biosignature is feasible on both practical and theoretical grounds. To promote cooperation in research, our Matlab source code and all the databases used for these calculations are available as post-publication open source software.

Methods

Gas phase calculations

Appendix I 2-A gives specifics on the gas phase calculations and here we outline the general methodology. To quantify thermodynamic disequilibrium, we model each atmosphere as a well-mixed closed system at a constant pressure (surface pressure or 1 bar for giant planets) and temperature (global mean surface temperature or the mean temperature at the 1 bar level for giant planets). Thermodynamic theory states that

for a closed chemical system at constant temperature and pressure, chemical equilibrium is achieved when the Gibbs free energy of the system is minimized.

If there are N chemical species in an atmosphere containing n_i moles of each gas i, then the total Gibbs free energy of the system (in Joules) is:

$$\begin{aligned} G_{(T,\mathrm{P})} &= \sum_i^N \left(\frac{\partial G}{\partial n_i} \right)_{T,P} n_i = \sum_i^N \mu_i n_i \\ &= \sum_i^N \left(\mu_i - G^\circ_{i(T,P_r)} + G^\circ_{i(T,P_r)} \right) n_i \end{aligned} \tag{1}$$

Here, μ_i (J/mol) is the partial molar Gibbs free energy, or equivalently, the chemical potential (see Anderson (2005)), $G^\circ_{i(T,P_r)}$ is the standard partial molar Gibbs free energy of gas i at reference pressure P_r which is typically 1 bar or 1 atm depending on the database used. We have written the expression in the second line of equation (1) because of a basic relationship in thermodynamics (the definition of chemical potential) is:

$$\mu_i - G^\circ_{i(T,P_r)} = RT \ln\left(a_i\right) = RT \ln\left(\frac{f_i}{f_i^\circ} \right) = RT \ln \frac{\left(P_i \gamma_{fi}\right)}{\left(P_i \gamma_{fi}\right)^\circ} \tag{2}$$

Here, $a_i = f_i / f_i^\circ$, is the activity of species i, f_i denotes partial fugacity, f_i° is a reference partial fugacity, γ_{fi} is the activity coefficient of species i, with γ°_{fi} a standard value, and P_i is partial pressure of species i. See Anderson (2005, p198-208) for a derivation of equation (2). The activities of reacting species are given by:

$$a_i = \left(\frac{f_i}{f_i^\circ} \right) = P_i \gamma_{fi} = \frac{P n_i}{n_T} \gamma_{fi} \tag{3}$$

where we have taken $f_i = 1$ bar as the reference state, n_i is the number of moles of species i, n_T is the total number of moles, and $P = \sum_i P_i$ is the total pressure by Dalton's Law.

Substitution of equations (2) and (3) into equation (1) gives the following expression for the Gibbs free energy of an atmosphere, where we drop the 'N' in the summation to avoid clutter:

$$G_{(T,\mathrm{P})} = \sum_i n_i (G^\circ_{i\,(T,\mathrm{P}_r)} + RT \ln(a_i)) = \sum_i n_i (G^\circ_{i\,(T,\mathrm{P}_r)} + RT \ln(P n_i \gamma_{fi} / n_T)) \tag{4}$$

This is a form of Gibbs free energy used in previous Gibbs free energy minimization schemes minimum (Eriksson 1971; Eriksson 1975; Venot et al. 2013; White et al. 1958). Here, $G_{(T,\mathrm{P})}$ is the Gibbs free energy of the system at constant temperature, *T*, and constant pressure, *P*. The number of moles of the *i*-th atmospheric species is given by n_i, the standard Gibbs free energy of the *i*-th species at some reference pressure P_r is given by $G^{\circ}_{i\,(T,\mathrm{P}_r)}$, and R = 8.314 J/mol is the universal gas constant. Variables γ_{fi} and n_T were defined earlier. The summation in equation (4) is over all molecular species in the planet's atmosphere. For purely gas phase calculations we will take $n_T = 1$ so that mixing ratios can be substituted for n_i and all Gibbs energy results will be in units of joules per mole of atmosphere. For example, for Earth, $n_{O_2} \approx 0.21$ and $n_{N_2} \approx 0.78$.

In practice, Gibbs free energy is only defined relative to some reference energy, and so we substitute absolute Gibbs energies for Gibbs energies of formation to obtain:

$$\Delta G_{(T,P)} = \sum_i n_i(\Delta_f G^{\circ}_{i\,(T,\mathrm{P}_r)} + RT\ln(P_i\gamma_{fi})) = \sum_i n_i(\Delta_f G^{\circ}_{i\,(T,\mathrm{P}_r)} + RT\ln(Pn_i\gamma_{fi}/n_T)) \quad (5)$$

Here, $\Delta_f G^{\circ}_{i\,(T,\mathrm{P}_r)}$ is the standard free energy of formation for the *i*-th species. This is defined as the free energy change associated with forming the *i*-th species from its constituent elements at temperature *T* and pressure P_r. It can be shown that the minimum of equation (4) is identical to the minimum of equation (5) (see Appendix I 2-B for this proof), and so in practice we find the equilibrium state by finding the equilibrium n_i that minimize equation (5), which we represent with an overbar as $\bar{n}_i$.

Temperature dependent standard Gibbs free energies of formation were calculated from enthalpies and entropies of formation retrieved from NASA's thermodynamic database (Burcat & Ruscic 2005). Some atmospheres such as that of Venus have high surface temperature and pressure, and so their constituent gases exhibit non-ideal behavior. We account for this by calculating temperature and pressure dependent fugacity coefficients for each species using the Soave equation as described in Walas (1985, p146). The Soave equation is an empirical equation of state that accounts for the non-zero volume of particles and attractive forces between pairs of particles. To calculate fugacity coefficients for a known mixture of gases at a specified temperature and pressure, the critical temperatures, critical pressures, acentric factors (a measure of non-sphericity of molecules) and binary interaction parameters for all the constituent species are required. We obtained critical temperatures, critical pressures and acentric factors from Perry et al. (2008, section 2-136). Tests indicate that binary interaction parameters have a negligible effect on the overall Gibbs energy changes we are interested in, and so all binary interaction parameters were assumed

to be zero in our analysis (see Appendix I 2-A). Because the fugacity coefficient is a function of species concentration, the fugacity coefficients of all gaseous species were recalculated at every iteration in our optimization routine to ensure convergence to the correct equilibrium. Typically, including fugacity coefficients does not change the results very much for Earth-like temperatures and pressures. However, for high-pressure atmospheres such as Venus, fugacity coefficients are important because the departures from ideal gas behavior are appreciable.

For any observed planetary atmosphere with a composition specified by mole fractions n_i, the equilibrium composition can be found by determining the mole fractions $\bar{n}_i$ that minimize $\Delta G_{(T,P)}$ in equation (5) subject to the constraint that atoms are conserved. The atom constraint condition is given by:

$$\textit{Equilibrium moles of element } k = \textit{Observed moles of element } k$$
$$\sum_i \nu_{ki} \bar{n}_i = \sum_i \nu_{ki} n_i \qquad (6)$$

Here, ν_{ki} is the number of atoms of element *k* per molecule of the *i*-th species.

The above framework is a constrained, non-linear optimization problem: the equilibrium state of an atmosphere can be found by minimizing equation (5) subject to equation (6). We used an interior points method (Byrd et al. 2000; Byrd et al. 1999) implemented using Matlab's *fmincon* function to solve this optimization problem. Interior points is an efficient and reliable optimization technique known to be useful for chemical equilibrium problems (see Karpov et al. (1997) and references therein). For gas phase Gibbs energy minimization the equation to be optimized is convex (has non-negative second derivative) and so any local minimum will be the single global minimum (White et al. 1958).

To quantify the chemical disequilibrium in a planet's atmosphere, we define the "available Gibbs energy", Φ, as the difference in Gibbs free energy between the observed (initial) state and the equilibrium state:

$$\Phi \equiv G_{(T,P)}(n_i) - G_{(T,P)}(\bar{n}_i) \qquad (7)$$

Since Gibbs free energy is only defined relative to some reference energy, in practice we compute available Gibbs energy using this equivalent expression:

$$\Phi = \Delta G_{(T,P)}(n_i) - \Delta G_{(T,P)}(\bar{n}_i) \qquad (8)$$

See Appendix I 2-B for a proof of the equivalence of equations (7) and (8). The available Gibbs energy, Φ, has units of joules per mole of atmosphere. Thermodynamic theory states that this Gibbs free energy difference is the maximum useful work that can be extracted from the system. In other words, Φ is the untapped chemical free energy in a planet's atmosphere and so provides our metric of disequilibrium.

Multiphase calculations

The numerical approach described above applies to gaseous systems only such as Mars, Venus and Jupiter. To calculate chemical disequilibrium for planets with surface oceans, we reformulate the Gibbs energy expression for multiphase systems. Appendix I 2-C gives specifics of the multiphase calculations and here we provide a general overview. We follow Karpov et al. (1997), and use the following expression for the Gibbs energy of a multiphase system:

$$\Delta G_{(T,P)} = \sum_i c_i n_i + \sum_\alpha \sum_{i\in\alpha} n_i RT \ln(n_i / n_\alpha) - \sum_{j=aqueous\ species} n_j RT \ln(n_w / n_{aq})$$

$$c_i = \begin{cases} \Delta_f G^\circ_{i\,(T,\mathrm{P})} + RT\ln(\gamma_{fi}) + RT\ln(P), & i \in gas \\ \Delta_f G^\circ_{i\,(T,\mathrm{P})} + RT\ln(\gamma_{aw}), & i \in water \\ \Delta_f G^\circ_{i\,(T,\mathrm{P})} + RT\ln(\gamma_{ai}) + RT\ln(55.5084), & i \in aqueous \end{cases} \quad (9)$$

Here, we have simplified equations in Karpov et al. (1997) to exclude solid phases and non-water pure liquids because we don't consider such systems in this study. In addition to the variables already defined above, we have the following:

α = index for the phase (gaseous, water or aqueous).

n_α = total number of moles of species in phase α.

n_w = total number of moles of liquid water in the system.

n_{aq} = total number of moles of aqueous species in the system.

γ_{aw} = activity coefficient of water.

γ_{ai} = activity coefficient of the i-th aqueous species.

We see that equation (9) for the gas phase system ($c_i, i \in gas$) is identical to equation (5) if we let $n_\alpha = n_T$.

To calculate the equilibrium state of Earth's atmosphere-ocean system, we minimize equation (9) above subject to the constraint that atoms and charge are conserved, where the latter means that aqueous systems are electroneutral. The atom constraint is identical to that used for the gaseous systems as defined by equation (6). The charge constraint is given by:

$$Total\ charge\ in\ equilibrium = Total\ charge\ in\ observed\ state$$
$$\sum_i q_i \bar{n}_i = \sum_i q_i n_i \quad (10)$$

Here, q_i, is the charge per molecule of the *i*-th species. Just as for the gaseous calculations, the Gibbs energy difference between the observed and equilibrium states, Φ, can be calculated once the equilibrium state is determined.

Temperature and pressure dependent Gibbs free energies of formation for aqueous species were calculated from the SPRONS96 database in SUPCRT (Johnson et al. 1992) and the methodology described in Walther (2009). We assumed that the Born coefficients, which describe species-specific solvation properties, would have a negligible effect on Gibbs energies and so those terms were dropped from the calculations. Activity coefficients for aqueous species were approximated using the Truesdell-Jones equation and thermodynamic coefficients from Langmuir (1997, p133) (see Appendix I 2-C). For Earth, the available Gibbs energy is quite sensitive to water activity. Thus rather than use the approximation above, the activity coefficient for water was calculated rigorously using a simplified form of the Pitzer equations (Marion & Kargel 2007) and Pitzer coefficients from Appelo and Postma (2005) and Marion (2002).

Finding the equilibrium state for multiphase systems is more challenging than for single-phase gaseous systems. The Matlab function *fmincon* was once again used to implement the optimization, but this time we provided the analytic first derivative gradient for the Gibbs energy function in equation (9). This ensured more rapid and reliable convergence. For multiphase Gibbs energy minimization problems there is no guarantee that the local minima equal the global minimum (Nichita et al. 2002). Consequently, we implemented a simple global minimum search by iterating over a large ensemble of initial conditions and selecting the solution from the ensemble with the minimum of the minima (see Appendix I 2-C for details).

Semi-analytic validation

Validation of gas phase calculations was initially done using a classic textbook case from Balzhiser et al. (1972, p. 513-527) which was found to match our numerical calculations. This textbook case was a gas phase reaction of ethane and steam at 1000K to form H_2, CO and various hydrocarbons. We also correctly solved the equilibrium using the method of Lagrange multipliers as a check.

Furthermore, to corroborate the numerical Gibbs free energy calculations for planetary atmospheres, we also approximated the available Gibbs energy in each atmosphere using a simple analytic expression. For a single reaction between arbitrary reactants and products,

$$AR_1 + BR_2 \rightleftharpoons CP_1 + DP_2 \qquad (11)$$

The Gibbs energy of this reaction is given by:

$$\Delta_r G = \Delta_r G^\circ + RT\ln(Q) = \Delta_r G^\circ + RT\ln\left(\frac{{a_{P1}}^C {a_{P2}}^D}{{a_{R1}}^A {a_{R2}}^B}\right) \quad (12)$$

Here, A, B, C and D are the stoichiometric coefficients representing reactants R_1, R_2, products P_1 and P_2, respectively. The activity of each species is a_X, R is the universal gas constant and T is the temperature of the system. The left hand side of equation (12), $\Delta_r G$, is the change in Gibbs energy of the system per A moles of reactant R_1 and B moles of reactant R_2 that are converted to products. The standard free energy of the reaction, $\Delta_r G^\circ$, represents the Gibbs energy of the reaction when the activities of all species equal unity. At equilibrium, the left hand side of equation (12) equals zero. This equilibrium can be found by appropriate substitution for each of the activities in terms of initial abundances and the total moles reacted to reach equilibrium (the only unknown variable), and by solving the resultant polynomial (see Appendix I 2-D). This equilibrium condition is equivalent to minimizing the Gibbs energy of the same system using equation (5).

The available Gibbs energy of the system, Φ, can be obtained by integrating $\Delta_r G$ from the initial state to the equilibrium state. Strictly speaking, this semi-analytic approach can only be applied to systems of gases where there is only one possible reaction, and not to complex mixtures of gases such as planetary atmospheres. However, this calculation can be repeated for all the key reactions in a planet's atmosphere, and the summed available Gibbs energies can be compared to the numerical result from Gibbs energy minimization. The key reactions for these semi-analytic calculations were chosen using the important redox couples identified by chemical intuition for each atmosphere. The two approaches are not exactly equivalent because treating each reaction independently does not account for interactions between multiple reactions. To simplify the semi-analytic calculations, we also assumed that the total moles in the atmosphere remained unchanged as the reaction proceeds. Consequently, we expect small differences between the semi-analytic and numerical approaches. Appendix I 2-D gives step-by-step detail on semi-analytic procedures. The semi-analytic approximations described above for gas phase systems can also be applied to aqueous reactions in a multiphase system such as the Earth.

Validation using Aspen Plus

Both gaseous and multiphase calculations were validated using the commercial software package Aspen Plus (Version 8.6), which is commonly used in chemical engineering. Aspen Plus provided a completely independent check of our calculations because it uses different thermodynamic databases and property models to both our Matlab calculations and semi-analytic approximations. We used an equilibrium reactor called "RGIBBS" in Aspen Plus to implement gas phase and multiphase equilibrium calculations by Gibbs

free energy minimization. We also used the Peng-Robinson equation of state (Prausnitz et al. 1999) model for gas phase calculations, which is appropriate for the temperatures and pressures we are interested in. For multiphase calculations, we used a "Flash2" phase separator in the Aspen Plus model in addition to an RGIBBS reactor, which ensured that the phases of aqueous species were correctly assigned. Without the phase separator, the equilibrium results were unphysical, and the resultant Gibbs energy change was inaccurate. We report results from the Electrolyte Non-Random Two Liquid (ELECNRTL) model in the main text (e.g. see Prausnitz et al. (1999) chapter 6). ELECNRTL is the recommended activity coefficient model for calculations involving electrolytes (Aspen Technology Inc. 2000). Appendix I 2-E explains the Aspen Plus multiphase calculation in more detail, and reports results for a different electrolyte model.

Planetary data

The observed atmospheric compositions used in this analysis were obtained from a variety of up-to-date sources. The atmospheric composition of Venus at the surface was taken from Fegley (2014, p. 131) and Krasnopolsky and Lefèvre (2013, p. 64). The atmospheric composition of Mars at the surface was taken from Lodders and Fegley (1998) but updated with *Curiosity Rover* observations (Baines et al. 2014; Mahaffy et al. 2013). The atmospheric composition of Jupiter at 1 bar was taken from Lodders and Fegley (1998) but updated using the compilation in Irwin (2009, p. 100-3). The atmospheric composition of Titan at the surface was taken from the review by Catling (2015b). Uranus' atmospheric composition at 1 bar was inferred from the review by Irwin (2009, p. 124), Lodders and Fegley (1998) and Catling (2015b). Finally, Earth's atmospheric composition was assumed to be that of the US Standard Atmosphere and the abundance of dissolved ions in average seawater was obtained from Pilson (2012, p. 59). Nitrate abundance was obtained from Gruber (2008, p. 13).

Results

Tables 1-7 show equilibrium calculations for the Solar System atmospheres. The format of each table is the same: the first column lists the species present in each body's atmosphere, the second column gives the observed mixing ratios of these species, and the third column is the species abundances at equilibrium, as determined by our Gibbs free energy minimization code. The fourth column is an independent validation of our calculations where the equilibrium abundances are determined using the commercial software package, Aspen Plus. The equilibrium abundances from our Gibbs energy minimization and from Aspen Plus match very closely in every case. Bolded rows highlight the species where abundances change during the reaction to equilibrium. Figures 1-7 are the graphical representation of tables 1-7, respectively. Observed (black bars) and equilibrium (grey bars) abundances of all species for each atmosphere are plotted on a log scale. We only plot the equilibrium abundances from our Gibbs energy minimization calculations and not from Aspen Plus since the differences are barely visible. All equilibrium calculations are performed

at observed mean surface temperature and pressure conditions (for terrestrial planets), or at 1 bar and the mean temperature at 1 bar (for giant planets with no surface), unless stated otherwise.

Note that although the observed abundances in the tables and figures are mixing ratios, the equilibrium abundances do not sum to exactly unity. The equilibrium molar abundances are instead the moles of each species that remain when 1 mole of the observed atmosphere reacts to equilibrium (reaction to equilibrium conserves atoms but does not conserve the number of moles in an atmosphere). We chose not to renormalize the equilibrium abundances to obtain mixing ratios because it was easier to identify which species are involved in reactions from the tables without normalization.

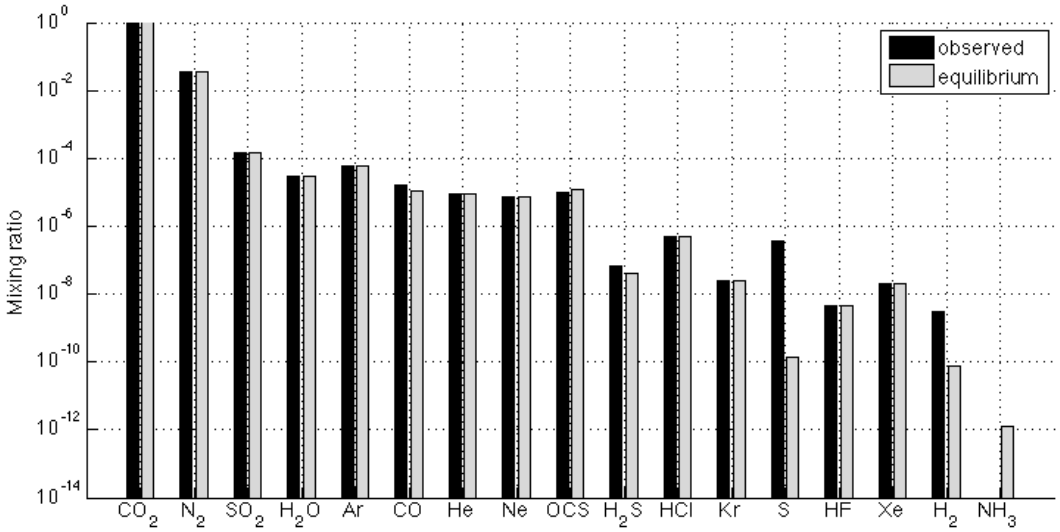

*Figure 2-1: Equilibrium calculation for Venus' atmosphere. The black bars show the observed mixing ratios of all known species in Venus' atmosphere at the surface level (*T*=735.3 K,* P*=92.1 bar). The grey bars show the equilibrium abundances of each of these species as determined by our Gibbs free energy minimization code. The black bars are the column 2 abundances in table 1, and the grey bars are the column 3 abundances in table 1. Notice the loss of S and reduction of CO and H_2S at equilibrium.*

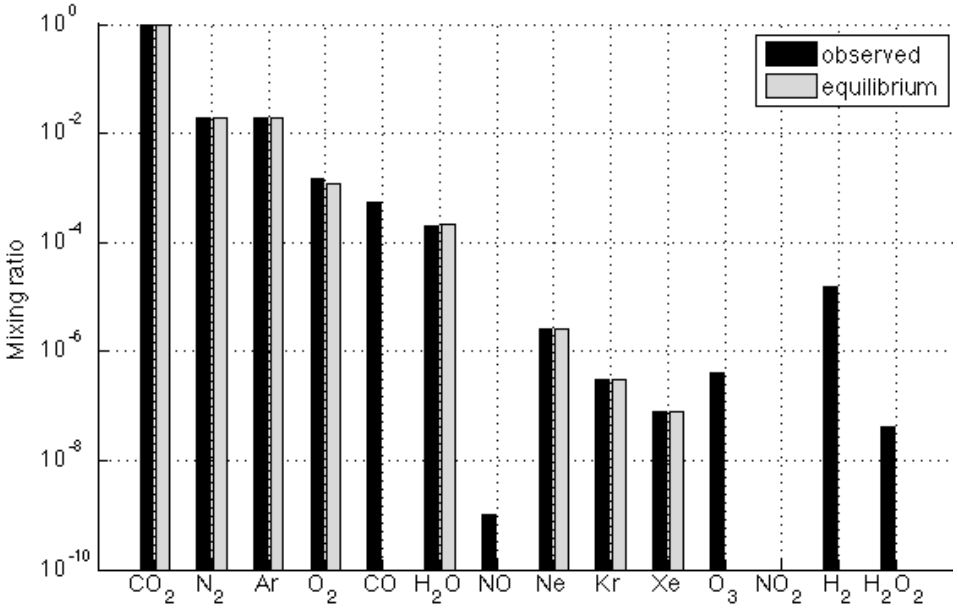

Figure 2-2: Equilibrium calculation for Mars' atmosphere. The black bars show the observed mixing ratios of all known species in Mars' atmosphere at the surface level (T=214 K, P=0.006 bar). The grey bars show the equilibrium abundances of each of these species as determined by our Gibbs free energy minimization code. The black bars are the column 2 abundances in table 2, and the grey bars are the column 3 abundances in table 2. Notice the loss of CO and reduction of O_2 at equilibrium. The compensating increase in CO_2 is too small to be visible on this figure.

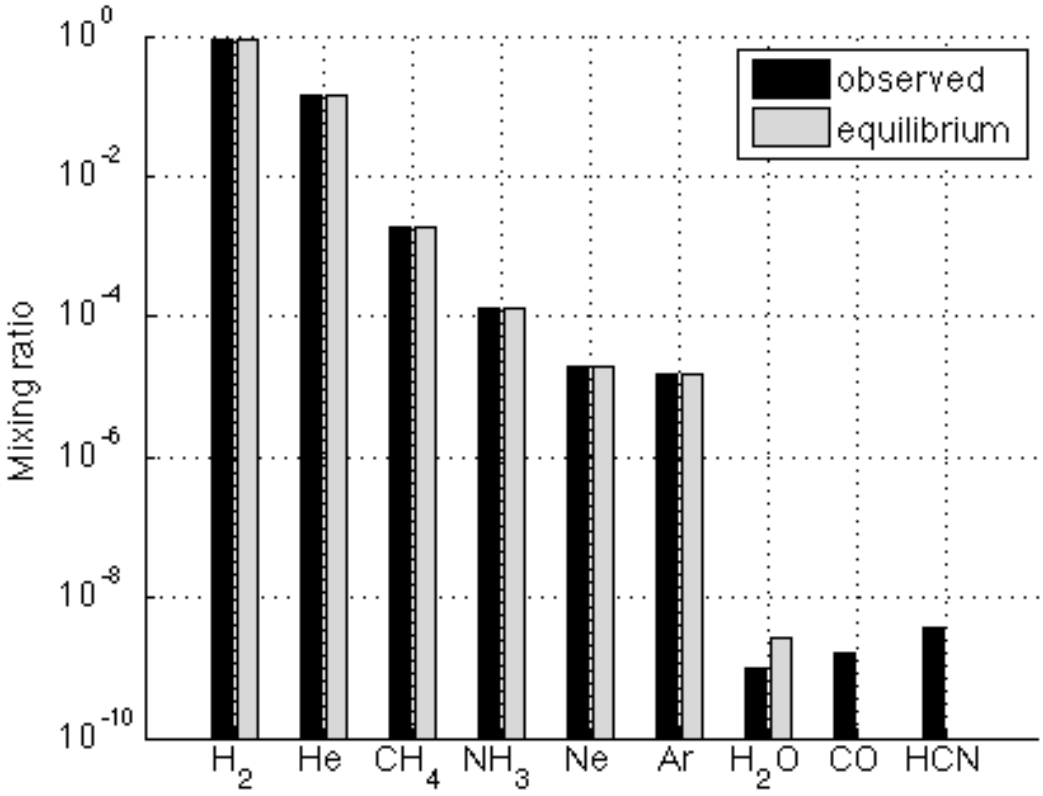

Figure 2-3: Equilibrium calculation for Jupiter's atmosphere. The black bars show the observed mixing ratios of all known species in Jupiter's atmosphere at the 1 bar level (T=165 K). The grey bars show the equilibrium abundances of each of these species as determined by our Gibbs free energy minimization code. The black bars are the column 2 abundances in table 3, and the grey bars are the column 3 abundances in table 3. Notice the loss of CO and HCN at equilibrium.

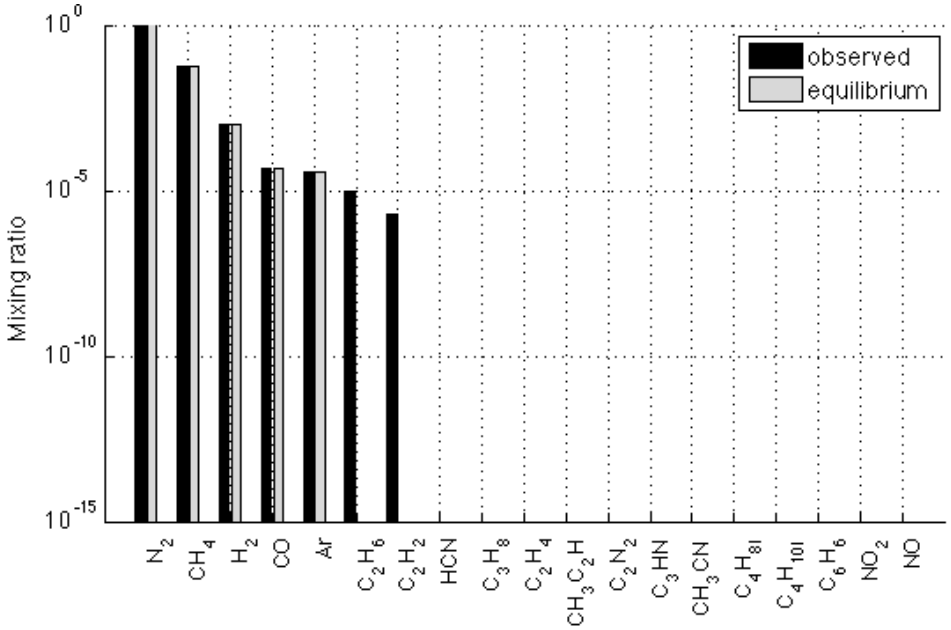

Figure 2-4: Equilibrium calculation for Titan's atmosphere. The black bars show the observed mixing ratios of all known species in Titan's atmosphere at the surface level (T=93.65K, P=1.46 bar). The grey bars show the equilibrium abundances of each of these species as determined by our Gibbs free energy minimization code. The black bars are the column 2 abundances in table 4, and the grey bars are the column 3 abundances in table 4. Notice the loss of ethane (C_2H_6) and acetylene (C_2H_2) at equilibrium.

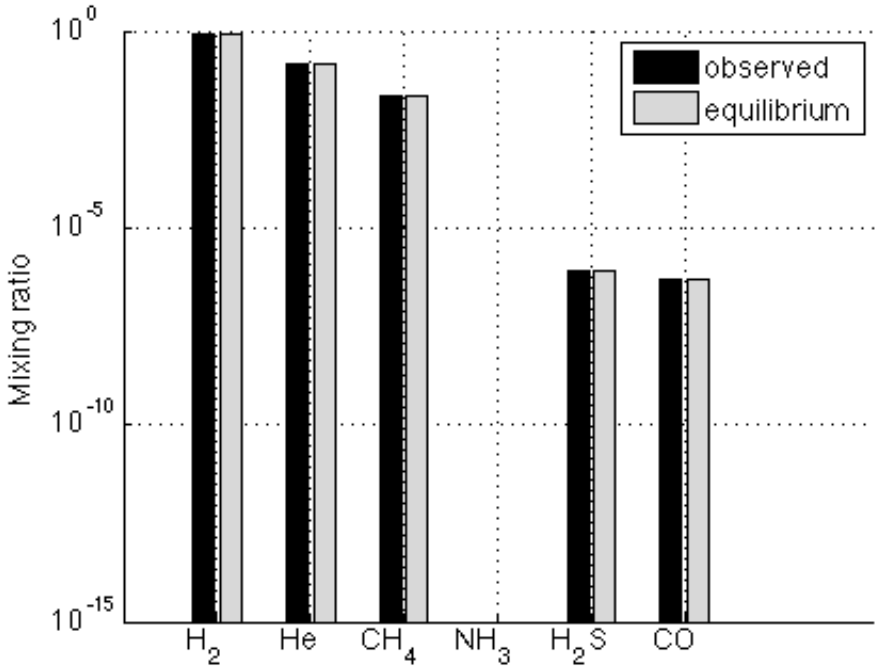

Figure 2-5:Equilibrium calculation for Uranus' atmosphere. The black bars show the observed mixing ratios of all known species in Uranus' atmosphere at the 1 bar level (T=75K). The grey bars show the equilibrium abundances of each of these species as determined by our Gibbs free energy minimization code. The black bars are the column 2 abundances in table 5a, and the grey bars are the column 3 abundances in table 5a. There is no change in species abundances by reaction to equilibrium.

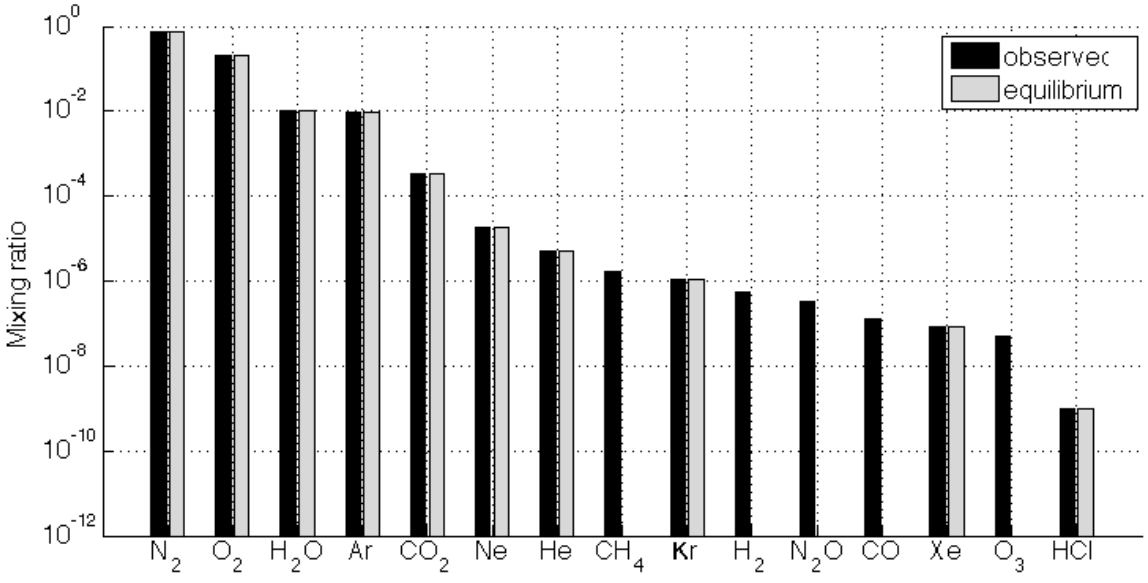

Figure 2-6: Equilibrium calculation for Earth's atmosphere (not including ocean). The black bars show the observed mixing ratios of all known species in Earth's atmosphere at the surface level (T=288.15 K, P=1.013 bar). The grey bars show the equilibrium abundances of each of these species as determined by our Gibbs free energy minimization code. The black bars are the column 2 abundances in table 6, and the grey bars are the column 3 abundances in table 6. Notice the loss of reduced species (CH_4, H_2, CO) at equilibrium.

Table 8 shows the available Gibbs energy, Φ (defined in equation (7)) in each planet's atmosphere, and figure 8a is a graphical representation of these results. The second column in table 8 gives the available Gibbs energy as determined by our own numerical code for Gibbs energy minimization. Column 3 shows the semi-analytic approximation of available Gibbs energy that were calculated by choosing key reactions, finding their equilibria independently, and summing the Gibbs energy changes associated with each reaction (see methods section). Column 4 is the available Gibbs energy in each atmosphere as determined by the commercial software package, Aspen Plus. In almost every case, the available Gibbs energies from these three methods are consistent to within a few percent or better. The excellent agreement is encouraging because Aspen Plus uses different thermodynamic databases and models to our Gibbs energy minimization calculations. Column 5 gives the Gibbs free energy of each planet as reported by Lovelock (1975). The discrepancies between their results and our results are attributable to much improved knowledge of atmospheric compositions and our more accurate computational techniques (see below).

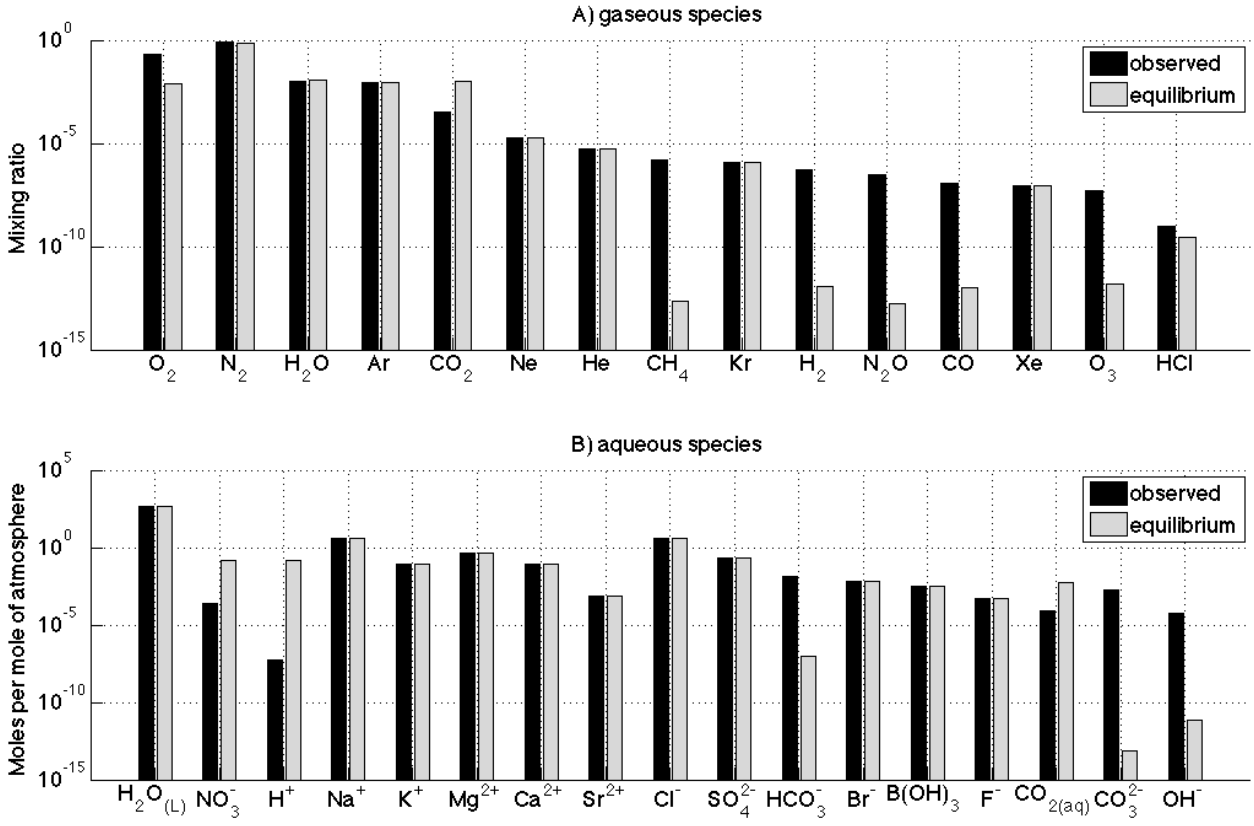

Figure 2-7: Multiphase equilibrium calculation for Earth's atmosphere-ocean system. The black bars show the observed mixing ratios and abundances of all species in Earth's atmosphere and oceans at the surface level (T=288.15 K, P=1.013 bar). The grey bars show the equilibrium abundances of each of these species as determined by our Gibbs free energy minimization code. The black bars are the column 2 abundances in table 7, and the grey bars are the column 3 abundances in table 7. A) Shows all gas phase species whereas B) shows all aqueous species. Notice that in equilibrium there is a large decrease in O_2 since oxygen is converted to nitric acid (H^+ and NO_3^- increase) by reaction (21).

We now discuss what accounts for the disequilibrium in each atmosphere. We do this by identifying the key gases that are in disequilibrium and describing how the chemical conditions on each body give rise to various disequilibria.

Venus

The disequilibrium in Venus' lower atmosphere is comparatively small, which is expected because the high pressure and temperature favors chemical reactions that push the atmosphere close to equilibrium (Yung & DeMore 1999, p292). There is little difference between the observed abundances and equilibrium abundances (figure 1, table 1) except for very minor species. Consequently, the available Gibbs energy in Venus' atmosphere is only ≈0.06 J/mol (table 8).

The largest contributor to the disequilibrium in Venus' atmosphere (in terms of available energy) is the coexistence of elemental sulfur (S) and carbon dioxide (CO_2). Semi-analytic calculations predict that the following reaction should deplete all the elemental sulfur in Venus' atmosphere:

$$2CO_2 + S \rightleftharpoons SO_2 + 2CO \qquad (13)$$

Gibbs energy minimization calculations confirm that elemental sulfur is absent in equilibrium. The disequilibrium in Venus' atmosphere is maintained by photochemistry; photochemical dissociation of SO_2 and OCS in the upper atmosphere maintains out of equilibrium sulfur chemistry (Yung & DeMore 1999, p. 292).

Table 2-1: Equilibrium calculation for Venus' atmosphere (T=735.3 K, P=92.1 bar). The second column gives the observed surface mixing ratios of all species in Venus' atmosphere and the third column gives the equilibrium abundances of each species as determined by our own Gibbs free energy minimization Matlab code. The fourth column is an independent validation of the equilibrium abundances calculated using the commercial software package, Aspen Plus. The fifth column gives the change in abundance for each species according to our Gibbs energy minimization (column three minus column two). Bolded rows highlight the species where abundances change during the reaction to equilibrium. The available Gibbs energy from our own code is Φ = 0.0596 J/mol.

Species	Initial mixing ratio	Final abundance (*fmincon*)	Final abundance (*Aspen*)	Final – initial abundance (*fmincon*)
CO_2	**0.965**	**0.965004**	**0.9650041**	**0.0000039**

N_2*	0.034715	0.034715	0.034715	-6.21E-13
SO_2	**0.00015**	**0.000148**	**0.000147949**	**-0.00000197**
H_2O	**0.00003**	**3.00329E-05**	**3.00295E-05**	**3.29E-08**
Ar	0.000061	0.000061	0.000061	0
CO	**0.000017**	**1.07569E-05**	**1.04986E-05**	**-0.00000624**
He	0.000009	0.000009	0.000009	0
Ne	0.000007	0.000007	0.000007	0
OCS	**0.00001**	**1.23452E-05**	**1.24294E-05**	**0.00000235**
H_2S	**0.00000007**	**4.00713E-08**	**4.13474E-08**	**-2.99E-08**
HCl	0.0000005	0.0000005	0.0000005	0
Kr	0.000000025	0.000000025	0.000000025	0
S	**0.00000035**	**1.34652E-10**	**2.1696E-17**	**-0.00000035**
HF	4.5E-09	4.5E-09	4.5E-09	0
Xe	0.00000002	0.00000002	0.00000002	0
H_2	**0.000000003**	**7.5802E-11**	**2.13576E-09**	**-2.92E-09**
NH_3	**1E-14**	**1.25215E-12**	**1.1679E-14**	**1.24E-12**

*N2 was slightly modified from textbook value to ensure mixing ratios summed to 1.

Mars

The disequilibrium in Mars' atmosphere is large compared to other Solar System atmospheres. The available Gibbs energy in Mars' atmosphere, 136 J/mol, is 1-2 orders of magnitude greater than every other atmosphere we consider except for Earth's atmosphere-ocean system. Figure 2 and table 2 show several abundant constituents in Mars' atmosphere with observed mixing ratios substantially different from equilibrium abundances.

The largest contributor to disequilibrium in Mars' atmosphere (in terms of available energy) is the coexistence of CO and O_2. Both semi-analytic and numerical calculations predict that, in equilibrium, all the CO should be oxidized by O_2 to form CO_2 by the following reaction:

$$2CO + O_2 \rightleftharpoons 2CO_2 \qquad (14)$$

This is confirmed by the stoichiometry of the change in abundances from the numerical calculation (column 5, table 2). Reaction to equilibrium decreases the abundance of O_2 by 2.8538×10^{-4} moles and decreases the abundance of CO by 5.57×10^{-4} moles, i.e. almost a 1:2 ratio. The abundance of CO_2 increases by 5.57×10^{-4} moles. The stoichiometry is not exactly the same as equation (14) because oxygen is also depleted by reaction with hydrogen gas by the following reaction:

$$2H_2 + O_2 \rightleftharpoons 2H_2O \qquad (15)$$

Since numerical calculations indicate that hydrogen decreases by 0.15×10^{-4} moles (column 5, table 2), this implies molecular oxygen must decrease by $0.15\times10^{-4}/2 = 0.075\times10^{-4}$ moles. Subtracting this decrease from

the overall change in oxygen yields $(2.8538\text{-}0.075)\times10^{-4} = 2.7788\times10^{-4}$ moles, which is a closer match to the stoichiometry in equation (14). The remaining discrepancy is similarly explained by the reaction of ozone to form molecular oxygen:

$$2O_3 \rightleftharpoons 3O_2 \qquad (16)$$

Disequilibrium in Mars' atmosphere is maintained by photochemistry. The photodissociation of CO_2 continuously replenishes CO in the Martian atmosphere (Nair et al. 1994; Zahnle et al. 2008). The Martian atmosphere also has an overabundance of H_2 and O_3, both of which are maintained by photodissociation of water.

Table 2-2: Equilibrium calculation for Mars' atmosphere (T=214K, P= 0.006 bar). Columns are the same as in table 1. The initial mixing ratios are surface abundances. The available Gibbs energy from our own code is Φ *= 136.3 J/mol.*

Species	Initial mixing ratio	Final abundance (*fmincon*)	Final abundance (*Aspen*)	Final – initial abundance (*fmincon*)
CO_2	**0.9597**	**0.960257**	**0.960257**	**0.000557**
N_2	0.0189	0.0189	0.0189	5E-10
Ar*	0.019165	0.019165	0.0191646	0
O_2	**0.00146**	**0.001175**	**0.00117462**	**-0.00028538**
CO	**0.000557**	**5.51991E-17**	**0**	**-0.000557**
H_2O	**0.0002**	**0.000215**	**0.00021504**	**0.000015**
NO	**0.000000001**	**2.36011E-16**	**1.96E-24**	**-0.000000001**
Ne	0.0000025	0.0000025	0.0000025	0
Kr	0.0000003	0.0000003	0.0000003	0
Xe	0.00000008	0.00000008	0.00000008	0
O_3	**0.0000004**	**8.702E-17**	**0**	**-0.0000004**
NO_2	1E-30	8.84675E-16	6.19E-17	8.85E-16
H_2	**0.000015**	**6.01993E-17**	**0**	**-0.000015**
H_2O_2	**0.00000004**	**1.19914E-16**	**0**	**-0.00000004**

*Ar was modified slightly from textbook value to ensure mixing ratios summed to 1.

The difference between the available Gibbs energy in Mars' atmosphere and the available energy in other photochemically driven atmospheric disequilibria can be partly explained by differences in atmospheric column mass and chemical complexity. Since Mars' atmosphere is more tenuous than other atmospheres, and lacks species (e.g., chlorine-bearing gases) that enable more pathways of catalytic recombination of CO_2, photochemical reactions have a greater effect on overall composition. In contrast, photochemistry on Venus does not result in large available Gibbs energy per mole of atmosphere because the thick atmosphere along with efficient catalysts buffers its effect on composition. The CO_2 column photodissociation rates on Mars and Venus are comparable, 2×10^{12} molecules/cm^2/s (Huguenin et al. 1977) and 7.6×10^{12}

molecules/cm^2/s (Bougher et al. 1997, p. 448), respectively, whereas the SO_2 column photodissociation rate, or equivalently the H_2SO_4 production rate, on Venus is ~5.6×10^{11} molecules/cm^2/s (Krasnopolsky 2015; Zhang et al. 2012) . However, the column mass is larger on Venus. The column mass is P/g, where P is surface pressure and g is gravitational acceleration. On Venus, the column mass is 93.3×10^5 Pa/ 8.87 m/s^2 = 1,051,680 kg/m^2 (taking the pressure at the mean elevation), whereas on Mars the column mass is 600 Pa/ 3.711 m/s^2 = 159.1 kg/m^2, so the Venus:Mars ratio is 1,051,680/159.1 ~ 6,600. Whereas Mars has catalytic recombination of CO_2 from only odd hydrogen species, Venus has more efficient catalytic cycles involving Cl, N and H species for CO_2 recombination (Yung & DeMore 1999, p. 249,288), such that O_2 on Venus has an upper limit concentration <0.3 ppmv. Consequently, the products of CO_2 dissociation do not significantly influence the disequilibrium on Venus; instead, sulfur chemistry makes the dominant contribution, as discussed earlier. The net result is that the available free energy in Venus' atmosphere is ~2000 times smaller than that of Mars (table 8).

Note that Mars' atmospheric composition varies seasonally via CO_2 exchange with polar caps, and on longer timescales obliquity cycles will modulate atmospheric CO_2 due to regolith adsorption. However, these changes in atmospheric composition are unlikely to have a large effect on the available energy in Mars' atmosphere. The total CO_2 reservoir in the regolith and the polar ice is equivalent to 5-30 mbar CO_2 (Covey et al. 2013, p. 171). Zahnle et al. (2008) used a 1D photochemical model to compute self-consistent Mars atmospheres with pCO_2 varying from 1-100 mbar, thereby encompassing the range of atmospheric variability from seasonal and obliquity variations. We computed the available energy for this range of photochemical outputs and found that it was less than 200 J/mol regardless of pCO_2. Although the photochemical model calculates the water volume mixing ratio from a specified relative humidity, H_2O is redox neutral and so changing its abundance will not have a large effect on available energy.

Jupiter

The disequilibrium in Jupiter's atmosphere at the 1 bar level is very small compared to other atmospheres in the Solar System (≈0.001 J/mol). The observed mixing ratios and equilibrium abundances (table 3, figure 3) are virtually identical; the largest changes are at the parts per billion level. The small disequilibrium in Jupiter's atmosphere is attributable to the coexistence of HCN with H_2 and the coexistence of CO with H_2. Both numerical and semi-analytic calculations predict that HCN and CO should be completely depleted in equilibrium by the following reactions

$$3H_2(g) + HCN(g) \rightleftharpoons CH_4(g) + NH_3(g) \quad (17)$$

$$3H_2 + CO \rightleftharpoons CH_4 + H_2O \quad (18)$$

This is confirmed by the stoichiometry of the change in abundances from the numerical calculation (column 5, table 3): HCN and CO abundances decrease by 3.6×10^{-9} and 1.6×10^{-9} moles, respectively, whereas NH_3 and H_2O abundances increase by 3.6×10^{-9} and 1.6×10^{-9} moles, respectively. Based on these numbers and equations (17) and (18), we would predict that CH_4 abundance should increase by $(3.6+1.4)\times10^{-9} = 5.2\times10^{-9}$ moles, and that H_2 abundance should decrease by $3\times(3.6\times10^{-9} + 1.6\times10^{-9}) = 1.56\times10^{-9}$ moles. These predictions exactly match the observed changes in these species in table 3.

It is not surprising that Jupiter's atmosphere is very close to equilibrium. Photochemically produced disequilibrium species are vigorously mixed into the high temperature interior (1000 K) where they are hydrogenated to reform equilibrium species (Lewis 2012, p. 209-212). The small disequilibrium that remains is attributable to a combination of deeper vertical mixing, material delivery, and photochemistry. CO is thermodynamically favored in the very high-temperature interior and deep vertical mixing delivers it to the upper atmosphere (Prinn & Barshay 1977), although some infall of material from space is required to explain observed CO abundances (Bézard et al. 2002). HCN is also thermodynamically favored in the interior, but observed abundances are best explained by photochemical sources (Kaye & Strobel 1983).

Table 2-3: Equilibrium calculation for Jupiter's atmosphere. Columns are the same as in table 1. The initial mixing ratios are abundances at the 1 bar level (T=165K). The available Gibbs energy from our own code is Φ *= 0.00103 J/mol.*

Species	Initial mixing ratio	Final abundance (*fmincon*)	Final abundance (*Aspen*)	Final – initial abundance (*fmincon*)
H_2	**0.862**	**0.86199998**	**0.862**	**-1.56E-08**
He*	0.136024	0.136024	0.136024	0
CH_4	**0.00181**	**0.001810005**	**0.00181001**	**5.2E-09**
NH_3	**0.00013**	**0.000130004**	**0.000130004**	**3.6E-09**
Ne	0.0000199	0.0000199	0.0000199	0
Ar	0.0000157	0.0000157	0.0000157	0
H_2O	**0.000000001**	**2.6E-09**	**2.6E-09**	**1.6E-09**
CO	**1.6E-09**	**1.13471E-19**	**0**	**-1.6E-09**
HCN	**3.6E-09**	**9.49988E-20**	**0**	**-3.6E-09**

*He was modified from textbook value to ensure mixing ratios summed to 1.

We repeated the equilibrium calculation for Jupiter at the 1 millilbar level. This is of interest for exoplanet characterization since infrared spectroscopy may be limited to probing the millibar level of Jovian-like atmospheres due to thick clouds or hazes. The mean temperature at 1 millibar is approximately equal to the temperature at 1 bar due to the temperature inversion in Jupiter's stratosphere, and consequently any difference in available Gibbs energy can be ascribed to changing mixing ratios. Using stratospheric species abundances from Irwin (2009, p. 101), we found the available Gibbs energy in Jupiter's atmosphere at 1

millibar to be 0.35 J/mol. This disequilibrium can be ascribed to photochemically replenished organics such as C_2H_6, and to a lesser extent C_2H_2 and C_2H_4.

Titan

The moderate disequilibrium in Titan's atmosphere (≈1.2 J/mol) is also driven by photochemistry. Both ethane (C_2H_6) and acetylene (C_2H_2) exist in Titan's atmosphere, whereas semi-analytic and numerical calculations predict that these species should be depleted in equilibrium by reactions with H_2 to form CH_4:

$$C_2H_6 + H_2 \rightleftharpoons 2CH_4 \quad (19)$$

$$C_2H_2 + 3H_2 \rightleftharpoons 2CH_4 \quad (20)$$

Table 4 confirms this stoichiometrically: ethane and acetylene abundances decrease by 1×10^{-5} and 2×10^{-6}, respectively, by reaction to equilibrium (table 4). From the equations above, this would imply that CH_4 abundance should increase by $2\times (1\times10^{-5}+2\times10^{-6}) = 2.4\times10^{-5}$ whereas hydrogen abundance should decrease by $3\times2\times10^{-6}+1\times10^{-5}=1.6\times10^{-5}$. These predictions exactly match the observed changes in these species in table 4.

We have not included Titan's hydrocarbon lakes in this calculation for several reasons. Firstly, the thermodynamics of cold hydrocarbon solutions is beyond the scope of this study and poorly known. Second, the composition of lakes on Titan and the degree to which they are variable are unknown. Third, current hypothetical estimates of lake composition (Cordier et al. 2009; Glein & Shock 2013) are based on purely thermodynamic equilibrium models and so are inappropriate for revealing disequilibrium. The total volume of Titan's lakes is estimated to be 32,000 km^3 (Lorenz et al. 2014). If we assume the lake density is 654 kg/m^3, which is the density of liquid ethane at 92.5 K (Younglove & Ely 1987), then the total mass of the lakes is 2.1×10^{16} kg. The surface pressure on Titan is 1.5 bar, the surface area is 8.3×10^7 km^2, and the surface gravity is 1.35 ms^{-2}. This implies the mass of the atmosphere is $(8.3\times10^7\times1000^2\ m^2)\times(10^5\times1.5\ Pa)/(1.35\ ms^{-2}) = 9.2\times10^{18}$ kg. Thus, the mass of the lakes is 0.2% the mass of Titan's atmosphere. Disequilibrium species at the parts per thousand level can impact the available energy, as evidence by the CO-O_2 pairing in Mars' atmosphere. Consequently, if Titan's lakes are in chemical disequilibrium with the atmosphere, then the available Gibbs energy of the total fluid reservoir may be larger than the atmosphere-only result we report here.

Table 2-4: Equilibrium calculation for Titan's atmosphere (T=93.65K, P=1.46 bar). Columns are the same as in table 1. The initial mixing ratios are surface abundances. The available Gibbs energy from our own code is Φ *= 1.21 J/mol. NA indicates that these species were not included in the Aspen Plus calculation.*

Species	Initial mixing ratio	Final abundance (*fmincon*)	Final abundance (*Aspen*)	Final – initial abundance (*fmincon*)
N_2*	0.94179679	0.94179679	0.9417968	0
CH_4	**0.05712**	**0.057144**	**0.057144**	**0.000024**
H_2	**0.00099**	**0.000974**	**0.000974**	**-0.000016**
CO	**0.000047**	**4.7E-05**	0.000047	-3.46E-19
Ar	0.00003421	0.00003421	0.0000342	0
C_2H_6	**0.00001**	**3.97606E-19**	**0**	**-0.00001**
C_2H_2	**0.000002**	**6.1423E-20**	**0**	**-0.000002**
HCN	1E-20	1.15092E-19	0	1.05E-19
C_3H_8	1E-20	1.9732E-19	0	1.87E-19
C_2H_4	1E-20	1.1886E-19	0	1.09E-19
CH_3C_2H	1E-20	5.65276E-20	NA	4.65E-20
C_2N_2	1E-20	4.97628E-20	0	3.98E-20
C_3HN	1E-20	3.86518E-20	NA	2.87E-20
CH_3CN	1E-20	1.11588E-19	NA	1.02E-19
C_4H_8_I	1E-20	8.17504E-20	NA	7.18E-20
C_4H_{10}_I	1E-20	1.38594E-19	NA	1.29E-19
C_6H_6	1E-20	2.69708E-20	0	1.7E-20
NO_2	1E-20	1.18993E-19	0	1.09E-19
NO	1E-20	1.36611E-19	0	1.27E-19

*N2 was modified from textbook value to ensure mixing ratios summed to 1.

Uranus

Observational knowledge of Uranus' atmosphere is limited and so it is difficult to calculate disequilibrium at the 1 bar level. Table 5a shows the observed abundances at 1 bar; there is insufficient diversity of molecular species for any reactions to occur. The observed composition is the same as the equilibrium composition, and the available Gibbs energy in Uranus' troposphere is nominally 0 J/mol. In reality, there are probably trace species at 1 bar that contribute to a small disequilibrium. To place an upper bound on the disequilibrium in Uranus' atmosphere, we included trace species from the stratosphere in our calculations (Table 5b). Of course, the stratosphere for most planets with thick atmospheres and shortwave stratospheric absorbers is located vertically above the ~0.1 bar level (Robinson & Catling 2014b) and so is not at the 1 bar level that we use for Gibbs energy calculations. Even so, when semi-analytic and numerical calculations are repeated for this case, we find the maximum disequilibrium in Uranus' atmosphere is still comparatively small, 0.097 J/mol.

Table 2-5 (a): Equilibrium calculation for Uranus' atmosphere. Columns are the same as in table 1. The initial mixing ratios are abundances at the 1 bar level (T=75K). The available Gibbs energy from our own code is Φ *= 0 J/mol. (b) Equilibrium calculation for Uranus' atmosphere with all stratospheric trace species included. Columns are the same as in table 1. The calculation is*

performed at P=1 bar and T=75K despite the inclusion of stratospheric species to give an upper bound on the free energy at the 1 bar level. The available Gibbs energy from our own code (with all traced species included) is Φ *= 0.0971 J/mol.*

Species	Initial mixing ratio	Final abundance (*fmincon*)	Final abundance (*Aspen*)	Final – initial abundance (*fmincon*)
H_2	0.825	0.825	0.825	0
He*	0.1519987	0.1519987	0.1519987	0
CH_4	0.023	0.023	0.023	0
NH_3	1E-15	1E-15	0	0
H_2S	0.0000008	0.0000008	0.0000008	0
CO	0.0000005	0.0000005	0.0000005	0

*He was modified from textbook value to ensure mixing ratios summed to 1.

Species	Initial mixing ratio	Final abundance (*fmincon*)	Final abundance (*Aspen*)	Final – initial abundance (*fmincon*)
H_2	**0.825**	**0.82499846**	**0.8249985**	**-0.00000154**
He*	0.15199857	0.15199857	0.1519986	0
CH_4	**0.023**	**0.02300054**	**0.0230005**	**0.00000054**
NH_3	0.0000001	0.0000001	0.0000001	0
H_2S	0.0000008	0.0000008	0.0000008	0
CO	**0.0000005**	**1.0905E-19**	**0**	**-0.0000005**
H_2O	**0.000000006**	**5.06E-07**	**0.000000506**	**0.0000005**
C_2H_6	**0.00000001**	**3.4293E-19**	**0**	**-0.00000001**
C_2H_2	**0.00000001**	**5.77147E-20**	**0**	**-0.00000001**

*He was modified from the textbook value to ensure mixing ratios summed to 1.

Saturn and Neptune

Saturn and Neptune were excluded from our analysis because of their close similarity to Jupiter and Uranus, respectively. Essentially, in Jupiter and Uranus, we chose a representative of the gas and ice giants, respectively.

Earth

We calculated the disequilibrium in Earth's atmosphere for two different cases. Firstly, we considered only the Earth's atmosphere (figure 6, table 6). There are minor differences between the observed atmospheric composition and the equilibrium composition. The largest contributor to gas phase disequilibrium in Earth's atmosphere is the coexistence of O_2 and CH_4, and the available Gibbs energy in the atmosphere is only 1.5 J/mol, which is not unusual compared to other Solar System atmospheres. The O_2 and CH_4 couple contributes ~90% of this gas phase disequilibrium (1.3 J/mol).

Table 2-6: Purely gas phase equilibrium calculation for Earth's atmosphere (ocean not included). Columns are the same as in table 1. The initial mixing ratios are surface abundances (T=288.15K, P= 1.013 bar). The available Gibbs energy for Earth (atmosphere only) from our code is Φ *= 1.51 J/mol.*

Species	Initial mixing ratio	Final abundance (*fmincon*)	Final abundance (*Aspen*)	Final – initial abundance (*fmincon*)
N_2	**0.773095598**	**0.773095914**	**0.7730921**	**3.16826E-07**
O_2	**0.2073826**	**0.2073791**	**0.2073829**	**-3.46776E-06**
H_2O	**0.00990082**	**0.00990473**	**0.00990473**	**3.91082E-06**
Ar	0.009247366	0.009247366	0.00924737	0
CO_2	**0.000346529**	**0.000348336**	0.000348336	1.8069E-06
Ne	1.79997E-05	1.79997E-05	0.000018	0
He	5.18803E-06	5.18803E-06	0.00000519	-2.5411E-21
CH_4	**1.68314E-06**	**2.5343E-20**	**1.13E-48**	**-1.68314E-06**
Kr	1.12869E-06	1.12869E-06	0.00000113	0
H_2	**5.4455E-07**	**1.0381E-19**	**4.08E-32**	**-5.44545E-07**
N_2O	**3.16826E-07**	**3.3401E-19**	**3.28E-20**	**-3.16826E-07**
CO	**1.2376E-07**	**8.7068E-20**	**2.18E-32**	**-1.2376E-07**
Xe	8.61371E-08	8.61371E-08	8.61E-08	0
O_3	**4.95041E-08**	**1.64391E-19**	**1.97E-30**	**-4.95041E-08**
HCl	9.90082E-10	9.90082E-10	9.9E-10	-6.20385E-25

*Taken US standard atmosphere (dry) and added 1% water vapor, then renormalized everything to ensure mixing ratios add to 1.

Next, we consider the multiphase equilibrium calculation that includes the Earth's atmosphere and oceans with dissolved ion species (figure 7, table 7). In this case, the disequilibrium in Earth's atmosphere-ocean system is very large; the available Gibbs energy is 2326 J/mol of atmosphere.

The large disequilibrium is attributable to the coexistence of N_2, O_2 and liquid water. Both numerical and semi-analytic calculations predict that these three species should react to form nitrate and hydrogen ions according to the following reaction:

$$2N_2(g) + 5O_2(g) + 2H_2O(l) \rightleftharpoons 4H^+(aq) + 4\,NO_3^-(aq) \qquad (21)$$

In equilibrium, most of the oxygen in Earth's atmosphere reacts to form hydrogen ions and nitrate (table 7). It has been known for many decades that the coexistence of N_2, O_2, and H_2O is the largest contributor to disequilibrium in Earth's atmosphere ocean system (Hutchinson 1954, p399; Lewis & Randall 1923; Lovelock 1975; Sillén 1966). However, this is the first time the free energy associated with that disequilibrium has been accurately calculated. Lovelock (1975) reported that the free energy in Earth's atmosphere-ocean system was 5.5×10^4 J/mol (table 8), which is over an order of magnitude larger than our result. He did not describe their methodology, but we suspect that he assumed the Gibbs energy of the N_2-

O_2-H_2O reaction does not change as the reaction proceeds, and simply multiplied the Gibbs energy of the reaction (at observed abundances) by the number of moles of oxygen in Earth's atmosphere. This approach also assumes the reaction goes to completion with total O_2 removal rather than equilibrium. Preliminary analyses by the authors of this study (Catling & Bergsman 2009; Catling & Bergsman 2010) reached a similar result using this methodology. Both the semi-analytic and numerical calculations in this study account for the fact that the Gibbs energy of the reaction diminishes rapidly as oxygen in the atmosphere is depleted, and so the available Gibbs energy in Earth's atmosphere-ocean system, 2326 J/mol, is smaller than previously reported.

Table 2-7: Multiphase equilibrium calculation for Earth's atmosphere-ocean system (T=288.15K, P= 1.013 bar). Columns are the same as in table 1. The initial mixing ratios are surface abundances. Aqueous species are italicized. The available Gibbs energy for Earth's atmosphere-ocean system from our code is Φ *= 2326 J/mol. NA indicates that these species were not included in the Aspen Plus calculation. Note the large changes in nitrate,* H^+ *ions and oxygen.*

Species	Initial moles	Final abundance (*fmincon*)	Final abundance (*Aspen*)	Final – initial abundance (*fmincon*)
$H_2O_{(l)}$	**436.7881549**	**436.7217842**	**436.709**	**-0.066370669**
O_2	**0.207382567**	**0.008094666**	**1.50756E-05**	**-0.199287902**
N_2	**0.773095598**	**0.693382141**	**0.69014709**	**-0.079713457**
NO_3(-)	***0.00023499***	***0.159662537***	***0.166132***	***0.159427547***
H(+)	***5.10711E-08***	***0.141936633***	***0.1484065***	***0.141936582***
$H_2O_{(g)}$	**0.00990082**	**0.01229017**	**0.0119409**	**0.00238935**
Ar	0.009247366	0.009247366	0.009247366	0
$CO_{2(g)}$	**0.000346529**	**0.010835944**	**0.00943268**	**0.010489415**
Ne	1.79997E-05	1.79997E-05	1.79997E-05	0
He	5.18803E-06	5.18803E-06	5.18803E-06	0
CH_4	**1.68314E-06**	**2.32128E-13**	**0**	**-1.68314E-06**
Kr	1.12869E-06	1.12869E-06	1.1287E-06	0
H_2	**5.44545E-07**	**1.15773E-12**	**0**	**-5.44544E-07**
N_2O	**3.16826E-07**	**1.66811E-13**	**NA**	**-3.16826E-07**
CO	**1.2376E-07**	**1.001E-12**	**0**	**-1.23759E-07**
Xe	8.61371E-08	8.61371E-08	8.61372E-08	0
O_3	**4.95041E-08**	**1.43837E-12**	**0**	**-4.95027E-08**
HCl	**9.90082E-10**	**2.83979E-10**	**0**	**-7.06103E-10**
Na(+)	*3.672916562*	*3.672916562*	*3.672917*	*0*
K(+)	*0.079974781*	*0.079974781*	*0.0799747*	*0*
Mg(+2)	*0.413816618*	*0.413816618*	*0.4138166*	*0*
Ca(+2)	*0.08052309*	*0.08052309*	*0.080523*	*0*
Sr(+2)	*0.000709668*	*0.000709668*	*0.000709669*	*0*
Cl(-)	***4.275870063***	***4.275870063***	***4.27587***	***7.061E-10***
SO_4(-2)	*0.221125177*	*0.221125177*	*0.2211252*	*0*

HCO_3(-)	***0.013911382***	***9.08865E-08***	***5.59323E-07***	***-0.013911291***
Br(-)	*0.00661104*	*0.00661104*	*0.00661104*	*0*
$B(OH)_3$	*0.003258522*	*0.003258522*	*NA*	*0*
F(-)	*0.000532643*	*0.000532643*	*0.000532643*	*0*
$CO2_{(aq)}$	***7.598E-05***	***0.005262085***	***0.00666488***	***0.005186105***
CO3(-2)	***0.001762422***	***7.76602E-14***	***0***	***-0.001762422***
OH(-)	***5.48309E-05***	***7.33759E-12***	***4.1902E-12***	***-5.48309E-05***

Of course, the equilibrium metric is only a hypothetical way of assessing untapped free energy. In reality, O_2 also reacts with surface minerals (oxidative weathering) and would be even more depleted with additional free energy if solids were included in the equilibrium model. But we restrict ourselves to gas and gas-liquid equilibrium because those are tractable ways of comparing planets that are tied to quantities that can be observed remotely (see more in discussion section).

We confirmed that the available Gibbs energy in Earth's atmosphere-ocean system is attributable to reaction (21) by repeating the multiphase calculation but excluding H^+ and NO_3^-. In this case the available Gibbs energy is only 6 J/mol. If we only include the five most important species (N_2, O_2, H_2O, H^+ and NO_3^-) in multiphase equilibrium calculations, then the available Gibbs energy change is 1812 J/mol (note this includes the effects of changing water activity – see below for details). The difference between this and the total available energy for the Earth system is attributable to carbon-bearing species.

Table 2-8: Comparison of the available Gibbs free energy, Φ, in Solar System atmospheres (defined in equation (7)). The second column gives Φ for each atmosphere as determined by our Gibbs energy minimization calculations. The third column is our semi-analytic approximation of the available Gibbs energy calculated from summing the Gibbs energy changes associated with key reactions (see main text and Appendix I 2-D). The fourth column is an independent verification of Φ using the commercial software package, Aspen Plus. The fifth report compares our values to those of Lovelock (1975).

	Available Gibbs energy, Φ (J/mol of atmosphere)†	Validation, Φ (J/mol of atmosphere)		Lovelock (1975) Φ (J/mol of atmosphere)
		Semi-analytic approximation	Aspen Plus	
Venus	0.059598	0.0565586	0.060099	5
Earth(atm)	1.51348	1.5072	1.52564	Not reported
Earth	2325.76	1723.65★	2348*	55000
Mars	136.3485	136.8070	136.3506	13
Jupiter	0.001032077	0.00103205	0.0010228	<1
Titan	1.2126495	1.212617	1.208787	Not reported
Uranus**	0.0971394	0.0983	0.09713801	Not reported

★The discrepancy between the numerical and semi-analytic results for the Earth is expected because the semi-analytic approximation does not take into account changing water activity. See the main text and table 9 for a more detailed explanation.

*Note that different electrolyte models in Aspen Plus produce slightly different Gibbs energy changes. The available Gibbs energy using the Electrolyte Non-Random Two Liquid (ELECNRTL) model is 2348 J/mol, whereas the PITZER electrolyte returns a Gibbs energy change of 2205 J/mol (see Appendix I 2-E for a full description of multiphase Aspen Plus calculations).

†Calculated at surface pressure and temperature for Venus, Earth, Mars and Titan. Calculated at 1 bar and T = 165 K and T = 75 K for Jupiter and Uranus, respectively.

**Unrealistically includes stratospheric species and gaseous water vapor so this is an upper bound on free energy.

The dissolution of hydrogen ions and nitrate in the ocean by equation (21) acidifies the ocean, which affects the carbonate-CO_2 system. By Le Châtelier's principle, as the ocean is acidified, carbon in the form of carbonate and bicarbonate ions converts to atmospheric CO_2 and dissolved CO_2:

$$CO_2 + H_2O \rightleftharpoons H_2CO_3 \rightleftharpoons H^+ + HCO_3^- \rightleftharpoons 2H^+ + CO_3^{-2} \qquad (22)$$

This reaction shifts to the left as the concentration of hydrogen ions is increased. The Gibbs energy change associated with this shift adds to the overall Gibbs energy change in the Earth's atmosphere-ocean system. Additionally, the dissolution of nitrate and hydrogen ions in water decreases the water activity, which further contributes to the overall Gibbs energy change. If water activity is held fixed, then the available Gibbs energy for Earth is around 600 J/mol less than if water activity is included.

Validating our results for the Earth atmosphere-ocean system is more complex than for gas phase systems. This is because the semi-analytic method we have adopted does not account for the decrease in water activity due to increased nitrate and hydrogen ion abundances. Rather than attempt to compute water activities analytically, we calculated the Gibbs energy change associated with equation (21) in isolation, and compared this to the numerical Gibbs energy minimization calculation using only the five species in this reaction and with water activity fixed to equal 1. The available Gibbs energies for these two cases are shown in table 9; the two values agree to within 1%. Next, we computed the available energy semi-analytically using both reaction (21) and two key reactions that involve carbon-bearing species (see Appendix I 2-D). This was compared to the numerical Gibbs energy minimization calculation for the same set of species with the water activity set equal to 1. In this case, the available Gibbs energy values also agreed to within 1% (table 9). The difference between this result and the complete numerical calculation

can be explained by the effect of water activity. In the numerical calculations the water activity decreases from 0.981877 to 0.981284 from observed to equilibrium state. Following equation (9), this corresponds to a change in Gibbs free energy of:

$$\begin{aligned}\Delta G &\approx n_w RT\left(\ln\gamma_1 - \ln\gamma_2\right)\\ &= 436\times 8.314\times 288.15\left(-0.01828897 + 0.01889366\right)\\ &= 631\ \text{J/mol}\end{aligned} \qquad (23)$$

Here, n_w = 436 moles of H_2O(l) per mole of atmosphere, which is derived from the moles of H_2O in the ocean (7.67×10^{22} =1.38×10^{21} kg/(0.018 mol H_2O/kg)) and moles of air (1.76×10^{20}) as their ratio, 436 = $7.67\times10^{22}/1.76\times10^{20}$. The value of 631 J/mol is approximately equal to the difference between the numerical calculation including carbon species (water activity=1) and the full numerical calculation (2326 – 1716 = 610 J/mol).

Table 2-9: Semi-analytic validation of the numerical calculation of the available Gibbs free energy, Φ, in the Earth atmosphere-ocean system.

Species included in calculation	Available energy, Φ (J/mol)	
	Semi-analytic approximation	Numerical calculation (*fmincon*)
N_2, O_2, H_2O, H+ and NO_3- only. Water activity=1.	1051	1059
Five species above plus carbon-bearing species. Water activity=1.	1723	1716
All species and water activity included.	NA	2326

We conclude that the total available Gibbs energy of the Earth atmosphere-ocean, 2326 J/mol, can be explained almost completely by the nitrate reaction (1059 J/mol), the change in carbon-bearing species due to ocean acidification (657 J/mol), and the associated change in water activity (610 J/mol). This conclusion is supported by both numerical and semi-analytic calculations. We do not account for the pressure decrease in our Gibbs energy calculations from depleting the atmosphere of oxygen given that Gibbs energy is defined for a system at constant pressure and temperature. Our multiphase calculations for the Earth should be treated as a constant-pressure approximation.

Although the coexistence of O_2 and CH_4 is the largest contributor to disequilibrium for a calculation of Earth's atmosphere excluding the oceans, this pair provides a small contribution to the disequilibrium in the total atmosphere-ocean system. If methane is excluded from the Earth atmosphere-ocean equilibrium calculation, then the available Gibbs energy changes from 2325.76 J/mol to 2324.46 J/mol. Similarly, semi-

analytic calculations for the reaction, $2O_2 + CH_4 \rightleftharpoons CO_2 + 2H_2O$ yield a Gibbs energy change of only 1.3 J/mol. Methane doesn't contribute much to thermodynamic disequilibrium because of its low abundance of 1.7 ppmv (in the US Standard Atmosphere, noting that anthropogenic emissions mean that the current mean global abundance is slightly higher at ~1.8 ppmv). This doesn't imply that the O_2-CH_4 disequilibrium is unimportant for life detection purposes. A compelling argument for biogenic fluxes can be made from the coexistence of O_2 and CH_4 in Earth's atmosphere based on kinetic lifetimes. However, the O_2-CH_4 pairing is not an important contributor to the available Gibbs energy of thermodynamic disequilibrium in Earth's atmosphere-ocean system.

To express available Gibbs energy as a dimensionless metric, figure 8b plots the available Gibbs free energy in each planet's atmosphere normalized by *RT*, where *T* is the mean temperature for each planet. The value *RT* is the molar thermal energy and depends on solar flux along with Bond albedo and greenhouse effect. Thus, the normalization is a first order and rough correction for the fact that the inner planets receive more free energy input from the Sun that can drive disequilibrium. Figure 8b is similar to figure 8a because surface or 1 bar temperatures vary by an order of magnitude at most, whereas the available Gibbs energies vary by many orders of magnitude. In figure 8b the Earth stands out as only planet in Solar System with chemical disequilibrium comparable in magnitude to thermal energy.

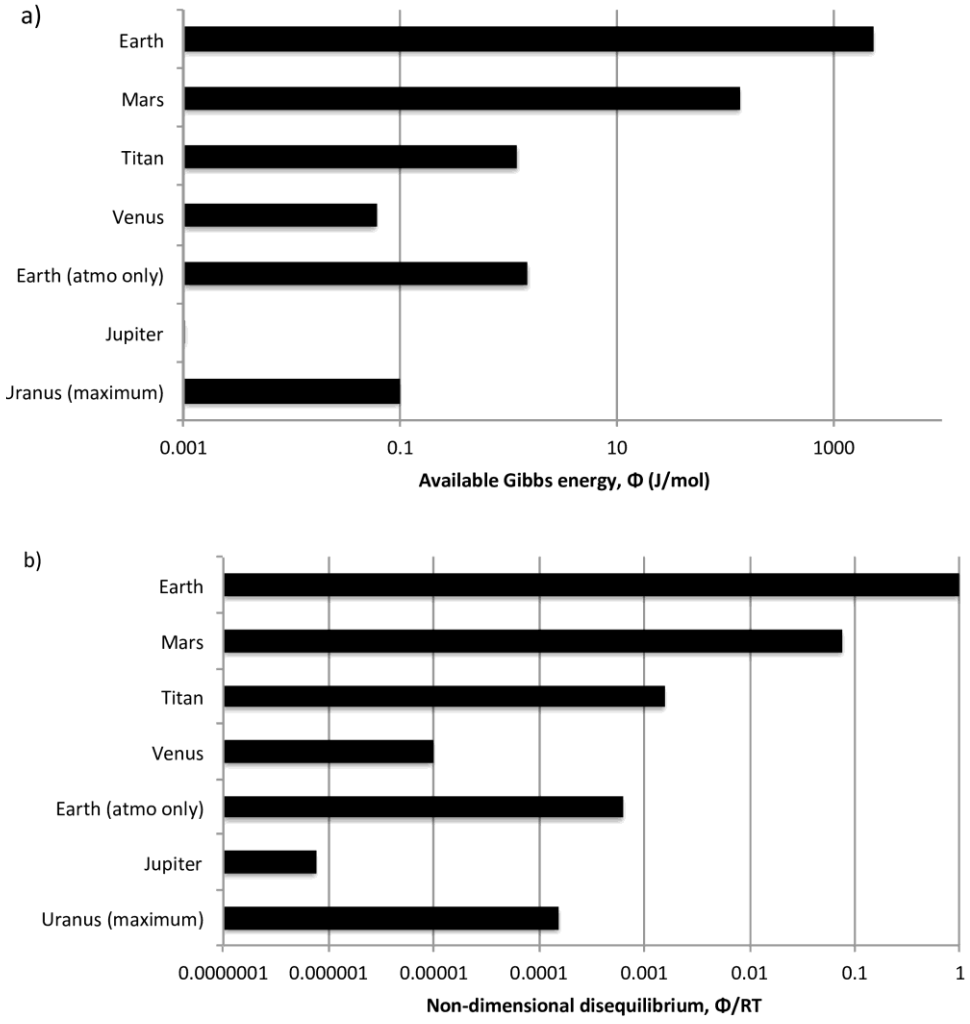

Figure 2-8: Comparison of the available Gibbs free energy, Φ, in Solar System atmospheres as determined by our Gibbs free energy minimization calculations. The available Gibbs free energies in A) correspond to the second column in table 8. The free energy in the Earth atmosphere-ocean system is more than an order of magnitude greater than any other planetary atmosphere in the Solar System. B) gives the dimensionless free energy for each planet's atmosphere (available Gibbs energy Φ divided by RT*). This roughly corrects for the fact that the inner planets receive more free energy from the Sun that is available to drive chemical disequilibrium. Equilibria are calculated at surface pressure and temperature for Venus, Earth, Mars and Titan, and at 1 bar and T = 165 K and T = 75 K for Jupiter and Uranus, respectively.*

Discussion

Interpretation of thermodynamic disequilibrium

Earth is unique in the Solar System as the only planet with both a large disequilibrium in its atmosphere-ocean system and a productive surface biosphere (with the caveat that we have not included Titan's lakes in our calculations). This disequilibrium is maintained by life. Atmospheric O_2 is produced almost exclusively by oxygenic photosynthesis, and atmospheric N_2 is regulated by bacterial nitrification and denitrification. Were denitrification to shut off and biologic N fixation left to operate, the N_2 lifetime would be ~10 myr (Jacob 1999, chapter 6).

In the absence of any biogenic fluxes or geological oxygen sinks such as oxidative weathering, reaction (21) would proceed slowly due to lightning, eventually depleting the atmosphere of oxygen (there is some abiotic denitrification but the flux is very small compared to biological denitrification (Devol 2008)). The modern rate of production of nitrogen oxide radicals NOx (=NO + NO_2) from lightning is 2-20 Tg(N)/year (Rakov & Uman 2007). OH radicals or ozone further oxidize NOx species intro nitrate that ends up on Earth's surface. Given that the mixing ratio of N_2 decreases by approximately 0.08 in our equilibrium calculations, and that the total number of moles of air in the atmosphere is 1.76×10^{20}, this implies that 1.408×10^{19} moles of N_2 (2.816×10^{19} moles of N) are converted to nitrate by reaction to equilibrium. Therefore, it would take approximately $2.816\times10^{19}/(2\text{-}20\times10^{20}/14)$ = 20-200 million years for atmospheric oxygen to be depleted by lightning and converted to nitrate. The coexistence of oxygen, nitrogen and liquid water in the Earth's atmosphere-ocean system is thus evidence a biosphere acting over geologic timescales. Capone et al. (2006) also noted that denitrification sustains atmospheric nitrogen on Earth, and that although there are abiotic pathways that deplete N_2 (namely lightning), nitrates are not easily converted back to N_2 abiotically. In contrast, Kasting et al. (1993b) argued than on the prebiotic Earth, most of the Earth's nitrogen would reside in the atmosphere in steady state. This is because nitrate is reduced to ammonia in mid-ocean ridge hydrothermal systems, which may then return to the atmosphere and be photochemically converted back to N_2. In practice, however, the reduction of nitrate will also yield ammonium (Bada & Miller 1968; Smirnov et al. 2008), which will be subsequently sequestered into clay minerals and thereby removed from the atmosphere-ocean reservoir (Summers et al. 2012).

It is worth considering why this large disequilibrium exists in Earth's atmosphere-ocean system, and whether we would expect other biospheres to generate large disequilibria. In some respects, Earth's large disequilibrium is surprising since life typically exploits environmental free energy gradients rather than generate them. In fact, the O_2-N_2-water disequilibrium is an incidental byproduct of oxygenic photosynthesis. In addition to producing molecular oxygen, oxygenic photosynthesis also produces large quantities of organic carbon that is buried in sediments. Despite ongoing nitrification and the thermodynamic favorability of reaction (21), nitrate does not accumulate and deplete the atmosphere of oxygen. This is because denitrifying microbes in anoxic sediments exploit the redox gradient that exists between reduced organic carbon and nitrate (Devol 2008). Without oxygenic photosynthesis producing both O_2 and reduced carbon, Earth's atmosphere-ocean disequilibrium would not persist.

In our calculated equilibrium for the Earth atmosphere-ocean system, the molar abundance of H^+ ions is 0.14 moles per mole of atmosphere, which corresponds to an ocean pH of 1.7. Lewis and Randall (1923, p567-568) recognized that the equilibrium state of the Earth's atmosphere-ocean system would be highly acidic: "Even starting with water and air, we see... that nitric acid should form... until it reaches a concentration... where the calculated equilibrium exists. It is to be hoped that nature will not discover a catalyst for this reaction, which would permit all of the oxygen and part of the nitrogen of the air to turn the oceans into dilute nitric acid". However, the low pH equilibrium state that we obtain is unlikely to be the state actually realized if life disappeared from the Earth, volcanic fluxes ceased, and the system relaxed to equilibrium. In practice, acidic ocean pH from nitrate dissolution would be buffered by reaction with the crust, for instance by delivery of cations from continental weathering or weathering of seafloor basalt. Nevertheless, we have done calculations where the ocean pH is buffered to pH 8.2, and the Gibbs free energy from reaction to equilibrium is several times larger than our original result.

This discussion highlights the point that we have not included any interactions with solid states of matter in our equilibrium calculations. If the Earth's atmosphere-ocean system were allowed to relax to equilibrium, then almost all of the atmospheric O_2 would react with the crust via oxidative weathering. There would be a large Gibbs energy change associated with this crustal oxidation. Additionally, there is a large disequilibrium between organic carbon and ferric iron in the crust, both of which have accumulated over time because of photosynthesis and the escape of hydrogen to space (Catling et al. 2001b). Although there are 3.7×10^{19} moles of O_2 in the atmosphere and oceans, there are 5.1×10^{20} moles O_2 equivalent Fe^{3+} and sulfate in sedimentary rocks, and $1.6\text{-}2.5\times10^{21}$ moles O_2 equivalent excess Fe^{3+} in igneous and high grade metamorphic rocks (Catling et al. 2001b; Hayes & Waldbauer 2006a; Sleep 2005b). These crustal oxidants are in disequilibrium with the $\leq1.3\times10^{21}$ moles O_2 equivalent reduced organic carbon in the crust (Catling et al. 2001b; Wedepohl 1995). Thus, we expect the disequilibrium in Earth's entire crustal reservoir

to be several orders of magnitude greater than the disequilibrium in the atmosphere-ocean system in isolation.

However, we chose to exclude interactions with solid phases since we are interested in disequilibrium as a biosignature for exoplanets; the composition of exoplanet crustal material will not be accessible to remote sensing. Instead, our available Gibbs energy metric captures disequilibrium in the gaseous and aqueous phases. In principle, atmospheric composition and the presence of an ocean can be inferred from future telescope observations.

The thermodynamic biosignature metric described in this paper is complementary to kinetic biosignature metrics concerning the fluxes and timescales of gases that should quickly react, such as coexisting oxygen and methane. For example, if the atmospheric abundances of oxygen and methane can be observed, and the abiotic sinks for oxygen and methane can be estimated, then the magnitude of source fluxes required to maintain steady state can be estimated. Biogenic processes may be invoked if these source fluxes are implausibly large compared to all known abiotic sources of oxygen and methane. We calculate that in thermodynamic chemical equilibrium, all CH_4 would be absent from the Earth's atmosphere (see results). The average lifetime of a CH_4 molecule from photochemical models is ~10 years, and so we can deduce an estimate of the required CH_4 flux. For consumption of 1.7 ppmv CH_4 in 10 years: $(1.7 \times 10^{-6}) \times (1.8 \times 10^{20}$ moles air) / (10 years) = 3.1×10^{13} moles CH_4 /year flux. The magnitude of this flux is large and on the Earth is dominantly (~90%) biogenic (Kirschke et al. 2013).

These flux arguments can be extended to estimate the surface biomass (Seager et al. 2013), or the minimal driving power (Simoncini et al. 2013) required to maintain steady-state atmospheric abundances. These estimates could provide additional insight into whether the observed disequilibrium is plausibly biogenic in origin: for instance, if the biomass estimate is unreasonably large, or if the driving power is comparable to abiotic processes, the inference to biology is weakened.

It should be noted that our gas phase calculations for the Earth are entirely consistent with the minimal driving power calculations in Simoncini et al. (2013). We determined that the available energy from the CH_4 and O_2 reaction in Earth's atmosphere is 1.3 Joules per mole of atmosphere (see results section). Because there are 1.8×10^{20} moles in Earth's atmosphere, this implies the total available energy in Earth's atmosphere due to this pairing is $1.3 \times 1.8 \times 10^{20} = 2.34 \times 10^{20}$ J. The turnover lifetime of CH_4 in Earth's atmosphere is approximately 10 years (Dlugokencky et al. 1998; Prinn et al. 2001). If we assume that all the CH_4 in Earth's atmosphere is oxidized in 10 years (3.15×10^8 seconds) on average, then the "power" from the CH_4-O_2 reaction according to our calculations will be the free energy release spread over this time:

Power = $(2.34\times10^{20})/(3.15\times10^{8})$ = 0.7 TW . Simoncini et al. (2013) also found the power required to maintain the O_2-CH_4 disequilibrium to be 0.7 TW.

We have shown that large thermodynamic disequilibria coincide with surface biology in the Solar System, but whether chemical disequilibrium would be a useful metric for identifying exoplanet biospheres remains an open question. In principle, low-flux abiotic processes with slow kinetics could maintain a large atmospheric chemical disequilibrium. For example, the reaction between H_2 and N_2 is kinetically inhibited at Earth surface conditions, and so these species could coexist in thermodynamic disequilibrium for long timescales with very small replenishing fluxes (assuming a super Earth with sufficient gravity to retain hydrogen). In practice, however, there are few kinetic barriers to gas phase reactions at Earth-like temperatures and pressures, and so sizeable disequilibria from abiotic processes may be rare. In future work, it would be helpful to apply this metric to model exoplanet atmospheres to determine if there are any plausible false positives scenarios, i.e. dead worlds with large available Gibbs energy. For example, a Mars-like atmosphere with different CO, O_2 and H_2 abundances -perhaps due to elevated UV irradiation or different outgassed species - could perhaps have a large thermodynamic disequilibrium in the absence of life. Future work should also investigate how abiotic disequilibrium in Solar System atmospheres may have varied since 4.56 Ga.

Practicality of thermodynamic disequilibrium as exoplanet biosignature

The main advantage of using thermodynamic disequilibrium for biosphere detection over kinetic metrics is that it requires minimal auxiliary assumptions. Whereas kinetic arguments require abiotic surface sinks to be estimated, the calculation of gas phase chemical equilibrium in a planet's atmosphere requires only bulk atmosphere abundances, surface temperature, and pressure; future observations could be used to infer all three of these (Des Marais et al. 2002a; Misra et al. 2014). Schwieterman et al. (2015b) recently demonstrated that it is possible to constrain the abundance of molecular nitrogen due to its tendency to form N_2-N_2 dimers, which are spectrally active at 4.3 μm. Multiphase calculations for atmosphere-ocean systems require knowledge of a surface ocean. In principle, it is possible to infer the presence of exoplanet oceans using ocean glint (Robinson et al. 2010), and the approximate surface extent of oceans may be estimated with time-resolved photometry (Cowan et al. 2009). The sensitivity of our metric to ocean volume is discussed below. Recall also that our multiphase calculations do not fully capture the disequilibrium in the surface reservoirs since they neglect any reactions with the crust (see above).

In principle, the abundances of dissolved ions and ocean pH would also be required to calculate the atmosphere-ocean disequilibrium for an exo-Earth. However, the available Gibbs energy in Earth's atmosphere-ocean system is relatively insensitive to these variables. Table 10 shows the sensitivity of the

available Gibbs energy in Earth's atmosphere-ocean system to variables that could not be measured remotely (or would be difficult to observe remotely) on exoplanets. Key findings are summarized below.

Table 2-10: Sensitivity of the numerical calculations of the available Gibbs energy, Φ , in the Earth's atmosphere-ocean system to perturbations in variables that are unobservable or difficult to observe for exoplanets.

		Available energy, Φ (J/mol)
Temperature	T= 273.15 K	1634.78
	T= 288.15 K	2325.76
	T= 298.15 K	2824.48
Pressure	0.1 bar	1354.20
	1.013 bar	2325.76
	10 bar	3891.96
	1000 bar	6878.35
Ocean pH	2	1983.28
	4	2314.26
	6	2325.71
	8.187 (Earth)	2325.76
	12	2325.65
Salinity	0 mol/kg	2290.01
	1.1 mol/kg	2325.76
	11.1 mol/kg	2276.40
Ocean volume	0.1 Earth ocean	413.62
	0.5 Earth ocean	1442.95
	1 Earth ocean	2325.76
	2 Earth oceans	4188.27
	10 Earth oceans	8956.34
	50 Earth oceans	12626.22

The available Gibbs energy of the Earth's atmosphere ocean system is largely insensitive to both ocean salinity and pH. Only at extremely low pH values (pH=2) does the available energy decrease by around 15% since the equilibrium of reaction (21) is pushed to the left. This insensitivity arises because the starting abundance of hydrogen ions is many orders of magnitude less than the equilibrium abundance, and so changes to the initial abundance (pH) does not affect the equilibrium state very much. This suggests the pH and salinity of exoplanet oceans do not need to be known to estimate the available Gibbs energy in their atmosphere-ocean systems.

The available Gibbs energy of the Earth system is moderately sensitive to ocean volume. Increasing ocean volume by a factor of 10 increases the available Gibbs energy of a factor of 4. The disequilibrium in an exoplanet atmosphere-ocean system could be overestimated if oceans are extremely shallow. For example, if the Earth's oceans were only 10% of their current volume then the available Gibbs energy in the Earth system would be 413 J/mol, only ~3 times larger than our value calculated for Mars (table 8).

Various observational techniques have been proposed to both detect oceans (Gaidos & Williams 2004; Robinson et al. 2010; Zugger et al. 2010), and to map the ocean-land fraction for terrestrial exoplanets using time resolved photometry (Cowan et al. 2009; Cowan & Strait 2013; Fujii & Kawahara 2012). These studies suggest that a ~10 m space telescope should be able to obtain a coarse surface map of an Earth-analog at 10 pc. Given observations of surface ocean fraction, it may be possible to constrain ocean depth from geophysical theory. For example, the typical strength or rock would not support a large topographic elevation between seafloor and land. In the case of granitic continents and a basaltic seafloor, the maximum possible ocean depth with exposed continents is approximately equal to $11.4 \times g_{Earth} / g_{planet}\ km$, where g_{Earth} is the surface gravity of the Earth and g_{planet} is the surface gravity of the planet of interest (Cowan & Abbot 2014). Of course, for planets with no land and very deep oceans (~1000 km), ocean volume could be constrained by mass and radius observations. Putting a lower limit on ocean depth is more challenging, but several possibilities exist. Heat flow from planetary interiors is uneven due to the large spacing of convective cells in a viscous fluid, and will therefore inevitably create some topographic relief (Davies 1998). Consequently, the elevation distributions of the terrestrial Solar System planets all extend over several kilometers (Melosh 2011, p. 42). It may also be possible to put a lower bound on ocean volume using thermal inertia arguments and observed variations in a planet's infrared flux over its orbit (Gaidos & Williams 2004). By combining land-ocean maps, thermal inertia observations, and geophysical constraints on topography, estimates of ocean volume may be obtainable for some exoplanets, but solving this problem is beyond the scope of the current paper.

Our equilibrium calculation for the Earth atmosphere-ocean system is a simplification because we have assumed the entire atmosphere and ocean are at a mean global temperature and sea-level pressure (T=15°C and P=1.013 bar). In practice, the air temperature varies over the surface, ocean temperature typically decreases with depth, and pressure increases by several orders of magnitude in the deep ocean. To investigate the sensitivity of the available Gibbs energy to these variations we repeated the equilibrium calculation for a wide range of pressures and temperatures. The available Gibbs energy of the Earth's atmosphere-ocean system is moderately sensitive to these changes (table 10). At 0°C the available Gibbs energy is around 30% lower than the value at the observed mean surface temperature, 15°C. If temperature

is instead increased to 25°C then the available Gibbs energy increases by around 20%. Changing the pressure by an order of magnitude in either direction results in a change in available Gibbs energy by approximately a factor of two, though at very high pressures (1000 bar) the available Gibbs energy asymptotes to a value of nearly 7000 J/mol. These results demonstrate that the available Gibbs energy of the Earth atmosphere-ocean system may be somewhat different if spatial variations in temperature and pressure are accounted for, but that our result (~2300 J/mol) is accurate to well within an order of magnitude. This sensitivity analysis also establishes that it is not necessary to determine the surface temperature and pressure of exoplanets with high precision to estimate the available Gibbs energy of their atmosphere-ocean systems.

In summary, sensitivity analysis suggests that with good observations it might be possible to calculate thermodynamic disequilibrium for exoplanets. The gas-phase calculations have no strong sensitivities to difficult-to-observe variables such as ocean volume, and so thermodynamic disequilibrium could be accurately calculated from remote observations. Additionally, gas phase reactions are much more weakly dependent on pressure and temperature than multiphase reactions. For multiphase calculations, it may be possible to estimate thermodynamic disequilibrium to the correct order of magnitude. An important caveat on this result is that the available Gibbs energy of the Earth is moderately sensitive to ocean volume, and it may be challenging to put a lower bound on ocean depth.

Future work will assess the sensitivity of our metric to potential uncertainties in the inferences from future telescopic observations, which are expected because of limitations such as spectroscopic resolution. Such work is beyond the scope of the current paper, the purpose of which is to describe our basic methodology and discuss results for Solar System bodies.

Conclusions

- We have quantified the atmospheric chemical disequilibrium for Solar System planets with thick atmospheres. The magnitude of the purely gas phase disequilibrium in Earth's atmosphere, 1.5 J/mol, is not unusual by Solar System standards.
- However, a multiphase equilibrium calculation reveals that the disequilibrium in Earth's atmosphere-ocean system, 2326 J/mol, is at least an order of magnitude larger than any other atmosphere in the Solar System. Note that we did not do a full multiphase calculation for Titan because the mean composition of all its hydrocarbon lakes is not known, so we are comparing the Gibbs energy of Earth's atmosphere-ocean system to other solar system atmospheres only.
- Earth's disequilibrium is not caused by O_2-CH_4 pairing (a contribution of only 1.3 J/mol) but rather by the disequilibrium between N_2-O_2-H_2O(l). This disequilibrium is maintained by life. Oxygenic

photosynthesis replenishes molecular oxygen and the oxidation of fixed nitrogen and biological denitrification prevents the accumulation of nitrate in the ocean.

- The atmospheric composition of terrestrial exoplanets will be accessible to future telescopes, and so gas phase thermodynamic disequilibrium may be readily calculated for these planets' atmospheres. It may also be possible to estimate the multiphase disequilibrium for exoplanets if surface oceans can be detected and volumetrically constrained.
- Further work will be required to evaluate the utility of thermodynamic disequilibrium as a generalized metric for surface biospheres.

Chapter 3 - Disequilibrium biosignatures on the early Earth

"Consequently, if my theory be true, it is indisputable that before the lowest Silurian stratum was deposited, long periods elapsed, as long as, or probably far longer than, the whole interval from the Silurian age to the present day; and that during these vast, yet quite unknown, periods of time, the world swarmed with living creatures." – Charles Darwin, On the Origin of Species.

The previous chapter described how the modern Earth possesses a large disequilibrium in its atmosphere-ocean system due to the presence of oxygen. But even if life is common in the universe, how likely is it that oxygen biosignatures will exist elsewhere? The history of Earth's atmospheric composition, as revealed by proxies and modeling, reveals that modern oxygen abundances (~20% by volume) have only been present for the last one-eighth of Earth's history (e.g. Farquhar et al. 2000; Lyons et al. 2014; Pavlov & Kasting 2002a); this despite evidence for an origin of life as early as 3.5-4.1 Ga (Bell et al. 2015; Tashiro et al. 2017; Van Kranendonk et al. 2008) and evidence for oxygen-producing photosynthesis as early as 3.0 Ga (Planavsky et al. 2014b). Moreover, oxygenic photosynthesis is a complex metabolism that seems to have to evolved only once during the history of life on Earth (Knoll 2008; Lane 2002). Exploring alternative biosignatures to oxygen thus seems prudent.

At the very least, it would be reassuring if there were a way to detect life on Earth at different times in its evolution. In this chapter we apply our disequilibrium calculations to the Archean (4.0-2.5 Ga) and Proterozoic (2.5-0.541 Ga) to quantify disequilibrium over Earth history and look for other novel biosignature combinations.

This chapter was published in collaboration with Stephanie Olson and David C. Catling in Science Advances (Krissansen-Totton et al. (2018). Disequilibrium biosignatures over Earth history and implications for detecting exoplanet life, Science Advances, 4, eaao5747, DOI:10.1126/sciadv.aao5747).

PLANETARY SCIENCE

Disequilibrium biosignatures over Earth history and implications for detecting exoplanet life

Joshua Krissansen-Totton,[1,2]* Stephanie Olson,[3] David C. Catling[1,2]

Chemical disequilibrium in planetary atmospheres has been proposed as a generalized method for detecting life on exoplanets through remote spectroscopy. Among solar system planets with substantial atmospheres, the modern Earth has the largest thermodynamic chemical disequilibrium due to the presence of life. However, how this disequilibrium changed over time and, in particular, the biogenic disequilibria maintained in the anoxic Archean or less oxic Proterozoic eons are unknown. We calculate the atmosphere-ocean disequilibrium in the Precambrian using conservative proxy- and model-based estimates of early atmospheric and oceanic compositions. We omit crustal solids because subsurface composition is not detectable on exoplanets, unlike above-surface volatiles. We find that (i) disequilibrium increased through time in step with the rise of oxygen; (ii) both the Proterozoic and Phanerozoic may have had remotely detectable biogenic disequilibria due to the coexistence of O_2, N_2, and liquid water; and (iii) the Archean had a biogenic disequilibrium caused by the coexistence of N_2, CH_4, CO_2, and liquid water, which, for an exoplanet twin, may be remotely detectable. On the basis of this disequilibrium, we argue that the simultaneous detection of abundant CH_4 and CO_2 in a habitable exoplanet's atmosphere is a potential biosignature. Specifically, we show that methane mixing ratios greater than 10^{-3} are potentially biogenic, whereas those exceeding 10^{-2} are likely biogenic due to the difficulty in maintaining large abiotic methane fluxes to support high methane levels in anoxic atmospheres. Biogenicity would be strengthened by the absence of abundant CO, which should not coexist in a biological scenario.

INTRODUCTION

Life produces waste gases that modify an atmosphere's composition, and it will soon be possible to look for such biosignature gases on exoplanets using telescopic observations. In the near future, a high-contrast imaging system coupled to a spectrograph on the Very Large Telescope may allow the detection of biosignature gases on the nearest exoplanets (*1*). The James Webb Space Telescope (JWST), scheduled to launch in 2019, will search for biosignature gases on transiting exoplanets such as the TRAPPIST-1 system (*2*, *3*). In the 2020s, three large ground telescopes—the European Extremely Large Telescope, the Thirty Meter Telescope, and the Giant Magellan Telescope—could look for oxygen, water vapor, and carbon dioxide on nearby exoplanets (*4*–*6*), whereas the Wide-Field Infrared Survey Telescope may also be capable of detecting biosignature gases on planets orbiting close stars (*7*). In the more distant future, next-generation space telescopes could survey our stellar neighborhood for biosignatures (*8*, *9*).

Considerable attention has been given to O_2 as a biosignature gas because it is challenging to produce in large quantities without oxygenic photosynthesis (*10*). Although several pathological scenarios have been proposed whereby a terrestrial planet in the habitable zone might accumulate abiotic oxygen, additional contextual information can rule out these false-positive scenarios (*10*), whereas some doubt the realism of some of these false-positive concepts (*11*).

However, even if oxygenic photosynthesis is present, it does not guarantee detectable levels of atmospheric oxygen. There was virtually no oxygen in the Archean eon [4.0 to 2.5 billion years ago (Ga)] (*12*) despite the possible origin of oxygenic photosynthesis by 3.0 Ga (*13*). Oxygen levels in the Proterozoic eon (2.5 to 0.541 Ga) are disputed, but some proxy estimates imply remotely undetectable levels (*14*). More generally, we do not know whether oxygenic photosynthesis is a likely evolutionary development. Oxygenic photosynthesis is enzymatically complex and only evolved once on Earth (*15*).

For all these reasons, alternative approaches to biosignatures are needed. Previous studies have explored hydrocarbons and their hazes, organosulfur compounds, and biological pigments as biosignatures for anoxic worlds similar to the early Earth [reviewed by Schwieterman *et al.* (*16*)], but these approaches rely on specific metabolisms with high productivities.

A more general biosignature, which has not been considered for the early Earth, is atmospheric chemical disequilibrium, evident in the coexistence of two or more long-term incompatible gases (*17*–*20*). The modern O_2-CH_4 redox couple is widely believed to be a compelling disequilibrium biosignature because of the short kinetic lifetime (~10 years) of methane in Earth's atmosphere (*21*, *22*), which requires a substantial source flux of CH_4 in excess of reasonable abiogenic sources.

A number of arguments against the concept of disequilibrium biosignatures have been proposed. Kleidon [(*23*), p. 250] notes that atmospheric disequilibrium between O_2 and CH_4 exists because of incomplete decomposition of organic matter. The power associated with this leakage of unused free energy is a small fraction (0.3%) of power involved in photosynthesis, and so, it is argued that atmospheric chemical disequilibrium is not a good indicator of biospheric activity. However, chemical disequilibrium need not map to the amount of biological production to be a good biosignature—it merely has to reveal the existence of life. The methane flux required to sustain observed quantities of methane in the modern Earth's oxidizing atmosphere is greater than what abiotic processes could plausibly provide, and thus, biological methane leakage must be invoked to explain the persistent disequilibrium. In addition, it has been argued that the disequilibrium in the Earth's atmosphere is merely a reflection of high oxygen levels and that statements

[1]Department of Earth and Space Sciences/Astrobiology Program, University of Washington, Seattle, WA 98195, USA. [2]Virtual Planetary Laboratory, University of Washington, Seattle, WA 98195, USA. [3]Department of Earth Sciences and NASA Astrobiology Institute, University of California, Riverside, Riverside, CA 92521, USA.
*Corresponding author. Email: joshkt@uw.edu

about disequilibrium therefore reduce to statements about oxygen (*24*). However, in this paper, we show that there was an important biogenic disequilibrium in the anoxic Archean atmosphere.

Previously, we quantified the thermodynamic disequilibrium in solar system atmospheres by taking observed compositions, reacting them numerically to chemical thermodynamic equilibrium, and calculating the Gibbs free energy difference between observed and equilibrium states (*25*). Earth's purely gas-phase disequilibrium, as measured by available Gibbs free energy, is 1.5 J/mol of atmosphere and largely attributable to the O_2-CH_4 thermodynamic disequilibrium. The magnitude of this disequilibrium is not large compared to the abiogenic disequilibrium calculated for other solar system bodies, but given the kinetic considerations discussed above, CH_4 and O_2 remain a robust disequilibrium biosignature. In contrast, when the Earth's entire fluid envelope (the atmosphere-ocean reservoir) is considered, the disequilibrium is very large (2326 J/mol) due to the coexistence of O_2, N_2, and liquid water. These three species should react to form nitric acid in thermodynamic equilibrium. Krissansen-Totton *et al.* (*25*) discuss how this biogenic disequilibrium is potentially detectable on exoplanets similar to the modern Earth.

Although Earth's chemical disequilibrium is large today, how the disequilibrium changed through Earth history has not been quantified—whether it was large in the Precambrian when there was less atmospheric oxygen, and whether biogenic species would have contributed in an anoxic atmosphere. The N_2-O_2-H_2O and O_2-CH_4 disequilibrium biosignatures may not have been present for much of Earth history because the atmosphere had 20 ± 10% O_2 for only the last one-eighth of its history and virtually no O_2 in the Archean [reviewed by Catling and Kasting (*26*), chap. 10]. Consequently, we seek to calculate the thermodynamic disequilibrium for the Archean, Proterozoic, and Phanerozoic atmosphere-ocean systems. We explore how Earth's atmosphere-ocean disequilibrium has coevolved with life and find that the results suggest a novel disequilibrium biosignature for Archean-like exoplanets.

RESULTS

Approach for calculating thermodynamic disequilibrium

We calculated chemical thermodynamic disequilibrium in the atmosphere-ocean system according to the methodology shown schematically in Fig. 1 and fully described in Materials and Methods. Our MATLAB code is available on the website of the lead author. Given an assumed composition for the atmosphere and ocean of the early Earth, we react the whole system to thermodynamic equilibrium using Gibbs energy minimization. The equilibrium abundances of reactive constituents differ from the initial abundances, but atoms and charge are conserved. We neglect solids and most nonvolatile aqueous species because our focus is on remotely observable disequilibria (justified further in Discussion and in section S1).

To quantify the chemical thermodynamic disequilibrium in a planet's atmosphere-ocean system, we define the "available Gibbs energy" as the difference in Gibbs free energy between the initial (observed) state and the equilibrium state

$$\Phi \equiv G_{(T,P)}(\mathbf{n}_{\text{initial}}) - G_{(T,P)}(\mathbf{n}_{\text{final}}) \quad (1)$$

The available Gibbs energy, Φ, has units of joules per mole of atmosphere. The vector $\mathbf{n}_{\text{initial}}$ contains the abundances of all the atmospheric and ocean constituents of the initial state, whereas $\mathbf{n}_{\text{final}}$ contains abundances of the final state. This Gibbs free energy difference is the maximum useful work that can be extracted from the system. That is, Φ is the untapped chemical free energy in a planet's atmosphere and so provides our metric of disequilibrium. Note that when we discuss life exploiting the free energy in a planet's atmosphere, we are referring to surface (or subsurface) life consuming atmospheric gases. Although there are microbes that are adapted to survival in the upper troposphere (*27*), no known organism subsists independently of the surface.

Table 1 shows estimates of the composition of the atmosphere and ocean in the Precambrian, adopted as initial abundances in our

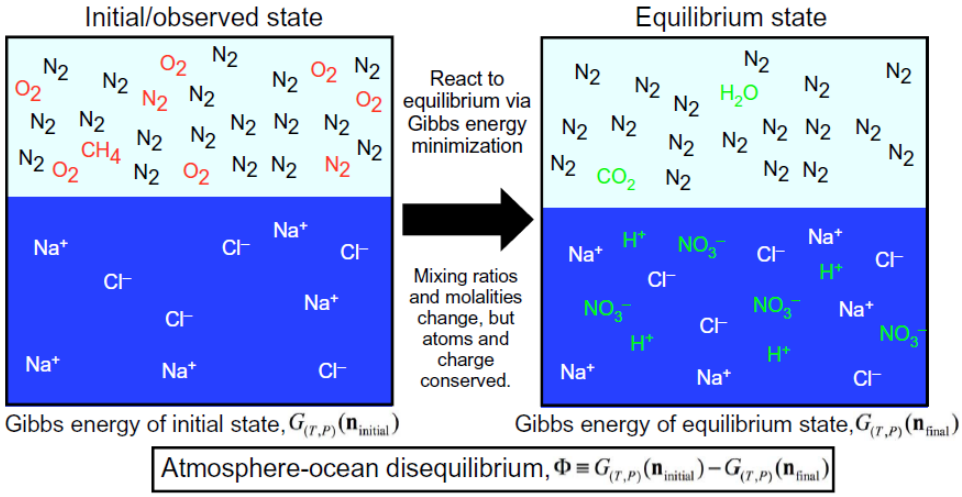

Fig. 1. Schematic of methodology for calculating atmosphere-ocean disequilibrium. We quantify the disequilibrium of the atmosphere-ocean system by calculating the difference in Gibbs energy between the initial and final states. The species in this particular example show the important reactions to produce equilibrium for the Phanerozoic atmosphere-ocean system, namely, the reaction of N_2, O_2, and liquid water to form nitric acid, and methane oxidation to CO_2 and H_2O. Red species denote gases that change when reacted to equilibrium, whereas green species are created by equilibration. Details of aqueous carbonate system speciation are not shown.

Table 1. Assumed initial atmosphere-ocean composition for Archean and Proterozoic.

Atmospheric species	Archean range			Proterozoic range		
	Mixing ratio		Reference/explanation	Mixing ratio		Reference/explanation
	Minimum disequilibrium	Maximum disequilibrium		Minimum disequilibrium	Maximum disequilibrium	
N_2(g)	0.98	0.5	Mixing ratios sum to 1	0.99	0.86	Mixing ratios sum to 1
O_2(g)	1×10^{-10}	2×10^{-7}	(*39*)	0.0001	0.03	(*14*, *76*)
CH_4(g)	0.0001	0.01	(*77*)	3×10^{-6}	1×10^{-4}	(*78*, *79*)
CO_2(g)	0.001	0.5	(*80*, *81*)	0.0001	0.1	(*80*, *81*)
H_2(g)	0	0.0001	(*59*)	0	2×10^{-6}	(*82*)
N_2O(g)	0	0	No denitrification so negligible production	0	1×10^{-6}	(*79*, *83*)
NH_3(g)	0	1×10^{-9}	(*84*)	0	0	Negligible in bulk atmosphere
O_3(g)	0	0	Negligible in bulk atmosphere	0	0	Negligible in bulk atmosphere (*79*)
CO(g)	0	0.001	(*59*)	0	2×10^{-7}	(*82*)
Ocean species	**Molality (mmol/kg)**		**Reference/explanation**	**Molality (mmol/kg)**		**Reference/explanation**
	Minimum disequilibrium	**Maximum disequilibrium**		**Minimum disequilibrium**	**Maximum disequilibrium**	
Na^+	550	586	Charge balance	547	549	Charge balance
Cl^-	546	546	Modern value	546	546	Modern value
SO_4^{2-}	0	0.2	(*85*, *86*)	0.25	5	(*87*, *88*)
H_2S	0	0.004	In euxinic oceans using a Black Sea analog*	0	0.004	In euxinic oceans using a Black Sea analog*
NH_4^+	0	0.050	Set by phosphorus† assuming Redfield ratios and the presence of N fixation, given that N fixation evolved early (*89*)	0	0.050	Set by phosphorus† assuming Redfield ratios
NO_3^-	0	0	Anoxic bulk ocean	0	0	Anoxic bulk ocean
Alkalinity	4	40	(*29*); Krissansen-Totton *et al.*, in preparation	1.0	3.0	(*29*); Krissansen-Totton *et al.*, in preparation
pH	8.0	6.3	Carbon chemistry equilibrium‡	8.4	6.0	Carbon chemistry equilibrium‡

*The concentration of H_2S in the Black Sea is around 400 μmol/kg (*90*). However, <1 to 10% of the Precambrian seafloor was euxinic (*91*), which implies <1% euxinia by volume because euxinic continental slopes are much shallower than the deep ocean. Thus, we assumed 4 μmol/kg as an upper limit for bulk ocean aqueous H_2S. †The maximum subsurface concentration of NH_4^+ is ultimately controlled by flux of phosphate from continental weathering. Assuming a modern dissolved phosphate abundance of ~2 μmol/kg, this implies an ammonium abundance of 32 μmol/kg assuming a 1:16 Redfield ratio. Results are largely insensitive to initial abundances of NH_4^+ (Fig. 5). ‡pH is calculated from alkalinity and P_{CO_2} assuming chemical equilibrium.

calculations. Plausible ranges for atmospheric mixing ratios and aqueous species molalities are taken from the literature, which includes proxy estimates and theoretical modeling. For both the Archean and Proterozoic, we calculate two end-member cases, denoted maximum and minimum disequilibrium. The maximum disequilibrium case assumes the largest possible mixing ratios and molalities of reactive species from the literature, whereas the minimum disequilibrium case assumes the converse. In the assumed initial ocean chemistry, $[Na^+]$, a conservative nonreactive ion, is adjusted to achieve charge balance. Similarly, the initial mixing ratio of N_2 is adjusted in every case to ensure that mixing ratios sum to unity.

Calculations were performed at 1-bar surface pressure for which partial pressures are numerically equivalent to mixing ratio constraints, but in the Supplementary Materials, we repeat our Archean calculations at both higher and lower pressures and find that changing atmospheric pressure has little effect on the results. Unless stated otherwise, initial dissolved gas abundances were calculated using Henry's law with coefficients from the National Institute of Standards and Technology (NIST) database (*28*). The errors introduced by assuming saturation for dissolved species are discussed in section S1 and found to be small. Initial water vapor abundances are also determined using Henry's law. In practice, tropospheric water vapor is spatially and

temporally highly variable (0 to 4%) and controlled by the dynamics of the hydrological cycle, but using Henry's law yields an initial abundance (1.6%) consistent with this empirical range.

Ranges for ocean carbonate alkalinity, which is defined as the charge-weighted sum of carbon-bearing ions, $2[CO_3^{2-}] + [HCO_3^-]$, are based loosely on the study of Halevy and Bachan (*29*). However, in the Supplementary Materials, we investigate the sensitivity of our results to different assumed alkalinities and find that our key conclusions are unchanged.

Given alkalinity and atmospheric P_{CO_2} (partial pressure of CO_2), we calculate ocean pH, carbonate, and bicarbonate concentrations from equilibrium chemistry. This procedure ensures that out-of-equilibrium carbon chemistry does not contribute to our disequilibrium calculations. Of course, in calculating disequilibria, carbonate speciation may be shifted by the reaction of other species in the system.

A commercial chemical engineering software package called Aspen Plus (version 8.6) was used to validate all the MATLAB calculations reported in this paper [see the study of Krissansen-Totton *et al.* (*25*) for full description of its implementation]. Tables comparing MATLAB and Aspen results are reported in section S2. In general, MATLAB and Aspen outputs agree to within 10% or better. Small differences are expected because the thermodynamic models in our MATLAB code differ from those in Aspen Plus. However, unlike the proprietary code, ours is open source and so fully transparent.

Thermodynamic disequilibrium over Earth history

Here, we report results for our maximum and minimum disequilibrium in the Proterozoic and Archean. If the true atmosphere and ocean abundances are bounded by the values in Table 1, then the minimum and maximum disequilibria we calculate will encompass the true disequilibrium of the Earth's atmosphere-ocean system through time.

Figure 2 shows our calculated evolution of Earth's atmosphere-ocean disequilibrium. The modern atmosphere-ocean disequilibrium was analyzed at length by Krissansen-Totton *et al.* (*25*). In Fig. 2, the Phanerozoic Earth range was determined by using the abundances from (*25*) but varying initial oxygen mixing ratios from 0.1 to 0.3, which is the range inferred for the Phanerozoic (*30*). Two ranges are provided for the Proterozoic representing different assumptions about Proterozoic oxygen. We find that Earth's atmosphere-ocean disequilibrium was the smallest in the Archean, increased with the initial rise of oxygen during the Paleoproterozoic Great Oxidation Event, and then increased again after a second major increase in oxygen during the Neoproterozoic (Fig. 2).

The calculations that follow explain the evolution of Precambrian disequilibrium and which species are out of equilibrium and therefore contributing to the available Gibbs energy. This gives insight into how the disequilibria are affected by life and which species could serve as biosignatures.

The Proterozoic disequilibrium and species that contribute to it

The available Gibbs energy for the maximum Proterozoic case is 884 J/mol, and the initial and equilibrium abundances for this case are shown in Fig. 3. We computed the contribution of individual reactions to this Gibbs energy by repeating the equilibrium calculation without the reaction products of specific reactions and by checking the results against semianalytic calculations (*25*).

The largest source of disequilibrium in the Proterozoic is the same as for the modern Earth: The levels of N_2, O_2, and liquid water should not coexist but rather react to form nitric acid

$$5O_2 + 2N_2 + 2H_2O \rightarrow 4H^+ + 4NO_3^- \quad (2)$$

The depletion of O_2 and the increase in H^+ and NO_3^- are seen in Fig. 3. The formation of nitric acid also drives carbon speciation to a new equilibrium (section S3). Nitric acid formation and subsequent adjustment of carbon speciation contributes ~640 J/mol, the majority of Proterozoic atmosphere-ocean disequilibrium (72%).

Other reactions that contribute to the maximum Proterozoic disequilibrium are shown in section S3. Methane oxidation contributes considerably (75 J/mol) to the maximum Proterozoic disequilibrium because assumed methane abundances are much higher than on the modern Earth

$$CH_4 + 2O_2 \rightarrow 2H_2O + CO_2 \quad (3)$$

For the minimum Proterozoic case, the disequilibrium is still dominated by nitrate formation, but the available energy is only 9.5 J/mol due to lower initial P_{O_2} (partial pressure of oxygen). Figure S1 shows the initial and equilibrium abundances for the minimum Proterozoic case,

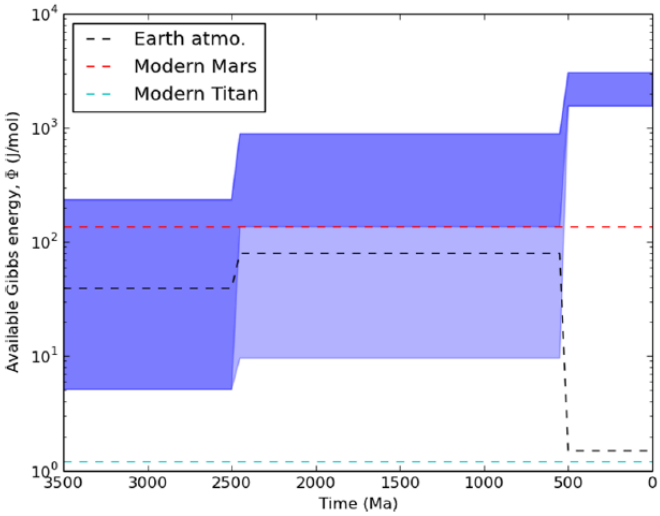

Fig. 2. The evolution of Earth's atmosphere-ocean disequilibrium through time, as measured by available Gibbs free energy. The blue shaded regions show the evolution of Earth's atmosphere-ocean disequilibrium. The wide ranges in the Archean and Proterozoic span our minimum and maximum disequilibrium scenarios. The large ranges are attributable to uncertainties in the atmospheric composition in each eon, mainly uncertain P_{CH_4} in the Archean and uncertain P_{O_2} in the Proterozoic. The two shadings for the Proterozoic represent different assumptions about atmospheric oxygen levels that represent divergent views in the current literature. Darker blue denotes P_{O_2} > 2% PAL (present atmospheric level), whereas lighter blue denotes P_{O_2} < 2% PAL. We calculate a secular increase in Earth's atmosphere-ocean disequilibrium over Earth history, correlated with the history of atmospheric oxygen. The black dashed line shows the upper bound of the Earth's atmosphere-only disequilibrium through time. We also include the modern (photochemically produced) disequilibria of Mars (red dashed) and Titan (blue dashed) for comparison (*25*). The abiotically produced disequilibria of all the other solar system planets are ≪1 J/mol (*25*).

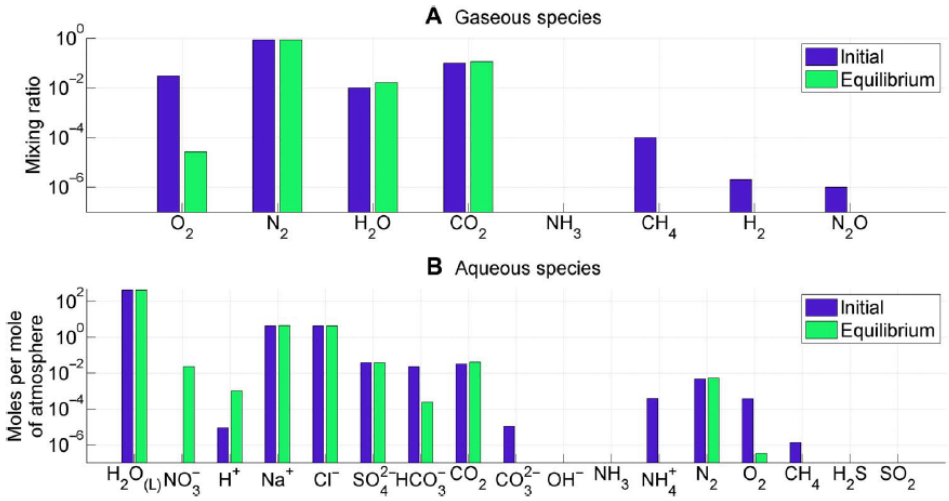

Fig. 3. Atmosphere-ocean disequilibrium in the Proterozoic (maximum disequilibrium scenario). Blue bars denote assumed initial abundances from the literature, and green bars denote equilibrium abundances calculated using Gibbs free energy minimization. Subplots separate (**A**) atmospheric species and (**B**) ocean species. The most important contribution to Proterozoic disequilibrium is the coexistence of atmospheric oxygen, nitrogen, and liquid water. These three species are lessened in abundance by reaction to equilibrium to form aqueous H^+ and NO_3^-. Changes in carbonate speciation caused by the decrease in ocean pH also contribute to the overall Gibbs energy change.

and tables S1 and S2 record numerical abundances for both maximum and minimum Proterozoic cases.

The Archean disequilibrium and species that contribute to it

The initial and equilibrium abundances for the maximum Archean case are shown in Fig. 4. The available Gibbs energy for the maximum Archean case is 234 J/mol, which is dominated by the coexistence of CO_2, N_2, CH_4, and liquid water. These four species should not coexist but rather should react to form ammonium and bicarbonate, depleting almost all atmospheric methane (99.8% of the initial CH_4 is consumed by reaction to equilibrium)

$$5CO_2 + 4N_2 + 3CH_4 + 14H_2O \rightarrow 8NH_4^+ + 8HCO_3^- \quad (4)$$

The depletion of CH_4 and increase in NH_4^+ and HCO_3^- are seen in Fig. 4. This reaction alone contributes ~170 J/mol (74%) of the maximum Archean disequilibrium. Other reactions that contribute to the maximum Archean disequilibrium are shown in section S3.

The available energy for the minimum Archean case is 5.1 J/mol, but even in this case, CH_4 is 99.99% depleted with respect to its initial abundance at equilibrium, demonstrating that CH_4 should not coexist in equilibrium with N_2-CO_2-H_2O (liquid) across a broad range of initial conditions. Figure S2 shows the initial and equilibrium abundances for the minimum Archean case. Tables S4 and S5 also record numerical abundances for both maximum and minimum Archean cases.

DISCUSSION

Disequilibria and the history of life

Our results show that Earth's disequilibrium has been strongly affected by life. The evolution of Earth's atmosphere-ocean disequilibrium follows the rise of biogenic oxygen (Fig. 2) similar to how the use of energy by life over Earth history was changed by an anaerobic to aerobic transition (*31*). Our calculated quantitative evolution of Earth's atmosphere-ocean thermodynamic disequilibrium is also consistent with qualitative speculations about the evolution of free energy dissipation by the biosphere through time [figure 12.5 of Kleidon (*23*)]. Oxygenic photosynthesis maintains disequilibrium in the Proterozoic and Phanerozoic by replenishing O_2 against O_2 sinks. Oxygenic photosynthesis also replenishes N_2 because the organic matter used in nitrate reduction and subsequent denitrification is produced by oxygenic photosynthesis (although approximately half of the N_2 replenishment comes from outgassing—see below for a more detailed discussion of nitrogen cycling). The emergence of oxygenic photosynthesis and the associated rise in primary productivity increased the disequilibrium of Earth's atmosphere-ocean system. Disequilibrium increased again in the Phanerozoic because oxygenic photosynthesis left a larger imprint on the environment following the Neoproterozoic rise of oxygen.

Before the advent of oxygenic photosynthesis, we calculate that Earth's disequilibrium was probably smaller than at any subsequent time (Fig. 2). If Archean life was exclusively chemotrophic, then it may have decreased a preexisting abiotic disequilibrium, mostly from the H_2-CO_2 pair in the atmosphere (*32*). With the advent of anoxygenic photosynthesis, the atmosphere-ocean disequilibrium may have increased because additional electron donors become available that were not limited by atmospheric abiotic disequilibrium. For example, Fe-oxidizing phototrophs produce organic carbon through the following net reaction

$$4Fe^{2+} + CO_2 + 11H_2O + h\nu \rightarrow 4Fe(OH)_3 + CH_2O + 8H^+ \quad (5)$$

The organic matter produced may then be converted to methane by anaerobic processing, thereby adding to the Archean atmosphere-ocean disequilibrium without the need for outgassed electron donors like H_2; methane is eventually photochemically oxidized to CO_2, thereby closing the cycle. We do not attempt to capture this change in Fig. 2 because we lack sufficient constraints about the advent of types of anoxygenic photosynthesis and their relative influence on atmospheric composition.

However, in both scenarios of anoxygenic photosynthesis and chemotrophy, the Archean biosphere does not drive the atmosphere-ocean system toward equilibrium. Instead, a CH_4-N_2-H_2O-CO_2

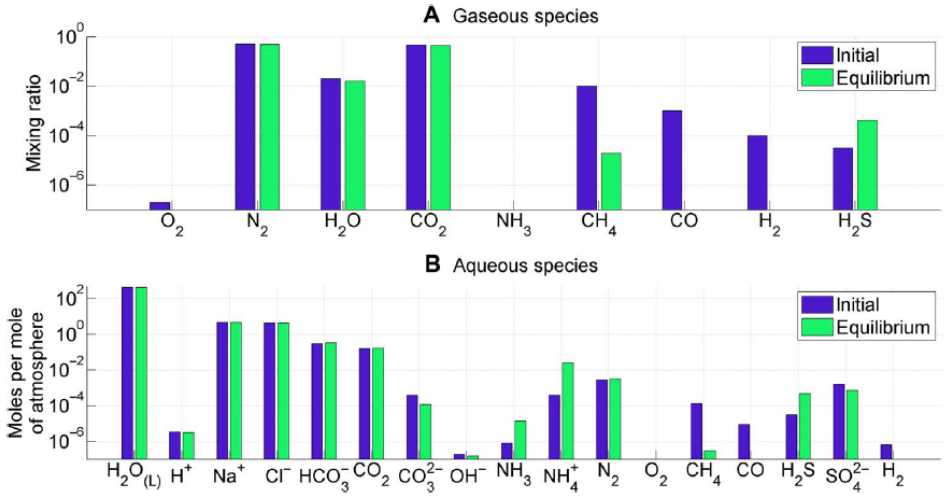

Fig. 4. Atmosphere-ocean disequilibrium in the Archean (maximum disequilibrium scenario). Blue bars denote assumed initial abundances from the literature, and green bars denote equilibrium abundances calculated using Gibbs free energy minimization. Subplots separate (**A**) atmospheric species and (**B**) ocean species. The most important contribution to Archean disequilibrium is the coexistence of atmospheric CH_4, N_2, CO_2, and liquid water. These four species are lessened in abundance by reaction to equilibrium to form aqueous HCO_3^- and NH_4^+. Oxidation of CO and H_2 also contributes to the overall Gibbs energy change.

disequilibrium persists, maintained by methanogens (albeit smaller in the chemotrophic case). After the emergence of oxygenic photosynthesis, but before the rise of oxygen, the CH_4-N_2-H_2O-CO_2 disequilibrium may have increased further due to a larger biological CH_4 flux from the anaerobic processing of organic matter as the productivity of the biosphere increased.

Figure 2 also shows the evolution of Earth's atmosphere-only disequilibrium (bounded by the black dashed line). The atmosphere-only disequilibrium decreases with time and thus does not reflect the rise of oxygen or the growth of primary productivity since 3.5 Ga. This illustrates the importance of including the oceans when quantifying disequilibrium in fluid reservoirs.

An interesting question emerges from this analysis: Given that Earth's atmosphere-ocean system has been massively out of equilibrium since the early Archean, why has life not evolved to consume this "free lunch"? In particular, why have no metabolisms evolved to exploit the N_2-O_2-H_2O disequilibrium present after the Archean? Nitrogen-fixing bacteria and nitrifiers convert N_2 to nitrate, and although the nitrification step yields free energy, no known organism obtains energy by combining these two reactions. Lewis and Randall [(*33*), pp. 567–568] were the first to recognize that N_2, O_2, and water were out of equilibrium in the Earth system, and they argued that it was fortunate for us that life had not evolved to catalyze their reaction because, otherwise, the atmosphere would have been depleted of oxygen and the oceans turned to dilute nitric acid.

In reality, it is hard to predict what the end result of such evolutionary innovation would be. Atmospheric oxygen would be replenished to some extent by photosynthesis, but nitrogen might be drawn down faster than it could be replenished because there are abundant cations in the crust to neutralize nitric acid oceans, and because dissolved ammonium could be incorporated into clays where it would accumulate. If the atmospheric drawdown were sufficiently severe, then it could even result in a global glaciation due to the loss of pressure broadening from nitrogen. Although anthropic reasoning accounts for why such a metabolism never evolved, a more satisfying explanation is that the kinetic barriers to the N_2-O_2-H_2O reaction are insurmountable. The process by which N_2 is converted to nitrate by Earth life is complex with multiple steps: Nitrogen fixers expend energy to convert N_2 to NH_3 under anaerobic conditions (or with adaptations to overcome high oxygen levels) to overcome an activation energy barrier (*34*), and nitrifiers oxidize NH_3 to nitrate under aerobic conditions. Perhaps, the enzymatic machinery required to split the N_2 triple bond and combine these two steps under aerobic conditions is too complex and energy-intensive to maintain.

Practicality of early Earth disequilibrium biosignatures

The most important disequilibrium species in both the Proterozoic (O_2, N_2, ocean) and the Archean (CH_4, N_2, CO_2, ocean) are, in principle, detectable on exoplanets. In the Archean, high CH_4 should be readily detectable (*35*), and CO_2 has abundant absorption features (*36*). Nitrogen absorbs at 4.15 μm due to N_4, which could be used to infer N_2 partial pressure (*37*). Note that it is not necessary to precisely constrain N_2 partial pressure to estimate the CH_4-N_2-CO_2-H_2O thermodynamic disequilibrium. For example, for a maximum Archean disequilibrium scenario with very low N_2 partial pressure (0.02 bar) and high CO_2 (0.95 bar), the available Gibbs energy is 151 J/mol (table S8). So long as there is sufficient N_2 (and CO_2) to react with CH_4 until reaction (*4*) goes to completion, then a large thermodynamic disequilibrium will exist between N_2, CO, CH_4, and liquid water. Various techniques have been proposed to detect surface oceans including glint, polarization, and surface mapping [reviewed by Fujii *et al.* (*38*)] (see section S4 for further discussion).

The remote detectability of oxygen in the Proterozoic atmosphere depends on abundance. If Proterozoic P_{O_2} was <0.1% PAL (present atmospheric level), as has been suggested from one interpretation of Cr isotopes (*14*), then it may not be possible to detect O_2 on a "Proterozoic Exo-Earth" with next-generation telescopes (*35*). Extremely low Proterozoic oxygen, however, is difficult to reconcile with photochemical models that show that O_2 levels between 10^{-6} PAL and 0.1% PAL are unstable against small perturbations in the O_2 source flux (*39*), favoring P_{O_2} closer to the upper boundary used for our maximum disequilibrium calculations. In either case, O_3, a photochemical product of O_2, could be detected even if O_2 itself could not (*35*, *40*).

Regardless of uncertainty about precise abundances of O_2 and CH_4 over Earth history, it is possible to design telescopes capable

of constraining the disequilibrium atmospheric constituents described above. A potential problem for quantifying disequilibrium from observations is its sensitivity to variables that are difficult or impossible to observe, such as ocean composition and ocean volume. In the study of Krissansen-Totton *et al.* (*25*), we showed the modern Earth's N_2-O_2-H_2O disequilibrium is relatively insensitive to these variables. The same is true for large Proterozoic disequilibria, which involve the same species.

For the Archean CO_2-N_2-CH_4-H_2O disequilibrium, the equilibrium abundances are insensitive to the unobservable NH_4^+ and HCO_3^- ocean molalities. This insensitivity is shown in Fig. 5, which plots the fractional depletion of methane in equilibrium as a function of initial aqueous species molalities. Unless both NH_4^+ and HCO_3^- are extremely high, methane should be depleted in equilibrium. Section S4 shows that Archean disequilibrium is robust to uncertainties in ocean composition, volume, temperature, and pressure. The magnitude of the Archean thermodynamic disequilibrium typically varies by less than a factor of 2 across a wide range of assumptions about ocean pH, alkalinity, salinity, volume, temperatures, and pressure.

Interpretation of early Earth disequilibrium

Would the detection of CH_4, N_2, CO_2, and an H_2O ocean be a reliable exoplanet biosignature? The thermodynamic disequilibria of modern Mars and Titan are overplotted in Fig. 2, and it can be seen that the abiotic photochemical disequilibrium of Mars is comparable in magnitude to the biological disequilibrium of the early Earth. Clearly, the magnitude of atmospheric disequilibrium does not—on its own—indicate the presence of life. Further interpretation is necessary.

In general, atmospheric disequilibria are the product of the generation of free energy balanced by the dissipation of free energy. A large thermodynamic disequilibrium could be the consequence of either a high free energy generation rate or a low dissipation rate (*22*). For this reason, to evaluate the CH_4-N_2-CO_2-H_2O disequilibrium biosignature, it is necessary to consider the photochemical lifetime of CH_4 in such an atmosphere (that is, the rate of free energy dissipation) and possible abiotic sources of CH_4 (rate of free energy generation).

Even in reducing atmospheres, CH_4 has a geologically short lifetime. Diffusion-limited hydrogen escape would deplete an Earth-like planet of atmospheric methane in ~30 thousand years [(*26*), p. 215]. Consequently, we would not expect a CH_4-N_2-CO_2-H_2O (liquid) disequilibrium to persist without a substantial flux of CH_4 from a planet's surface that is typical of biology. We argue below that large abiotic CH_4 fluxes are unlikely and that, where they do occur, they can probably be distinguished by context.

Mantle-derived methane is an implausible abiotic source and could be distinguished by the coexistence of carbon monoxide. Pressure-temperature conditions in the Earth's shallow mantle (<~100 km) strongly favor CO_2 over CH_4. Any deep mantle CH_4 would be converted to CO_2 by rapid equilibration long before reaching the surface (*41*). For terrestrial planets with a more reducing mantle than Earth, significant CH_4 outgassing is conceivable. However, a highly reducing mantle would also produce huge CO fluxes (see section S5), and because CO has few abiotic sinks and detectable spectral features (*42*), mantle-derived methane could readily be identified by coexisting CO. In addition, outgassed CO is unlikely to persist in abundance in the atmospheres of inhabited planets because CO is an excellent source of microbial free energy and carbon (*43*).

A much discussed scenario for abiotic methane generation is through hydrothermal alteration of crustal mafic rocks (serpentinization), which produces H_2, followed by Fischer-Tropsch type (FTT) synthesis. Following the study of Fiebig *et al.* (*44*), we estimate the maximum possible abiotic methane flux, F_{CH_4} (mol/year), that could be generated from this process, as follows

$$F_{CH_4} = \frac{P_{Crust}}{M_{FeO}} fr_{FeO} fr_{H_2} fr_{CH_4} \quad (6)$$

Here, P_{Crust} is the crustal production rate in kilogram per year, M_{FeO} is the molar mass of FeO in kilogram per mole, fr_{FeO} is the weight % (wt %) of FeO in newly produced crust, fr_{H_2} is the maximum fraction of FeO that is converted to H_2 by serpentinization reactions, and fr_{CH_4} is the maximum fractional conversion of H_2 to CH_4 by FTT reactions. Assuming plausible ranges for these unknown variables and sampling their ranges uniformly, we produce a probability distribution for the maximum possible abiotic methane flux.

Today, magma emplacement from ridges, arcs, and plumes is 5.7×10^{13} kg/year (*45*), and with a generous assumption that crustal production may have been 10× higher on the early Earth, we take crustal production, P_{Crust}, to range from 5.7×10^{13} to 5.7×10^{14} kg/year. Whether these high crustal production rates are likely for terrestrial exoplanets is an open question, given that some argue that Archean Earth's crustal production may not have been much greater than modern (*46*). In addition, it might be possible to put some constraints on exoplanet crustal production rates from observable planetary properties (*47*).

Hydrothermal alteration is ultimately limited by the availability of FeO. The Earth's basaltic oceanic crust is ~10 wt % FeO, which would imply a modern FeO production rate of $0.1 \times 5.7 \times 10^{13}/(0.056 + 0.016) = 79$ Tmol FeO/year. We will allow fractional FeO content, fr_{FeO}, to vary

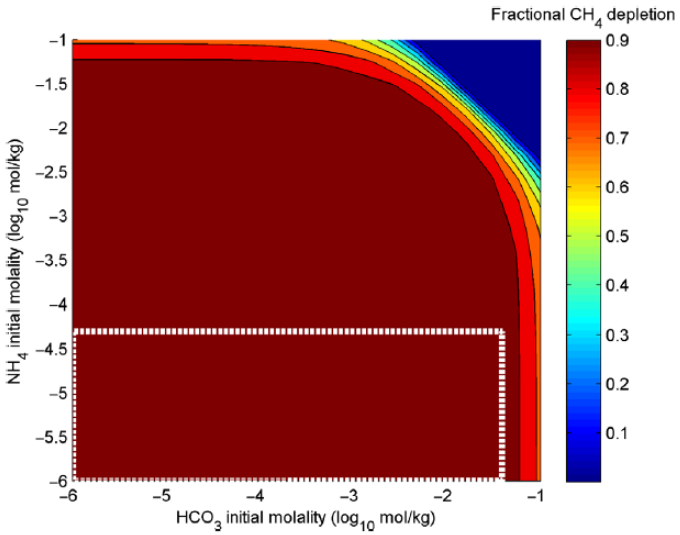

Fig. 5. Sensitivity of Archean disequilibrium to bicarbonate molality and ammonium molality in ocean, quantities that are probably impossible to directly observe for exoplanets. Colors shows fraction of methane depleted in equilibrium, as determined by semianalytic calculations. In this case, $P_{CO_2} = 0.49$ bar, $P_{N_2} = 0.5$ bar, and $P_{CH_4} = 0.01$ bar. As can be seen, most parts of parameter space have high CH_4 depletion, that is, CH_4 is in disequilibrium. Thus, unless both bicarbonate and ammonium molalities are extremely large, detectable quantities of methane are out of equilibrium with an N_2-CO_2 atmosphere and ocean. The white dashed line box denotes the plausible Archean range.

from 10 to 25 wt %, considering possible Mars- or Moon-like crustal compositions.

A key unknown is what fraction of FeO is oxidized by water to liberate H_2, fr_{H_2}. A naïve upper estimate would assume that all the crustal FeO is oxidized to yield H_2 by the following equation

$$3FeO + H_2O \rightarrow Fe_3O_4 + H_2 \quad (7)$$

Such an assumption is unrealistic, however. On Earth, multiple lines of evidence suggest that the H_2 production rate from serpentinization is around 0.2 Tmol/year (*48*, *49*), which is 0.25% of the total FeO production, two orders of magnitude less than a one-third theoretical maximum from the stoichiometry of Eq. 7. We take $fr_{FeO} = 0.0025$ as our lower bound for the fractional conversion of H_2 to FeO. On the modern Earth, H_2 production is low because only 12% of crustal Fe^{2+} is converted to Fe^{3+} as water cannot permeate all the oceanic crust (*45*). Furthermore, only 1 to 2% is due to serpentinization; the remaining 10 to 11% is from oxidation by sulfate, which does not generate H_2 [(*26*), chap. 10; (*45*)]. Most of the H_2 produced from serpentinization is derived from ultramafic, slow-spreading crust, which only constitutes 24% of the total crustal production (*48*). A nonlinear relationship also exists between degree of serpentinization and H_2 production, and for <50% serpentinization, negligible H_2 is generated (*49*). For the upper bound, we generously assume that the entirety of an Exo-Earth's FeO oxidation is due to H_2-producing serpentinization through Eq. 7, as might occur with more ultramafic crust, giving $fr_{FeO} = 0.12/3 = 0.04$.

The fractional conversion of H_2 to CH_4, fr_{CH_4}, is the final parameter for calculating maximum abiotic CH_4 fluxes. For maximum conversion, we assume that all H_2 makes CH_4 via FTT synthesis

$$CO_2 + 4H_2 \rightarrow 2H_2O + CH_4 \quad (8)$$

That is, we assume $fr_{CH_4} = 0.25$, aware that this is an overestimate. The conversion of CO_2 to CH_4 by Eq. 8 is thermodynamically favorable in low-temperature hydrothermal systems, but it is unclear whether natural systems can overcome kinetic barriers on a global scale without biological catalysts. Although evidence from field studies suggests that abiotic methane is generated in some hydrothermal systems (*44*, *50*), laboratory experiments typically find very low methane yields from FTT synthesis from olivine. High experimental methane production has been reported (*51*, *52*), but similar experiments with ^{13}C-labeled carbon have shown that the methane produced is derived from background organic carbon contamination (*53*, *54*). Only very specific laboratory conditions yield high CH_4 production from olivine. For example, when pressure is low enough for gas-phase reactions, abiotic CH_4 production is high (*53*), but it is unlikely that gas-phase reactions would occur at great depth in the crust (*44*). Similarly, the presence of Fe-Ni catalysts enables CH_4 production (*55*), but most of Earth's crust is not sufficiently reducing to have such catalysts (*41*). Guzmán-Marmolejo *et al.* (*56*) argued that CH_4 production is further restricted by CO_2 availability in the crust, limiting H_2/CH_4 ratios to ~13. Higher CO_2 concentrations are unlikely to overcome this restriction because Fe^{2+} will be incorporated into siderite rather than form magnetite and H_2 (*57*). Empirically, H_2/CH_4 ratios in hydrothermal systems are highly variable (*48*), so it is clear that the kinetic barriers to CH_4 formation and CO_2 limitations are generally present.

For our lower bound on fr_{CH_4}, we will adopt the empirical average from ultramafic-hosted hydrothermal fluids, $H_2/CH_4 = 12$ [table 1 of Keir (*48*)], which implies $fr_{CH_4} = 1/16$, although this likely overestimates global methane production for the reasons discussed above.

Figure 6 shows the probability distribution for F_{CH_4} obtained by uniformly sampling our chosen ranges for P_{Crust}, fr_{FeO}, fr_{H_2}, and fr_{CH_4}. Both the modern biological methane flux (*58*) and plausible biological Archean fluxes (*59*) are much larger than the distribution of maximum abiotic fluxes. On the basis of current understanding, the conditions required to generate large fluxes of abiotic methane are specific and implausible: All unknown variables need to be at the high end of their ranges, and our upper estimate for fr_{H_2} must be an underestimate. However, underestimation of fr_{H_2} is implausible because for fast rates of crustal production, fractional conversion of FeO to H_2 will, if anything, be lower than on Earth because water will permeate a smaller fraction of the total crust given faster spreading rates and thicker crust. In addition, the gas-phase reactions required to overcome kinetic barriers to CH_4 production will be inhibited at greater crustal thicknesses (*44*).

Impacts have also been proposed as a source of abiotic methane. During an impact, Fe or Ni catalysts in an asteroid could produce CH_4 from CO and H_2. Kress and McKay (*60*) modeled the kinetics of CH_4 production during the cooling of an impactor fireball and concluded that this could produce an abiotic methane flux during the late heavy bombardment greater than the modern Earth's biological flux. However, an exceptionally high mass flux is required. Using more plausible mass fluxes, Kasting (*61*) estimated an abiotic methane flux from impactors to be only ~0.3 Tmol/year at 3.8 Ga. This could potentially be increased to 1 Tmol/year if all impact ejecta are serpentinized. However, this too is unrealistically large because complete 12:1 FeO oxidation to CH_4 production is far from guaranteed, as discussed above. In any case, for terrestrial exoplanets, it may be possible to rule out large impactor fluxes from the system age, dust levels, or the absence of transiting planetesimals. For very high impactor fluxes, observable atmospheric consequences such as dust or CO may be detectable.

We conclude that large abiotic sources of CH_4 are either improbable or identifiable with other observations. Furthermore, the rich absorption

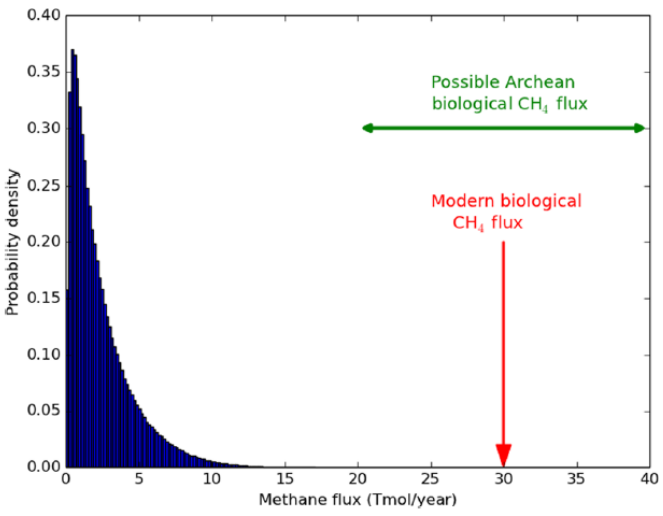

Fig. 6. Probability distribution for maximum abiotic methane production from serpentinization on Earth-like planets. This distribution was generated by sampling generous ranges for crustal production rates, FeO wt %, maximum fractional conversion of FeO to H_2, and maximum fractional conversion of H_2 to CH_4, and then calculating the resultant methane flux 1 million times (see the main text). The modern biological flux (*58*) and plausible biological Archean flux (*59*) far exceed the maximum possible abiotic flux. These results support the hypothesis that the co-detection of abundant CH_4 and CO_2 on a habitable exoplanet is a plausible biosignature.

spectra of CO_2, CH_4, and water vapor mean that they are the most readily detectable gases on an exoplanet with an anoxic atmosphere in the near future. Confirmation of a liquid water ocean and atmospheric N_2 that contribute to the full disequilibrium of an Archean Earth twin would require follow-up observations with next-generation space telescopes. However, the detection of CO_2 and CH_4 alone on a habitable exoplanet is a potential disequilibrium biosignature because carbon is present at the extreme ends of the redox ladder (the +4 and −4 states). This CO_2-CH_4 disequilibrium pair is more compelling than CH_4 alone, which could be primordial from a migrated icy world or outgassed from an extremely reducing mantle. An atmosphere rich in CO_2 and CH_4 has been proposed to explain a warm early Mars (*62*), but this atmosphere would be very transient (<1 million years) because CH_4 released from clathrates would be rapidly photodissociated.

Kinetic and geological considerations

The mere detection of CO_2 and CH_4 (and the absence of CO) does not necessarily imply the presence of life. Instead, it is desirable to calculate the necessary methane source flux given observed atmospheric abundances and the stellar spectrum (*56*). If the inferred source flux is greater than any known plausible abiotic mechanism (Fig. 6), or if plausible abiotic fluxes can be ruled out by contextual information, then life would be left as a reasonable hypothesis. For planets with anoxic atmospheres such as the CO_2-CH_4-N_2 atmospheres considered here, the methane abundance is set by the balance between photochemical destruction of methane with subsequent diffusion-limited hydrogen escape and the methane source flux from the surface (see section S6 for details). Thus, given an observed atmospheric CH_4 abundance, it is possible to infer the minimum CH_4 flux required to maintain this. Calculations (section S6) suggest that CH_4 abundances in excess of 10^{-3} imply methane source fluxes in excess of 7 Tmol/year, which is likely biological, whereas CH_4 abundances in excess of 10^{-2} imply methane source fluxes in excess of 50 Tmol/year, which is very likely biological (compare Fig. 6), when seen in combination with CO_2 and the absence of CO. These results are largely independent of stellar type, but more precise photochemical calculations ought to be applied in the future to better estimate implied fluxes from abundances.

The CO_2-CH_4 pair might be the most easily detectable exoplanet biosignature. For habitable planets around M-dwarfs with Earth-like biogenic fluxes, the transit transmission features from CO_2 and CH_4 may require shorter integration times to resolve than O_2 or O_3 features with JWST (*63*).

The kinetics and geological cycling of atmospheric nitrogen are also worth considering, given their contribution to disequilibria in both anoxic and oxic atmospheres. In (*25*), we presented a calculation to show that if life disappeared from Earth, lightning would convert atmospheric N_2 and O_2 to nitrate, depleting atmospheric oxygen in 20 to 200 Ma. In contrast, it has been argued that nitrate may be reduced to ammonia in mid-ocean ridge hydrothermal systems, which can then return to the atmosphere and be photochemically oxidized back to N_2 (*64*). However, the reduction of nitrate will yield ammonium, which is readily sequestered into silicates (*65*, *66*). Nitrogen-bearing crust may then be subducted, where some nitrogen may return to the atmosphere via arc volcanism, but the rest will continue to the mantle because of the stability of ammonium-bearing silicates at high temperatures (*67*). It is therefore reasonable to expect an N_2-O_2-H_2O disequilibrium to disappear without the continuing influence of life, although the precise time scale for the depletion of oxygen and nitrogen will depend on geological cycling that is difficult to quantify. Atmospheric N_2 persists on Venus because it is in equilibrium with the CO_2-dominated atmosphere (*25*) and there is no mechanism to draw down N_2 into the crust because of the lack of water.

Solid-state disequilibria

We have not included solid states of matter in our equilibrium calculations. In reality, if the modern Earth's atmosphere-ocean system were allowed to relax to equilibrium, then much of the atmospheric O_2 would react with the crust via oxidative weathering, and some dissolved carbon may form carbonate-bearing rocks. There is also a large disequilibrium between organic carbon and ferric iron in the crust, both of which have accumulated over time from photosynthesis and hydrogen escape, that far exceeds the disequilibrium in the fluid reservoir (*25*). Although there are 3.7×10^{19} mol O_2 in the atmosphere and oceans, there are 5.1×10^{20} mol O_2 equivalent Fe^{3+} and sulfate in sedimentary rocks, and ~2×10^{21} mol O_2 equivalent excess Fe^{3+} in igneous and metamorphic rocks (*68*). These crustal rocks are in disequilibrium with the <1.3×10^{21} mol O_2 equivalent reduced carbon in the crust (*68*). We therefore expect the biogenic disequilibrium in Earth's crustal reservoir to be several orders of magnitude larger than that of the atmosphere-ocean system (*25*).

However, we chose to ignore solid species because we are interested in remotely detectable disequilibrium biosignatures; detailed crustal compositions cannot be measured for exoplanets, and so, we restrict ourselves to the observable fluid reservoirs. Adding solid phases would not diminish any of the disequilibria described in our analysis but would potentially make the total available energy larger.

One potentially detectable solid-state disequilibrium not considered here is the disequilibrium between atmospheric oxygen and reduced carbon on the surface in the form of biomass [(*23*), p. 336]. In principle, surface biomass is detectable through the vegetative red edge (*16*). However, on the modern Earth, even if all the surface biomass (4.4×10^{17} Tmol C) were oxidized, only 1% of atmospheric oxygen would be depleted (*69*). Biomass oxidation through the following reaction yields 478 kJ/mol

$$CH_2O + O_2 \rightarrow CO_2 + H_2O \quad (9)$$

Therefore, the available energy from oxidizing all surface biomass is approximately (4.4×10^{17} mol × 478 kJ/mol)/(1.8×10^{20} mol) = 1200 J/mol of atmosphere. This dwarfs the ~1 J/mol from atmospheric methane oxidation but is only half the size of the N_2-O_2-H_2O disequilibrium on the modern Earth.

The simultaneous detection of atmospheric oxygen and a vegetative red edge would obviously be a more compelling biosignature than oxygen alone. However, we do not account for surface biomass in our disequilibrium through time calculations because quantifying surface organic biomass on exoplanets would be extremely challenging. Tinetti *et al.* (*70*) showed that the vegetative red edge is potentially detectable with next-generation direct imaging, though challenging with realistic clouds. However, it is not possible to map a red edge detection to surface biomass because near-infrared reflectance depends on numerous vegetation properties such as leaf thickness and canopy structure (*71*). Tinetti *et al.* (*70*) also considered marine plankton detectability and found that even on planets with shallow oceans and an order of magnitude more plankton than the modern Earth, the disc-integrated spectral features would be weaker than the vegetation signal.

CONCLUSIONS

Given current knowledge of the evolution of the atmosphere since the Archean, we calculate that Earth's atmosphere has been in thermodynamic chemical disequilibrium since the early Archean as a result of life. The magnitude of this disequilibrium has increased through time, correlated with increases in atmospheric oxygen and probable growth in biomass. The contributions to disequilibrium from solid states of matter were not included in these calculations because our focus is on properties that would be remotely detectable on exoplanets in the future.

In the Proterozoic and Phanerozoic, the coexistence of N_2, O_2, and liquid H_2O was the largest contributor to chemical disequilibrium. Both N_2 and O_2 are replenished by biology, and this disequilibrium would not persist in the absence of life because almost all the O_2 would be converted to nitric acid in the ocean. A smaller thermodynamic contribution to disequilibrium came from the CH_4-O_2 couple, which remains a compelling biosignature due to the short kinetic lifetime of CH_4 in O_2-rich atmospheres.

In the Archean, we show that likely levels of N_2, CH_4, and CO_2 in the presence of liquid H_2O were the largest contributors to disequilibrium. Without life continuously replenishing atmospheric CH_4, this disequilibrium would not have persisted because CH_4 would have been photolytically destroyed in the upper atmosphere. Large abiogenic fluxes of CH_4 (>10 Tmol/year) needed to support high abiogenic CH_4 abundances are very unlikely to occur on Earth-like exoplanets, and where they do occur, they can probably be identified through context.

The CH_4-N_2-CO_2-H_2O disequilibrium is thus a potentially detectable biosignature for Earth-like exoplanets with anoxic atmospheres and microbial biospheres. The simultaneous detection of abundant CH_4 and CO_2 (and the absence of CO) on an ostensibly habitable exoplanet would be strongly suggestive of biology. Specifically, methane mixing ratios $>10^{-3}$ would imply surface fluxes that are potentially biological, whereas mixing ratios $>10^{-2}$ would imply surface fluxes that are likely biological. Biology allows for the coexisting large redox separation of CH_4 and CO_2 and also readily consumes CO.

MATERIALS AND METHODS

Multiphase disequilibrium calculations

The methodology described here updates that used by Krissansen-Totton *et al.* (*25*). To calculate thermodynamic equilibrium for multiphase systems, we followed Karpov *et al.* (*72*) and used the following expression for the Gibbs energy of a multiphase system (relative to some reference state)

$$\Delta G_{(T,P)} = \sum_i c_i n_i + \sum_\alpha \sum_{i\in\alpha} n_i RT \ln(n_i/n_\alpha) - \sum_{j=\text{aqueous species}} n_j RT \ln(n_w/n_{aq})$$

$$c_i = \begin{cases} \Delta_f G^\circ_{i(T,P)} + RT\ln(\gamma_{fi}) + RT\ln(P), & i \in \text{gas} \\ \Delta_f G^\circ_{i(T,P)} + RT\ln(\gamma_{aw}), & i \in \text{water} \\ \Delta_f G^\circ_{i(T,P)} + RT\ln(\gamma_{ai}) + RT\ln(55.5084), & i \in \text{aqueous} \end{cases} \quad (10)$$

Here, we have simplified equations in (*72*) to exclude solid phases and nonwater pure liquids because we do not consider such systems in this study. The variables are defined as follows: n_i is the number of moles of the ith species (note that the vector $\mathbf{n}$ consists of the set of n_i); $\Delta_f G^\circ_i(T,P)$ is the standard free energy of formation for the ith species at temperature, T, and pressure, P [see (*25*) for explanation of how these were calculated and what databases were used]; α is the index for the phase (gaseous, water, or aqueous); n_α is the total number of moles of species in phase α; n_w is the total number of moles of liquid water in the system; n_{aq} is the total number of moles of aqueous species in the system; γ_{aw} is the activity coefficient of water; γ_{ai} is the activity coefficient of the ith aqueous species; γ_{fi} is the fugacity coefficient of the ith gaseous species; R is the universal gas constant; T is the temperature of the system (K), a constant; and P is the pressure of the system (bar), a constant.

To calculate the equilibrium state of the Earth's atmosphere-ocean system, we minimize Eq. 10 subject to the constraint that atoms and charge are conserved, where the latter means that aqueous systems are electroneutral (*25*).

Several improvements to our multiphase equilibrium calculations have been made from the version described by Krissansen-Totton *et al.* (*25*). Most importantly, activity coefficients for all aqueous species are calculated using the Pitzer equations rather than the Truesdell-Jones equation. This proved to be important for accurately capturing the Gibbs energy changes for Archean-like atmosphere-ocean systems. Activity coefficients for cations, M, and anions, X, were specified by the following equations (*73*)

$$\begin{aligned} &\ln(\gamma_M) = z_M^2 F + \sum_{\text{all anions}} m_a(2B_{Ma} + ZC_{Ma}) \\ &\ln(\gamma_X) = z_X^2 F + \sum_{\text{all cations}} m_c(2B_{cX} + ZC_{cX}) \\ &\text{where} \\ &F = -A_\phi\left[\frac{I^{0.5}}{1+bI^{0.5}} + \frac{2}{b}\ln(1+bI^{0.5})\right] + \sum_{\text{all pairs}} m_a m_c B'_{Ma} \\ &Z = \sum_i m_i|z_i| \\ &B_{MX} = B^{(0)}_{MX} + B^{(1)}_{MX} f(\alpha_1 I^{1/2}) + B^{(2)}_{MX} f(\alpha_2 I^{1/2}) \\ &f(x) = \frac{2[1-(1+x)\exp(-x)]}{x^2} \\ &B'_{MX} = \frac{B^{(1)}_{MX} f'(\alpha_1 I^{1/2})}{I} + \frac{B^{(2)}_{MX} f'(\alpha_2 I^{1/2})}{I} \\ &f'(x) = \frac{-2[1-(1+x+x^2/2)\exp(-x)]}{x^2} \end{aligned} \quad (11)$$

Here, the variables are defined as follows: m_i is the molality of the ith aqueous species; m_a is the molality of the anion; m_c is the molality of the cation; z_i is the charge of the zth aqueous species; I is the ionic strength of the solution, $I = 0.5\sum_i m_i z_i^2$; $\alpha_1 = 2.0$ $\text{kg}^{0.5}\text{mol}^{-0.5}$, $\alpha_2 = 0$ $\text{kg}^{0.5}\text{mol}^{-0.5}$ for all binary systems except 2:2 electrolytes; and $\alpha_1 = 1.4$ $\text{kg}^{0.5}\text{mol}^{-0.5}$, $\alpha_2 = 12$ $\text{kg}^{0.5}\text{mol}^{-0.5}$ for 2:2 electrolytes; $b = 1.2$ $\text{kg}^{0.5}\text{mol}^{-0.5}$ and $A_\phi = 0.3915$ $\text{kg}^{0.5}\text{mol}^{-0.5}$ are constants.

$B^{(0)}_{MX}$, $B^{(1)}_{MX}$, $B^{(2)}_{MX}$, C_{MX} are species-specific binary interaction parameters that were obtained from Appelo and Postma (*74*) and Marion (*75*). Note that we have adopted a simplified version of the Pitzer equations by ignoring cation-cation and anion-anion interactions, neutral solute parameters, and triple particle parameters. The excellent agreement between MATLAB and Aspen calculations confirms that neglecting

these terms is a reasonable approximation. Methods for calculating fugacity coefficients and the activity of water are the same as those by Krissansen-Totton *et al.* (*25*).

SUPPLEMENTARY MATERIALS

Supplementary material for this article is available at http://advances.sciencemag.org/cgi/content/full/4/1/eaao5747/DC1

Supplementary Text

section S1. The omission of solids, redox-sensitive nonvolatile aqueous species, and ocean heterogeneity

section S2. Full results and Aspen Plus validation

section S3. Reactions associated with Precambrian disequilibria and their Gibbs energy contributions

section S4. Sensitivity of available Gibbs energy to difficult-to-observe variables

section S5. Abiotic CH_4 formation from high-temperature processes

section S6. Atmospheric kinetics of methane destruction

fig. S1. Atmosphere-ocean disequilibrium in the Proterozoic (minimum disequilibrium scenario).

fig. S2. Atmosphere-ocean disequilibrium in the Archean (minimum disequilibrium scenario).

fig. S3. Relationship between methane fluxes and atmospheric abundances.

table S1. Proterozoic maximum disequilibrium.

table S2. Proterozoic minimum disequilibrium.

table S3. Proterozoic disequilibrium with 2% PAL of O_2.

table S4. Archean maximum disequilibrium.

table S5. Archean minimum disequilibrium.

table S6. Reactions contributing to Proterozoic disequilibrium.

table S7. Reactions contributing to Archean disequilibrium.

table S8. Sensitivity of Archean disequilibrium to difficult-to-observe variables.

References (*92*–*105*)

REFERENCES AND NOTES

1. C. Lovis, I. Snellen, D. Mouillet, F. Pepe, F. Wildi, N. Astudillo-Defru, J.-L. Beuzit, X. Bonfils, A. Cheetham, U. Conod, X. Delfosse, D. Ehrenreich, P. Figueira, T. Forveille, J. H. C. Martins, S. P. Quanz, N. C. Santos, H.-M. Schmid, D. Ségransan, S. Udry, Atmospheric characterization of Proxima b by coupling the SPHERE high-contrast imager to the ESPRESSO spectrograph. *Astron. Astrophys.* **599**, A16 (2017).
2. J. K. Barstow, P. G. Irwin, Habitable worlds with JWST: Transit spectroscopy of the TRAPPIST-1 system? *Mon. Not. R. Astron. Soc. Lett.* **461**, L92–L96 (2016).
3. M. Gillon, A. H. M. J. Triaud, B.-O. Demory, E. Jehin, E. Agol, K. M. Deck, S. M. Lederer, J. de Wit, A. Burdanov, J. G. Ingalls, E. Bolmont, J. Leconte, S. N. Raymond, F. Selsis, M. Turbet, K. Barkaoui, A. Burgasser, M. R. Burleigh, S. J. Carey, A. Chaushev, C. M. Copperwheat, L. Delrez, C. S. Fernandes, D. L. Holdsworth, E. J. Kotze, V. Van Grootel, Y. Almleaky, Z. Benkhaldoun, P. Magain, D. Queloz, Seven temperate terrestrial planets around the nearby ultracool dwarf star TRAPPIST-1. *Nature* **542**, 456–460 (2017).
4. I. Snellen, R. de Kok, J. L. Birkby, B. Brandl, M. Brogi, C. Keller, M. Kenworthy, H. Schwarz, R. Stuik, Combining high-dispersion spectroscopy with high contrast imaging: Probing rocky planets around our nearest neighbors. *Astron. Astrophys.* **576**, A59 (2015).
5. I. A. G. Snellen, R. J. de Kok, R. le Poole, M. Brogi, J. Birkby, Finding extraterrestrial life using ground-based high-dispersion spectroscopy. *Astrophys. J.* **764**, 182 (2013).
6. F. Rodler, M. López-Morales, Feasibility studies for the detection of O_2 in an earth-like exoplanet. *Astrophys. J.* **781**, 54 (2014).
7. D. Spergel, N. Gehrels, C. Baltay, D. Bennett, J. Breckinridge, M. Donahue, A. Dressler, B. S. Gaudi, T. Greene, O. Guyon, C. Hirata, J. Kalirai, N. J. Kasdin, B. Macintosh, W. Moos, S. Perlmutter, M. Postman, B. Rauscher, J. Rhodes, Y. Wang, D. Weinberg, D. Benford, M. Hudson, W. -S. Jeong, Y. Mellier, W. Traub, T. Yamada, P. Capak, J. Colbert, D. Masters, M. Penny, D. Savransky, D. Stern, N. Zimmerman, R. Barry, L. Bartusek, K. Carpenter, E. Cheng, D. Content, F. Dekens, R. Demers, K. Grady, C. Jackson, G. Kuan, J. Kruk, M. Melton, B. Nemati, B. Parvin, I. Poberezhskiy, C. Peddie, J. Ruffa, J. K. Wallace, A. Whipple, E. Wollack, F. Zhao, Wide-Field InfrarRed survey telescope-astrophysics focused telescope assets WFIRST-AFTA 2015 report. http://arxiv.org/abs/1503.03757 (2015).
8. J. Dalcanton, S. Seager, S. Aigrain, S. Battel, N. Brandt, C. Conroy, L. Feinberg, S. Gezari, O. Guyon, W. Harris, C. Hirata, J. Mather, M. Postman, D. Redding, D. Schiminovich, H. P. Stahl, J. Tumlinson, From cosmic birth to living earths: The future of UVOIR space astronomy. http://arxiv.org/abs/1507.04779 (2015).
9. B. Mennesson, S. Gaudi, S. Seager, K. Cahoy, S. Domagal-Goldman, L. Feinberg, O. Guyon, J. Kasdin, C. Marois, D. Mawet, M. Tamura, D. Mouillet, T. Prusti, A. Quirrenbach, T. Robinson, L. Rogers, P. Scowen, R. Somerville, K. Stapelfeldt, D. Stern, M. Still, M. Turnbull, J. Booth, A. Kiessling, G. Kuan, K. Warfield, The habitable exoplanet (HabEx) imaging mission: Preliminary science drivers and technical requirements, *SPIE Astronomical Telescopes + Instrumentation*, Edinburgh, UK, 2016 (International Society for Optics and Photonics, 2016).
10. V. S. Meadows, Reflections on O_2 as a biosignature in exoplanetary atmospheres. *Astrobiology* **17**, 1022–1052 (2017).
11. K. J. Zahnle, D. C. Catling, The cosmic shoreline: The evidence that escape determines which planets have atmospheres, and what this may mean for Proxima Centauri b. *Astrophys. J.* **843**, 122 (2017).
12. J. Farquhar, H. Bao, M. Thiemens Atmospheric influence of Earth's earliest sulfur cycle. *Science* **289**, 756–758 (2000).
13. N. J. Planavsky, D. Asael, A. Hofmann, C. T. Reinhard, S. V. Lalonde, A. Knudsen, X. Wang, F. O. Ossa, E. Pecoits, A. J. B. Smith, N. J. Beukes, A. Bekker, T. M. Johnson, K. O. Konhauser, T. W. Lyons, O. J. Rouxel, Evidence for oxygenic photosynthesis half a billion years before the Great Oxidation Event. *Nat. Geosci.* **7**, 283–286 (2014).
14. N. J. Planavsky, C. T. Reinhard, X. Wang, D. Thomson, P. McGoldrick, R. H. Rainbird, T. Johnson, W. W. Fischer, T. W. Lyons, Low Mid-Proterozoic atmospheric oxygen levels and the delayed rise of animals. *Science* **346**, 635–638 (2014).
15. A. H. Knoll, Cyanobacteria and earth history. *Cyanobacteria Mol. Biol. Genom. Evol.* **484** (2008).
16. E. W. Schwieterman, N. Y. Kiang, M. N. Parenteau, C. E. Harman, S. DasSarma, T. M. Fisher, G. N. Arney, H. E. Hartnett, C. T. Reinhard, S. L. Olson, V. S. Meadows, C. S. Cockell, S. I. Walker, J. L. Grenfell, S. Hegde, S. Rugheimer, R. Hu, T. W. Lyons, Exoplanet biosignatures: A review of remotely detectable signs of life. http://arxiv.org/abs/1705.05791 (2017).
17. J. E. Lovelock, A physical basis for life detection experiments. *Nature* **207**, 568–570 (1965).
18. D. R. Hitchcock, J. E. Lovelock, Life detection by atmospheric analysis. *Icarus* **7**, 149–159 (1967).
19. C. S. Cockell, A. Léger, M. Fridlund, T. M. Herbst, L. Kaltenegger, O. Absil, C. Beichman, W. Benz, M. Blanc, A. Brack, A. Chelli, L. Colangeli, H. Cottin, F. Coudé du Foresto, W. C. Danchi, D. Defrère, J.-W. den Herder, C. Eiroa, J. Greaves, T. Henning, K. J. Johnston, H. Jones, L. Labadie, H. Lammer, R. Launhardt, P. Lawson, O. P. Lay, J.-M. LeDuigou, R. Liseau, F. Malbet, S. R. Martin, D. Mawet, D. Mourard, C. Moutou, L. M. Mugnier, M. Ollivier, F. Paresce, A. Quirrenbach, Y. D. Rabbia, J. A. Raven, H. J. A. Rottgering, D. Rouan, N. C. Santos, F. Selsis, E. Serabyn, H. Shibai, M. Tamura, E. Thiébaut, F. Westall, G. J. White, *Darwin*—A mission to detect and search for life on extrasolar planets. *Astrobiology* **9**, 1–22 (2009).
20. C. Sagan, W. R. Thompson, R. Carlson, D. Gurnett, C. Hord, A search for life on Earth from the Galileo spacecraft. *Nature* **365**, 715–721 (1993).
21. R. G. Prinn, J. Huang, R. F. Weiss, D. M. Cunnold, P. J. Fraser, P. G. Simmonds, A. McCulloch, C. Harth, P. Salameh, S. O'Doherty, R. H. J. Wang, L. Porter, B. R. Miller, Evidence for substantial variations of atmospheric hydroxyl radicals in the past two decades. *Science* **292**, 1882–1888 (2001).
22. E. Simoncini, N. Virgo, A. Kleidon, Quantifying drivers of chemical disequilibrium: Theory and application to methane in the Earth's atmosphere. *Earth Syst. Dyn.* **4**, 317–331 (2013).
23. A. Kleidon, *Thermodynamic Foundations of the Earth System* (Cambridge Univ. Press, 2016).
24. S. Seager, W. Bains, The search for signs of life on exoplanets at the interface of chemistry and planetary science. *Sci. Adv.* **1**, e1500047 (2015).
25. J. Krissansen-Totton, D. S. Bergsman, D. C. Catling, On detecting biospheres from chemical thermodynamic disequilibrium in planetary atmospheres. *Astrobiology* **16**, 39–67 (2016).
26. D. C. Catling, J. Kasting, *Atmospheric Evolution on Inhabited and Lifeless Worlds* (Cambridge Univ. Press, 2017).
27. N. DeLeon-Rodriguez, T. L. Lathem, L. M. Rodriguez-R, J. M. Barazesh, B. E. Anderson, A. J. Beyersdorf, L. D. Ziemba, M. Bergin, A. Nenes, K. T. Konstantinidisa, Microbiome of the upper troposphere: Species composition and prevalence, effects of tropical storms, and atmospheric implications. *Proc. Natl. Acad. Sci. U.S.A.* **110**, 2575–2580 (2013).
28. R. Sander, Henry's law constants, in *NIST Chemistry WebBook, NIST Standard Reference Database* (National Institute of Standards and Technology, 1999).
29. I. Halevy, A. Bachan, The geologic history of seawater pH. *Science* **355**, 1069–1071 (2017).
30. R. A. Berner, D. J. Beerling, R. Dudley, J. M. Robinson, R. A. Wildman Jr., Phanerozoic atmospheric oxygen. *Annu. Rev. Earth Planet. Sci.* **31**, 105–134 (2003).
31. O. P. Judson, The energy expansions of evolution. *Nat. Ecol. Evol.* **1**, 0138 (2017).
32. C. B. Pilcher, Biosignatures of early Earths. *Astrobiology* **3**, 471–486 (2003).
33. G. N. Lewis, M. Randall, *Thermodynamics and the Free Energy of Chemical Substances* (McGraw-Hill, 1923).
34. P. Fay, Oxygen relations of nitrogen fixation in cyanobacteria. *Microbiol. Rev.* **56**, 340–373 (1992).

35. C. T. Reinhard, S. L. Olson, E. W. Schwieterman, T. W. Lyons, False negatives for remote life detection on ocean-bearing planets: Lessons from the early Earth. *Astrobiology* **17**, 287–297 (2017).
36. D. C. Catling, J. Krissansen-Totton, N. Y. Kiang, D. Crisp, T. D. Robinson, S. DasSarma, A. Rushby, A. Del Genio, W. Bains, S. Domagal-Goldman, Exoplanet biosignatures: A framework for their assessment. http://arxiv.org/abs/1705.06381 (2017).
37. E. W. Schwieterman, T. D. Robinson, V. S. Meadows, A. Misra, S. Domagal-Goldman, Detecting and constraining N_2 abundances in planetary atmospheres using collisional pairs. *Astrophys. J.* **810**, 57 (2015).
38. Y. Fujii, D. Angerhausen, R. Deitrick, S. Domagal-Goldman, J. L. Grenfell, Y. Hori, S. R. Kane, E. Palle, H. Rauer, N. Siegler, K. Stapelfeldt, K. B. Stevenson, Exoplanet biosignatures: Observational prospects. http://arxiv.org/abs/1705.07098 (2017).
39. K. Zahnle, M. Claire, D. Catling, The loss of mass-independent fractionation in sulfur due to a Palaeoproterozoic collapse of atmospheric methane. *Geobiology* **4**, 271–283 (2006).
40. S. R. Heap, Detecting biomarkers in exoplanetary atmospheres with terrestrial planet finder. *EAS Publ. Ser.* **41**, 517–520 (2010).
41. T. M. McCollom, Laboratory simulations of abiotic hydrocarbon formation in Earth's deep subsurface. *Rev. Mineral. Geochem.* **75**, 467–494 (2013).
42. E. W. Schwieterman, V. S. Meadows, S. D. Domagal-Goldman, D. Deming, G. N. Arney, R. Luger, C. E. Harman, A. Misra, R. Barnes, Identifying planetary biosignature impostors: Spectral features of CO and O_4 resulting from abiotic O_2/O_3 production. *Astrophys. J. Lett.* **819**, L13 (2016).
43. K. Zahnle, R. S. Freedman, D. C. Catling, Is there methane on Mars? *Icarus* **212**, 493–503 (2011).
44. J. Fiebig, A. B. Woodland, J. Spangenberg, W. Oschmann, Natural evidence for rapid abiogenic hydrothermal generation of CH_4. *Geochim. Cosmochim. Acta* **71**, 3028–3039 (2007).
45. C. Lécuyer, Y. Ricard, Long-term fluxes and budget of ferric iron: Implication for the redox states of the Earth's mantle and atmosphere. *Earth Planet. Sci. Lett.* **165**, 197–211 (1999).
46. J. Korenaga, Plate tectonics, flood basalts and the evolution of Earth's oceans. *Terra Nova* **20**, 419–439 (2008).
47. D. Valencia, R. J. O'Connell, D. D. Sasselov Inevitability of plate tectonics on super-Earths. *Astrophys. J., Lett.* **670**, L45 (2007).
48. R. S. Keir A note on the fluxes of abiogenic methane and hydrogen from mid-ocean ridges. *Geophys. Res. Lett.* **37** (2010).
49. M. Cannat, F. Fontaine, J. Escartin, Serpentinization and associated hydrogen and methane fluxes at slow spreading ridges. *Geophys. Monogr. Ser.* 241–264 (2010).
50. A. S. Bradley, R. E. Summons, Multiple origins of methane at the Lost City Hydrothermal Field. *Earth Planet. Sci. Lett.* **297**, 34–41 (2010).
51. C. Oze, L. C. Jones, J. I. Goldsmith, R. J. Rosenbauer, Differentiating biotic from abiotic methane genesis in hydrothermally active planetary surfaces. *Proc. Natl. Acad. Sci. U.S.A.* **109**, 9750–9754 (2012).
52. A. Neubeck, N. T. Duc, D. Bastviken, P. Crill, N. G. Holm, Formation of H_2 and CH_4 by weathering of olivine at temperatures between 30 and 70°C. *Geochem. Trans.* **12**, 6 (2011).
53. T. M. McCollom, Abiotic methane formation during experimental serpentinization of olivine. *Proc. Natl. Acad. Sci. U.S.A.* **113**, 13965–13970 (2016).
54. N. G. Grozeva, F. Klein, J. S. Seewald, S. P. Sylva, Experimental study of carbonate formation in oceanic peridotite. *Geochim. Cosmochim. Acta* **199**, 264–286 (2017).
55. J. Horita, M. E. Berndt, Abiogenic methane formation and isotopic fractionation under hydrothermal conditions. *Science* **285**, 1055–1057 (1999).
56. A. Guzmán-Marmolejo, A. Segura, E. Escobar-Briones, Abiotic production of methane in terrestrial planets. *Astrobiology* **13**, 550–559 (2013).
57. L. C. Jones, R. Rosenbauer, J. I. Goldsmith, C. Oze, Carbonate control of H_2 and CH_4 production in serpentinization systems at elevated P-Ts. *Geophys. Res. Lett.* **37**, L14306 (2010).
58. K. L. Denman, G. Brasseur, A. Chidthaisong, P. Ciais, P. M. Cox, R. E. Dickinson, Couplings between changes in the climate system and biogeochemistry in *Climate Change 2007: The Physical Science Basis*, S. Solomon, Ed. (Cambridge Univ. Press, 2007).
59. P. Kharecha, J. Kasting, J. Siefert, A coupled atmosphere–ecosystem model of the early Archean Earth. *Geobiology* **3**, 53–76 (2005).
60. M. E. Kress, C. P. McKay, Formation of methane in comet impacts: Implications for Earth, Mars, and Titan. *Icarus* **168**, 475–483 (2004).
61. J. F. Kasting, Methane and climate during the Precambrian era. *Precambrian Res.* **137**, 119–129 (2005).
62. E. S. Kite, M. A. Mischna, P. Gao, Y. L. Yung, Climate optimum on Mars initiated by atmospheric collapse. http://arxiv.org/abs/1709.08302 (2017).
63. V. S. Meadows, G. N. Arney, E. W. Schwieterman, J. Lustig-Yaeger, A. P. Lincowski, T. Robinson, S. D. Domagal-Goldman, R. K. Barnes, D. P. Fleming, R. Deitrick, R. Luger, P. E. Driscoll, T. R. Quinn, D. Crisp, The habitability of Proxima Centauri b: II: Environmental states and observational discriminants. http://arxiv.org/abs/1608.08620 (2016).
64. J. F. Kasting, D. P. Whitmire, R. T. Reynolds, Habitable zones around main sequence stars. *Icarus* **101**, 108–128 (1993).
65. N. H. Sleep, D. K. Bird, M. T. Rosing, Biological effects on the source of geoneutrinos. *Int. J. Mod. Phys. A* **28**, 1330047 (2013).
66. V. Šucha, P. Uhlík, J. Madejová, S. Petit, I. Kraus, Particle properties of hydrothermal ammonium-bearing illite-smectite. *Clays Clay Miner.* **55**, 36–44 (2007).
67. A. Watenphul, B. Wunder, R. Wirth, W. Heinrich Ammonium-bearing clinopyroxene: A potential nitrogen reservoir in the Earth's mantle. *Chem. Geol.* **270**, 240–248 (2010).
68. D. C. Catling, K. J. Zahnle, C. P. McKay, Biogenic methane, hydrogen escape, and the irreversible oxidation of early Earth. *Science* **293**, 839–843 (2001).
69. D. C. Catling, M. W. Claire, How Earth's atmosphere evolved to an oxic state: A status report. *Earth Planet. Sci. Lett.* **237**, 1–20 (2005).
70. G. Tinetti, V. S. Meadows, D. Crisp, N. Y. Kiang, B. H. Kahn, E. Bosc, E. Fishbein, T. Velusamy, M. Turnbull, Detectability of planetary characteristics in disk-averaged spectra II: Synthetic spectra and light-curves of earth. *Astrobiology* **6**, 881–900 (2006).
71. N. Y. Kiang, J. Siefert, R. E. Blankenship, Spectral signatures of photosynthesis. I. Review of Earth organisms. *Astrobiology* **7**, 222–251 (2007).
72. I. K. Karpov, K. V. Chudnenko, D. A. Kulik, Modeling chemical mass transfer in geochemical processes; thermodynamic relations, conditions of equilibria and numerical algorithms. *Am. J. Sci.* **297**, 767–806 (1997).
73. G. M. Marion, J. S. Kargel, *Cold Aqueous Planetary Geochemistry with FREZCHEM: From Modeling to the Search for Life at the Limits* (Springer Science & Business Media, 2007).
74. C. A. J. Appelo, D. Postma, *Geochemistry, Groundwater and Pollution* (CRC Press, 2005).
75. G. M. Marion, A molal-based model for strong acid chemistry at low temperatures (<200 to 298 K). *Geochim. Cosmochim. Acta* **66**, 2499–2516 (2002).
76. T. W. Lyons, C. T. Reinhard, N. J. Planavsky, The rise of oxygen in Earth's early ocean and atmosphere. *Nature* **506**, 307–315 (2014).
77. J. F. Kasting, L. L. Brown, The early atmosphere as a source of biogenic compounds, in *The Molecular Origins of Life*, A. Brack, Ed. (Cambridge Univ. Press, 1998), pp. 35–56.
78. S. L. Olson, C. T. Reinhard, T. W. Lyons, Limited role for methane in the mid-Proterozoic greenhouse. *Proc. Natl. Acad. Sci. U.S.A.* **113**, 11447–11452 (2016).
79. J. L. Grenfell, S. Gebauer, P. von Paris, M. Godolt, P. Hedelt, A. Patzer, H. Rauer, B. Stracke, Sensitivity of biomarkers to changes in chemical emissions in the Earth's Proterozoic atmosphere. *Icarus* **211**, 81–88 (2011).
80. N. D. Sheldon, Precambrian paleosols and atmospheric CO_2 levels. *Precambrian Res.* **147**, 148–155 (2006).
81. Y. Kanzaki, T. Murakami, Estimates of atmospheric CO_2 in the Neoarchean–Paleoproterozoic from paleosols. *Geochim. Cosmochim. Acta* **159**, 190–219 (2015).
82. A. Segura, K. Krelove, J. F. Kasting, D. Sommerlatt, V. Meadows, D. Crisp, M. Cohen, E. Mlawer, Ozone concentrations and ultraviolet fluxes on Earth-like planets around other stars. *Astrobiology* **3**, 689–708 (2003).
83. A. L. Roberson, J. Roadt, I. Halevy, J. Kasting, Greenhouse warming by nitrous oxide and methane in the Proterozoic Eon. *Geobiology* **9**, 313–320 (2011).
84. E. Wolf, O. Toon, Fractal organic hazes provided an ultraviolet shield for early Earth. *Science* **328**, 1266–1268 (2010).
85. S. A. Crowe, G. Paris, S. Katsev, C. Jones, S.-T. Kim, A. L. Zerkle, S. Nomosatryo, D. A. Fowle, J. F. Adkins, A. L. Sessions, J. Farquhar, D. E. Canfield, Sulfate was a trace constituent of Archean seawater. *Science* **346**, 735–739 (2014).
86. K. S. Habicht, M. Gade, B. Thamdrup, P. Berg, D. E. Canfield, Calibration of sulfate levels in the Archean ocean. *Science* **298**, 2372–2374 (2002).
87. L. C. Kah, T. W. Lyons, T. D. Frank, Low marine sulphate and protracted oxygenation of the Proterozoic biosphere. *Nature* **431**, 834–838 (2004).
88. C. Scott, B. A. Wing, A. Bekker, N. J. Planavsky, P. Medvedev, S. M. Bates, M. Yun, T. W. Lyons, Pyrite multiple-sulfur isotope evidence for rapid expansion and contraction of the early Paleoproterozoic seawater sulfate reservoir. *Earth Planet. Sci. Lett.* **389**, 95–104 (2014).
89. E. E. Stüeken, R. Buick, B. M. Guy, M. C. Koehler, Isotopic evidence for biological nitrogen fixation by molybdenum-nitrogenase from 3.2 Gyr. *Nature* **520**, 666–669 (2015).
90. R. Sweeney, I. Kaplan, Stable isotope composition of dissolved sulfate and hydrogen sulfide in the Black Sea. *Mar. Chem.* **9**, 145–152 (1980).
91. C. T. Reinhard, N. J. Planavsky, L. J. Robbins, C. A. Partin, B. C. Gille, S. V. Lalonde, A. Bekker, K. O. Konhauser, T. W. Lyons, Proterozoic ocean redox and biogeochemical stasis. *Proc. Natl. Acad. Sci. U.S.A.* **110**, 5357–5362 (2013).
92. V. A. Samarkin, M. T. Madigan, M. W. Bowles, K. L. Casciotti, J. C. Priscu, C. P. McKay, S. B. Joye, Abiotic nitrous oxide emission from the hypersaline Don Juan Pond in Antarctica. *Nat. Geosci.* **3**, 341–344 (2010).
93. L. M. François, J.-C. Gérard, Reducing power of ferrous iron in the Archean ocean, 1. Contribution of photosynthetic oxygen. *Paleoceanography* **1**, 355–368 (1986).

94. L. A. Derry, Causes and consequences of mid-Proterozoic anoxia. *Geophys. Res. Lett.* **42**, 8538–8546 (2015).
95. S. L. Olson, L. R. Kump, J. F. Kasting, Quantifying the areal extent and dissolved oxygen concentrations of Archean oxygen oases. *Chem. Geol.* **362**, 35–43 (2013).
96. C. T. Reinhard, N. J. Planavsky, S. L. Olson, T. W. Lyons, D. H. Erwin, Earth's oxygen cycle and the evolution of animal life. *Proc. Natl. Acad. Sci. U.S.A.* **113**, 8933–8938 (2016).
97. S. M. Som, R. Buick, J. W. Hagadorn, T. S. Blake, J. M. Perreault, J. P. Harnmeijer, D. C. Catling, Earth's air pressure 2.7 billion years ago constrained to less than half of modern levels. *Nat. Geosci.* **9**, 448–451 (2016).
98. S. M. Som, D. C. Catling, J. P. Harnmeijer, P. M. Polivka, R. Buick, Air density 2.7 billion years ago limited to less than twice modern levels by fossil raindrop imprints. *Nature* **484**, 359–362 (2012).
99. B. Marty, L. Zimmermann, M. Pujol, R. Burgess, P. Philippot, Nitrogen isotopic composition and density of the Archean atmosphere. *Science* **342**, 101–104 (2013).
100. S. Ryan, E. J. Dlugokencky, P. P. Tans, M. E. Trudeau, Mauna Loa volcano is not a methane source: Implications for Mars. *Geophys. Res. Lett.* **33**, L12301 (2006).
101. C. D. K. Herd, The oxygen fugacity of olivine-phyric martian basalts and the components within the mantle and crust of Mars. *Meteorit. Planet. Sci.* **38**, 1793–1805 (2003).
102. C.-T. A. Lee, J. S. Lackey, Global continental arc flare-ups and their relation to long-term greenhouse conditions. *Elements* **11**, 125–130 (2015).
103. G. Etiope, B. Sherwood Lollar, Abiotic methane on Earth. *Rev. Geophys.* **51**, 276–299 (2013).
104. A. A. Pavlov, L. L. Brown, J. F. Kasting, UV shielding of NH_3 and O_2 by organic hazes in the Archean atmosphere. *J. Geophys. Res.* **106**, 23267–23287 (2001).
105. J. L. Linsky, K. France, T. Ayres, Computing intrinsic Lyα fluxes of F5 V to M5 V stars. *Astrophys. J.* **766**, 69–78 (2013).

Acknowledgments: We thank J. Lustig-Yaeger for helpful discussions. We also thank A. Kleidon, N. Sleep, and the anonymous reviewer for numerous comments that greatly improved the manuscript. **Funding:** This work was supported by the NASA Astrobiology Institute's Virtual Planetary Laboratory (grant NNA13AA93A) and the NASA Exobiology Program (grant NNX15AL23G) awarded to D.C.C. J.K.-T. is supported by NASA Headquarters under the NASA Earth and Space Science Fellowship program (grant NNX15AR63H).
Author contributions: D.C.C. conceived the project. J.K.-T. and D.C.C. contributed to creating the code and performing the analysis. S.O. compiled estimates of the early Earth's atmosphere and ocean composition. All authors contributed to the drafting of the manuscript. **Competing interests:** The authors declare that they have no competing interests. **Data and materials availability:** All data needed to evaluate the conclusions in the paper are present in the paper and/or the Supplementary Materials. Our MATLAB code for calculating multiphase equilibrium is available on the website of the lead author.

Submitted 17 August 2017
Accepted 19 December 2017
Published 24 January 2018
10.1126/sciadv.aao5747

Citation: J. Krissansen-Totton, S. Olson, D. C. Catling, Disequilibrium biosignatures over Earth history and implications for detecting exoplanet life. *Sci. Adv.* **4**, eaao5747 (2018).

Chapter 4 - The detectability of disequilibrium biosignatures

"He tini nga whetu e ngaro I te kapua iti. Many stars cannot be concealed by a small cloud." – Maori proverb

This chapter explores the practical question of whether the disequilibrium biosignatures described in preceding chapters are detectable with next-generation space telescopes. Specifically, the detectability of biosignatures with NASA's upcoming James Webb Space Telescope (JWST) is examined. JWST will be the first telescope potentially capable of measuring the atmospheric constituents of temperate, rocky exoplanets (Barstow & Irwin 2016; Deming et al. 2009; Greene et al. 2016; Kaltenegger & Traub 2009; Morley et al. 2017). However, JWST observing time will be limited, and temperate, terrestrial planet observations will probably require many coadded transits to improve signal-to-noise. In anticipation of these difficult observations and the challenging interpretive questions that will inevitably follow, this chapter investigates whether looking for disequilibrium biosignatures will be feasible with JWST. The relative detectability of modern Earth-like oxygen biosignatures and Archean Earth-like methane + carbon dioxide biosignatures are compared. The nearby transiting planet TRAPPIST-1e is used as a case study for these calculations (Gillon et al. 2017).

Portions of this chapter were originally published in collaboration with Ryan Garland, Patrick Irwin and David C. Catling in The Astronomical Journal (Krissansen-Totton et al. (2018). Detectability of biosignatures in anoxic atmospheres with the James Webb Space Telescope: A TRAPPIST-1e case study, The Astronomical Journal, 156, 3, DOI:10.3847/1538-3881/aad564).

Abstract

The James Webb Space Telescope (JWST) may be capable of finding biogenic gases in the atmospheres of habitable exoplanets around low mass stars. Considerable attention has been given to the detectability of biogenic oxygen, which could be found using an ozone proxy, but ozone detection with JWST will be extremely challenging, even for the most favorable targets. Here, we investigate the detectability of biosignatures in anoxic atmospheres analogous to those that likely existed on the early Earth. Arguably, such anoxic biosignatures could be more prevalent than oxygen biosignatures if life exists elsewhere. Specifically, we simulate JWST retrievals of TRAPPIST-1e to determine whether the methane plus carbon dioxide disequilibrium biosignature pair is detectable in transit transmission. We find that ~10 transits using the Near InfraRed Spectrograph (NIRSpec) prism instrument may be sufficient to detect carbon dioxide and constrain methane abundances sufficiently well to rule out known, non-biological CH_4 production scenarios to ~90% confidence. Furthermore, it might be possible to put an upper limit on carbon monoxide abundances that would help rule out non-biological methane-production scenarios, assuming the surface biosphere would efficiently drawdown atmospheric CO. Our results are relatively insensitive to high altitude clouds and instrument noise floor assumptions, although stellar heterogeneity and variability may present challenges.

Introduction

The James Webb Space Telescope (JWST) will provide the first opportunity to look for non-intelligent life beyond the solar system. To date, much of the focus on exoplanet biosignatures has been on molecular oxygen (Brandt & Spiegel 2014; Owen 1980) and its photochemical product ozone (e.g. Domagal-Goldman et al. 2014; Harman et al. 2015a; Leger et al. 1993; Meadows et al. 2018b; Segura et al. 2003; Tian et al. 2014). Oxygen is an excellent biosignature gas because it is challenging to produce in large quantities without life, and although hypothetical false-positives scenarios have been proposed, a growing understanding exists of how they might be distinguished using contextual clues (Harman & Domagal-Goldman 2018; Meadows 2017; Meadows et al. 2018b; Schwieterman et al. 2016).

However, even if life is widespread in the cosmos there is no guarantee that oxygen-rich biosignatures are common. Oxygenic photosynthesis is an extremely complex metabolism that only evolved once in Earth history (Knoll 2008; Mulkidjanian et al. 2006), and the emergence of oxygenic photosynthesis does not necessarily guarantee an oxygen-rich atmosphere because biogenic oxygen sources may be overwhelmed by non-biological sinks (Catling & Claire 2005). Oxygen concentrations may stabilize at low, but difficult to detect levels (Reinhard et al. 2017), and the accumulation of oxygen on planets around M-dwarfs may be especially difficult due to the low flux of visible photons (Lehmer et al. 2018).

These limitations led Krissansen-Totton et al. (2018) to propose the combination of carbon dioxide (CO_2) and abundant biogenic methane (CH_4) as an alternative biosignature for anoxic atmospheres. Carbon dioxide and methane would have been out of chemical equilibrium on the early Earth during the Archean eon (4.0-2.5 Ga), and their coexistence cannot be explained without a continuous replenishing flux of CH_4, which demands a biological source. Specifically, for terrestrial planets, > 0.1% methane abundance is potentially biogenic and > 1% is probably biogenic due to the low likelihood of producing such large quantities of methane through relatively inefficient non-biological processes such as serpentinization followed by Fischer-Tropsch-type reactions (Krissansen-Totton et al. 2018). Furthermore, the inference of biology could be strengthened by the non-detection of carbon monoxide (CO) because several non-biological scenarios that produce CH_4 would also be expected to produce CO (Krissansen-Totton et al. 2018).

The ability of JWST to characterize terrestrial planets and detect oxygen-ozone biosignatures has been studied extensively (Barstow & Irwin 2016; Deming et al. 2009; Greene et al. 2016; Kaltenegger & Traub 2009; Morley et al. 2017). Barstow et al. (2015) modeled the modern Earth transiting an M6V star and found that a year of primary transits might be sufficient for a tentative detection of CO_2 and O_3. Irwin et al. (2014) also demonstrated that atmospheric characterization of Earth-like planets around M-dwarfs is possible. Barstow and Irwin (2016) applied these calculations specifically to the TRAPPIST-1 system (Gillon et al. 2017) and found that for modern Earth-like atmospheres 30-60 transits would be necessary to reliably detect Earth-like O_3 levels on 1b, 1c, and 1d. The outer planets (1e, 1f, 1g) are more likely to be habitable (Turbet et al. 2018; Wolf 2017), but O_3 detection would require even more transits in these cases (Barstow & Irwin 2016). These detections are barely feasible given the expected lifetime of the JWST mission and the position of TRAPPIST-1 in the sky close to the ecliptic, which limits the star's viewing by JWST.

The retrieval studies cited above used optimal estimation techniques and assumed photon limited noise with some allowance for instrument throughput, but others have performed Markov Chain Monte Carlo (MCMC) retrievals with more realistic instrument simulators. Greene et al. (2016) simulated a MCMC retrieval on a single transit of a cool (500 K) super Earth and found that H_2O and CH_4 detections might be possible in cloud and haze free atmospheres. Morley et al. (2017) calculated the number of primary transits required to rule out a flat spectrum to 5σ for TRAPPIST-1 planets and found relatively few (10 or less) would be needed for TRAPPIST-1e. Batalha et al. (2018) performed an information analysis to show that a partial saturation strategy using the NIRSpec instrument could plausibly constrain the atmospheric composition of terrestrial planets. However, the detectability of the CH_4+CO_2 biosignature combination has not been investigated.

Here, we simulated retrievals to investigate the detectability of CO_2+CH_4 biosignatures with JWST. The relatively primitive nature of methanogenesis (Weiss et al. 2016) and its antiquity on Earth (Wolfe & Fournier 2018) suggests that this anoxic biosignature is probably more common than oxygen-ozone biosignatures (Krissansen-Totton et al. 2018). Here, we demonstrate that it is also more easily detectable than ozone in transit transmission observations with JWST. We focus on TRAPPIST-1e because climate models suggest its surface conditions are potentially habitable for a wide range of atmospheric compositions (Turbet et al. 2018; Wolf 2017) and because it is the only TRAPPIST-1 planet with a bulk composition consistent with an Earth-like iron core (Suissa & Kipping 2018). However, our results apply similarly to TRAPPIST-1f and 1g, and other nearby, habitable planets that will be discovered by the Transiting Exoplanet Survey Satellite (TESS) mission (Kempton et al. 2018). Finally, we present calculations showing how JWST detections of CH_4 and CO_2 might be used to quantitatively evaluate the likelihood of a surface biosphere.

Methods

Transmission spectra for TRAPPIST-1 planets were calculated using the NEMESIS radiative transfer code (Irwin et al. 2008). NEMESIS uses a correlated-k radiative transfer scheme (Goody & Yung 1995; Lacis & Oinas 1991), and in this study k-tables were calculated from the HITRAN 2008 line database (Rothman et al. 2009), except for methane Near Infrared (NIR) band data, which was taken from Karkoschka and Tomasko (2010). The k-tables were calculated at a spectral resolution of 0.025 μm at 20 temperatures in the range 70-400 K, and 20 pressures equally spaced in log space from 3.1×10^{-7} to 20.3 bar (see Irwin et al. (2014) for further details).

We generated synthetic spectra for TRAPPIST-1e by adopting recent mass (Grimm et al. 2018) and radius (Delrez et al. 2018) estimates and assuming an atmospheric composition. We initially assume a 1-bar Archean-like atmospheric composition dominated by N_2, with 5% CO_2, 0.5% CH_4, and 10 ppb CO, where all gas mixing ratios are constant with altitude. Our chosen methane abundance is representative of plausible biogenic methane fluxes on the early Earth (Kharecha et al. 2005), whereas the high CO_2 abundance was chosen to ensure a habitable surface climate (Turbet et al. 2018; Wolf 2017) whilst avoiding significant haze-formation (Arney et al. 2017), which we do not include in our nominal retrieval. We also considered a modern Earth analog of TRAPPIST-1e with 20% O_2, 290 ppm CO_2, 1.7 ppm CH_4, and 0.1 ppm CO. To be generous for ozone retrieval (since we will argue that ozone retrieval is difficult) we assumed a very high estimate of 0.01% O_3. This concentration is about ~10 times higher than the peak ozone abundance of 10 ppmv in the modern Earth's stratosphere at ~25 km altitude. Our assumed O_3 concentration is also ~10x higher than the predicted peak ozone abundance for an Earth-like Proxima Centauri b calculated self-

consistently using a photochemical model and assuming Earth-like biological fluxes (Meadows et al. 2018a).

For synthetic spectra, assumptions were also made about atmospheric structure and water vapor. Both atmospheres were assumed to be isothermal above 0.1 bar (Robinson & Catling 2014a), and follow a moist adiabatic lapse rate below 0.1 bar with a smoothed transition between the two regions. The stratospheric temperature was assumed to be 214 K, which is the skin temperature of the modern Earth. The atmospheric temperature profile was not calculated using a climate model, but this is unlikely to affect our results significantly because transmission spectra are relatively insensitive to atmospheric temperature structure. For both the Archean Earth and modern Earth cases, atmospheric water vapor was assumed to be 1%, or water vapor saturation (whichever is smaller). This vastly overestimates stratospheric water vapor content because the cold trap limits stratospheric water vapor mixing ratios to a few ppmv on the modern Earth (Oman et al. 2008) and $<10^{-6}$ for early Earth-like atmospheres (Kasting & Ackerman 1986). However, 1% water vapor represents a pessimistic end-member assumption about the extent to which water vapor absorption features could obscure those of CH_4 and CO_2. Sensitivity tests with ppmv stratospheric water vapor show that posterior uncertainties in CH_4 and CO_2 are decreased by lowering stratospheric H_2O (not shown). Our stellar spectrum for TRAPPIST-1 was identical to that adopted in Barstow and Irwin (2016).

Initially, we assumed all atmospheres were cloud free, but later tested a grey, single layer cloud model. In this model, clouds are described by three parameters: nadir optical depth, cloud base pressure, and fractional scale height. If parameters are chosen to represent Earth-like water clouds (e.g. Irwin et al. 2014) the transit spectrum is truncated at around ~20 km (0.05 bar) above the surface, which we found has a minimal impact on the retrieval. Instead, we chose cloud parameters to truncate the transmission spectrum at ~30 km (0.01 bar) to approximate opacity due to very high altitude clouds, an organic haze (e.g. Arney et al. 2017), or sulfate aerosols (Misra et al. 2015).

To add realistic observational noise to our synthetic spectra, we used the JWST instrument simulator PandExo (Batalha et al. 2017). NIRSpec prism was used to simulate Archean Earth-like spectra because its 0.6-5.3 μm range allows simultaneous coverage of CH_4, CO_2, and CO absorption features, whereas both NIRSpec prism and the Mid InfraRed Instrument (MIRI) Low Resolution Spectrometer (LRS) were used to simulate modern Earth-like spectra because MIRI's 5-12 μm range includes the 9.6 um ozone band. Additionally, we adopted the partial saturation strategy described in Batalha et al. (2018) for NIRSpec prism to increase the observing efficiency from 33% to 72%. Unless stated otherwise, we assume zero noise floor, equal time in and out of transit, and 80% saturation level (for MIRI LRS). For convenience, we also binned NIRSpec and MIRI spectra to constant-width bins equal to the size of the largest resolution element in each instrument. This results in some information loss but is unlikely to significantly impact our retrievals.

Typically, we will add random noise instances to the true spectrum to generate synthetic spectra for retrieval. However, we sometimes place the midpoint of all data points on the true spectrum to ensure posteriors are centered on true values and not biased by a handful of data points. Feng et al. (2018) demonstrated that these centered posteriors are essentially identical to the summation of posteriors from many individual noise realizations.

To solve the inverse problem and retrieve planet parameters we used the Nested Sampling algorithm (Feroz & Hobson 2008; Feroz et al. 2009) implemented using PyMultiNest (Buchner et al. 2014). Nested Sampling is a Bayesian retrieval algorithm that samples equal-likelihood regions of prior-space to explicitly calculate the Bayesian evidence, the denominator in Bayes' theorem. Posterior probability distributions for unknown parameters can then be calculated from the Bayesian evidence (Feroz et al. 2009). We compared posteriors to those from emcee (Foreman-Mackey et al. 2013) and they were virtually identical to Nested Sampling posteriors for retrievals with the same priors and likelihood function. Table 1 shows the input parameter values and their uniform priors for the Archean Earth-like and modern Earth-like spectra.

Table 4-1: Assumed parameter values used to create synthetic spectra, and uniform prior ranges adopted for simulated retrieval.

	Archean Earth-like TRAPPIST-1e		Modern Earth-like TRAPPIST-1e		Archean Earth-like TRAPPIST-1e with clouds	
	Assumed value	Uniform prior	Assumed value	Uniform prior	Assumed value	Uniform prior
Log(CH_4)	-2.3010 (0.5%)	[-8.0,0.0]	-5.77 (1.7 ppm)	[-8.0,0.0]	-2.3010 (0.5%)	[-8.0,0.0]
Log(CO_2)	-1.3010 (5%)	[-8.0,0.0]	-3.5367 (290 ppm)	[-8.0,0.0]	-1.3010 (5%)	[-8.0,0.0]
Log(CO)	-8.0 (10 ppb)	[-8.0,0.0]	-6.91 (0.1 ppm)	[-8.0,0.0]	-8.0 (10 ppb)	[-8.0,0.0]
Log (H_2O)	-2.0 (1%)	[-8.0,0.0]	-2.0 (1%)	[-8.0,0.0]	-2.0 (1%)	[-8.0,0.0]
Log(O_2)	N/A	N/A	-0.69897 (20%)	[-8.0,0.0]	N/A	N/A
Log(O_3)	N/A	N/A	-4.0 (0.01%)	[-8.0,0.0]	N/A	N/A
Radius [R_{Earth}]	0.91	[0.8,1.1]	0.91	[0.8,1.1]	0.91	[0.8,1.1]
Mass* [M_{Earth}]	0.772	σ=0.077*	0.772	σ=0.077*	0.772	σ=0.077*
P_{surf} (log (bar))	0.0	[-3,2]	0.0	[-3,2]	0.0	[-3,2]

T_{strat} (K)	214.4	[100,400]	214.4	[100,400]	214.4	[100,400]
$P_{cloud\text{-}base}$ (log(bar))	N/A	N/A	N/A	N/A	-0.48148 (0.3 bar)	[-3,2]**
Optical depth (log(τ))	N/A	N/A	N/A	N/A	1 (10)	[-10,5]
Fractional scale height, log(FSH)	N/A	N/A	N/A	N/A	-0.5 (0.32)	[-2,1]

*Rather than use a uniform prior for planet mass, we adopt the mass distribution obtained from transit timing variations in Grimm et al. (2018). This distribution is accurately approximated by a Gaussian with a mean of 0.772 M_{Earth} and σ=0.077 M_{Earth}. Note that the posterior distribution for planet mass is nearly identical to this prior because mass is not constrained by transit observations.

**Cloud base pressure is constrained to always be smaller than the surface pressure.

Results

Fig. 1a and 1b show the Archean Earth-like NIRSpec prism transmission spectrum for TRAPPIST-1e generated using PandExo. The median fitted spectrum from the Nested Sampling retrieval with 95% credible intervals are also plotted. Fig. 2 shows the corresponding posterior probability distributions for the 8 model parameters defined in Table 1. The assumed input ("true") parameter values are over-plotted as vertical and horizontal blue lines on these posteriors. For this 10-transit case, both CO_2 and CH_4 are detectable, and it is possible to constrain the CH_4 abundance ($\log(CH_4) = -2.23^{+0.78}_{-0.96}$). Additionally, a tentative upper limit can be placed on CO abundance (CO < 652 ppm with 90% credibility). Surface pressure cannot be well-constrained, which contributes to the uncertainty in mixing ratio abundances because absorption features can be explained by high abundances and low total pressure, or low abundances and high total pressure (Benneke & Seager 2012). This degeneracy can be seen in the joint distributions in Fig. 2 where there is a negative correlation between gas mixing ratios (particularly CH_4 and CO_2) and surface pressure. There is a related degeneracy between planet radius and surface pressure because smaller planet radii must be offset by a large surface pressure to fit the same transit depth. Note that our radius parameter is defined as the solid body radius. In Appendix I 4-B we repeat the retrieval defining radius as the 1 mbar planet radius. This alternative formulation produces joint distributions for gas abundances and radius that are tightly anticorrelated, but the marginal distributions for gas abundances are unchanged.

Transit spectroscopy does not provide strong constraints on atmospheric temperature structure, but the stratospheric temperature posterior in Fig. 2 is constrained by our tight prior on planet mass from Grimm et al. (2018). This prior for planet mass breaks the degeneracy between mass and stratospheric temperature.

Without it, these two parameters would be strongly positively correlated because atmospheric scale height is proportional to temperature/gravity.

Fig. 1c and 1d show the modern Earth-like transmission spectrum for TRAPPIST-1e from NIRSpec prism, whereas Fig. 1e and 1f show the modern Earth-like transmission spectrum for TRAPPIST-1e from MIRI LRS. Fig. 3 shows a comparison between the posterior distributions for methane abundance from the Archean Earth-like case (Fig. 3a), the ozone abundances the modern Earth-like case using NIRSpec prism (Fig. 3b), and the modern Earth-like case using MIRI LRS (Fig. 3c). Since constraining CH_4 abundance is crucial for determining the biogenicity of CH_4-CO_2 disequilibria, and ozone is the most easily observable biosignature gas for modern Earth-like atmospheres, this figure directly contrasts the detectability of Archean-Earth and modern-Earth biosignatures. Whereas it is possible to constrain CH_4 abundances to within 1-2 orders of magnitude with 10 transits with NIRSpec prism, even high assumed O_3 typically cannot be detected with 10 transits with either NIRSpec prism or MIRI LRS. This is because the uncertainties in transit depth are much larger around prominent ozone features than they are around CH_4 absorption features (Fig. 1).

Fig. 4 shows how the uncertainty in key model parameters changes as the number of co-added transits is increased (Archean Earth-like case). Increasing the number of transits reduces the uncertainty in almost all model parameters, but there are diminishing returns beyond 10 transits, consistent with Batalha et al. (2018). However, 30-50 transits would reduce the 66% credible interval in CH_4 abundance by ~0.5 log unit (and similarly for the 95% credible interval). Tighter constraints on methane abundances would enable stronger inferences to life (see below).

All the results described above are for cloud-free atmospheres. Fig. 5 shows selected posterior probability distributions for our cloudy Archean case. Here, the "true" cloud parameters were chosen to truncate the spectrum at ~30 km (0.01 bar), which is significantly cloudier than the modern Earth where high clouds truncate the transmission spectrum at around 20 km (Irwin et al. 2014). Nonetheless, both CO_2 and CH_4 are detectable, and CH_4 abundances are still constrained ($\log(CH_4) = -2.57^{+0.90}_{-1.09}$), albeit less tightly than the no cloud case.

In summary, these simulated retrievals suggest that the CH_4-CO_2 disequilibrium biosignature is detectable for Archean Earth-like planets with JWST in ~10 transits. Additionally, it may be possible to place an upper bound on CO to help rule out non-biological scenarios (see discussion for further consideration of non-biological CO production). This biosignature combination should be easier to detect than oxygen or ozone biosignatures with JWST, and the presence of Earth-like clouds should not impede the retrieval.

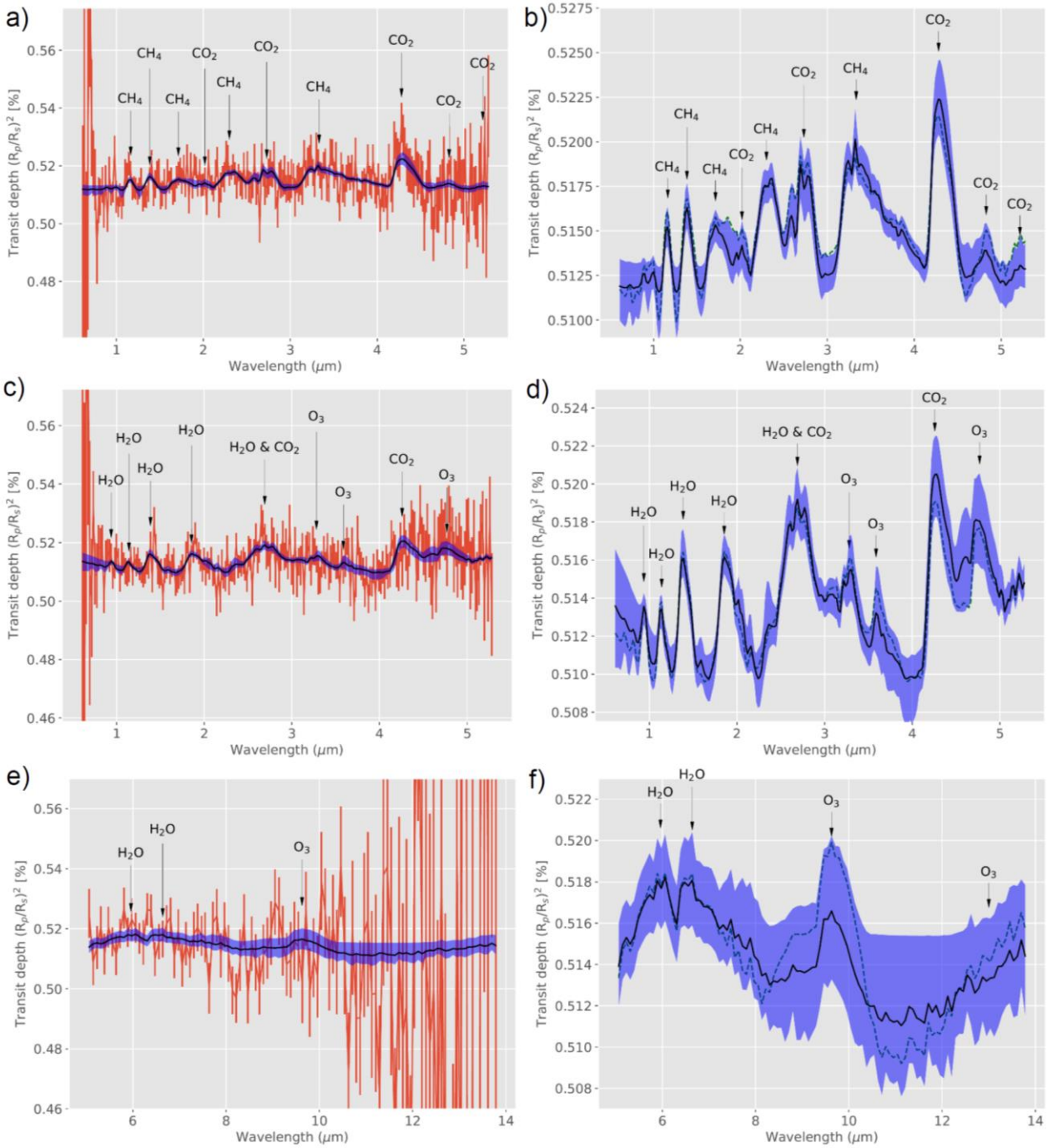

Figure 4-1: Synthetic and fitted spectra for 10 transits of TRAPPIST-1e with no clouds where RP and RS are the radii of the planet and star, respectively. Left-side panels show typical noise realizations using PandExo (red lines), the median fitted spectrum calculated using the Nested Sampling retrieval algorithm (black lines) with 95% credible intervals from the retrieval (blue shaded regions). The right-side panels show the same median fit and 95% credible intervals, in addition to the true synthetic spectrum (green-dashed line). The right-side panels have a smaller y-axis range such that individual spectral features can be more easily seen. Top row shows the Archean Earth-like case using NIRSpec prism, the middle row shows the modern Earth-like case using NIRSpec prism, and bottom row shows the modern Earth-like case using MIRI LRS. Key molecular absorption features are labeled. Note that stratospheric water vapor abundances are assumed to be unrealistically high to maximize the possible obscuration of CH4 and CO2 features (see main text).

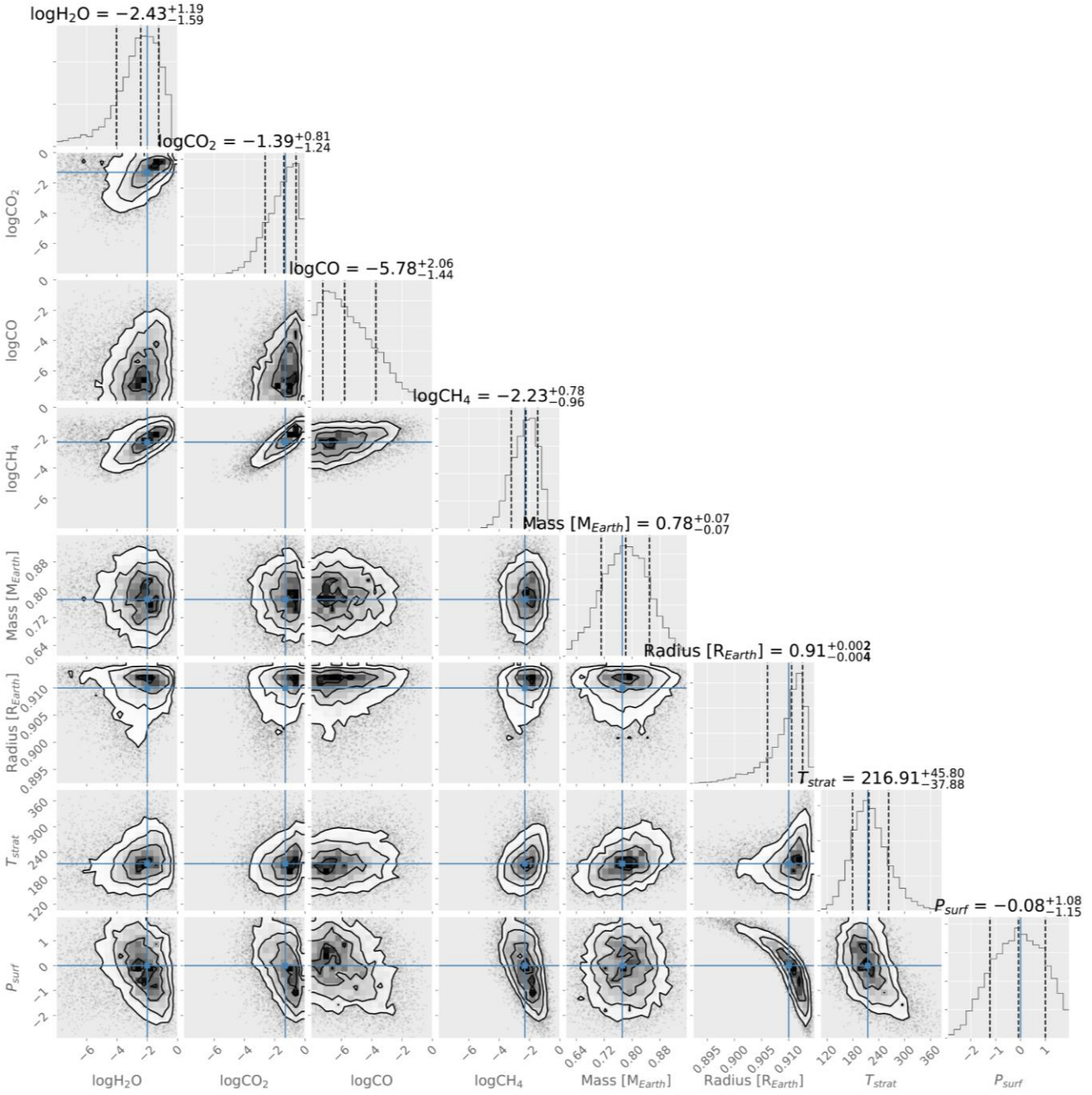

Figure 4-2: Posterior probability distributions for retrieved parameters for 10 transits of an Archean Earth-like TRAPPIST-1e with no clouds using NIRSpec prism produced using the plotting script corner.py (Foreman-Mackey 2016). Diagonal elements are marginal distributions, off-diagonal elements are joint distributions, and vertical and horizontal blue lines are "true" values. The marginal distributions show that CH_4 and CO_2 are detectable, and that CH_4 abundances can be constrained to within a few orders of magnitude. It is also possible to put tentative upper bound on CO abundance. For this retrieval, the midpoint of all spectral data points was the true spectrum to ensure posteriors were centered on true values, but note that individual noise realizations may vary (Feng et al. 2018) (Fig. 3a).

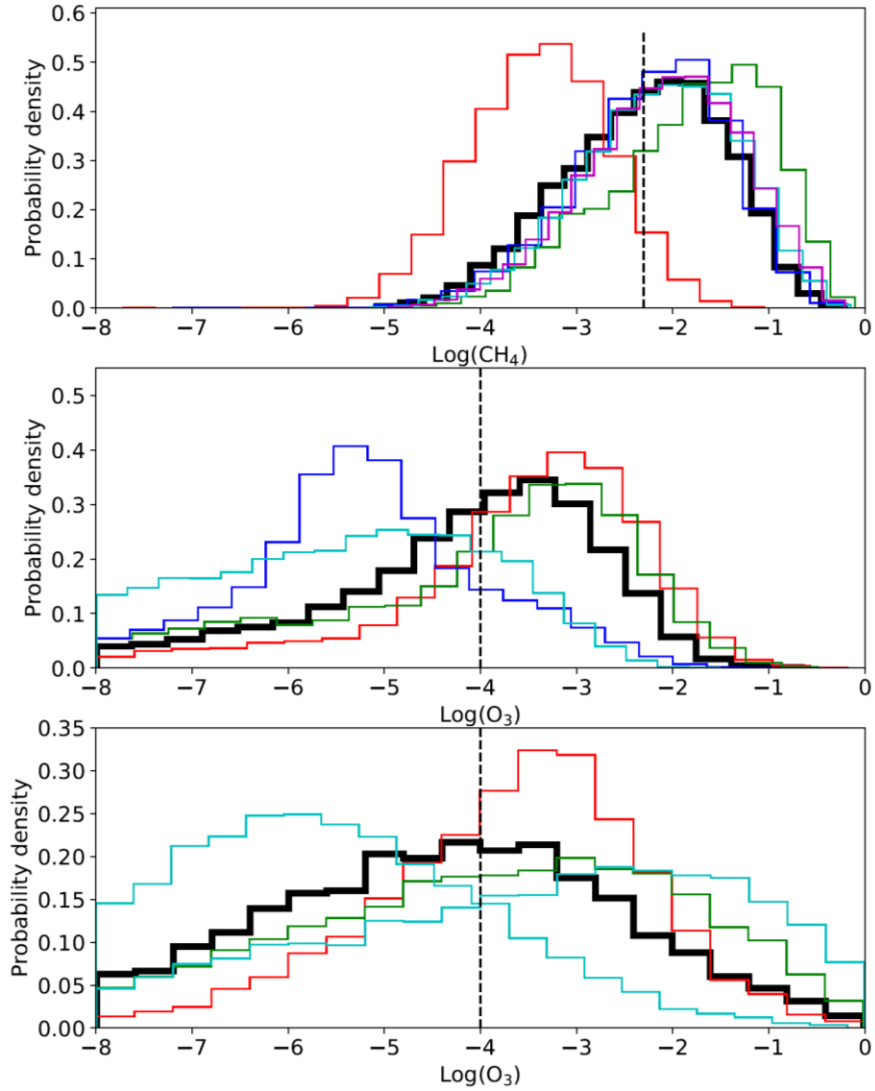

Figure 4-3: Comparison of (a) CH_4 posteriors from Archean Earth-like NIRSpec prism case, (b) O_3 posteriors from modern Earth-like NIRSpec prism case, and (c) O_3 posteriors from modern Earth-like MIRI LRS case (all three are for 10 coadded transits of TRAPPIST-1e with no clouds). Bold black lines show posteriors for noise realizations centered on true values (Feng et al. 2018), whereas thin colored lines show randomized noise realizations (see main text). Vertical black dashed lines denote the "true" parameter values. It is possible to detect and constrain Archean-like biogenic CH_4 abundances with NIRSpec prism, whereas for the same number of transits, O_3 detection is not possible with either NIRSpec or MIRI. Note that O_3 mixing ratios of 10^{-4} are far larger than what would realistically be expected on an inhabited planet, and so O_3 detection would likely be even more challenging than (b) and (c) imply.

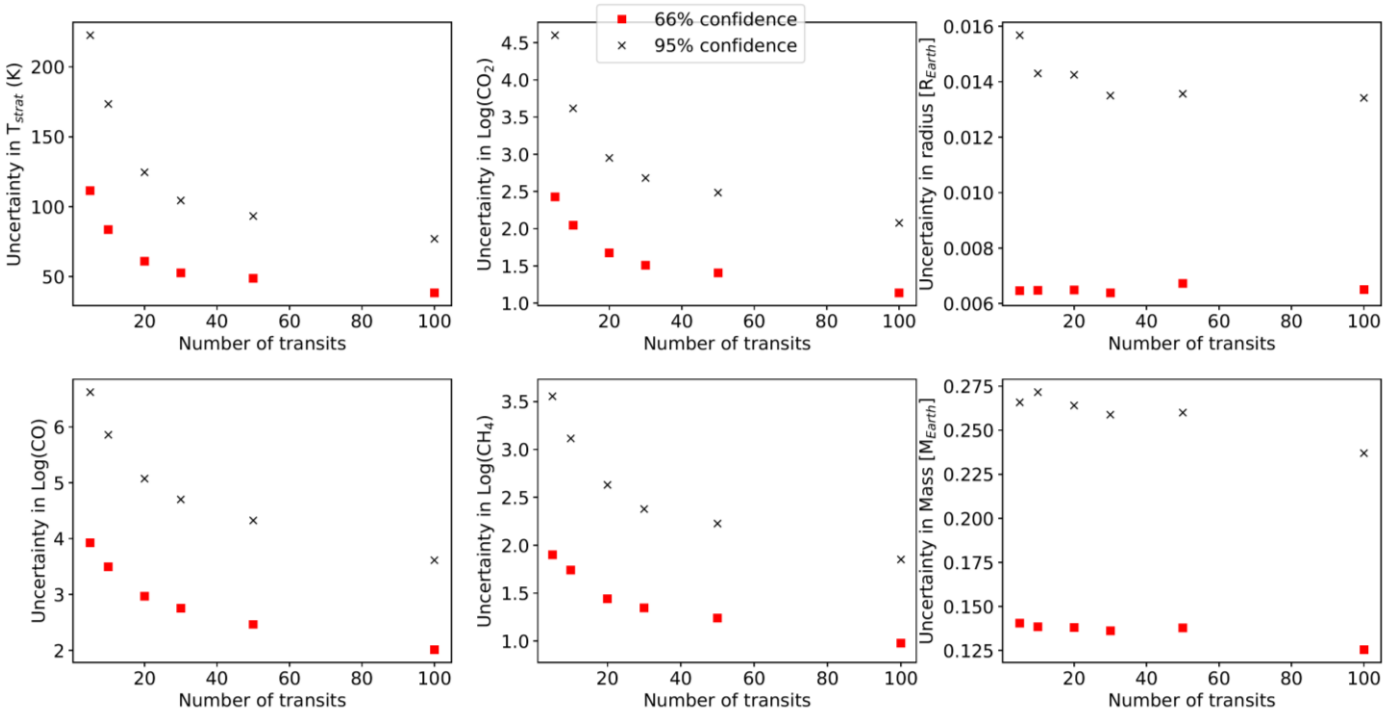

Figure 4-4: Uncertainty in parameter posteriors as a function of number of transits. Red squares and black crosses show 66% and 95% credible interval uncertainties, respectively. These results are in general agreement with those of Batalha et al. (2018) which show diminishing returns with more transits. However, 30-50 transits would reduce uncertainty in CH_4 compared to the 10 transit case, and therefore allow a stronger inference to biology (see discussion). For all the retrievals plotted above, the midpoint of all spectral data points was the true spectrum to reduce stochastic variation in posteriors (Feng et al. 2018).

Discussion

The results reported here are broadly consistent with those of Greene et al. (2016), who performed MCMC retrievals for simulated JWST transit transmission observations of a cloud-free, 500 K super-Earth with a CH_4 mixing ratio of 4.3×10^{-4} and negligible CO_2 and CO. Their posterior distribution for CH_4 extends across 2-3 log units, in agreement with our Fig. 2. Additionally, their retrieved upper limit for CO is consistent with our Fig. 2, although they were unable to constrain the CO_2 mixing ratio. Note however, that Greene et al. (2016) only considered a single transit, their assumed planet-to-star radius was less favorable than for the TRAPPIST-1 system, and they combined a different suite of instruments, and so some differences are expected. Our results are also broadly consistent with those of Morley et al. (2017) who calculate that <10 transits are required to rule out a flat spectrum at 5σ confidence for TRAPPIST-1e with a CO_2-rich atmosphere.

Ultimately, we would like to use gas abundance constraints from JWST observations to evaluate the probability of a planet hosting life. One possible approach is to convert the methane abundance posterior to a probability distribution for the required surface CH_4 flux, which if large can imply a biogenic source. In oxic atmospheres, methane abundances are controlled by the balance between surface sources and

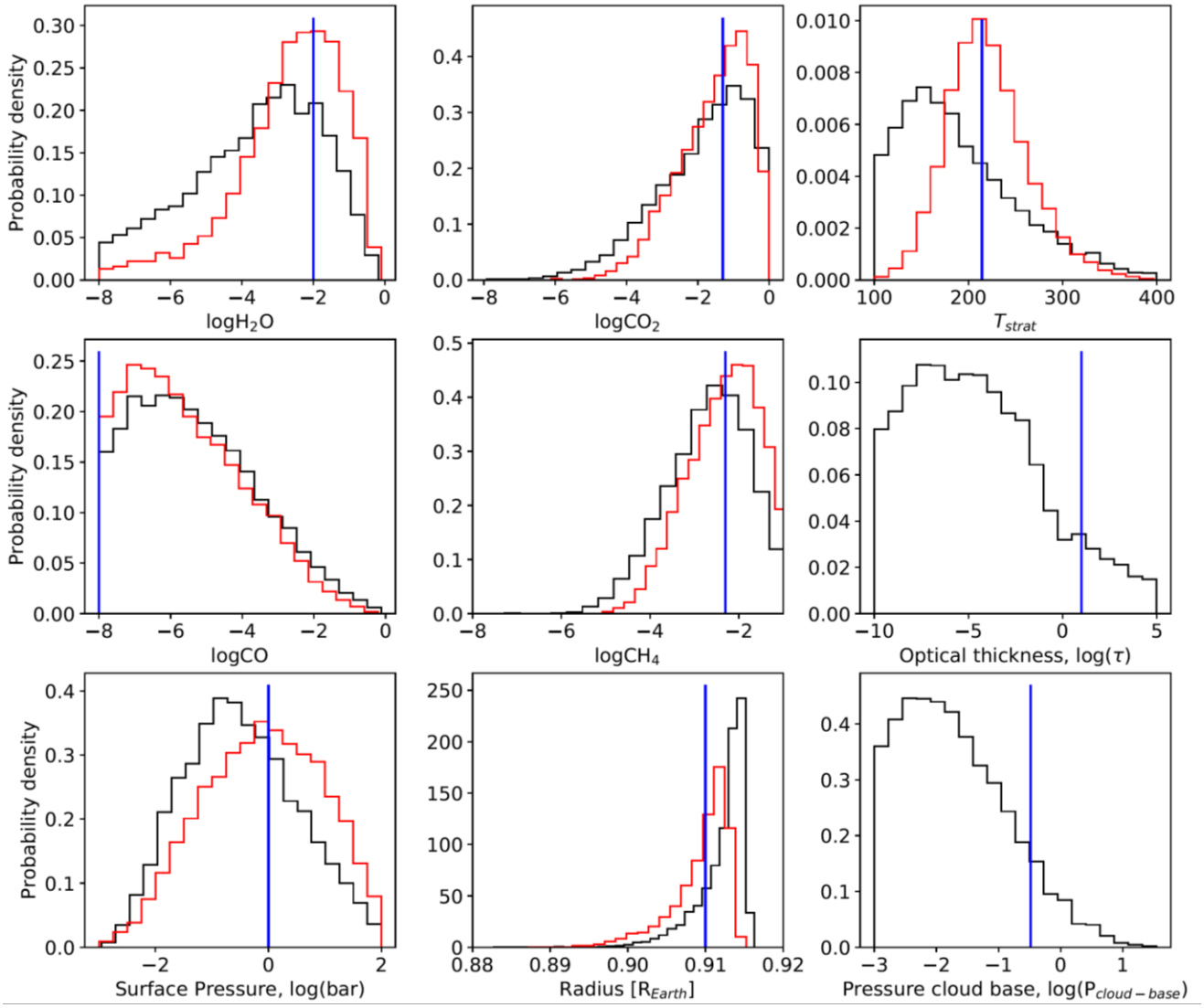

Figure 4-5: Posterior probability distributions for selected parameters for 10 transits of an Archean Earth-like TRAPPIST-1e with high clouds using NIRSpec prism. Black lines denote posterior probability distributions for the cloudy case, red lines denote posterior distributions for the no-cloud Archean case (Fig. 2) for comparison, and blue vertical lines denote "true" values. Clouds widen the posterior probability distributions for gas abundances somewhat, but even for this high cloud case where the transmission spectrum is truncated at ~30 km (0.01 bar), CO_2 and CH_4 detection is possible. Posteriors for fractional scale height and planet mass are not plotted.

destruction via oxidation reactions with OH radicals, which in turn depend on the UV stellar spectrum (Rugheimer et al. 2015; Segura et al. 2005). However, in anoxic atmospheres such as the Archean Earth, before the advent of oxygenic photosynthesis, the CH_4 surface flux is approximately balanced by photolysis in the upper atmosphere by Lyman-alpha (121 nm) photons, and the rate at which CH_4 molecules are delivered to the upper atmosphere is, in turn, controlled by diffusion-limited hydrogen escape (Krissansen-Totton et al. 2018; Pavlov et al. 2001b; Zahnle 1986). Therefore by assuming diffusion-limited escape, an inferred distribution for the minimum methane surface flux can be derived and compared to theoretical

probability distributions for the maximum abiotic methane flux (e.g. Krissansen-Totton et al. 2018). Specifically, the inferred flux distribution can be repeatedly randomly sampled, and for each sampled flux value, the probability of this flux being non-biological is obtained. This probability is found by integrating the theoretical non-biological production distribution from the sampled flux value to infinity (Fig. 6). By repeating this procedure thousands of times, an average probability for the observed atmosphere being attributable by non-biological mechanisms is obtained (Fig. 6).

For our nominal Archean Earth-like 10 transit case, the probability of abiotic processes being able to explain the observed methane abundance is only 9%, although this varies considerably with different spectral noise realizations (ranging from 4% to 39% for different realizations in Fig. 3a). For 50 transits, the probability of attributing the observed methane to nonbiological processes drops to just 2%. The non-biological methane production distribution adopted from Krissansen-Totton et al. (2018) is a first attempt, and more work is needed on the geochemistry of non-biological methane production and its possible contextual clues. For example, the framework described in Fig. 6 implicitly assumed that CO and CH_4 outgassing scenarios have been ruled out by the non-detection of atmospheric CO. However, these calculations demonstrate that searching for biosignatures in anoxic atmospheres is feasible with JWST for TRAPPIST-1e. Furthermore, biosignature detection for TRAPPIST-1f and 1g is even more favorable than for 1e due to the lower bulk density of these planets (not shown). If TESS discovers nearby transiting, habitable planets upon which anoxic biosignatures are later detected with JWST, then an even stronger case for biology might be made when placed in a Bayesian framework for calculating the probability of life's presence (Catling et al. 2018).

Note that in our assumed distribution, the maximum non-biological methane flux (Fig. 6c) is very conservative, implying that our abiotic production probabilities may be too high. Guzmán-Marmolejo et al. (2013) argued that fluxes greater than ~1 Tmol CH_4/yr are difficult to explain without life, and they used a photochemical model to show non-biological methane abundances should therefore not exceed ~10 ppm. Our assumed non-biological methane flux distribution allows for higher fluxes because we allow for a broader range of crustal production rates and don't assume that CO_2 availability limits CH_4 production (Krissansen-Totton et al. 2018).

One caveat on the results described above is that heterogeneity and variability in the transit light source were not considered. It is debated whether these effects could cause large uncertainties for transit observations of late M-dwarfs. Rackham et al. (2018) argued that unocculted star spots could result in stellar contamination features in the TRAPPIST-1 transit transmission spectra that are comparable or larger in magnitude than the expected atmospheric features. Subsequently, Zhang et al. (2018) showed that this stellar model could explain recent Hubble Space Telescope (HST) and Spitzer observations of the TRAPPIST-1 planets by invoking ~30% spot coverage on the star's surface. However, a recent analysis of

TRAPPIST-1 transit data from K2, SPECULOOS, Liverpool, and Spitzer telescopes ruled out the high spot coverage models of Rackham et al. (2018) and Zhang et al. (2018). Stellar models with a small coverage fraction of bright faculae are a better fit to transit data, and would not have as large an impact on planetary NIR transmission spectra (Ducrot et al. 2018; Morris et al. 2018).

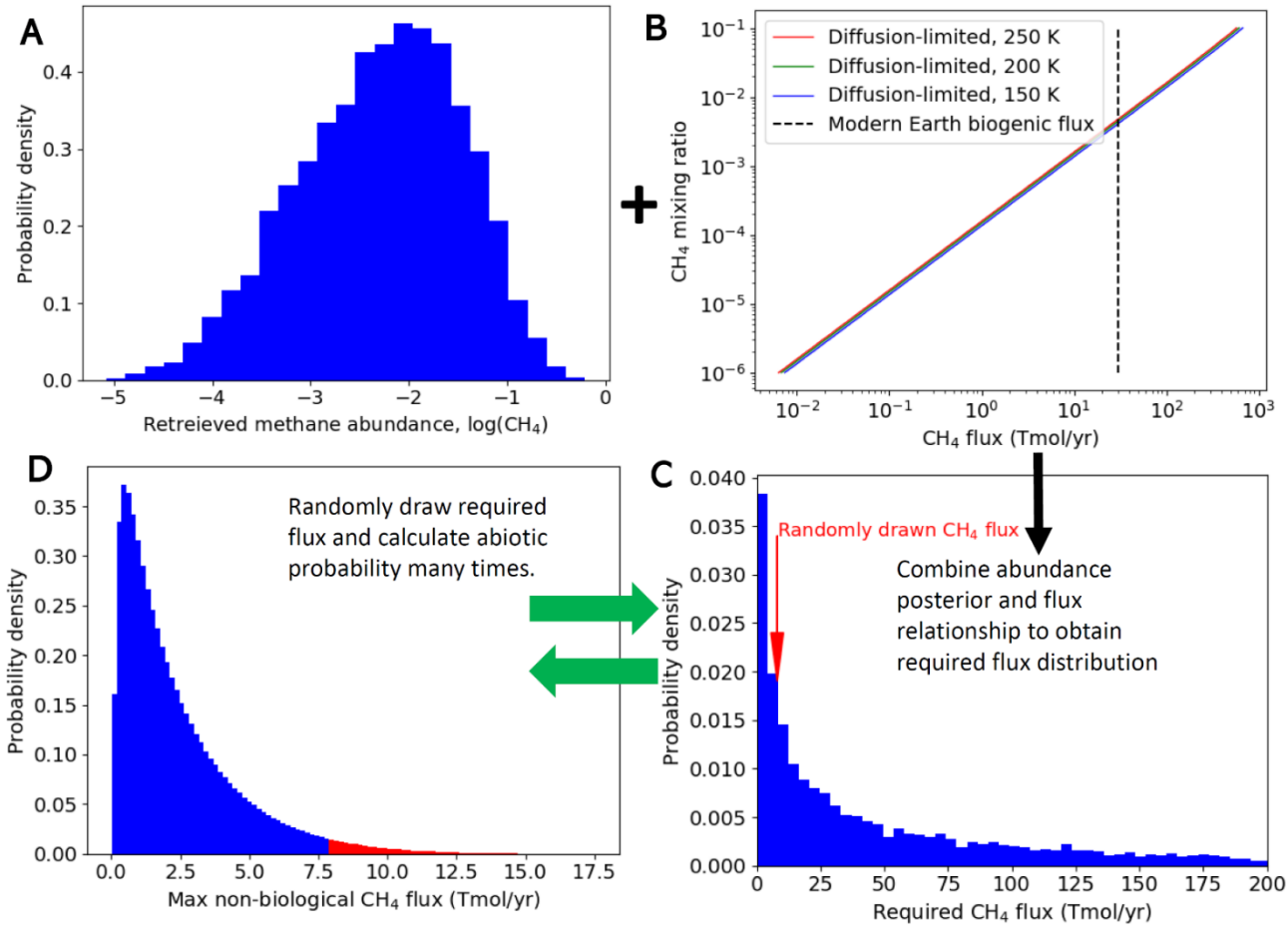

Figure 4-6: One approach to making probabilistic inferences to biology from atmospheric abundance constraints. The posterior distribution for CH_4 (A) is converted to a necessary replenishing surface flux distribution (C) by assuming diffusion-limited escape (B, adapted from Krissansen-Totton et al. (2018)). This distribution for the required flux (C) is then repeatedly sampled, and each sampled value is compared to a theoretical distribution for the maximum non-biological methane flux (D, adapted from Krissansen-Totton et al. (2018)). Specifically, the probability of the sampled flux occurring via non-biological processes is found by integrating the (D) from the sampled flux value to infinity. For example, if 8 Tmol/yr is drawn from (C, red arrow), then the probability of this being nonbiological is obtained by integrating (D) from 8 Tmol/yr to infinity (red color region). This is repeated 10,000 times, and the average of these values is the probability that the observed methane abundance can be explained by non-biological processes.

Another caveat is that we optimistically assumed no noise floor and no instrumental noise other than that already prescribed in PandExo. However, we performed sensitivity tests where we repeated our Archean Earth-like retrievals with a 40 ppm noise floor and found $\log(CH_4) = -2.21^{+0.76}_{-0.93}$. This is similar to the

nominal case because the largest CH_4 absorption features lie in regions of the spectrum where the noise level is above the noise floor. Changes in uncertainties in other atmospheric parameters are modest.

Finally, several simplifications were made in forward modeling that could affect the retrieval. For example, we assumed constant mixing ratios with altitude, which is unrealistic for some species such as CH_4 due to photochemical destruction at high altitude. However, self-consistent photochemical models of Archean-like atmospheres show that CH_4 only declines in abundance above 50-60 km (Kharecha et al. 2005; Zahnle et al. 2006), whereas the transit spectrum is mostly sensitive to abundances in the 10-60 km range (for Earth-like atmospheric structure). Nonetheless, future retrievals should be performed with self-consistent climate and photochemistry to more accurately constrain mixing ratios. Retrieved CH_4 abundances from models that assume constant mixing ratios with altitude should be seen as lower limits on tropospheric CH_4 abundances. Additionally, a photochemical model should be used to more accurately relate CH_4 surface fluxes to CH_4 mixing ratios rather than the diffusion-limited calculations adopted in Fig. 6b. This is because this relationship is CO_2-dependent as higher pCO_2 shields CH_4 from Lyman-alpha photons (Pavlov et al. 2001b).

Although this study is focused on JWST retrievals, it is worth noting that future telescopes such as the Large-Aperture UV-Optical-Infrared (LUVOIR) mission could perform transit spectroscopy out to ~5 μm (Bolcar et al. 2016) and could therefore constrain CO_2, CH_4, and CO gas abundances much more precisely than JWST (Krissansen-Totton et al. 2019).

Photochemical production of CO and CO anti-biosignatures

Krissansen-Totton et al. (2018) argued that absence of CO would strengthen the CH_4+CO_2 disequilibrium biosignature because (i) scenarios that generate CH_4 abiotically such as impacts or outgassing from a strongly reduced mantle would also produce CO, and so the absence of CO would rule out these scenarios and (ii) CO is a free lunch that ought to be readily consumed by microbes, and so its persistence suggests the absence of biology. CO may also be generated photochemically from CO_2-dissociation and could potentially accumulate to high abundances around M-dwarfs because of the shape of the UV spectrum (Harman et al. 2015a; Nava-Sedeno et al. 2016). Consequently, the absence of CO (with abundant CH_4 and CO_2) in the atmospheres of habitable planets around M-dwarfs is arguably a more compelling biosignature than around G-stars because it implies a large, presumably biological, sink for CO to balance photochemical production or other forms of abiotic production.

It could be argued that the CH_4 and CO_2 in the atmosphere of an M-dwarf planet will often be accompanied by photochemically-produced CO, and so the absence of CO is unlikely. However, on inhabited planets biological CO consumption would likely increase to draw down photochemically-produced CO to below

detectable thresholds. In Appendix I 4-A, we present thermodynamic calculations demonstrating that if CO-consumers exploit the available free energy, then for the Archean Earth-like atmospheres considered in this study, the steady state CO abundance would not exceed a few ppmv, and would more likely be a few ppbv. We assume free energy-limited CO-consumption is appropriate because the only other substrate required for CO oxidation is water, which would not be limiting on habitable zone planets. Furthermore, the fluxes required to draw down worst-case scenario photochemical CO-production are only a few percent of the modern Earth's gross productivity, which suggests that nutrient availability is unlikely to limit CO consumption in most cases (see Appendix I 4-A).

In practice, CO may accumulate to somewhat higher values because biological consumption of CO in the ocean is limited by the transfer of gas across the atmosphere-ocean interface. For example, Kharecha et al. (2005) modeled the biogeochemical cycles of the Archean atmosphere and biosphere and found that CO mixing ratios could be 10^{-6} to 10^{-4} in the presence of acetogens due to the limited transfer of CO across the atmosphere-ocean interface. Future work ought to incorporate CO-consumption into biogeochemical models of inhabited planets around M-dwarfs to better quantify likely CO abundances under different stellar spectra and nutrient-limitation scenarios.

Conclusions

From simulated spectra and subsequent retrievals, we conclude that the CH_4+CO_2 minus CO biosignature combination in anoxic atmospheres (proposed by Krissansen-Totton et al. (2018)) is potentially detectable with JWST for nearby transiting planets such as TRAPPIST-1e. For cloud-free conditions, 10 transits may be enough to constrain abundances of all three gases. The potential significance of discovering extraterrestrial biospheres means a strong case exists for searching for this disequilibrium biosignature combination on habitable exoplanets with JWST.

Oxygen-rich planetary atmospheres would take time to evolve due to the reactivity of O_2 and the required prior biological evolution of water-splitting photosynthesis. We have thus argued that if life exists elsewhere then the CH_4+CO_2 minus CO biosignature is probably much more common than the oxygen-ozone biosignature. In addition, here we have demonstrated that the biosignature combination of CH_4+CO_2 minus CO in anoxic, Archean-like atmospheres will be easier to detect than ozone with JWST.

Retrieved posterior probability distributions of CH_4 abundances can be combined with theoretical calculations of maximum non-biological methane production to calculate the probability that the observed CH_4 can be explained by non-biological processes. We find that JWST observations could be used to make quantitative inferences about the chance of the data being attributable to extraterrestrial biology. For Archean Earth-like methane levels on TRAPPIST-1e, we make a preliminary estimate that for 10 transits

the probability of abiotic processes being responsible for the methane would be ~9%. For 50 transits, the probability drops to 2%. Moreover, we note that there is debate about whether the efficacy of abiotic methane production has been overestimated (see Krissansen-Totton et al. (2018)), and so these probabilities for abiotic explanations likely err on the conservative side.

Chapter 5 - Constraining the operation of Earth's carbon cycle

"If the quantity of carbonic acid increases in geometric progression, the augmentation of the temperature will increase nearly in arithmetical progression." – Svante Arrhenius, 1896.

Understanding and assessing planetary habitability can both guide the search for the biosignatures and help bolster (or refute) any purported biosignature detections. The most important requirement for exoplanet habitability is surface liquid water, and whether liquid water can persist on a planet's surface depends primarily on surface temperature.

When considering the evolution of Earth's surface temperature through time an apparent paradox emerges: the sun was ~30% less bright in the Archean, which would trigger global glaciation given the modern Earth's atmospheric composition (Sagan & Mullen 1972). However, there is abundant geological evidence that this did not occur. How was Earth's habitability maintained over billions of years?

The apparent resolution is that the carbon cycle behaves as a natural thermostat, buffering Earth's temperature against changes in insolation (Walker et al. 1981). This occurs because silicate weathering, a sink for atmospheric carbon, is a temperature dependent process (Walker et al. 1981). Comparable natural thermostats are hypothesized to buffer the climates of terrestrial exoplanets (Abbot et al. 2012; Rushby et al. 2018). However, despite this mechanism being the widely accepted textbook explanation of Earth's continuous habitability, the quantitative behavior of the Earth's carbon cycle on long timescales is not well known. This chapter uses proxy data and an inverse model of Earth's carbon cycle to constrain the strength of weathering feedbacks and other key carbon cycling parameters.

The long-term response of the Earth system to anthropogenic CO_2 emissions will ultimately be controlled by the same carbon cycle feedbacks that have regulated Earth's temperature on geological timescales (Archer 2005; Archer et al. 2009). The results of the analysis presented in this chapter thus have implications for the long-term consequences of fossil fuel burning.

This chapter was published in collaboration with David C. Catling in Nature Communications (Krissansen-Totton and Catling (2017). Constraining climate sensitivity and continental versus seafloor weathering using an inverse geological carbon cycle model, Nature Communications, DOI:10.1038/NCOMMS15423).

nature COMMUNICATIONS

ARTICLE

Received 15 Jun 2016 | Accepted 27 Mar 2017 | Published 22 May 2017

DOI: 10.1038/ncomms15423 OPEN

Constraining climate sensitivity and continental versus seafloor weathering using an inverse geological carbon cycle model

Joshua Krissansen-Totton[1] & David C. Catling[1]

The relative influences of tectonics, continental weathering and seafloor weathering in controlling the geological carbon cycle are unknown. Here we develop a new carbon cycle model that explicitly captures the kinetics of seafloor weathering to investigate carbon fluxes and the evolution of atmospheric CO_2 and ocean pH since 100 Myr ago. We compare model outputs to proxy data, and rigorously constrain model parameters using Bayesian inverse methods. Assuming our forward model is an accurate representation of the carbon cycle, to fit proxies the temperature dependence of continental weathering must be weaker than commonly assumed. We find that 15–31 °C (1σ) surface warming is required to double the continental weathering flux, versus 3–10 °C in previous work. In addition, continental weatherability has increased 1.7–3.3 times since 100 Myr ago, demanding explanation by uplift and sea-level changes. The average Earth system climate sensitivity is $5.6^{+1.3}_{-1.2}$ K (1σ) per CO_2 doubling, which is notably higher than fast-feedback estimates. These conclusions are robust to assumptions about outgassing, modern fluxes and seafloor weathering kinetics.

[1] Department of Earth and Space Sciences/Astrobiology Program, University of Washington, Seattle, Washington 98195-1310, USA. Correspondence and requests for materials should be addressed to J.K.-T. (email: joshkt@uw.edu).

Determining what controls the geological carbon cycle is crucial for understanding climate stability, planetary habitability and the long-term consequences of anthropogenic carbon emissions. On long timescales, carbon inputs into the atmosphere–ocean system must balance outputs otherwise atmospheric CO_2 would be depleted leading to a runaway icehouse, or CO_2 would accumulate and become excessively abundant within 10–100 Myr ago (ref. 1). Thus, a negative feedback must stabilize the carbon cycle and global climate on geological timescales.

The carbonate–silicate weathering cycle described by Walker *et al.*[2] is widely believed to provide a negative feedback[3]. In this picture, climatic warming from abundant atmospheric CO_2 enhances silicate weathering and delivers more carbon to the ocean where it precipitates to form carbonate rocks. Conversely, climatic cooling due to low CO_2 reduces silicate weathering and dampens CO_2 drawdown. The temperature dependence of silicate weathering effectively provides a natural thermostat to stabilize climate[2].

Although the carbonate–silicate thermostat is now part of textbook Earth science[4], the link between global climate, CO_2 and silicate weathering rates is unclear. Gaillardet *et al.*[5] found no overall correlation between weathering rates and temperature on a global scale. Some regional field studies also fail to find a relationship[6]. Furthermore, strongly temperature-dependent continental weathering is argued to contradict the conventional interpretation of the Phanerozoic strontium isotope record[7]. Weatherability changes due to uplift, lithology and biology have all been proposed as alternative drivers of the carbon cycle[8–11]. Indeed, Walker[12] himself changed his opinion to suspecting greater sensitivity of weathering rate to the aforementioned factors than to CO_2. Some models of the Cenozoic carbon cycle also suggest sizeable weatherability changes for reproducing observed pCO_2 and carbon isotope histories[13].

However, weatherability changes alone do not provide a clear negative feedback to balance the carbon cycle. An alternative or complimentary negative feedback to continental silicate weathering is seafloor weathering[7,14–17]. Seafloor weathering occurs because seawater circulates through upper oceanic crust in low-temperature, off-axis hydrothermal systems. Reactions with basalt release calcium ions, which precipitates calcium carbonate within veins and pores of the oceanic crust[18,19]. If the rate of basalt dissolution and precipitation is linked—directly or indirectly—to the carbon content of the atmosphere–ocean system, then seafloor weathering could provide an important negative feedback.

Here it is useful to think in terms of carbonate alkalinity, $[HCO_3^-]+2[CO_3^{2-}]$, which—neglecting the small contribution from weak acid anions and water dissociation products—must balance the sum of conservative cations minus conservative anions, $([Na^+]+2[Mg^{2+}]+2[Ca^{2+}]+[K^+]+\ldots-[Cl^-]-2[SO_4^{2-}]-[Br^-]-\ldots)$. Thus, dissolution of basalt, which releases alkaline earth and alkali metal cations, generates carbonate alkalinity to neutralize the positive ions in solution. In other words, carbon speciation adjusts in response to the addition of conservative cations to ensure charge balance.

Caldeira[20] used simple geochemical models to show that the pH dependence of seafloor weathering is too weak to be an important carbon cycle feedback, concluding that continental weathering dominates. However, recent studies challenge this conclusion: Mesozoic-aged oceanic crust has substantially higher carbonate content compared to Cenozoic-aged cores[18], and this elevated carbonate content is due to enhanced Mesozoic carbonate precipitation and not carbonate accumulation later[21]. In addition, these seafloor carbonates can only be explained by alkalinity released from basalt dissolution; alkalinity released from continental weathering is insufficient[16]. Temperature-dependent seafloor weathering could explain both the observed change in seafloor carbonate abundance since the Mesozoic and the strontium isotope record[17]. These studies justify re-examining the importance of seafloor weathering in the global carbon cycle.

Previous attempts to incorporate seafloor weathering into carbon cycle models have produced conflicting results, and temperature dependencies are often omitted[7,20]. Brady and Gíslason[14] conducted experiments to find the pCO_2 dependence and temperature dependence of seafloor weathering rates, which they summarized as:

$$r_{\text{dissolution}} \propto (R_{CO_2})^{\mu} = \left(\frac{pCO_2}{pCO_2^{\text{mod}}}\right)^{\mu} \quad (1)$$

Here R_{CO_2} is the partial pressure of atmospheric CO_2 (pCO_2) relative to preindustrial modern ($pCO_2^{\text{mod}} = 280$ p.p.m.), $\mu = 0.23$ is the best-fit CO_2 dependence and $\mu = 0.32$ is the best-fit temperature dependence. This approximation, with varying values for μ, has been adopted in several subsequent models, which suggest that seafloor weathering was an important negative feedback during at least some of Earth's history[10,15,22].

Subsuming the pH dependence, temperature dependence and ocean chemistry dependence of seafloor weathering into a CO_2 dependence (such as equation (1)) is potentially problematic because it does not explicitly capture dissolution kinetics, and so the value for μ that combines the temperature, pH and ocean chemistry weathering dependencies must be either guessed or fitted (for example, ref. 15). Models such as GEOCARB and its various incarnations[3,23] similarly do not incorporate seafloor weathering accurately because they lack ocean chemistry. Some models attempt to capture dissolution kinetics. However, these models have highly simplified ocean chemistry[24], assume a constant temperature of dissolution[25] or do not reproduce the observed increase[17] in seafloor basalt dissolution[26].

Here we develop a new open source model for testing competing hypotheses about the global carbon cycle. Our model explicitly calculates ocean chemistry and includes pH-dependent and temperature-dependent kinetics based on laboratory and empirical studies. This is an improvement over previous models that subsumed pH dependence and temperature dependence into an overall indirect CO_2 dependence with an arbitrary functional relationship (equation (1)), or only considered pH dependence in isolation[20,25]. In addition, we use a new parameterization linking deep-ocean temperatures to surface temperatures, and thus seafloor weathering to climate. The Cenozoic (66–0 Myr ago) and Mesozoic (252–66 Myr ago) are particularly useful eras to model because of their relatively abundant proxy records of ocean composition and geochemistry. Thus, to validate our model, we apply it the last 100 Myr ago and compare model outputs with these proxies. We also use a Bayesian inversion to constrain model parameters quantitatively, including the temperature sensitivity of continental weathering, climate sensitivity, and continental weatherability changes. This approach makes minimal assumptions about carbon cycle processes. For instance, it is agnostic about whether Cretaceous outgassing was very high or comparable to present levels, and it allows for large changes in weatherability of both silicates and carbonates. Consequently, the novel probability distributions we obtain for parameters of interest are robust to model assumptions.

Results

Definition of parameters. We model the time evolution of the carbon cycle using two separate boxes representing the atmosphere–ocean and the pore-space in the seafloor (Fig. 1), loosely following Caldeira[20]. We track carbon and alkalinity

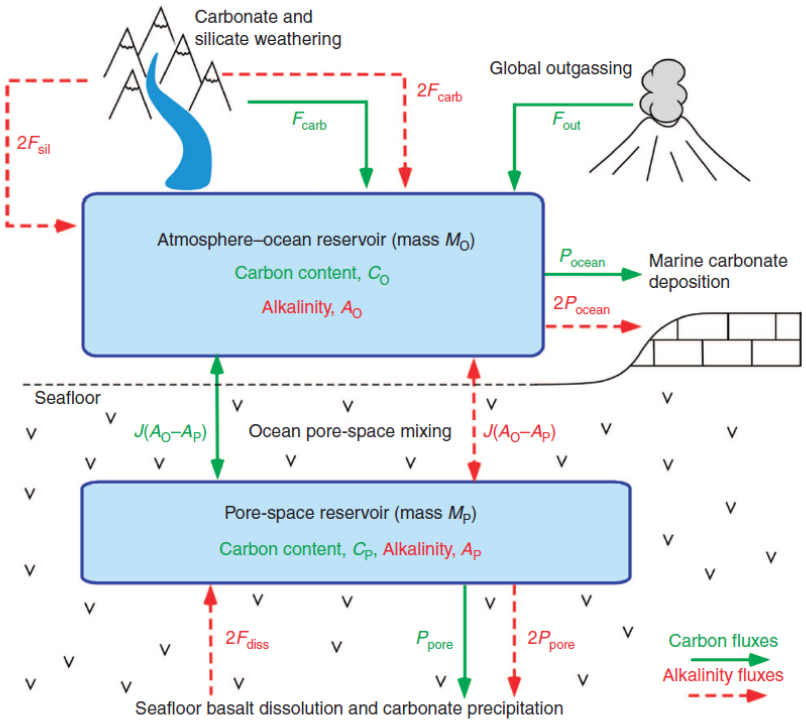

Figure 1 | Schematic representation of the box model used in this study. Carbon fluxes (Tmol C per year) are denoted by solid-green arrows, and alkalinity fluxes (Tmol eq per year) are denoted by red-dashed arrows. The fluxes into/out of the atmosphere–ocean are outgassing, F_{out}, silicate weathering, F_{sil}, carbonate weathering, F_{carb}, and marine carbonate precipitation, P_{ocean}. The fluxes into/out of the pore-space are basalt dissolution, F_{diss}, and pore-space carbonate precipitation, P_{pore}. Alkalinity fluxes are multiplied by two because the uptake or release of one mole of carbon as carbonate is balanced by a cation with a 2+ charge (typically Ca^{2+}). A constant mixing flux, J (kg per year), exchanges carbon and alkalinity between the atmosphere–ocean and pore-space.

fluxes into and between those boxes, and specify a constant mixing flux, J (kg per year) that determines how rapidly the ocean circulates through the pore-space. We assume that the bulk ocean is in equilibrium with the atmosphere. Consequently, our model is only appropriate for timescales greater than the mixing time of the ocean, $\sim$1,000 years.

For many free parameters, we assume a range of values rather than point estimates. Model outputs are presented as distributions over this range of parameter values, which ensures that our results are robust to uncertainties in parameters, as described below. The dynamical equations, flux parameterizations and initial conditions are described in the methods section. Here we summarize the key points necessary to understand the results.

Following Walker *et al.*[2], the continental silicate weathering flux is expressed as:

$$F_{sil} = \omega F_{sil}^{mod} \left(\frac{pCO_2}{pCO_2^{mod}} \right)^{\alpha} \exp(\Delta T_S / T_e) \qquad (2)$$

Here $\Delta T_S = T_S - T_S^{mod}$ is the difference in global mean surface temperatures relative to preindustrial modern, $T_S^{mod} = 285\,K$; ω is a dimensionless weatherability factor, F_{sil}^{mod} is the modern silicate weathering flux (Tmol per year) and α is an empirical constant (see Methods). An e-folding temperature, T_e, defines the temperature dependence of weathering, which can be related to an effective activation energy, E_a, as follows:

$$\frac{1}{T_e} \approx \frac{E_a}{RT_S^2} \qquad (3)$$

Here R is the universal gas constant.

In equation (2), we have combined both the direct kinetic temperature dependence and the temperature dependence of runoff in a single exponent. This is justifiable because an exponential kinetic dependence and a linear runoff dependence can be accurately approximated by an overall exponential (Supplementary Fig. 1). Walker *et al.*[2] also combine both effects to obtain an overall temperature dependence of $T_e = 13.7\,K$, which corresponds to an effective activation energy of $\sim 50\,kJ\,mol^{-1}$. Similarly, field measurements of chemical weathering fluxes from field studies suggest an activation energy of $74 \pm 29\,kJ\,mol^{-1}$ ($T_e = 9.1^{+5.9}_{-2.6}K$ (ref. 27)). GEOCARB III effectively uses an overall e-folding temperature of $T_e \sim 9.2\,K$, combining a direct temperature dependence and runoff coefficient[3]. We initially assume $T_e = 5$–$15\,K$, but later consider a broader range because a weak temperature dependence turns out to be required.

The factor ω represents all so-called 'external' variables affecting weatherability and encompasses changes in land area due to sea-level variations, changes in lithology, relief, biology and palaeogeography. Rather than attempt to explicitly model these different influences (for example, ref. 23), we address the inverse problem: how much does ω have to change to fit proxy data? The simplest approach is to assume a linear change in weatherability since the mid-Cretaceous, as follows,

$$\omega = 1 + W(t/100\,Myr) \qquad (4)$$

and find W, the unknown change in weatherability. Here t is millions of years ago (Myr ago). We initially assume $W = 0$ to examine the range of possible model outputs for no external weatherability changes. Later, we assume $W = -0.8$ to 0.2, corresponding to mid-Cretaceous weatherability that was between 80% less or 20% greater than modern.

We adopt a parameterized climate model, whereby changes in surface temperature, ΔT_S, are logarithmically related to pCO_2, with corrections for solar luminosity evolution and palaeogeography (see Methods). The climate sensitivity parameter, ΔT_{2x}, has units of Kelvin warming per CO_2 doubling. The Intergovernmental Panel on Climate Change (IPCC)[28] estimated equilibrium climate sensitivity within the range 1.5–4.5 K. We assume $\Delta T_{2x} = 1.5–8.0$ K, which encompasses a broad range.

Approach and context. Parameterizations for carbon cycle processes are uncertain, so we adopted two statistical techniques to extract robust conclusions. First, we ran the forward model for the range of parameters and initial values shown in Tables 1 and 2. Each range was sampled as a uniform distribution, and the forward model was run 10,000 times to build distributions for the time series model outputs such as pCO_2, pH and temperatures. The resulting distributions represent the full range of possible model outcomes given assumed parameterizations and parameter ranges. These distributions were then compared to proxy data, typically binned into 10 Myr ago intervals with large, conservative error bars (Supplementary Methods).

The second approach solved the inverse problem with Markov Chain Monte Carlo (MCMC) techniques using the *emcee* package[29] in python (Supplementary Methods). Here the parameter ranges and initial value ranges define uniform priors (Table 1). A likelihood function describes the goodness-of-fit with proxy data, and the forward model was run 10 million times to obtain posterior probability distributions for the model parameters. The inverse solution gauges the full extent to which proxy data constrain the operation of the carbon cycle. In particular, parameters such as climate sensitivity, weatherability changes and the temperature dependence of silicate weathering can be constrained.

Forward modelling. The forward model was run 10,000 times, repeatedly sampling the parameter ranges of Table 1. First, weatherability was assumed constant ($W = 0$) and a range for the temperature dependence of silicate weathering typically assumed in the literature was adopted ($T_e = 5–15$ K). Figure 2 shows the modelled 90% confidence intervals plotted alongside proxy data. Clearly, the model with commonly assumed ranges for parameters does not fit the data. In particular, deep-ocean temperatures, surface temperatures and seafloor carbonate precipitation at 100 Myr ago are considerably lower than Cretaceous proxies (Fig. 2d,f). Fits with pH and ocean saturation state are also poor.

Next, the calculation was repeated using a weaker temperature dependence of silicate weathering, $T_e = 30–40$ K (Fig. 3). Here the 90% model uncertainty envelopes broadly encompass the proxy data, but the fit is marginal. The model pCO_2 output is consistent with pCO_2 proxies, and the temperature and seafloor precipitation distributions mostly overlap with proxy data error bars. Similarly, if we repeat the calculation a third time with the original temperature dependence of silicate weathering ($T_e = 5–15$ K), but include sizeable weatherability changes ($W = -0.6$ to -0.4, that is, weatherability at 100 Myr ago between 40 and 60% the modern value), then the model plausibly fits the data (Supplementary Fig. 2). Temperature, pCO_2 and precipitation proxies fall broadly within the model uncertainty envelope, although the fits with ocean pH and saturation state are still poor.

The best fit (Fig. 4) is obtained by assuming both weak temperature dependence of silicate weathering ($T_e = 30–40$ K) and a large weatherability change ($W = -0.6$ to -0.4). The median model output then fits temperature and precipitation proxies well, and pCO_2, ocean saturation state and pH all fall within proxy error bars.

From these results, we conclude that either the temperature dependence of silicate weathering is weaker than is commonly assumed, and/or that weatherability has approximately doubled since 100 Myr ago. When both are true, the model best fits the

Table 1 | Parameter ranges and Bayesian Markov Chain Monte Carlo inversion results.

Variable	Prior (uniform)	Nominal model			Michaelis–Menten law	
		Median posterior value	68% Credible interval ($1-\sigma$)	90% Credible interval	Median posterior value	90% Credible interval
CO_2 dependence, α*	0.2–0.5	0.33	0.24–0.44	0.21–0.48	0.41	0.05–0.91
e-folding temp. dep. of cont. weathering, T_e (K)	5–50	34	22–45	17–48	31	14–48
Relative Cretaceous, weatherability, $1+W$	0.2–1.2	0.42	0.30–0.58	0.24–0.71	0.6	0.31–0.96
Climate sensitivity, ΔT_{2x} (K)	1.5–8.0	5.6	4.4–6.9	3.7–7.5	5.6	3.8–7.6
Relative Cretaceous outgassing, $1+V$	1.2–2.5	1.58	1.34–1.88	1.25–2.1	1.56	1.24–2.1
Carbonate weatherability modifier, $1+C_{WF}$	0.1–2.5	0.36	0.18–0.63	0.13–0.83	0.39	0.13–0.88
Modern outgassing, F_{out}^{mod} (Tmol C per year)	4–10	6.6	4.8–8.8	4.2–9.6	6.5	4.2–9.6
Modern carb. weathering, F_{carb}^{mod} (Tmol C per year)	7–14	11	8.2–12.9	7.4–13.7	11	7.4–13.7
Pore-space circulation time, τ (kyr)	20–1,000	570	239–847	100–949	555	88–945
Carbonate precip. coefficient, n	1.0–2.5	1.66	1.22–2.18	1.1–2.4	1.69	1.1–2.4
Modern seafloor dissolution relative to precipitation, x†	0.5–1.5	1.02	0.68–1.34	0.56–1.45	1.01	0.56–1.45
Surface-deep temp. gradient, a_{grad}	0.8–1.4	0.99	0.88–1.14	0.83–1.25	0.99	0.83–1.25
pH dependence seafloor, γ	0–0.5	0.27	0.11–0.43	0.04–0.48	0.27	0.04–0.48
Temp. dependence seafloor, E_{bas} (kJ mol^{-1})	40–110	75	53–97	45–106	76	45–106
Modern pelagic fraction, f_{PEL}	0.4–0.6	0.49	0.43–0.56	0.41–0.59	0.49	0.41–0.59
Spreading rate dep., β	0.0–1.0	0.47	0.15–0.82	0.05–0.94	0.49	0.05–0.95
Palaeogeography climate parameter, ΔP (K)	0.0–5.0	2.6	0.88–4.2	0.28–4.7	2.5	0.27–4.7

Column 1 shows the variables we wish to constrain using proxy data. Column 2 gives the uniform prior for each variable. These intervals also constitute the ranges assumed in the forward model analysis, unless stated otherwise. Columns 3–5 describe the posterior probability distributions for each variable for the nominal model. Columns 6–7 describe the posterior probability distributions for the modified model where the pCO_2 dependence of continental weathering is parameterized using the Michaelis–Menten law.
*For the Michaelis–Menten law, the prior for α is 0–1.0 (Supplementary Note 6), and so the posterior distribution is different to that of the nominal model.
†This constant defines the initial seafloor dissolution flux relative to the carbonate precipitation flux in the pore-space (see Table 2 for further details and formal definition).

Table 2 | Initial values or initial value ranges assumed in our model.

Variable	Initial value or initial range	References
Modern pore-space carbonate precipitation, P^{mod}_{pore} (Tmol C per year)	0.45*	[18] (see Supplementary Methods)
Modern seafloor dissolution, F^{mod}_{diss} (Tmol C per year)	0.225–0.675†	[16]
Modern outgassing, F^{mod}_{out} (Tmol C per year)	4–10	[23,76]
Modern carb. Weathering, F^{mod}_{carb} (Tmol C per year)	7–14	[77], their Table 2
Preindustrial mean surface temperature, T_S (K)	285	[2]
Modern ocean pH	8.2	[74]
Ocean Ca abundance (mMol kg^{-1})	10.03	Polynomial fit to Tyrrell and Zeebe[75], see Supplementary Fig. 8
Preindustrial atmospheric pCO_2 (p.p.m.)	280	—
Modern fraction pelagic precip. f_{PEL}	0.4–0.6	[78]

*Because we are adopting wide ranges for F^{mod}_{out} and F^{mod}_{carb}, it is unnecessary to include a range for P^{mod}_{pore} because its size relative to outgassing and weathering fluxes already encompasses a wide range (only the relative sizes of carbon cycle fluxes matter for predicting observable variables).
†Here we assume that $F^{mod}_{diss} = xP^{mod}_{pore}$, where $x = 0.5$–1.5. Coogan and Gillis[16] used a geochemical model of pore-space precipitation to show that at least 70% of pore-space precipitation is attributable to alkalinity release from basalt dissolution. Here we conservatively assume a lower limit of 50% instead. The upper limit is 150% to allow for the possibility that pore-space dissolution exceeds pore-space precipitation, and that the excess alkalinity is mixed into the ocean to form marine carbonates.

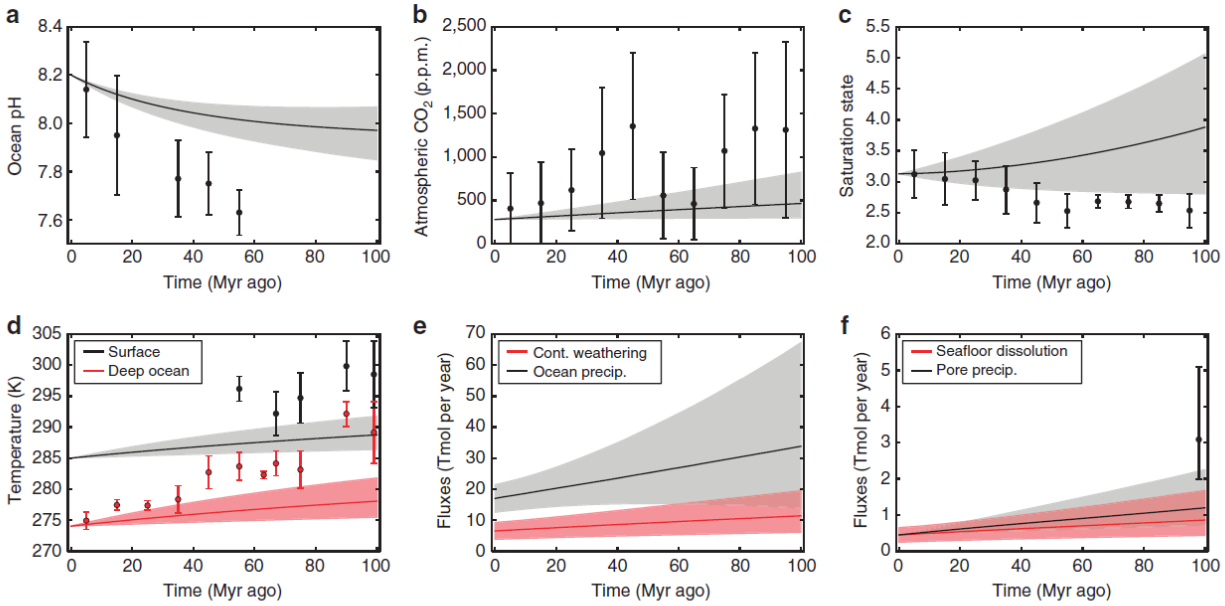

Figure 2 | Carbon cycle model with poor fit to data assuming conventional temperature dependence of continental weathering and no weatherability change. Selected model outputs and geochemical proxy data for a conventional temperature sensitivity range for continental weathering ($T_e = 5$–15 K), and no change in silicate weatherability over the last 100 Myr ago ($W = 0$). Grey- and red-shaded regions represent the model output 90% confidence obtained from 10,000 forward model runs using the parameter ranges described in Table 1. The grey- and red-solid lines are the median model outputs. Black and red dots represent binned geochemical proxy data, and error bars denote the range of binned proxy estimates (see main text for references and explanation). Panels denote (**a**) ocean pH, (**b**) atmospheric pCO_2, (**c**) ocean saturation state, (**d**) mean surface and deep ocean temperatures, (**e**) continental silicate weathering and ocean carbonate precipitation fluxes, and (**f**) seafloor dissolution and pore space carbonate precipitation fluxes. This case is a very poor fit to temperature and pH, and is a relatively poor fit to ocean saturation state and seafloor carbonate precipitation.

data. This result is robust to carbon cycle assumptions because the model distributions were calculated assuming the full parameter ranges in Table 1.

Bayesian MCMC inversion. The forward model results are qualitatively instructive, but Bayesian analysis allows more quantitative conclusions. MCMC techniques generated Fig. 5, which shows 95% credible intervals for the time evolution of carbon cycle variables. MCMC produces a much better fit than forward modelling because the algorithm converges to the maximum-likelihood region of parameter space. The distribution of model outcomes fits every proxy we considered within the 95% interval except one ocean pH data point. Distributions are also plotted for the relative and absolute change in seafloor dissolution, continental silicate weathering and continental carbonate weathering.

Figure 6 shows posterior probability distributions for selected model parameters, and Table 1 shows the best estimates for all parameters with uncertainty. To test the sensitivity of our results to weathering parameterizations, results are reported for both the nominal model (power-law pCO_2 dependence of continental weathering) and a Michaelis–Menten pCO_2 dependence law (Supplementary Note 6). For the nominal model, the temperature

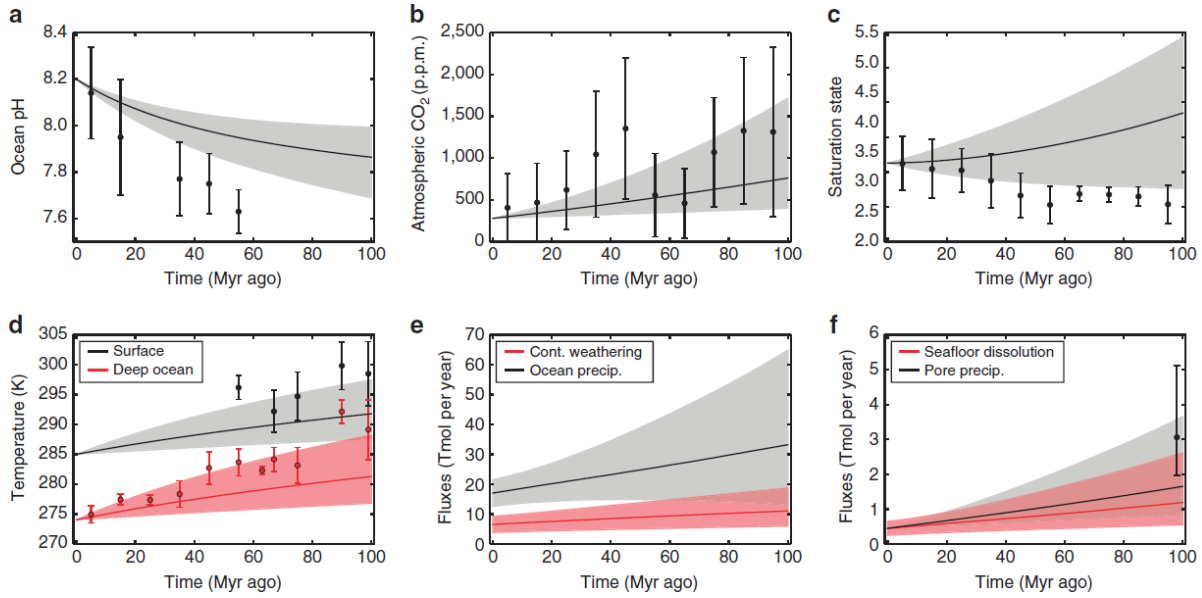

Figure 3 | Carbon cycle model with moderate fit to data assuming weak temperature dependence of continental weathering and no weatherability change. Selected model outputs and geochemical proxy data for a weak temperature dependence for continental weathering ($T_e = 30$–40 K) and no change in silicate weatherability over the last 100 Myr ago ($W = 0$). Grey- and red-shaded regions represent the model output 90% confidence obtained from 10,000 forward model runs using the parameter ranges described in Table 1. The grey- and red-solid lines are the median model outputs. Black and red dots represent binned geochemical proxy data, and error bars denote the range of binned proxy estimates (see main text for references and explanation). Panels denote (**a**) ocean pH, (**b**) atmospheric pCO_2, (**c**) ocean saturation state, (**d**) mean surface and deep ocean temperatures, (**e**) continental silicate weathering and ocean carbonate precipitation fluxes, and (**f**) seafloor dissolution and pore space carbonate precipitation fluxes. Here the model envelopes marginally encompass the proxy data. The upper end of the temperature and seafloor envelopes fit proxies, pCO_2 is an excellent fit, and the saturation state and ocean pH proxies are on the edge of the model envelope.

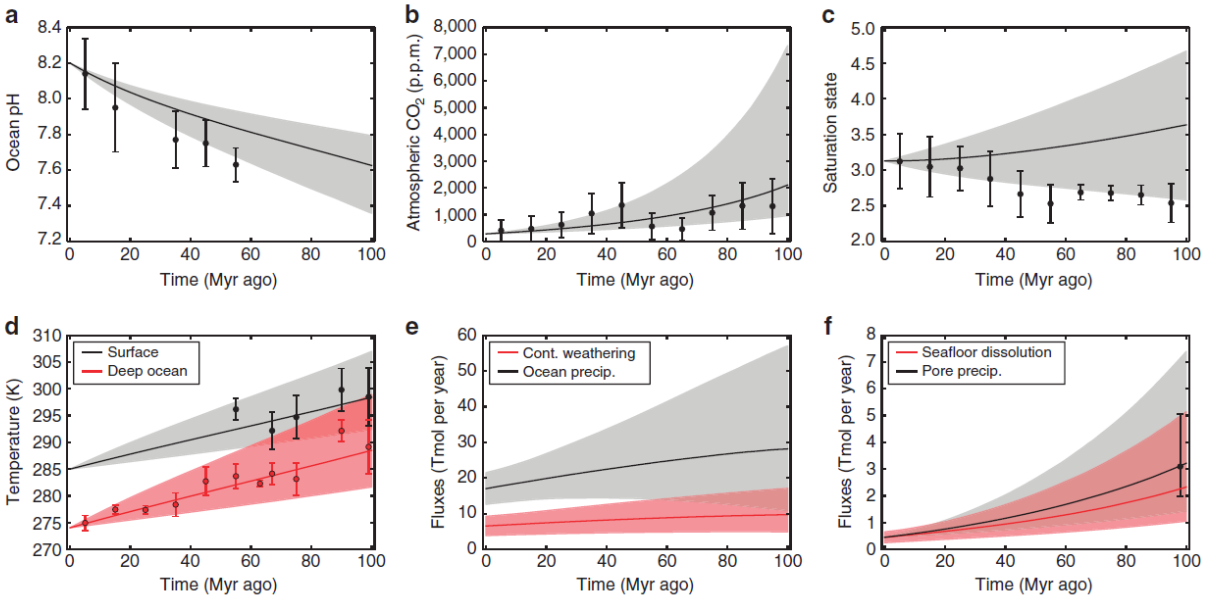

Figure 4 | Carbon cycle model with excellent fit to data assuming weak temperature dependence of continental weathering and a weatherability doubling since 100 Myr ago. Selected model outputs and geochemical proxy data for a weak temperature dependence for continental weathering ($T_e = 30$–40 K) and a 40–60% change in continental weatherability over the last 100 Myr ago ($W = -0.6$ to -0.4). Grey- and red-shaded regions represent the model output 90% confidence obtained from 10,000 forward model runs using the parameter ranges described in Table 1. The grey- and red-solid lines are the median model outputs. Black and red dots represent binned geochemical proxy data, and error bars denote the range of binned proxy estimates (see main text for references and explanation). Panels denote (**a**) ocean pH, (**b**) atmospheric pCO_2, (**c**) ocean saturation state, (**d**) mean surface and deep ocean temperatures, (**e**) continental silicate weathering and ocean carbonate precipitation fluxes, and (**f**) seafloor dissolution and pore space carbonate precipitation fluxes. Here the model envelopes are an excellent fit with proxy data. The median temperature and seafloor precipitation approximately coincide with geochemical proxies, and the saturation state, pH and pCO_2 envelopes all encompass their respective proxies.

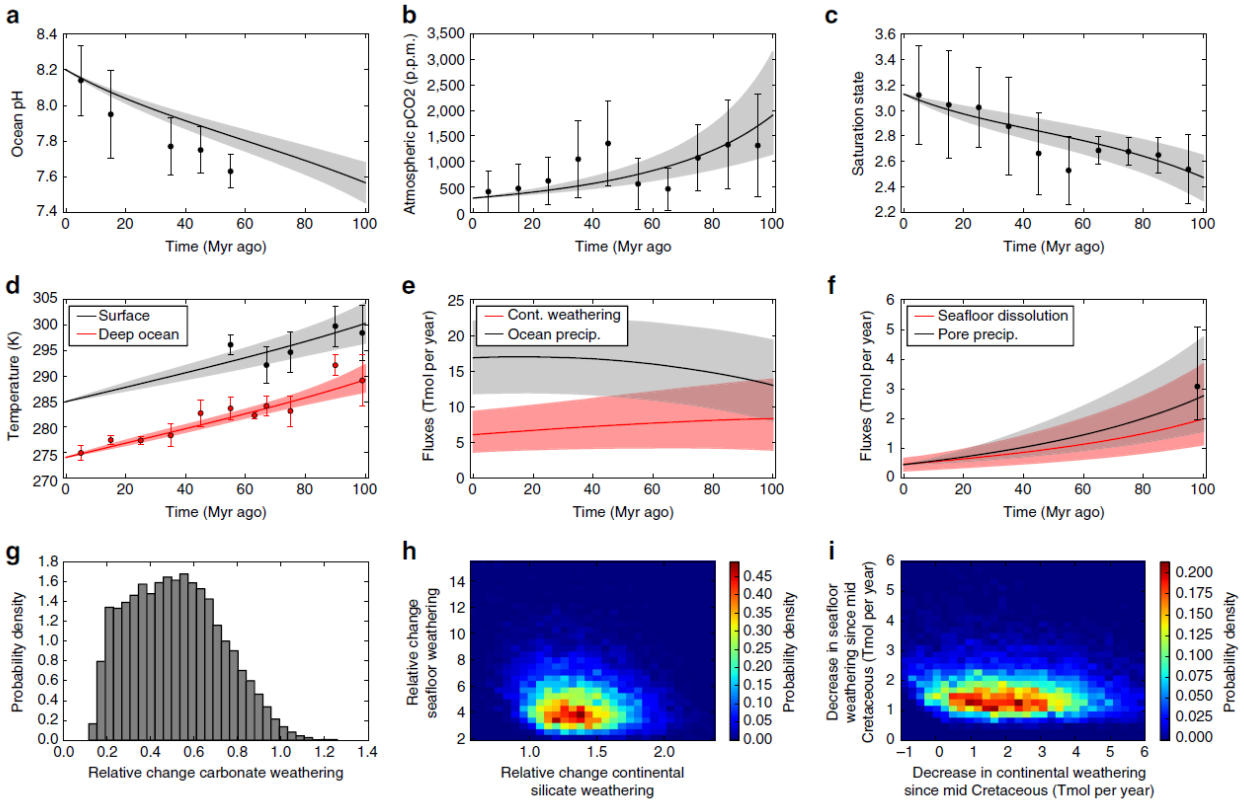

Figure 5 | Carbon cycle model fitted to data with Bayesian inverse analysis. Bayesian Markov Chain Monte Carlo (MCMC) results for the nominal model. (**a**–**f**) Grey- and red-shaded areas show 95% credible intervals for selected model outputs, and solid lines show median model outputs. Black and red circles are geochemical proxies, and error bars denote the range of binned proxy estimates (see main text). Note that the credible intervals encompass the Cretaceous proxies (within uncertainty) in almost all cases. (**g**–**i**) Probability distributions for the relative and absolute change in seafloor dissolution, continental silicate weathering and continental carbonate weathering. Relative changes refer to flux at 100 Myr ago relative to the modern flux.

dependence of silicate weathering is $T_e = 34^{+11}_{-11}$ K (1σ). This corresponds to a low effective activation energy of 20^{+10}_{-5} kJ mol^{-1} (1σ). Note that this effective activation energy incorporates all hydrological cycle feedbacks, not just the direct kinetic effect of temperature. Moreover, there is a 98% probability that $T_e \geq 15$ K ($E_a \leq 45$ kJ mol^{-1}). This suggests that the widely used range[2,3] of $T_e = 5$–15 K is incorrect. Intuitively, continental weathering must be weakly dependent on temperature because otherwise temperatures and pCO_2 would be too low, and ocean pH and saturation state values would be too high compared to geochemical proxies (Fig. 2).

The Bayesian inversion also implies that silicate weatherability in the Cretaceous was $42^{+16}_{-12}\%$ (1σ) of modern weatherability for the nominal model (Fig. 6). In addition, we can say there is a 95% probability that Cretaceous weatherability was $\leq 71\%$ of modern weatherability. This increase in weatherability is required in part because without it, Cretaceous silicate weathering would be too high to allow for the large observed seafloor weathering sink of carbon. But even if seafloor weathering is assumed to be negligible and removed from the likelihood function, then Cretaceous weatherability is $46^{+16}_{-13}\%$ modern weatherability. This small change is surprising because including seafloor weathering and its Cretaceous constraint effectively imposes a decreasing carbon sink, thereby allowing for a larger weatherability increase since 100 Myr ago and a weaker temperature sensitivity of continental weathering. However, the seafloor weathering sink is small compared to continental weathering, and so its omission only subtly affects the inversion. Instead, it is mostly temperature, pCO_2, pH and saturation state proxies that constrain the weatherability change.

The average equilibrium climate sensitivity over the last 100 Myr ago is constrained to $\Delta T_{2x} = 5.6^{+1.3}_{-1.2}$ K per CO_2 doubling (1σ) in the nominal model (Fig. 6). The 90% credible interval extends from 3.7 to 7.5 K, which is much higher than IPCC estimates. Low climate sensitivity is precluded by a lack of fit to pCO_2 and temperature proxies. The inverse analysis also suggests that Cretaceous outgassing was unlikely ($\sim$9% probability) to be greater than double modern outgassing to fit pCO_2 and temperature proxies.

In addition to the nominal model for continental weathering (equation (2)), we repeated the inverse analysis replacing the pCO_2 dependence of continental weathering with the Michaelis–Menten law:

$$F_{sil} = \omega F_{sil}^{mod} \left(\frac{2R_{CO_2}}{1 + R_{CO_2}} \right)^{\alpha} \exp(\Delta T_S / T_e) \qquad (5)$$

Using this modified parameterization, the results described above are largely unchanged (column 2, Fig. 6). The biggest difference between the two models is that the weatherability change required since 100 Myr ago is likely more modest under the Michaelis–Menten law than the nominal model, with a median Cretaceous value of 0.6 rather than 0.42.

Figure 5h shows the joint probability distribution for the relative change in continental silicate and seafloor weathering. We see the relative change in seafloor basalt dissolution at 100 Myr

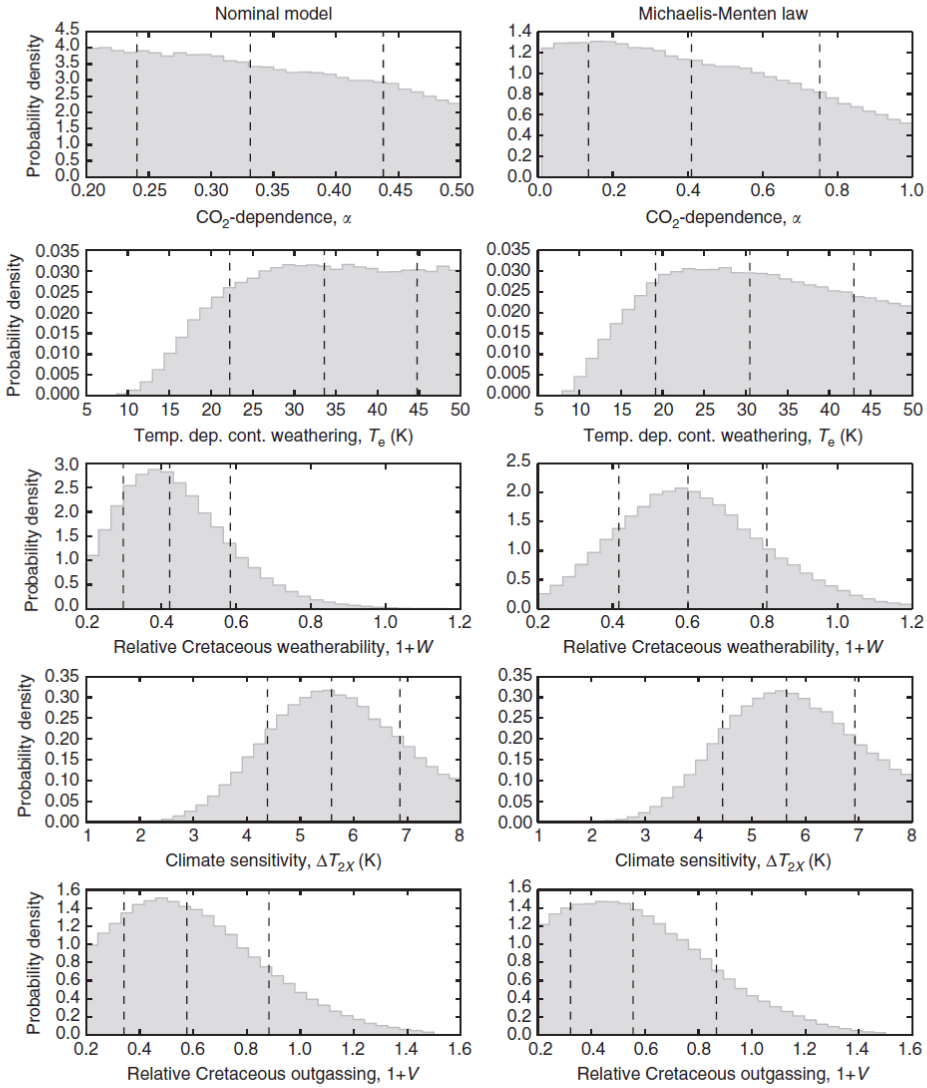

Figure 6 | Posterior probability distributions for selected carbon cycle variables from Bayesian inverse analysis. The first column is the posterior distributions from our nominal model, whereas the second column is distributions from a modified model, where the Michaelis–Menten law is used to describe the pCO_2 dependence of continental weathering. Results for the two parameterizations are similar. Dotted lines represent the median value with 1σ error bars. From the marginal distributions, we conclude that the temperature sensitivity of continental weathering is weak (T_e>15 K), Cretaceous silicate weatherability ($1+W$) was ~half modern weatherability, and the average equilibrium climate sensitivity is ~5.6 K for a CO_2 doubling.

ago is much larger (2.6–9.2x modern, 95% credible interval) than the relative change in continental silicate weathering (0.91–1.9x modern flux, 95% credible interval). We also observe that the continental weathering flux is probably greater than the seafloor weathering flux since 100 Myr ago (Fig. 5e,f). However, we cannot say whether the absolute change in the continental weathering sink is greater than the absolute change in the seafloor weathering sink (Fig. 5i). The carbonate weathering flux at 100 Myr ago was 18–94% the modern flux (95% credible interval, shown in Fig. 5g).

Supplementary Fig. 4 shows posterior probability distributions for variables that can only be tentatively constrained. For example, the retrieval suggests the gradient relating deep-ocean temperatures to surface temperature, a_{grad} (see equation (12)), is $0.99^{+0.15}_{-0.12}$ (1σ), consistent with the linear regression in Fig. 8 (see Methods). The timescale for one ocean volume to circulate through the pore-space is ~0.6 Myr, which suggests extremely short circulation times (for example, ref. 30) are unlikely, but not excluded. The effective activation energy for seafloor basalt dissolution is probably between 53 and 97 kJ mol^{-1} (1σ), in agreement with the 92 ± 7 kJ mol^{-1} value derived by Coogan and Dosso[17], and consistent with the range reported in field studies[31]. The median value of our posterior distribution is considerably higher than experimentally derived activation energies[14], perhaps suggesting that short-term experiments do not accurately capture temperature dependence on geological timescales, although our posterior distribution is sufficiently broad that these experimental activation energies cannot be excluded. Supplementary Fig. 5 shows probability distributions for the remaining variables, which are all unconstrained (flat posterior distributions).

Bayesian analysis sensitivity tests. Error bars for geochemical proxies might underestimate the true uncertainties, so how robust are our results to different proxies? The large weatherability change and weak temperature dependence of continental

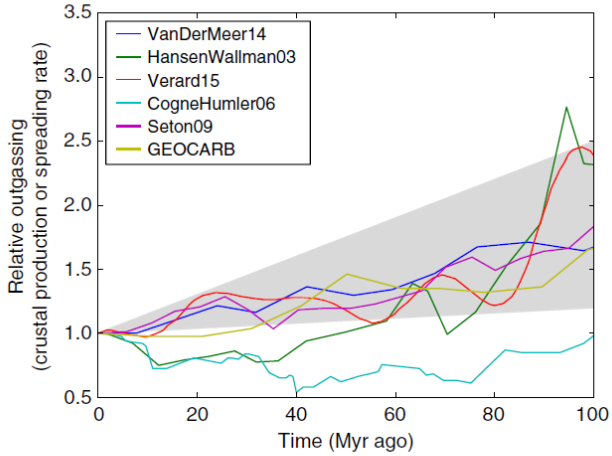

Figure 7 | Global outgassing reconstructions. Reconstructions of crustal production rates or spreading rates, relative to modern. These histories are assumed to reflect global outgassing histories. The studies listed in the legend are given in Supplementary Note 7. The grey region is the range of outgassing histories explored in our model.

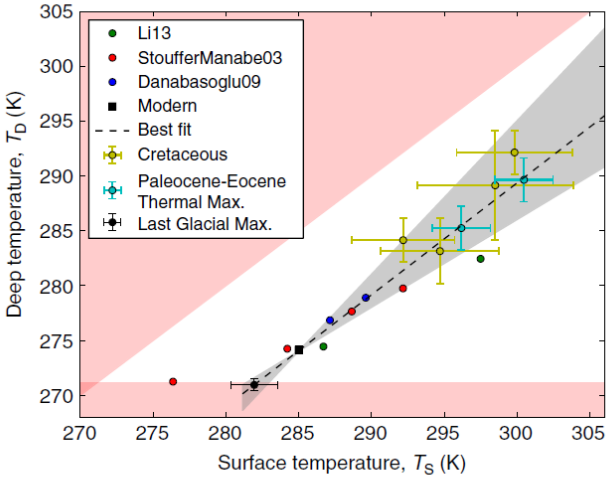

Figure 8 | Linear relationship between global mean surface temperature and deep-ocean temperature. Empirical relationship between deep-ocean temperatures and global mean surface temperatures, as determined by Global Circulation Model (GCM) outputs from the literature (coloured circles) and proxy data (coloured circles with error bars). The red regions are unphysical because the ocean is frozen or the deep ocean is warmer than the surface. The dotted line is the best fit to the proxies, $T_D = 1.02T_S - 16.67$, and the grey-shaded region is the range of T_D-T_S relationships considered in our model. See Supplementary Note 1 for full references, estimation of error bars, and further explanation.

weathering implied by our analysis do not depend on any single proxy. If the inverse analysis is repeated with the temperature, CO_2, pH, saturation state or seafloor weathering constraints individually omitted (equivalent to assuming we have no knowledge of these variables), then the posterior distributions for T_e and $1+W$ are largely unchanged (not shown). In fact, even if any two of those constraints are simultaneously omitted, the conclusions are unchanged. The posterior distributions for T_e and $1+W$ flatten only when three or more proxies are omitted.

In contrast, climate sensitivity results are less robust to proxies. If temperature constraints are omitted from the Bayesian analysis, then climate sensitivity is constrained to $\Delta T_{2x} = 4.5^{+2.1}_{-1.9}$ K, whereas if CO_2 constraints are omitted, then $\Delta T_{2x} = 3.7^{+1.5}_{-1.0}$ K. When both temperature and CO_2 proxy constraints are omitted, the posterior distribution for climate sensitivity becomes approximately flat. Thus, our conclusions regarding climate sensitivity are closely tied to temperature and pCO_2 proxies, as one might expect.

Discussion

Four important findings emerge. First, the e-folding temperature of continental weathering lies between 17 and 48 K (90% credible) compared to the generally assumed 5–15 K. Weak temperature sensitivity of continental weathering has been suggested in previous studies of the Cenozoic and Mesozoic[32], but here we have rigorously constrained the temperature dependence.

While laboratory experiments on silicate weathering show a strong temperature dependence, it is difficult to isolate the temperature dependence in field studies because temperature covaries with other variables that modulate weathering such as precipitation, vegetation, prior soil development and cation leaching[33]. In addition, the global silicate weathering flux is mixture of transport-limited and kinetically limited regimes, and so extrapolating from field studies to a global temperature dependence is challenging. Nonetheless, a growing literature shows weak correlation between silicate weathering rates and temperature and precipitation, but strong correlation with physical erosion, which is controlled by tectonic uplift[34–37]. In addition, reactive transport modelling reveals that weathering of granitic landscapes is mostly controlled by hydrological transport, not kinetics[38]. Hydrological modelling shows that the response of global silicate weathering rates to changes in temperature depends strongly on uplift, and that the overall temperature dependence is dominated by a weak, indirect runoff dependence[8].

Riebe *et al.*[39] used cosmonucleotides and mass balance arguments to infer long-term weathering rates for 42 diverse granitic landscapes. They found silicate weathering is predominantly transport limited, with an effective activation energy of only 14–24 kJ mol^{-1} (T_e = 28–48 K), consistent with our MCMC inversion. Our results thus support the notion that weathering is predominantly transport limited.

On long timescales, runoff rates could modulate erosion, so it is challenging to isolate climatic effects[5,40]. Nonetheless, a weaker silicate weathering feedback might suggest larger swings in temperature over Earth history, though extremes will be dampened by strongly temperature-dependent seafloor weathering and the direct CO_2 dependence of continental weathering.

The second important finding is that silicate rock weatherability at 100 Myr ago was considerably lower than the modern. Kump and Arthur[13] inferred Cenozoic weatherability through time by forcing a carbon cycle model with crustal production, exposed land area and organic burial from proxies. They found that to fit pCO_2 proxies, weatherability as defined here must increase by ~0.3 over the Cenozoic, or equivalently, $1+W = 0.53$ by linear extrapolation. In this study, the 1σ interval for $1+W$ extends from 0.3 to 0.58. Caves *et al.*[41] also calculated the time evolution of weatherability across the Cenozoic and found a secular increase consistent with this study.

Of several possible explanations for weatherability increases, most obviously, mid-Cretaceous sea-level was 85–270 m higher than today[42]. This implies that the continental land area was 10–27% less than modern (Fig. 3.3 in ref. 43). However, given that weatherability may be weaker than linearly related to area[23] and the posterior distribution for the weatherability change (Fig. 6), it is unlikely that sea-level variation alone can account for the required change in weatherability over the last 100 Myr ago.

Weatherability can also increase with continental relief. Greater uplift may result in more physical erosion and enhanced chemical weathering[8,9]. If mid-Cretaceous relief was considerably lower than modern relief, this could explain the required change in weatherability. Berner[23] used $^{87}Sr/^{86}Sr$ ratios and terrigeneous sediment abundances to conclude that continental relief in the mid-Cretaceous was ~60–80% modern (Fig. 2.2 in ref. 23). However, the conventional interpretation of the Sr isotope record has recently been challenged[17,44]. In particular, the Cenozoic $^{87}Sr/^{86}Sr$ record can be reproduced by a simple model of temperature-dependent seafloor weathering so that no changes in continental weatherability are required[17]. Nonetheless, if these nominal changes in relief are accepted, then the combined change in weatherability from sea-level variation and reduced uplift is 0.44–0.72, which could easily explain the weatherability change inferred from our Bayesian analysis.

Changes in lithology, palaeogeography and biology also have an impact on weatherability. Basaltic weathering contributes one-third of the global silicate weathering flux despite only constituting ~10% of the global silicate area[45]. Reconstructions of basaltic area through time vary by methodology[46,47], but recent analyses suggest a basaltic area at 100 Myr ago approximately double the modern area[10], seemingly implying that silicate weatherability was ~30% greater than today. This change has opposite sign to the change implied by our retrieval, suggesting that either the increase in relief since 100 Myr ago compensated for lithology changes, or basaltic weatherability has been overestimated[48]. Palaeogeography changes are one of the primary controls on weathering for much of the Phanerozoic[49], but for the last 100 Myr ago the effect of palaeogeography on weathering fluxes has been relatively muted (Fig. 8 in ref. 49 and Fig. 4 in ref. 50). Biologically mediated changes in weatherability due to the proliferation of angiosperms[51] or the emergence of ectomycorrhizal fungi[11] could also have contributed to the weatherability increase. However, both biological innovations occurred around 100 Myr ago, suggesting that they may not be important for the relevant time span. Consequently, the most probable contributors to the required increase in weatherability over the last 100 Myr ago are lower sea levels and enhanced uplift.

Our third key finding is that average Earth system climate sensitivity since 100 Myr ago is 3.7–7.5 K for a doubling of pCO_2 (90% credible), which is much larger than the IPCC[28] range, 1.5–4.5 K. Our result is broadly consistent with previous estimates of Earth system climate sensitivity based on palaeoclimate data[52,53], and supports the view that the long-term climate sensitivity of the Earth system is greater than the fast-feedback Charnay sensitivity captured by Global Circulation Models (GCMs). In addition, high climate sensitivity could help explain why extremely high pCO_2 (for example, 4,000 p.p.m.) levels are required to reproduce observed Cretaceous equator-to-pole temperature gradients in GCMs[54].

A caveat is that we have neglected other greenhouse gases (GHGs), which could lead to overestimating climate sensitivity. Indeed, Earth system models suggest that other GHGs may have contributed significantly (2–3 K) to Cretaceous and Eocene warmth[55]. However, this increase in GHG abundances is largely a vegetation response to warmer temperatures, and GHG feedbacks such as this are already implicitly captured in our overall pCO_2-dependent climate sensitivity. In principle, the omission of methane forcings could affect our results, but the changes in methane flux would have to be substantial to reduce our inferred climate sensitivity. The warming from other GHGs is only ~0.5 K from changes in boundary conditions between the Early Eocene and Late Cretaceous[55].

Fourth, although the continental weathering flux was probably larger than the seafloor weathering flux since 100 Myr ago (Fig. 5e,f), it is difficult to directly compare the importance of the two feedbacks. The temperature dependence of continental weathering is likely weak, but both the temperature dependence of seafloor weathering and the direct pCO_2 dependence of continental weathering are poorly constrained (Fig. 6; Supplementary Fig. 4). Consequently, we cannot say whether the absolute change in continental weathering since 100 Myr ago is greater or less than the change in seafloor weathering (Fig. 5i). In addition, conclusions regarding low-temperature sensitivity of continental weathering, weatherability changes and climate sensitivity hold irrespective of assumptions about seafloor weathering; these conclusions arise primarily from the fit to temperature, pCO_2, saturation state and pH proxies.

With that said, the temperature dependence of continental weathering ($E_a = 20^{+10}_{-5}$ kJ mol^{-1}) is weak compared to seafloor weathering ($E_{bas} = 75^{+22}_{-21}$ kJ mol^{-1}), and a secular decline in spreading rates over Earth history would imply more dominant seafloor weathering fluxes at earlier times since continental weathering has no direct spreading rate dependence. Taken together, these observations suggest that seafloor weathering feedback may have been an important feedback at earlier times in Earth's history.

All of our conclusions—to varying degrees—depend on the fidelity of proxies. We have attempted to minimize this source of error by adopting the broadest possible range of proxy estimates for pCO_2, temperature, saturation state, pH and the seafloor weathering sink (see Methods). The sensitivity analysis in the results section shows that the low-temperature sensitivity of continental weathering and the large weatherability increase since 100 Myr ago are robust. Even if current estimates of two proxies are highly uncertain or flawed, the remaining proxies tell a mutually consistent story on continental weathering. However, the same is not true for climate sensitivity. If proxies overestimate global mean temperatures in the Cretaceous, then Earth system climate sensitivity may be lower than our inverse analysis suggests. The same is true if real Cretaceous pCO_2 was much higher than proxy estimates.

To some extent, conclusions are sensitive to the mechanistic assumptions in our forward model. For example, the simple functional forms adopted for many biogeochemical fluxes and the reduction of spatially heterogeneous processes to zeroth order, globally averaged equations could influence our results. However, wherever possible, we used parameterizations that have a fundamental physical basis, such as the logarithmic dependence of climate on pCO_2 and the Arrhenius-style temperature dependence of weathering. In instances where the physical basis is uncertain, we adopted generalized power laws with widely varying exponents to describe relationships between variables, and introduced free parameters to account for unknown processes. Column 2 of Fig. 6, and Supplementary Note 6 explore the sensitivity of our results to different continental weathering parameterizations. We find that none of the key conclusions are changed by using different functional forms. Nonetheless, our quantitative estimates of key variables could be refined by better mechanistic understanding carbon cycle relationships. Specifically, the magnitude of the weatherability increase since 100 Myr ago is moderately sensitive to the choice of continental weathering function (Fig. 6; Supplementary Note 6).

Another potential limitation is that we are imposing linear trends in some model parameters, thereby potentially underfitting the data and underestimating the uncertainties in retrieved parameters. In Supplementary Note 5, we repeat our analysis with a simplified data set to show that our conclusions are robust to these linearity assumptions. Supplementary Note 4 also shows that possible changes in K-feldspar uptake[16] in the seafloor do not change our qualitative conclusions.

In summary, we presented a new geological carbon cycle model, which includes ocean chemistry and the kinetics of seafloor weathering, and applied it to the last 100 Myr ago. Model outputs were compared to proxies for temperature, atmospheric CO_2, seafloor carbonate content, ocean pH and ocean saturation state. A MCMC inversion rigorously constrained carbon cycle parameters given these data. Assuming that proxies are accurate and that our forward model accurately parameterizes the carbon cycle, we report five key conclusions. First, the temperature dependence of continental silicate weathering is considerably weaker than commonly assumed. Most carbon cycle models use an effective activation energy to $\sim$50–100 kJ mol^{-1}, whereas our results imply $E_a = 20^{+10}_{-5}$ kJ mol^{-1}, which suggests that continental silicate weathering is less effective at buffering climate against changes in outgassing or insolation. Second, mid-Cretaceous continental weatherability was 30–58% of modern weatherability (1σ), although the precise magnitude of the change is sensitive to the functional form adopted for continental weathering. This increase in weatherability since 100 Myr ago is best explained by continental uplift and sea-level decline. Third, the average Earth system climate sensitivity is $\Delta T_{2x} = 5.6^{+1.3}_{-1.2}$ K for a CO_2 doubling (1σ). This is considerably higher than fast-feedback estimates for the modern climate, and could explain why extremely high pCO_2 levels are required to reproduce greenhouse climates in GCMs. This result is derived assuming methane variations are fully captured by temperature-dependent feedbacks, and it is sensitive to uncertain temperature proxies. Fourth, Cretaceous outgassing was unlikely ($\sim$9% probability) to be greater than double modern outgassing. Finally, continental weathering is probably the dominant carbon sink throughout the last 100 Myr ago, and introducing seafloor weathering into our model has a relatively small effect on the inverse modelling results. However, the strong temperature sensitivity and spreading rate dependence of seafloor weathering implies that it could have been a dominant carbon sink earlier in Earth history.

Methods

Model description. Python code for the model is available open source from the first author's website. The time evolution of the carbon cycle is described by the following set of equations:

$$\begin{aligned}
\frac{dC_O}{dt} &= \frac{-J(C_O - C_P)}{M_O} + \frac{F_{out}}{M_O} + \frac{F_{carb}}{M_O} - \frac{P_{ocean}}{M_O} \\
\frac{dA_O}{dt} &= \frac{-J(A_O - A_P)}{M_O} + 2\frac{F_{sil}}{M_O} + 2\frac{F_{carb}}{M_O} - 2\frac{P_{ocean}}{M_O} \\
\frac{dC_P}{dt} &= \frac{J(C_O - C_P)}{M_P} - \frac{P_{pore}}{M_P} \\
\frac{dA_P}{dt} &= \frac{J(A_O - A_P)}{M_P} + 2\frac{F_{diss}}{M_P} - 2\frac{P_{pore}}{M_P}
\end{aligned} \tag{6}$$

Here C_O and C_P are the concentrations of carbon (Tmol C kg^{-1}) in the atmosphere–ocean and pore-space, respectively. The carbon concentration in the pore-space is equivalent to the dissolved inorganic carbon (DIC) abundance, $C_P = DIC_P$, whereas carbon in the atmosphere–ocean reservoir is equal to marine DIC plus atmospheric carbon, $C_O = DIC_O + pCO_2 \times s$, where s is a scaling factor equal to the ratio of total number of moles in the atmosphere divided by the mass of the ocean, $s = (1.8\times10^{20})/M_O$. Similarly, $A_O = ALK_O$ and $A_P = ALK_P$ are the carbonate alkalinities in the atmosphere–ocean and pore-space, respectively (Tmol eq kg^{-1}). The global outgassing flux (Tmol C per year) is specified by F_{out}, whereas the rates of continental silicate weathering and carbonate weathering are F_{sil} and F_{carb}, respectively (Tmol C per year). Seafloor weathering from basalt dissolution (Tmol eq per year) is F_{diss}, and the precipitation flux of carbonates (Tmol C per year) in the ocean and pore-space are given by P_{ocean} and P_{pore}, respectively. The mass of the ocean and the pore space is given by $M_O = 1.35\times10^{21}$ kg and $M_P = 1.35\times10^{19}$ kg, respectively[20]. We assume a range for J of $1.4\times10^{15} - 6.8\times10^{16}$ kg per year, which implies the time to circulate one ocean volume through the pore-space is between $\tau = 20$ and $\tau = 1{,}000$ kyr, consistent with estimates from Johnson and Pruis[56] and Caldeira[20].

A common simplification in carbon cycle modelling is to neglect carbonate weathering[15,22,24]. This is justified on the grounds that carbonate weathering does not constitute a net carbon source. On long timescales, the carbon consumption from silicate and seafloor weathering must balance carbon outgassing (plus any imbalance in organic weathering and burial), and this balance determines atmospheric CO_2 and climate. However, the saturation state of the ocean is affected by carbonate weathering, and so we include carbonate weathering to model ocean chemistry. We do not track crustal or mantle reservoirs, and the atmospheric reservoir of CO_2 is set by equilibrium partitioning with the ocean (see below). Because we are not tracking fluxes between the atmosphere and ocean, continental silicate weathering is not a carbon source or sink; the release of cations (alkalinity) from silicate dissolution does not directly add carbon to the combined atmosphere–ocean system. Instead, the cations consume carbon indirectly when they later precipitate as marine carbonates.

There is no surface ocean box in our model. This is because we are only interested in the changes in properties of the bulk ocean, which are determined by varying boundary conditions not by the deep-surface partitioning. In addition, we are focused on timescales $>10^6$ years, and so the dynamics of deep-surface ocean mixing are unimportant. If we were to partition the ocean into surface and deep, the main difference would be differential temperature dependence of carbon speciation. We also do not include organic carbon weathering and burial. This is justifiable because the negative feedback from oxidative weathering ensures they are approximately balanced[57]. Empirically, the carbon isotope record reveals that the organic burial fraction has changed by only $\sim$10% over the last 100 Myr ago[58]. Consequently, the change in the organic burial flux is likely modest and so the omission of organic carbon will not affect our conclusions.

The functional forms for the flux terms not already described in the main text are presented below.

Continental silicate weathering. The continental weathering parameterization was described in the main text except for the coefficient α in equation (2). This coefficient is assumed to be 0.2–0.5 (ref. 59). Strictly speaking, soil pCO_2 should replace atmospheric pCO_2 in equation (2) because soil pCO_2 determines soil pH, and therefore silicate dissolution rates. However, if modest changes in maximum biological productivity are allowed, then the range of CO_2 dependencies from the term $\left(pCO_2/pCO_2^{mod}\right)^{\alpha}$, with α varying from 0.2 to 0.5, is broadly equivalent to replacing atmospheric pCO_2 with soil pCO_2 (ref. 60; see Supplementary Fig. 6). Consequently, we retain atmospheric pCO_2 and pCO_2^{mod} in equation (2). To test the sensitivity of our results to weathering parameterizations, in addition to the pCO_2 power-law dependence in equation (2), we also consider a Michaelis–Menten law in the main text (see results).

The range adopted for relative Cretaceous weatherability, $1 + W$, is based on literature estimates[10,23,43,47,49] of how external factors may have affected weatherability, and extending the range in either direction does not markedly change our results. The weatherability factor, ω, can also be interpreted as the sensitivity of the weathering response to changes in pCO_2 and temperature. For example, an increase in ω implies that an increase in surface temperature will result in a larger change in the continental weathering flux, F_{sil}.

Continental carbonate weathering. We assume that carbonate weathering has the same functional form as silicate weathering, except for an additional dimensionless multiplicative factor, ω_{carb}, to allow for the possibility that carbonate weathering is subject to different temperature dependence, CO_2 dependence and weatherability factors:

$$F_{carb} = \omega_{carb}\ \omega F_{carb}^{mod}\left(\frac{pCO_2}{pCO_2^{mod}}\right)^{\alpha} \exp(\Delta T_S/T_e) \tag{7}$$

The carbonate weatherability factor is defined as follows:

$$\omega_{carb} = (1 + C_{WF}t/100\,\text{Myr}) \tag{8}$$

We assume a range of values for C_{WF} from -0.9 to 1.5 to allow for large differences between carbonate weathering and silicate weathering. For example, carbonates may have a lower effective activation energy compared to silicates because carbonate weathering is sensitive to runoff, whereas silicate weathering is sensitive to both runoff and a kinetic temperature effect[7,25]. Carbonate weathering may also have a different response to changes in uplift[23], or varying fluxes due to changes in the crustal reservoir of carbonates. It should be noted that changes in carbonate weathering only affect saturation state; the changes in CO_2, temperature and ocean pH due to carbonate weathering changes are negligible. This is because—as explained above—temperature and CO_2 are set by the balance between outgassing and silicate weathering plus seafloor weathering. Consequently, any conclusions drawn about those variables are unaffected by our formulation for carbonate weathering.

Climate model. To relate ΔT_S to pCO_2, we adopt the following climate model:

$$\Delta T_S = \Delta T_{2x}\left(\frac{ln\left(pCO_2/pCO_2^{mod}\right)}{\ln(2)} - \frac{t}{228\,\text{Myr}}\right) + \Delta P\left(\frac{t}{100\,\text{Myr}}\right) \tag{9}$$

Here ΔT_{2x} is the climate sensitivity parameter, ΔP is a palaeogeography parameter and the second term accounts for solar luminosity changes (Supplementary Note 2). We divide by ln(2) so that ΔT_{2x} has conventional units of Kelvin warming per CO_2

doubling. Supplementary Fig. 9 compares different climate parameterizations and GCM results from the literature and illustrates why equation (9) is suitable. The parameter ΔP is the secular cooling (in K) since the mid-Cretaceous due to palaeogeography changes. A review of GCM studies concluded that $\Delta P = 0$–3.0 K (ref. 52). We assume $\Delta P = 0$–5.0 K to be conservative, noting that some models suggest 5 K of warming from an Eocene continental configuration[61].

Outgassing. Estimates of Cenozoic and Mesozoic outgassing histories vary substantially. Figure 7 shows a variety of outgassing reconstructions from the literature expressed as crustal production or spreading rates, which are assumed to covary with global outgassing. Generally, these reconstructions suggest that global outgassing at 100 Ma was between 1.5x and 2.5x modern outgassing. This conclusion is based on several independent lines of evidence including reconstructions of plate extent and plate motion, seismic imaging of subducted plates, and reconstructions of seafloor age and depth (see Supplementary Note 7 for a summary of outgassing estimates with references). The outlying reconstruction in Figure 7 (aqua curve) is disputed because it uses a contentious crustal age distribution[42].

For simplicity, we assume a linear global outgassing history:

$$F_{\mathrm{out}} = F_{\mathrm{out}}^{\mathrm{mod}}(1 + Vt/100\ \mathrm{Myr}) \tag{10}$$

Here $F_{\mathrm{out}}^{\mathrm{mod}}$ is modern outgassing (Tmol C per year), t is time (in Myr ago) and V is a dimensionless scaling factor. Using crustal production or spreading rate as a proxy for global outgassing is a simplification because it ignores subaerial metamorphism and hot spot volcanism (for example, ref. 62). Given the uncertainty in these other contributions, we adopt a very broad range of outgassing histories since 100 Myr ago by assuming $V = 0.2$–1.5. Thus, we allow mid-Cretaceous outgassing to range from 20 to 150% greater than modern.

Basalt dissolution and seafloor weathering. The temperature dependence of seafloor weathering uses the following Arrhenius-style expression[17]:

$$F_{\mathrm{diss}} \propto \exp\left(-E_{\mathrm{bas}}/RT_{\mathrm{pore}}\right) \tag{11}$$

Here E_{bas} (kJ mol^{-1}) is the effective activation energy of basalt dissolution, R is the universal gas constant and T_{pore} is the pore-space temperature. Coogan and Dosso[17] reported an empirically derived activation energy of $E_{\mathrm{bas}} = 92 \pm 7$ kJ mol^{-1}, whereas experimental studies[14,31] of basalt dissolution suggest activation energies between 42 and 109 kJ mol^{-1}. We adopt a range of activation energies from $E_{\mathrm{bas}} = 40$ to110 kJ mol^{-1}.

Because Cenozoic and Mesozoic pore-space temperatures are controlled by deep-ocean temperature[17], we must determine the link between global mean surface temperatures and deep-ocean temperatures. Figure 8 shows mean global surface temperatures plotted against deep-ocean temperatures using output from fully coupled atmosphere–ocean GCMs and palaeoclimate proxy data (see Supplementary Note 1 for details). The relationship is described by an empirical linear fit:

$$T_{\mathrm{D}} = a_{\mathrm{grad}} T_{\mathrm{S}} + b_{\mathrm{int}} \tag{12}$$

Here T_{D} (K) is the mean deep-ocean temperature and T_{S} (K) is the mean surface temperature. The best-fit gradient and intercept are $a_{\mathrm{grad}} = 1.02$ and $b_{\mathrm{int}} = -16.7$, respectively. However, we assume a broad gradient range $a_{\mathrm{grad}} = 0.8$–1.4, whereas the intercept, $b_{\mathrm{int}} = 274.037 - a_{\mathrm{grad}} \times 285$ is chosen to ensure consistency with modern conditions. Figure 8 shows the range of possible $T_{\mathrm{D}} \propto T_{\mathrm{S}}$ relationships used in this study.

Our parameterization of deep-ocean temperature improves upon Brady and Gíslason[14] because ours is based on an ensemble of GCM results and globally averaged palaeoclimate proxies rather than a single climate model. In addition, Brady and Gíslason[14] overestimated the dependence of deep-ocean temperature on surface climate because their parameterization is based on a single near-equatorial latitude of 6.7°. The relationship between globally averaged abyssal temperatures and surface climate is more muted than the relationship with equatorial abyssal temperatures. This can be seen in our Fig. 8 and in Fig. 12 of Manabe and Bryan[63], despite the model of the latter being the basis for the Brady and Gíslason[14] parameterization.

To relate the pore-space temperature to the deep-ocean temperature, we adopt empirical results[17]. Oxygen isotopes indicate that for both the Cenozoic and Mesozoic, the mean pore-space temperature of seafloor carbonate precipitation is consistently $\sim$9 K warmer than the minimum temperature of seafloor carbonate precipitation (deep-ocean temperatures). Consequently, we assume $T_{\mathrm{pore}} = T_{\mathrm{D}} + 9$. This modification has a very minor effect on the model output because it is largely the change in temperature, and not its absolute value, that controls variations in the seafloor weathering flux.

Quantifying the pH dependence of seafloor weathering is more challenging because most experiments either fail to separate the pH and direct CO_2 effect[14], focus on individual minerals rather than whole-rock dissolution rates[64,65], or do not explore the full pH range relevant to seafloor weathering[66].

Gudbrandsson *et al.*[67] measure whole-rock crystalline basalt dissolution rates for $2 < \mathrm{pH} < 11$. They find that Ca release is a U-shape function of pH (their Fig. 8), where the minimum of the 'U' at 25 °C is somewhere between pH = 7 and pH = 9, depending on the assumptions made about the reactive surface area (experimental results are sparse and so are fitted with an analytic model of dissolution). Given the uncertainty in this dissolution curve, it is difficult to predict the sign of the dissolution change for a modest change in ocean pH. For example, a decline in pH from 8.2 to 7.4—which is approximately the change from the modern ocean to mid-Cretaceous—predicts a 20% decrease in Ca release according to one Gudbrandsson *et al.*[67], their Fig. 8f fit, and a 7% increase in Ca release according to the alternative Gudbrandsson *et al.*[67], their Fig. 8e fit. Either way, the change in dissolution is minor, and so a possible first order approximation is to assume basalt dissolution on the seafloor is independent of pH for the Mesozoic and Cenozoic.

However, the Gudbrandsson *et al.*[67] experiments may not accurately capture the pH dependence of seafloor weathering because they were not done in seawater and did not include carbon chemistry. Some experimental studies[65,68] show that olivine dissolution is CO_2-dependent at high pH values, ostensibly because abundant carbonate ions protect Si–O bonds, thereby decreasing dissolution with increasing DIC. In contrast, Golubev *et al.*[64] studied the effect of CO_2 on dissolution rates for a range of pH values and found that forsterite, diopside and hornblende do not have CO_2-dependent dissolution rates at any pH. Unfortunately, however, Golubev *et al.*[64] did not consider plagioclase, so their results cannot easily be extrapolated to the basaltic seafloor. Wolff-Boenisch *et al.*[66] showed that the CO_2 dependence of crystalline basalt is independent of CO_2 at low pH levels, but did not repeat the experiment at high pH values.

We allow for the possibility of pH dependence by setting the rate of dissolution proportional to $[\mathrm{H}^+]_{\mathrm{p}}^{\gamma}$, where γ varies from 0 (no pH dependence) to 0.5 (strong pH dependence dominated by basaltic glass dissolution):

$$F_{\mathrm{diss}} = k_{\mathrm{diss}}\left(\frac{F_{\mathrm{out}}}{F_{\mathrm{out}}^{\mathrm{mod}}}\right)^{\beta} \exp\left(-E_{\mathrm{bas}}/RT_{\mathrm{pore}}\right)\left(\frac{[\mathrm{H}^+]_{\mathrm{p}}}{[\mathrm{H}^+]_{\mathrm{p}}^{\mathrm{mod}}}\right)^{\gamma} \tag{13}$$

Here k_{diss} is a proportionality constant chosen to match the modern flux, $[\mathrm{H}^+]_{\mathrm{p}}$ is the hydrogen ion molality in the pore-space and $[\mathrm{H}^+]_{\mathrm{p}}^{\mathrm{mod}}$ is the modern molality. Because dissolution is dependent on crustal production and crustal production is proportional to global outgassing, we assume dissolution is dependent on outgassing with some unknown power–law relationship, defined by $\beta = 0$–1.

Better knowledge of the pH dependence, temperature dependence and CO_2 dependence of basalt dissolution would improve our constraints on the carbon cycle. Specifically, whole-rock dissolution experiments performed at high pH that separate the effects of pH and DIC would allow for more precise parameterizations of seafloor weathering.

Precipitation fluxes. The precipitation flux of marine carbonates, P_{ocean}, is the sum of the fluxes of shelf carbonates, P_{shelf}, and pelagic carbonates, P_{pelagic}:

$$P_{\mathrm{ocean}} = P_{\mathrm{shelf}} + P_{\mathrm{pelagic}} \tag{14}$$

Following Ridgwell[69], the shelf precipitation flux is given by:

$$P_{\mathrm{shelf}} = k_{\mathrm{shelf}}\frac{A_{\mathrm{shelf}}}{A_{\mathrm{shelf}}^{\mathrm{mod}}}(\Omega_{\mathrm{O}} - 1)^{n} \tag{15}$$

Here Ω_{O} is the saturation state of the ocean (defined below by equation (20)), A_{shelf} is the area of continental shelf available for carbonate precipitation, with $A_{\mathrm{shelf}}^{\mathrm{mod}}$ denoting the modern shelf area, and k_{shelf} is a proportionality constant. Shelf area is approximated by a polynomial fit (Supplementary Fig. 7) to reconstructed tropical shelf area from Walker *et al.*[70]. The exponent n defines the proportionality between the saturation state of the ocean and the precipitation flux. This is typically taken to be 1.7 based on the latitudinal dependence of carbonate accumulation and saturation state[71]. Rather than consider calcite and aragonite precipitation separately, we instead allow n to vary widely from 1.0 to 2.5.

The pelagic carbonate flux depends on the calcite compensation depth (CCD), Z_{CCD} (km), which can be calculated using the following equation[72]:

$$Z_{\mathrm{CCD}} = 4 + 6.25\ln(\Omega_{\mathrm{O}}) \tag{16}$$

Pelagic carbonate deposition is proportional to the fractional area above the CCD, $f(Z_{\mathrm{CCD}})$, which can be approximated by an exponential fit to hypsometric data[73]:

$$P_{\mathrm{pelagic}} \propto f(Z_{\mathrm{CCD}}) = 0.07\exp(Z_{\mathrm{CCD}}/2.2) \tag{17}$$

Equations (14–17) can then be combined to give the total ocean precipitation flux:

$$P_{\mathrm{ocean}} = k_{\mathrm{shelf}}\frac{A_{\mathrm{shelf}}}{A_{\mathrm{shelf}}^{\mathrm{mod}}}(\Omega_{\mathrm{O}} - 1)^{n} + k_{\mathrm{pelagic}}\Omega_{\mathrm{O}}^{2.84} \tag{18}$$

The proportionality constants k_{shelf} and k_{pelagic} are chosen to reproduce the modern partitioning between shelf and pelagic carbonates (see below). Here the precise functional form of equation (18) only matters for determining ocean saturation state; carbon fluxes, pCO_2 and temperatures are unaffected.

The pore-space carbonate precipitation flux is analogous to shelf precipitation except that there is no area dependence:

$$P_{\mathrm{pore}} = k_{\mathrm{pore}}(\Omega_{\mathrm{P}} - 1)^{n} \tag{19}$$

Here Ω_{P} is the saturation state of the pore-space and k_{pore} is a proportionality constant chosen to reproduce the modern flux. The exponent n is the same as for shelf precipitation. Repeating the inverse analysis allowing different exponents for

shelf and seafloor carbonate precipitation does not change results substantially (not shown).

Finally, the saturation state of the ocean and the pore-space are defined as follows:

$$\Omega_O = \frac{[Ca^{2+}][CO_3^{2-}]_O}{K_{sp}} \text{ and } \Omega_P = \frac{[Ca^{2+}][CO_3^{2-}]_P}{K_{sp}} \quad (20)$$

Here $K_{sp} = K_{sp}(T)$ is the temperature-dependent solubility product from Pilson[74]. Supplementary Methods explain how the solubility product is calculated.

Ocean chemistry. Alkalinity and DIC have the following standard definitions in our model, where ALK is often referred to as 'carbonate alkalinity' in the literature:

$$\begin{aligned} DIC &= [CO_3^{2-}] + [HCO_3^-] + [CO_2aq] \\ ALK &= 2[CO_3^{2-}] + [HCO_3^-] \end{aligned} \quad (21)$$

Given carbon and alkalinity in the atmosphere–ocean (C_O, ALK_O) or the pore-space (C_P, ALK_P), we can calculate ocean chemistry using the following set of equations[74]:

$$[CO_2aq] = pCO_2 \times H_{CO_2} \quad (22)$$

$$[HCO_3^-] = \frac{[CO_2aq] \times K_1^*}{[H^+]} \quad (23)$$

$$[CO_3^{2-}] = \frac{[HCO_3^-] \times K_2^*}{[H^+]} \quad (24)$$

$$\frac{ALK}{K_1^* K_2^*}\left(1 + \frac{s}{H_{CO_2}}\right)[H^+]^2 + \frac{(ALK - C)}{K_2^*}[H^+] + (ALK - 2C) = 0 \quad (25)$$

$$pH = -\log_{10}([H^+]) \quad (26)$$

Here H_{CO2} is the Henry's law constant for CO_2, $[CO_2aq]$ is the sum of the concentrations of free CO_2 and H_2CO_3, and K_1^* and K_2^* are the first and second apparent dissociation constants of carbonic acid, respectively. Temperature-dependent expressions for these constants can be found in Supplementary Methods. The set of equations described above must be solved separately for the ocean and the pore-space by substituting the generic carbon concentration and alkalinity (C, ALK) for (C_O, ALK_O) and (C_P, ALK_P), respectively. The scaling factor, s, is defined above with respect to equation (6). Equation (25) is derived by combining equations (21), (23) and (24) (Supplementary Methods). This quadratic can be solved to find $[H^+]$. Once this is known, then equations (22), (23) and (24) define the remaining carbon chemistry variables.

Rather than attempt to model the complexities of calcium and magnesium cycling in our model, we impose observed changes in $[Ca^{2+}]$ abundances from seawater inclusions[75]. In our model, changes in alkalinity are driven purely by weathering and carbonate precipitation. Thus, by imposing $[Ca^{2+}]$ variations, we are effectively assuming that observed $[Ca^{2+}]$ changes are offset by changes in other cations and anions, such that they have no direct effect on alkalinity, for example, magnesium exchange with the seafloor. We fit a third-order polynomial to the $[Ca^{2+}]$ reconstruction in Tyrrell and Zeebe[75] to achieve the fast computation times necessary for Bayesian inversion (Supplementary Fig. 8).

Initial conditions and numerical solution. Table 2 shows all the initial values assumed in our model or ranges for variables that are uncertain. All other initial values are fully determined by the variables in this table.

The system of differential equations describing the carbon cycle (equation (6)) was solved in Python using the ordinary differential equation integrator in the *SciPy* module. Model outputs were compared with equivalent steady-state calculations and were always in agreement to within a few per cent or better (Supplementary Note 3). This validates the numerical integration and implies that the time-dependent model is always in quasi steady state. In addition, the integrated flux imbalance over 100 Myr ago equals the change in the carbon reservoirs to within ~2% or better in every case, confirming that mass is being conserved in our model.

Proxies. The geochemical proxies plotted in Figs 2–5, and Supplementary Figs 2, 15 and 16 are described in Supplementary Methods. For each variable, we searched the literature for the broadest possible range of proxy estimates. Proxies were typically binned into 10 Myr ago intervals, and for each interval the best estimate was taken to be the midpoint of the full range of proxy estimates, while the 1σ uncertainty in the best estimate spanned the full range (Supplementary Figs 10–13). This conservative approach helps ensure that our conclusions are robust to uncertainties in different proxy methods.

Data availability. The binned proxy data used as inputs for this analysis along with the carbon cycle model code are available on the website of the first author. www.krisstott.com

References

1. Berner, R. A. & Caldeira, K. The need for mass balance and feedback in the geochemical carbon cycle. *Geology* **25**, 955–956 (1997).
2. Walker, J. C., Hays, P. & Kasting, J. F. A negative feedback mechanism for the long-term stabilization of Earth's surface temperature. *J. Geophys. Res. Oceans* **86**, 9776–9782 (1981).
3. Berner, R. A. & Kothavala, Z. GEOCARB III: a revised model of atmospheric CO_2 over Phanerozoic time. *Am. J. Sci.* **301**, 182–204 (2001).
4. Kump, L. R., Kasting, J. F. & Crane, R. G. *The Earth System* 3rd edn (Prentice Hall PTR, 2010).
5. Gaillardet, J., Dupré, B., Louvat, P. & Allegre, C. Global silicate weathering and CO_2 consumption rates deduced from the chemistry of large rivers. *Chem. Geol.* **159**, 3–30 (1999).
6. Huh, Y. & Edmond, J. M. The fluvial geochemistry of the rivers of Eastern Siberia: III. Tributaries of the Lena and Anabar draining the basement terrain of the Siberian Craton and the Trans-Baikal Highlands. *Geochim. Cosmochim. Acta* **63**, 967–987 (1999).
7. Francois, L. M. & Walker, J. Modelling the Phanerozoic carbon cycle and climate: constraints from the '7Sr/' rSr isotopic ratio of seawater. *Am. J. Sci.* **292**, 135 (1992).
8. Maher, K. & Chamberlain, C. Hydrologic regulation of chemical weathering and the geologic carbon cycle. *Science* **343**, 1502–1504 (2014).
9. Raymo, M. & Ruddiman, W. F. Tectonic forcing of late Cenozoic climate. *Nature* **359**, 117–122 (1992).
10. Mills, B., Daines, S. J. & Lenton, T. M. Changing tectonic controls on the long-term carbon cycle from Mesozoic to present. *Geochem. Geophys. Geosyst.* **15**, 4866–4884 (2014).
11. Taylor, L., Banwart, S., Leake, J. & Beerling, D. J. Modeling the evolutionary rise of ectomycorrhiza on sub-surface weathering environments and the geochemical carbon cycle. *Am. J. Sci.* **311**, 369–403 (2011).
12. Walker, J. C. *Biogeochemistry of Global Change* 3–28 (Springer, 1993).
13. Kump, L. R. & Arthur, M. A. *Tectonic Uplift and Climate Change*. (ed. Ruddiman, W.) 399–426 (Plenum Publishing, 1997).
14. Brady, P. V. & Gíslason, S. R. Seafloor weathering controls on atmospheric CO_2 and global climate. *Geochim. Cosmochim. Acta* **61**, 965–973 (1997).
15. Sleep, N. H. & Zahnle, K. Carbon dioxide cycling and implications for climate on ancient Earth. *J. Geophys. Res. Planets* **106**, 1373–1399 (2001).
16. Coogan, L. A. & Gillis, K. M. Evidence that low-temperature oceanic hydrothermal systems play an important role in the silicate-carbonate weathering cycle and long-term climate regulation. *Geochem. Geophys. Geosys.* **14**, 1771–1786 (2013).
17. Coogan, L. A. & Dosso, S. E. Alteration of ocean crust provides a strong temperature dependent feedback on the geological carbon cycle and is a primary driver of the Sr-isotopic composition of seawater. *Earth Planet. Sci. Lett.* **415**, 38–46 (2015).
18. Gillis, K. & Coogan, L. Secular variation in carbon uptake into the ocean crust. *Earth. Planet. Sci. Lett.* **302**, 385–392 (2011).
19. Alt, J. C. & Teagle, D. A. The uptake of carbon during alteration of ocean crust. *Geochim. Cosmochim. Acta* **63**, 1527–1535 (1999).
20. Caldeira, K. Long-term control of atmospheric carbon dioxide; low-temperature seafloor alteration or terrestrial silicate-rock weathering? *Am. J. Sci.* **295**, 1077–1114 (1995).
21. Coogan, L. A., Parrish, R. R. & Roberts, N. M. Early hydrothermal carbon uptake by the upper oceanic crust: insight from *in situ* U-Pb dating. *Geology* **44**, 147–150 (2016).
22. Foley, B. J. The role of plate tectonic-climate coupling and exposed land area in the development of habitable climates on rocky planets. *Astrophys. J.* **812**, 36 (2015).
23. Berner, R. A. *The Phanerozoic Carbon Cycle: CO_2 and O_2* (Oxford Univ. Press, 2004).
24. Abbot, D. S., Cowan, N. B. & Ciesla, F. J. Indication of insensitivity of planetary weathering behavior and habitable zone to surface land fraction. *Astrophys. J.* **756**, 178 (2012).
25. Le Hir, G., Ramstein, G., Donnadieu, Y. & Goddéris, Y. Scenario for the evolution of atmospheric pCO_2 during a snowball Earth. *Geology* **36**, 47–50 (2008).
26. Arvidson, R. S., Mackenzie, F. T. & Guidry, M. W. Geologic history of seawater: A MAGic approach to carbon chemistry and ocean ventilation. *Chem. Geol.* **362**, 287–304 (2013).
27. West, A. J., Galy, A. & Bickle, M. Tectonic and climatic controls on silicate weathering. *Earth Planet. Sci. Lett.* **235**, 211–228 (2005).
28. IPCC. *Climate Change 2013: the Physical Science Basis: Working Group I Contribution to the Fifth Assessment Report of the Intergovernmental Panel on Climate Change* (Cambridge Univ. Press (2014).
29. Foreman-Mackey, D., Hogg, D. W., Lang, D. & Goodman, J. emcee: the MCMC hammer. *Publ. Astron. Soc. Pac.* **125**, 306 (2013).

30. Nielsen, S. G. *et al.* Hydrothermal fluid fluxes calculated from the isotopic mass balance of thallium in the ocean crust. *Earth Planet. Sci. Lett.* **251,** 120–133 (2006).
31. White, A. F. & Buss, H. L. in *Surface and Ground Water, Weathering and Soils, Treatise on Geochemistry* 2nd edn (ed. Drever, J. I.) 115–155 (Elsevier, 2014).
32. Tajika, E. Carbon cycle and climate change during the Cretaceous inferred from a biogeochemical carbon cycle model. *Island Arc* **8,** 293–303 (1999).
33. Kump, L. R., Brantley, S. L. & Arthur, M. A. Chemical weathering, atmospheric CO_2, and climate. *Annu. Rev. Earth. Planet. Sci.* **28,** 611–667 (2000).
34. Hren, M. T., Hilley, G. E. & Chamberlain, C. P. The relationship between tectonic uplift and chemical weathering rates in the Washington Cascades: field measurements and model predictions. *Am. J. Sci.* **307,** 1041–1063 (2007).
35. Eiriksdottir, E. S., Gislason, S. R. & Oelkers, E. H. Does temperature or runoff control the feedback between chemical denudation and climate? Insights from NE Iceland. *Geochim. Cosmochim. Acta* **107,** 65–81 (2013).
36. Riebe, C. S., Kirchner, J. W., Granger, D. E. & Finkel, R. C. Strong tectonic and weak climatic control of long-term chemical weathering rates. *Geology* **29,** 511–514 (2001).
37. Von Blanckenburg, F. The control mechanisms of erosion and weathering at basin scale from cosmogenic nuclides in river sediment. *Earth Planet. Sci. Lett.* **237,** 462–479 (2005).
38. Maher, K. The dependence of chemical weathering rates on fluid residence time. *Earth Planet. Sci. Lett.* **294,** 101–110 (2010).
39. Riebe, C. S., Kirchner, J. W. & Finkel, R. C. Erosional and climatic effects on long-term chemical weathering rates in granitic landscapes spanning diverse climate regimes. *Earth Planet. Sci. Lett.* **224,** 547–562 (2004).
40. West, A. J. Thickness of the chemical weathering zone and implications for erosional and climatic drivers of weathering and for carbon-cycle feedbacks. *Geology* **40,** 811–814 (2012).
41. Caves, J. K., Jost, A. B., Lau, K. V. & Maher, K. Cenozoic carbon cycle imbalances and a variable weathering feedback. *Earth Planet. Sci. Lett.* **450,** 152–163 (2016).
42. Müller, R. D., Sdrolias, M., Gaina, C., Steinberger, B. & Heine, C. Long-term sea-level fluctuations driven by ocean basin dynamics. *Science* **319,** 1357–1362 (2008).
43. Skelton, P. W. *The Cretaceous World* (Cambridge Univ. Press, 2003).
44. Kashiwagi, H., Ogawa, Y. & Shikazono, N. Relationship between weathering, mountain uplift, and climate during the Cenozoic as deduced from the global carbon–strontium cycle model. *Palaeogeogr. Palaeoclimatol. Palaeoecol.* **270,** 139–149 (2008).
45. Dessert, C., Dupré, B., Gaillardet, J., François, L. M. & Allegre, C. J. Basalt weathering laws and the impact of basalt weathering on the global carbon cycle. *Chem. Geol.* **202,** 257–273 (2003).
46. Li, G. & Elderfield, H. Evolution of carbon cycle over the past 100 million years. *Geochim. Cosmochim. Acta* **103,** 11–25 (2013).
47. Bluth, G. J. & Kump, L. R. Phanerozoic paleogeology. *Am. J. Sci.* **291,** 284–308 (1991).
48. Jacobson, A. D., Andrews, M. G., Lehn, G. O. & Holmden, C. Silicate versus carbonate weathering in Iceland: new insights from Ca isotopes. *Earth Planet. Sci. Lett.* **416,** 132–142 (2015).
49. Goddéris, Y., Donnadieu, Y., Le Hir, G., Lefebvre, V. & Nardin, E. The role of palaeogeography in the Phanerozoic history of atmospheric CO_2 and climate. *Earth Sci. Rev.* **128,** 122–138 (2014).
50. Gibbs, M. T., Bluth, G. J., Fawcett, P. J. & Kump, L. R. Global chemical erosion over the last 250My: Variations due to changes in paleogeography, paleoclimate, and paleogeology. *Am. J. Sci.* **299,** 611–651 (1999).
51. Volk, T. Rise of angiosperms as a factor in long-term climatic cooling. *Geology* **17,** 107–110 (1989).
52. Royer, D., Pagani, M. & Beerling, D. Geobiological constraints on Earth system sensitivity to CO_2 during the Cretaceous and Cenozoic. *Geobiology* **10,** 298–310 (2012).
53. Park, J. & Royer, D. L. Geologic constraints on the glacial amplification of Phanerozoic climate sensitivity. *Am. J. Sci.* **311,** 1–26 (2011).
54. Pagani, M., Huber, M. & Sageman, B. in *Treatise on Geochemistry* 2nd edn (eds Holland, H. D. & Turekian, K. K.) 281–304 (Elsevier, 2014).
55. Beerling, D. J., Fox, A., Stevenson, D. S. & Valdes, P. J. Enhanced chemistry-climate feedbacks in past greenhouse worlds. *Proc. Natl Acad. Sci. USA* **108,** 9770–9775 (2011).
56. Johnson, H. P. & Pruis, M. J. Fluxes of fluid and heat from the oceanic crustal reservoir. *Earth Planet. Sci. Lett.* **216,** 565–574 (2003).
57. François, L. M., Walker, J. C. & Opdyke, B. N. The history of global weathering and the chemical evolution of the ocean-atmosphere system. *Evol. Earth Planets.* (eds Takahashi, E., Jeanloz, R. & Rubie, D.) 143–159 (American Geophysical Union, Washington DC, USA, 1993).
58. Katz, M. E. *et al.* Biological overprint of the geological carbon cycle. *Mar. Geol.* **217,** 323–338 (2005).
59. Schwartzman, D. *Life, Temperature, and the Earth: the Self-Organizing Biosphere* (Columbia Univ. Press, 2002).
60. Volk, T. Feedbacks between weathering and atmospheric CO2 over the last 100 million years. *Am. J. Sci.* **287,** 763–779 (1987).
61. Caballero, R. & Huber, M. State-dependent climate sensitivity in past warm climates and its implications for future climate projections. *Proc. Natl Acad. Sci. USA* **110,** 14162–14167 (2013).
62. Kashiwagi, H. Atmospheric carbon dioxide and climate change since the Late Jurassic (150Ma) derived from a global carbon cycle model. *Palaeogeogr. Palaeoclimatol. Palaeoecol.* **454,** 82–90 (2016).
63. Manabe, S. & Bryan, K. CO_2-induced change in a coupled ocean-atmosphere model and its paleoclimatic implications. *J. Geophys. Res. Oceans* **90,** 11689–11707 (1985).
64. Golubev, S. V., Pokrovsky, O. S. & Schott, J. Experimental determination of the effect of dissolved CO_2 on the dissolution kinetics of Mg and Ca silicates at 25 C. *Chem. Geol.* **217,** 227–238 (2005).
65. Pokrovsky, O. S. & Schott, J. Kinetics and mechanism of forsterite dissolution at 25 C and pH from 1 to 12. *Geochim. Cosmochim. Acta* **64,** 3313–3325 (2000).
66. Wolff-Boenisch, D., Wenau, S., Gislason, S. R. & Oelkers, E. H. Dissolution of basalts and peridotite in seawater, in the presence of ligands, and CO_2: implications for mineral sequestration of carbon dioxide. *Geochim. Cosmochim. Acta* **75,** 5510–5525 (2011).
67. Gudbrandsson, S., Wolff-Boenisch, D., Gislason, S. R. & Oelkers, E. H. An experimental study of crystalline basalt dissolution from 2 pH 11 and temperatures from 5 to 75° C. *Geochim. Cosmochim. Acta* **75,** 5496–5509 (2011).
68. Wogelius, R. A. & Walther, J. V. Olivine dissolution at 25 C: effects of pH, CO_2, and organic acids. *Geochim. Cosmochim. Acta* **55,** 943–954 (1991).
69. Ridgwell, A. A mid Mesozoic revolution in the regulation of ocean chemistry. *Mar. Geol.* **217,** 339–357 (2005).
70. Walker, L. J., Wilkinson, B. H. & Ivany, L. C. Continental drift and Phanerozoic carbonate accumulation in shallow-shelf and deep-marine settings. *J. Geol.* **110,** 75–87 (2002).
71. Opdyke, B. N. & Wilkinson, B. H. Carbonate mineral saturation state and cratonic limestone accumulation. *Am. J. Sci.* **293,** 217–217 (1993).
72. Broecker, W. S. & Takahashi, T. The relationship between lysocline depth and in situ carbonate ion concentration. *Deep Sea Res.* **25,** 65–95 (1978).
73. Sclater, J. G., Boyle, E. & Edmond, J. M. *Deep Drilling Results in the Atlantic Ocean: Continental Margins and Paleoenvironment*. (eds Talwani, M., Hay, W. & Ryan, W. B. F.) 235–248 (American Geophysical Union, Washington DC, USA, 1979).
74. Pilson, M. E. *An Introduction to the Chemistry of the Sea* (Prentice-Hall, Inc., 1998).
75. Tyrrell, T. & Zeebe, R. E. History of carbonate ion concentration over the last 100 million years. *Geochim. Cosmochim. Acta* **68,** 3521–3530 (2004).
76. Lee, C.-T. A. & Lackey, J. S. Global continental arc flare-ups and their relation to long-term greenhouse conditions. *Elements* **11,** 125–130 (2015).
77. Hartmann, J., Jansen, N., Dürr, H. H., Kempe, S. & Köhler, P. Global CO_2-consumption by chemical weathering: what is the contribution of highly active weathering regions? *Glob. Planet. Change* **69,** 185–194 (2009).
78. Iglesias-Rodriguez, M. D. *et al.* Progress made in study of ocean's calcium carbonate budget. *EOS* **83,** 365–375 (2002).

Acknowledgements

We thank Dorian Abbott, Lee Kump and the two anonymous reviewers whose comments greatly improved the manuscript. We also thank Giada Arney, Laurence Coogan, James Kasting, Rodrigo Luger and Chris Reinhard for helpful discussions. This work was supported by NASA Exobiology Program grant NNX15AL23G awarded to D.C.C. and by the NASA Astrobiology Institute's Virtual Planetary Laboratory, grant NNA13AA93A. J.K.-T. is supported by NASA Headquarters under the NASA Earth and Space Science Fellowship program, grant NNX15AR63H.

Author contributions

Both authors contributed to the conception of this project and the drafting of the manuscript. J.K.-T. created the model and performed the analysis.

Additional information

Supplementary Information accompanies this paper at http://www.nature.com/naturecommunications

Competing interests: The authors declare no competing financial interests.

Chapter 6 - The carbon cycle of the early Earth

"In every outthrust headland, in every curving beach, in every grain of sand there is the story of the earth." – Rachael Carson

What was the early Earth like? The answer to this question would inform our understanding of life's origins and early evolution. Additionally, since Earth is the only known example of a habitable and inhabited planet, understanding Earth's climate evolution is an important case study for predicting the climate evolution of terrestrial exoplanets.

Despite this, there is considerable debate over the climate and ocean pH of the early Earth (de Wit & Furnes 2016; Halevy & Bachan 2017; Hren et al. 2009; Kempe & Degens 1985; Knauth & Lowe 2003). In this chapter, the validated carbon cycle model developed in Chapter 5 is applied to all of Earth history to constrain environmental conditions in the Archean.

This chapter was published in collaboration with Giada Arney and David C. Catling in The Proceedings of the National Academy of Sciences USA (Krissansen-Totton et al. (2018). Constraining the climate and ocean pH of the early Earth with a geological carbon cycle model, Proceedings of the National Academy of Sciences USA, DOI:10.1073/pnas.1721296115).

Constraining the climate and ocean pH of the early Earth with a geological carbon cycle model

Joshua Krissansen-Totton[a,b,1], Giada N. Arney[b,c,d], and David C. Catling[a,b]

[a]Department of Earth and Space Sciences, University of Washington, Seattle, WA 98195; [b]Virtual Planetary Laboratory Team, NASA Astrobiology Institute, Seattle, WA 98195; [c]Planetary Systems Laboratory, NASA Goddard Space Flight Center, Greenbelt, MD 20771; and [d]Sellers Exoplanet Environments Collaboration, NASA Goddard Space Flight Center, Greenbelt, MD 20771

Edited by Mark H. Thiemens, University of California at San Diego, La Jolla, CA, and approved March 7, 2018 (received for review December 14, 2017)

The early Earth's environment is controversial. Climatic estimates range from hot to glacial, and inferred marine pH spans strongly alkaline to acidic. Better understanding of early climate and ocean chemistry would improve our knowledge of the origin of life and its coevolution with the environment. Here, we use a geological carbon cycle model with ocean chemistry to calculate self-consistent histories of climate and ocean pH. Our carbon cycle model includes an empirically justified temperature and pH dependence of seafloor weathering, allowing the relative importance of continental and seafloor weathering to be evaluated. We find that the Archean climate was likely temperate (0–50 °C) due to the combined negative feedbacks of continental and seafloor weathering. Ocean pH evolves monotonically from $6.6^{+0.6}_{-0.4}$ (2σ) at 4.0 Ga to $7.0^{+0.7}_{-0.5}$ (2σ) at the Archean–Proterozoic boundary, and to $7.9^{+0.1}_{-0.2}$ (2σ) at the Proterozoic–Phanerozoic boundary. This evolution is driven by the secular decline of pCO_2, which in turn is a consequence of increasing solar luminosity, but is moderated by carbonate alkalinity delivered from continental and seafloor weathering. Archean seafloor weathering may have been a comparable carbon sink to continental weathering, but is less dominant than previously assumed, and would not have induced global glaciation. We show how these conclusions are robust to a wide range of scenarios for continental growth, internal heat flow evolution and outgassing history, greenhouse gas abundances, and changes in the biotic enhancement of weathering.

carbon cycle | paleoclimate | Precambrian | ocean pH | weathering

Constraining the climate and ocean chemistry of the early Earth is crucial for understanding the emergence of life, the subsequent coevolution of life and the environment, and as a point of reference for evaluating the habitability of terrestrial exoplanets. However, the surface temperature of the early Earth is debated. Oxygen isotopes in chert have low $\delta^{18}O$ values in the Archean (1). If this isotope record reflects the temperature-dependent equilibrium fractionation of ^{18}O and ^{16}O between silica and seawater, then this would imply mean surface temperatures around 70 ± 15 °C at 3.3 Ga (2). A hot early Earth is also supported by possible evidence for a low viscosity Archean ocean (3), and the thermostability of reconstructed ancestral proteins (4), including those purportedly reflective of Archean photic zone temperatures (5). Silicon isotopes in cherts have also been interpreted to infer 60–80 °C Archean seawater temperatures (6).

Alternatively, the trend in $\delta^{18}O$ over Earth history has been interpreted as a change in the oxygen isotope composition of seawater (7), or hydrothermal alteration of the seafloor (8). Isotopic analyses using deuterium (9) and phosphates (10) report Archean surface temperatures <40 °C. Archean glacial deposits (ref. 11 and references therein) also suggest an early Earth with ice caps, or at least transient cool periods. A geological carbon cycle model of Sleep and Zahnle (12) predicts Archean and Hadean temperatures below 0 °C due to efficient seafloor weathering. An analysis combining general circulation model (GCM) outputs with a carbon cycle model predicts more moderate temperatures at 3.8 Ga (13). Resolving these conflicting interpretations would provide a better understanding of the conditions for the origin and early evolution of life.

Ocean pH is another important environmental parameter because it partitions carbon between the atmosphere and ocean and is thus linked to climate. Additionally, many biosynthetic pathways hypothesized to be important for the origin of life are strongly pH dependent (14–16), and so constraining the pH of the early ocean would inform their viability. Furthermore, bacterial biomineralization is favorable at higher environmental pH values because this allows cells to more easily attract cations through deprotonation (17). Arguably, low environmental pH values would be an obstacle to the evolution of advanced life due to biomineralization inhibition (18). Finally, many pO_2 proxies are pH dependent (19–21), and so understanding the history of pH would enable better quantification of the history of pO_2.

However, just as with climate, debate surrounds empirical constraints on Archean ocean pH. Empirical constraints are scant and conflicting. Based on the scarcity of gypsum pseudomorphs before 1.8 Ga, Grotzinger and Kasting (22) argued that the Archean ocean pH was likely between 5.7 and 8.6. However, others note the presence of Archean gypsum as early as 3.5 Ga (23); its scarcity could be explained by low sulfate (24). Blättler et al. (24) interpreted Archean Ca isotopes to reflect high Ca/alkalinity ratios, which in turn would rule out high pH and high pCO_2 values. Friend et al. (25) argued for qualitatively circumneutral to weakly alkaline Archean ocean pH based on rare Earth element anomalies.

Significance

The climate and ocean pH of the early Earth are important for understanding the origin and early evolution of life. However, estimates of early climate range from below freezing to over 70 °C, and ocean pH estimates span from strongly acidic to alkaline. To better constrain environmental conditions, we applied a self-consistent geological carbon cycle model to the last 4 billion years. The model predicts a temperate (0–50 °C) climate and circumneutral ocean pH throughout the Precambrian due to stabilizing feedbacks from continental and seafloor weathering. These environmental conditions under which life emerged and diversified were akin to the modern Earth. Similar stabilizing feedbacks on climate and ocean pH may operate on earthlike exoplanets, implying life elsewhere could emerge in comparable environments.

Author contributions: J.K.-T. and D.C.C. designed research; J.K.-T. performed research; J.K.-T., G.N.A., and D.C.C. analyzed data; G.N.A. performed climate model calculations; and J.K.-T. and D.C.C. wrote the paper.

The authors declare no conflict of interest.

This article is a PNAS Direct Submission.

Data deposition: The Python source code is available on GitHub (https://github.com/joshuakt/early-earth-carbon-cycle).

[1]To whom correspondence should be addressed. Email: joshkt@uw.edu.

This article contains supporting information online at www.pnas.org/lookup/suppl/doi:10.1073/pnas.1721296115/-/DCSupplemental.

Theoretical arguments for the evolution of ocean pH also disagree. By analogy with modern alkaline lakes, Kempe and Degens (26) argued for a pH 9–11 "soda ocean" on the early Earth, but mass balance challenges such an idea (27). Additionally, high pH oceans (>9.0) would shift the NH_3–NH_4^+ aqueous equilibrium toward NH_3, which would volatilize and fractionate nitrogen isotopes in a way that is not observed in marine sediments (28). The conventional view of the evolution of ocean pH is that the secular decline of pCO_2 over Earth history has driven an increase in ocean pH from acidic to modern slightly alkaline. For example, Halevy and Bachan (29) modeled ocean chemistry over Earth history with prescribed pCO_2 and climate histories, and reported a monotonic pH evolution broadly consistent with this view. However, it has also been argued that seafloor weathering buffered ocean pH to near-modern values throughout Earth history (12).

On long timescales, both climate and ocean pH are controlled by the geological carbon cycle. The conventional view of the carbon cycle is that carbon outgassing into the atmosphere–ocean system is balanced by continental silicate weathering and subsequent marine carbonate formation (30, 31). The weathering of silicates is temperature and pCO_2 dependent, which provides a natural thermostat to buffer climate against changes in stellar luminosity and outgassing. This mechanism is widely believed to explain the relative stability of Earth's climate despite a ~30% increase in solar luminosity since 4.0 Ga (31).

A possible complimentary negative feedback to continental weathering is provided by seafloor weathering. Such weathering occurs when the seawater circulating in off-axis hydrothermal systems reacts with the surrounding basalt and releases cations, which then precipitate as carbonates in the pore space (32, 33). If the rate of basalt dissolution and pore-space carbonate precipitation depends on the carbon content of the atmosphere–ocean system via pCO_2, temperature, or pH, then seafloor weathering could provide an additional negative feedback (12).

The existence of a negative feedback to balance the carbon cycle on million-year timescales is undisputed. Without it, atmospheric CO_2 would be depleted, leading to a runaway icehouse, or would accumulate to excessive levels (34). However, the relative importance of continental and seafloor weathering in providing this negative feedback, and the overall effectiveness of these climate-stabilizing and pH-buffering feedbacks on the early Earth are unknown.

In this study, we apply a geological carbon cycle model with ocean chemistry to the entirety of Earth history. The inclusion of ocean carbon chemistry enables us to model the evolution of ocean pH and realistically capture the pH-dependent and temperature-dependent kinetics of seafloor weathering. This is a significant improvement on previous geological carbon cycle models (e.g., refs. 12 and 35) that omit ocean chemistry and instead adopt an arbitrary power-law dependence on pCO_2 for seafloor weathering which, as we show, overestimates CO_2 drawdown on the early Earth. By coupling seafloor weathering to Earth's climate and the geological carbon cycle, we calculate self-consistent histories of Earth's climate and pH evolution, and evaluate the relative importance of continental and seafloor weathering through time. The pH evolution we calculate is therefore more robust than that of Halevy and Bachan (29) because, unlike their model, we do not prescribe pCO_2 and temperature histories.

Our approach remains agnostic on unresolved issues, such as the history of continental growth, internal heat flow, and the biological enhancement of weathering, because we include a broad range of values for these parameters. Our conclusions are therefore robust to uncertainties in Earth system evolution. We find that a hot early Earth is very unlikely, and pH should, on average, have monotonically increased since 4.0 Ga, buffered somewhat by continental and seafloor weathering.

Methods

The geological carbon cycle model builds on that described in Krissansen-Totton and Catling (36). Here, we summarize its key features, and additional details are provided in the *SI Appendix*. The Python source code is available on GitHub at github.com/joshuakt/early-earth-carbon-cycle.

We model the time evolution of the carbon cycle using two separate boxes representing the atmosphere–ocean system and the pore space in the seafloor (Fig. 1 and *SI Appendix A*). We track carbon and carbonate alkalinity fluxes into and between these boxes, and assume that the bulk ocean is in equilibrium with the atmosphere.

Many of the parameters in our model are uncertain, and so we adopt a range of values (*SI Appendix*, Table S1) based on spread in the literature rather than point estimates. Each parameter range was sampled uniformly, and the forward model was run 10,000 times to build distributions for model outputs such as pCO_2, pH, and temperature. Model outputs are compared with proxy data for pCO_2, temperature, and carbonate precipitation (*SI Appendix D*).

Continental silicate weathering is described by the following function:

$$F_{sil} = f_{bio} f_{land} F_{sil}^{mod} \left(\frac{pCO_2}{pCO_2^{mod}} \right)^{\alpha} \exp(\Delta T_S / T_e) \quad [1]$$

Here, f_{bio} is the biological enhancement of weathering (see below), f_{land} is the continental land fraction relative to modern, F_{sil}^{mod} is the modern continental silicate weathering flux (Tmol y^{-1}), $\Delta T_S = T_S - T_S^{mod}$ is the difference in global mean surface temperature, T_S, relative to preindustrial modern, T_S^{mod}. The exponent α is an empirical constant that determines the dependence of weathering on the partial pressure of carbon dioxide relative to modern, pCO_2/pCO_2^{mod}. An e-folding temperature, T_e, defines the temperature dependence of weathering. A similar expression for carbonate weathering is described in *SI Appendix A*.

The land fraction, f_{land}, and biological modifier, f_{bio}, account for the growth of continents and the biological enhancement of continental weathering, respectively. We adopt a broad range of continental growth curves that encompasses literature estimates (Fig. 2*A* and *SI Appendix A*). For our nominal model, we assume Archean land fraction was anywhere between 10% and 75% of modern land fraction (Fig. 2*A*), but we also consider a no-land Archean endmember (Fig. 2*B*).

To account for the possible biological enhancement of weathering in the Phanerozoic due to vascular land plants, lichens, bryophytes, and ectomycorrhizal fungi, we adopt a broad range of histories for the biological enhancement of weathering, f_{bio} (Fig. 2*C*). The lower end of this range is consistent with estimates of biotic enhancement of weathering from the literature (37–39).

The dissolution of basalt in the seafloor is dependent on the spreading rate, pore-space pH, and pore-space temperature (*SI Appendix A*). This formulation is based on the validated parameterization in ref. 36. Pore-space temperatures are a function of climate and geothermal heat flow. Empirical

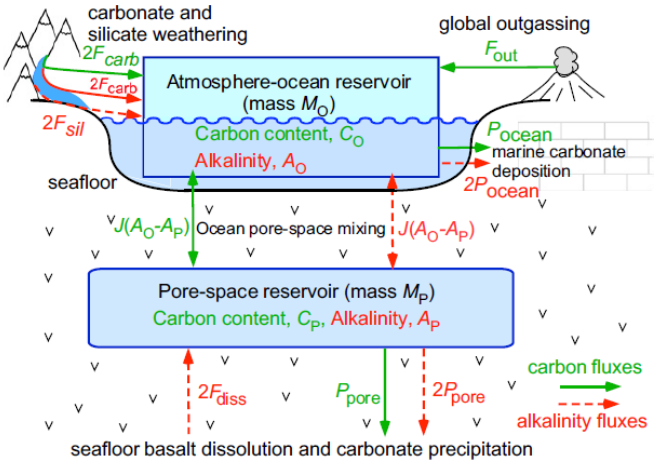

Fig. 1. Schematic of carbon cycle model used in this study. Carbon fluxes (Tmol C y^{-1}) are denoted by solid green arrows, and alkalinity fluxes (Tmol eq y^{-1}) are denoted by red dashed arrows. The fluxes into/out of the atmosphere–ocean system are outgassing, F_{out}, silicate weathering, F_{sil}, carbonate weathering, F_{carb}, and marine carbonate precipitation, P_{ocean}. The fluxes into/out of the pore space are basalt dissolution, F_{diss}, and pore-space carbonate precipitation, P_{pore}. Alkalinity fluxes are multiplied by 2 because the uptake or release of one mole of carbon as carbonate is balanced by a cation with a 2+ charge (typically Ca^{2+}). A constant mixing flux, J (kg y^{-1}), exchanges carbon and alkalinity between the atmosphere–ocean system and pore space.

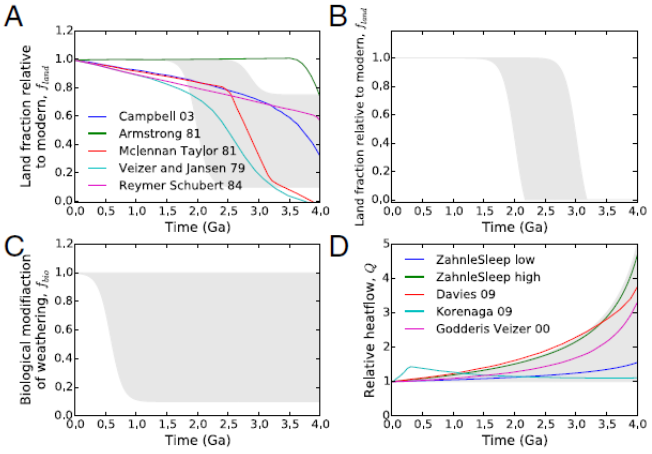

Fig. 2. Gray shaded regions are ranges assumed for selected model input parameters. (*A*) Range of continental growth curves assumed in our nominal model, f_{land}. Various literature estimates are plotted alongside the model growth curve (*SI Appendix A*). (*B*) Range of continental growth curves for an endmember of no Archean land; (*C*) range for biological enhancement of weathering histories, f_{bio}; and (*D*) range of internal heat flow histories, Q, compared with literature estimates (*SI Appendix A*).

data and fully coupled global climate models reveal a linear relationship between deep ocean temperature and surface climate (36). Equations relating pore-space temperature, deep ocean temperature, and sediment thickness are provided in *SI Appendix A*.

Carbon leaves the atmosphere–ocean system through carbonate precipitation in the ocean and pore space of the oceanic crust. At each time step, the carbon abundances and alkalinities are used to calculate the carbon speciation, atmospheric pCO_2, and saturation state assuming chemical equilibrium. Saturation states are then used to calculate carbonate precipitation fluxes (*SI Appendix A*). We allow calcium (Ca) abundance to evolve with alkalinity, effectively assuming no processes are affecting Ca abundances other than carbonate and silicate weathering, seafloor dissolution, and carbonate precipitation. The consequences of this simplification are explored in the sensitivity analysis in *SI Appendix C*. We do not track organic carbon burial because organic burial only constitutes 10–30% of total carbon burial for the vast majority of Earth history (40), and so the inorganic carbon cycle is the primary control.

The treatment of tectonic and interior processes is important for specifying outgassing and subduction flux histories. We avoid tracking crustal and mantle reservoirs because explicitly parameterizing how outgassing fluxes relate to crustal production and reservoirs assumes modern-style plate tectonics has operated throughout Earth history (e.g., ref. 12) and might not be valid. Evidence exists for Archean subduction in eclogitic diamonds (41) and sulfur mass-independent fractionation in ocean island basalts ostensibly derived from recycled Archean crust (42). However, other tectonic modes have been proposed for the early Earth such as heat-pipe volcanism (43), delamination and shallow convection (44), or a stagnant lid regime (45).

Our generalized parameterizations for heat flow, spreading rates, and outgassing histories are described in *SI Appendix A*. Fig. 2*D* shows our assumed range of internal heat flow histories compared with estimates from the literature. Spreading rate is connected to crustal production via a power law, which spans endmember cases (*SI Appendix A*). These parameterizations provide an extremely broad range of heat flow, outgassing, and crustal production histories, and do not assume a fixed coupling between these variables.

We used a 1D radiative convective model (46) to create a grid of mean surface temperatures as a function of solar luminosity and pCO_2. The grid of temperature outputs was fitted with a 2D polynomial (*SI Appendix E*). We initially neglect other greenhouse gases besides CO_2 and H_2O, albedo changes, and assumed a constant total pressure over Earth history. However, later we consider these influences, such as including methane (CH_4) in the Precambrian. The evolution of solar luminosity is conventionally parameterized (47).

Our model has been demonstrated for the last 100 Ma against abundant proxy data (36) and it can broadly reproduce Sleep and Zahnle (12) if we replace our kinetic formulation of seafloor weathering with their simpler CO_2-dependent expression (*SI Appendix B*). Agreement with ref. 12 confirms that the omission of crustal and mantle reservoirs does not affect our conclusions.

Results

Fig. 3 shows the evolution of the geological carbon cycle over Earth history according to our nominal model. Here, we have used our kinetic parameterization of seafloor weathering rather than the arbitrary pCO_2 power law adopted in previous studies (*SI Appendixes A* and *B*). We have also assumed a range of continental growth curves (Fig. 2*A*), a range of Phanerozoic biological weathering enhancements (Fig. 2*C*), and a range of temperature dependencies of weathering from ref. 36. Proxies for surface temperature, atmospheric pCO_2, and seafloor weathering flux are plotted alongside model outputs for comparison (*SI Appendix D*). For all results, both 95% confidence intervals and median values are plotted for key carbon cycle outputs. Median values are calculated at each time step, and consequently their evolution does not necessarily resemble the most probable time evolution of carbon cycle variables. In practice, however, most individual model realizations tend to track the median, at least qualitatively (*SI Appendix A*).

We observe that modeled temperatures are relatively constant throughout Earth history, with Archean temperatures ranging from 271 to 314 K. The combination of continental and seafloor weathering efficiently buffers climate against changes in luminosity, outgassing, and biological evolution. This temperature history is broadly consistent with glacial constraints and recent isotope proxies (Fig. 3*D*). The continental weathering buffer dominates over the seafloor weathering buffer for most of Earth history, but in the Archean the two carbon sinks are comparable (*SI Appendix*, Fig. S1). Indeed, if seafloor weathering were artificially held constant, then continental weathering alone may be unable to efficiently buffer the climate of the early Earth—the temperature distribution at 4.0 Ga extends to 370 K, and the atmospheric pCO_2 distribution extends to 7 bar (*SI Appendix*, Fig. S3).

In our nominal model, the median Archean surface temperature is slightly higher than modern surface temperatures. If solar evolution were the only driver of the carbon cycle, then Archean temperatures would necessarily be cooler than modern temperatures; weathering feedbacks can mitigate this cooling but not produce warming. Warmer Archean climates are possible because elevated internal heat flow, lower continental land fraction, and lessened biological enhancement of weathering all act to warm to Precambrian climate. These three factors produce a comparable warming effect (*SI Appendix*, Fig. S17*A* and *Appendix C*), although the magnitude of each is highly uncertain and so temperate Archean temperatures cannot be uniquely attributed to any one variable.

Continental and seafloor weathering also buffer ocean pH against changes in luminosity and outgassing. Ocean pH increases monotonically over Earth history from 6.3–7.2 at 4.0 Ga, to 6.5–7.7 at 2.5 Ga, and to the modern value of 8.2. The broad range of parameterizations does not tightly constrain the history of atmospheric pCO_2, but the model pCO_2 outputs encompass paleosol proxies (Fig. 3*B*).

The results described above assume an Archean landmass fraction between 0.1 and 0.75 times the modern land fraction. Next, we consider the endmember scenario of zero Archean landmass. This is unrealistic because abundant evidence exists for Archean land (48). However, a zero land fraction case could represent a scenario where continental fraction is sufficiently small that continental silicate weathering becomes supply limited (e.g., ref. 49).

Fig. 4 shows model outputs for the zero land fraction case. When continental weathering drops to zero, seafloor weathering increases dramatically to balance the carbon cycle (Fig. 4*F*). This is largely a consequence of the temperature-dependent feedback of seafloor weathering. The climate warms by 10–15 K (Fig. 4*D*) before the temperature-dependent seafloor weathering flux is sufficiently large to balance the carbon cycle. Even in this extreme case, the median Archean temperature is ~305 K, and the upper end of the temperature distribution at 4 Ga only extends to ~328 K, excluding a "hot" Archean of 60–80 °C. Archean pCO_2 (and pH) are slightly higher (lower) in the zero land case, but the seafloor weathering feedback is still an effective buffer.

Finally, we investigated whether the inclusion of methane as a Precambrian greenhouse gas would substantially change our results.

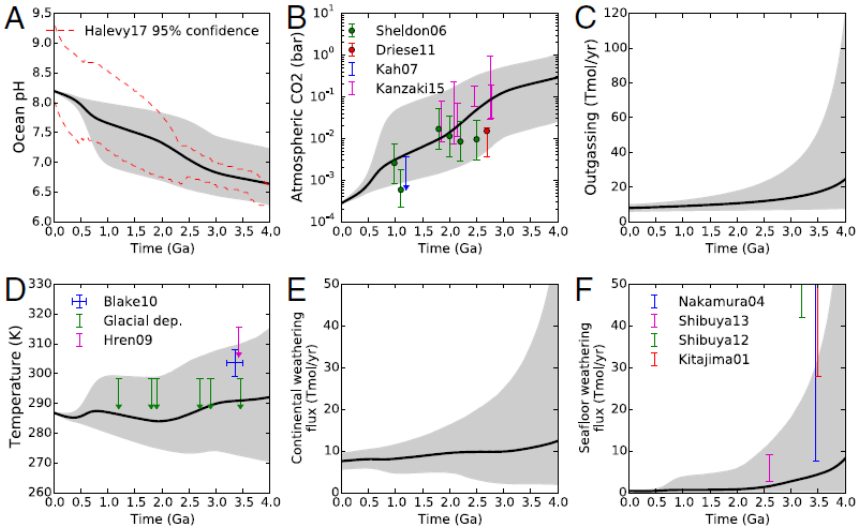

Fig. 3. Nominal model outputs. Gray shaded regions represent 95% confidence intervals, and black lines are the median outputs. (*A*) Ocean pH with the 95% confidence interval from Halevy and Bachan (29) plotted with red dashed lines for comparison. Our model predicts a monotonic evolution of pH from slightly acidic values at 4.0 Ga to slightly alkaline modern values. (*B*) Atmospheric pCO_2 plotted alongside proxies from the literature. (*C*) Global outgassing flux. (*D*) Mean surface temperature plotted alongside glacial and geochemical proxies from the literature. Our model predicts surface temperatures have been temperate throughout Earth history. (*E*) Continental silicate weathering flux. (*F*) Seafloor weathering flux plotted alongside flux estimates from Archean altered seafloor basalt. dep, deposit.

Fig. 5 shows model outputs where we have assumed 100 ppm Proterozoic methane and 1% Archean methane levels (*SI Appendix E*). The temperature changes are smaller than what might be expected if only methane levels were changing. This is because pCO_2 drops in response to the imposed temperature increase—pCO_2 must drop otherwise weathering sinks would exceed source fluxes. The pCO_2 distribution at 4.0 Ga is shifted downward relative to the nominal case with no other greenhouse cases, and ocean pH increases in response to this pCO_2 drop. Note that for parts of parameter space where $CO_2/CH_4 \gtrsim 0.2$ (50), our temperatures should be considered upper limits because a photochemical haze would form, cooling the climate (*SI Appendix E*).

Thus, even with considerable warming from an additional greenhouse gas, the median temperature at 4.0 Ga is below 300 K, and the temperature distribution extends to 320 K, again excluding a hot Archean. *SI Appendix*, Fig. S7 shows the results for the most extreme case of no Archean land and high methane abundances. Even in this extreme scenario, the seafloor weathering flux successfully buffers the climate to a median 4.0 Ga value of ~310 K. Archean pH values are closer to circumneutral when methane is included due to lower pCO_2, but there is still a monotonic evolution in pH over Earth history.

Discussion

Previously, Sleep and Zahnle (12) modeled the evolution of the geological carbon cycle over Earth history and reported the Hadean and Archean mean surface temperatures below 0 °C, unless atmospheric methane abundances were very high. In contrast, we find that Archean temperatures were likely temperate, regardless of methane abundances. This disparity can be ascribed to the differing treatments of seafloor weathering. Sleep and Zahnle (12) did not include ocean chemistry in their model (they effectively fix pH), and were thus forced to parameterize seafloor weathering using a power-law pCO_2 dependence with a fitted exponent. This parameterization overestimates the role of Archean seafloor weathering. Experiments with basalt dissolution reveal a weak pH dependence and a moderate temperature dependence, but no direct pCO_2 dependence (see discussion in ref. 36).

The change from a CO_2-dependent parameterization to a temperature-dependent parameterization means the seafloor weathering feedback better stabilizes climate against increasing luminosity. For a purely temperature-dependent weathering feedback, decreasing luminosity does not change climate, as the weathering flux must remain constant to maintain carbon cycle balance. Instead, CO_2 adjusts upwards to maintain the same temperature at lower insolation. In contrast, for a purely CO_2-dependent weathering feedback, a decrease in solar luminosity will result in a temperature decrease (see also *SI Appendix B*). In short, the pH-dependent and temperature-dependent seafloor weathering parameterization we apply stabilizes climate and prevents a globally glaciated early Earth. This result is broadly consistent with a single time point at 3.8 Ga that calculated equilibrium surface temperatures using a GCM and geological carbon cycle model (13).

The only way to produce Archean climates below 0 °C in our model is to assume the Archean outgassing flux was 1–5× lower than the modern flux (*SI Appendix*, Fig. S12). However, dramatically lowered Archean outgassing fluxes contradict known outgassing proxies and probably require both a stagnant lid tectonic regime and a mantle more reduced than zircon data suggest, which lowers the portion of outgassed CO_2 (*SI Appendix C*). Moreover, even when outgassing is low, frozen climates are not guaranteed (*SI Appendix*, Fig. S12).

Our model gives a monotonic evolution of ocean pH from 6.3–7.7 in the Archean (95% confidence), to 6.5–8.1 (95% confidence) in the Proterozoic, and increasing to 8.2 in the modern surface ocean. This history is broadly consistent with that of Halevy and Bachan (29) (Figs. 3 and 4). Halevy and Bachan (29) tracked Na, Cl, Mg, and K exchanges with continental and oceanic crust, and related these fluxes to the thermal evolution of the Earth. Minor constituents such as HS, NH_3, Fe^{2+}, and SO_4^{2-} were also considered. However, they prescribe many features of the carbon cycle rather than apply a self-consistent model as we have done here. Specifically, they imposed pCO_2 to ensure near-modern temperatures throughout Earth history. Consequently, the explicit temperature dependence of both seafloor and continental weathering were omitted. Additionally, subduction and outgassing were assumed to be directly proportional, a limited range of heat flow histories were adopted, and continental silicate weathering was described using an overall pCO_2 power-law dependence with no allowance for changing land fraction or biogenic enhancement weathering. Thus, the uncertainty envelopes for the early Earth ocean pH are underestimated in ref. 29 as can be seen by their uncertainty diminishing further back in time. Good agreement with the results of ref. 29 confirms that the details of ocean chemistry

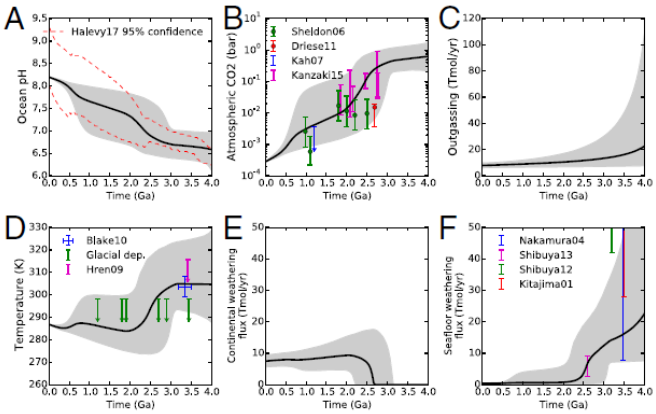

Fig. 4. No Archean land endmember scenario. Panels *A–F*, lines, and, shadings are the same as in Fig. 3. (*E*) Continental weathering drops to zero in the Archean, but (*F*) seafloor weathering increases due to its temperature dependence to balance the carbon cycle. This causes an increase in surface temperature in the Archean, (*D*) but conditions are still temperate throughout Earth history. The evolution of (*A*) ocean pH and (*B*) pCO_2 are similar to the nominal model. dep, deposit.

are of secondary importance to pH evolution, and that the monotonic evolution of pH is instead driven by solar luminosity evolution, buffered by enhanced continental and seafloor weathering under high pCO_2 conditions. The two models also agree because the carbon cycle buffers to near-modern temperatures, allowing the constant temperature assumption of ref. 29, but there is no way of knowing the effectiveness of the buffer without a self-consistent model of the carbon cycle.

One caveat for our results is that the ocean chemistry is incomplete. Specifically, Ca abundances in the ocean and pore space are controlled entirely by alkalinity fluxes from continental and seafloor weathering. In reality, Ca abundances are modulated by other processes such as the hydrothermal exchange of Ca and Mg in the seafloor, dolomitization, and clay formation (51). To explore whether neglecting these processes would affect our results we conducted sensitivity tests with a large ensemble of Ca evolutions (*SI Appendix C*). High Archean Ca abundances might be expected to produce more acidic oceans because carbonate abundances are lower for the same saturation state. However, this effect is buffered by decreases in Ca and CO_3^{2-} activity coefficients (complexing), and so model outputs look very similar to our nominal model for a broad range of Ca abundance trajectories (*SI Appendix*, Fig. S9).

In our nominal climate model, we did not include the effects of changing atmospheric pressure or albedo changes. These effects are likely to be modest compared with the other sources of uncertainty in our model. Lower surface albedo from a reduced Archean land fraction can contribute at most 5 W/m^2 of radiative forcing (52), which would cause only a few degrees of warming. Halving Archean total pressure—as has been suggested by paleopressure proxies (53)—would cool the Earth by ~5 K because of the loss of pressure broadening, thereby offsetting the lower land fraction (54). Changes in cloud cover could, in principle, induce larger warming, but the required conditions for >10 K warming are highly speculative (52). In any case, the effects of pressure changes and albedo changes are unlikely to affect our conclusions because the temperature changes they induce will be compensated by pCO_2 variations to balance the carbon cycle. Sensitivity analyses where massive amounts of Archean warming are imposed (+30 K) still result in temperate surface temperatures because of this pCO_2 compensation (*SI Appendix*, Fig. S10).

Although our model outputs are broadly consistent with paleosol proxies and glacial constraints, some disagreement occurs with selected seafloor weathering proxies. Proxies for seafloor carbonate precipitation were estimated by using the average carbonate abundances in Archean oceanic crust, scaled by the model spreading rate at that time multiplied by an assumed carbonatization depth (*SI Appendix D*). Our modeled seafloor carbonate precipitation fluxes agree with that of Nakamura and Kato (55) and Shibuya et al. (56), but undershoot crustal carbonate abundances reported by Shibuya et al. (57) and Kitajima et al. (58). It is difficult to construct a balanced carbon cycle model with seafloor weathering fluxes in excess of 100 Tmol C/y as these latter two studies imply, and so the discrepancy may be because those oceanic crust samples are not representative of global carbonatization flux, or because some of the carbonate is secondary. The only way to approach the carbonate abundances reported by Shibuya et al. (57) and Kitajima et al. (58) is to impose very high Archean outgassing (e.g., up to 60× the modern flux; *SI Appendix*, Fig. S11), but even then the fit is marginal. If high Archean crustal carbonate estimates were truly primary, then Archean outgassing would have been very high, and so Earth's internal heat flow would have decreased dramatically over Earth's history, contrary to Korenaga (59).

We conclude that current best knowledge of Earth's geologic carbon cycle precludes a hot Archean. Our results are insensitive to assumptions about ocean chemistry, internal evolution, and weathering parameterizations, so a hot early Earth would require some fundamental error in current understanding of the carbon cycle. Increasing the biotic enhancement of weathering by several orders of magnitude as proposed by Schwartzman (60) does not produce a hot Archean because this is mathematically equivalent to zeroing out the continental weathering flux (Fig. 4). In this case the temperature-dependent seafloor weathering feedback buffers the climate of the Earth to moderate temperatures (*SI Appendix*, Fig. S14). Dramatic temperature increases (or decreases) due to albedo changes also do not change our conclusions due to the buffering effect of the carbon cycle (see above). If both continental and seafloor weathering become supply limited (e.g., refs. 49 and 61), then temperatures could easily exceed 50 °C. However, in this case the carbon cycle would be out of balance, leading to excessive pCO_2 accumulation within a few hundred million years unless buffered by some other, unknown feedback.

Conclusions

The early Earth was probably temperate. Continental and seafloor weathering buffer Archean surface temperatures to 0–50 °C. This result holds for a broad range of assumptions about the evolution of internal heat flow, crustal production, spreading rates, and the biotic enhancement of continental weathering.

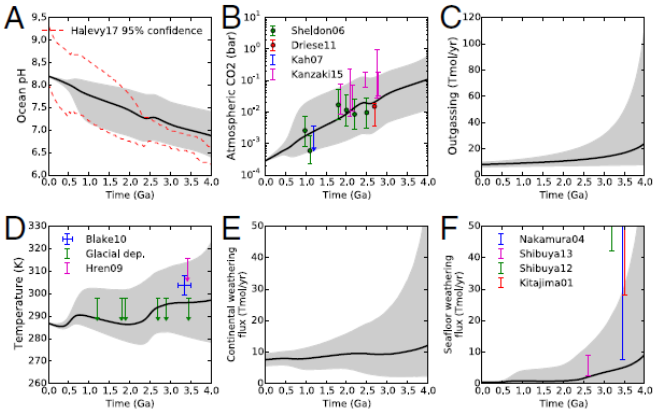

Fig. 5. Default continental growth range with imposed 100 ppm methane in the Proterozoic and 1% methane in the Archean. Panels *A–F*, lines, and, shadings are the same as in Fig. 3. (*D*) Temperature increases sharply in the Archean due to methane, but by less than what would be expected if pCO_2 were unchanged. In practice, there is a compensating decrease in atmospheric pCO_2, (*B*) which must occur to balance the carbon cycle. Otherwise temperatures would be too high and weathering sinks would exceed outgassing sources. Because pCO_2 is lower, Archean pH values are closer to circumneutral (*A*). dep, deposit.

Even in extreme scenarios with negligible subaerial Archean land and high methane abundances, a hot Archean (>50 °C) is unlikely. Sub-0 °C climates are also unlikely unless the Archean outgassing flux was unrealistically lower than the modern flux.

The seafloor weathering feedback is important, but less dominant than previously assumed. Consequently, the early Earth would not have been in a snowball state due to pCO_2 drawdown from seafloor weathering. In principle, little to no methane is required to maintain a habitable surface climate, although methane should be expected in the anoxic Archean atmosphere once methanogenesis evolved (ref. 62, chap. 11).

Ignoring transient excursions, the pH of Earth's ocean has evolved monotonically from $6.6^{+0.6}_{-0.4}$ at 4.0 Ga (2σ) to $7.0^{+0.7}_{-0.5}$ at 2.5 Ga (2σ), and 8.2 in the modern ocean. This evolution is robust to assumptions about ocean chemistry, internal heat flow, and other carbon cycle parameterizations. Consequently, similar feedbacks may control ocean pH and climate on other Earthlike planets with basaltic seafloors and silicate continents, suggesting that life elsewhere could emerge in comparable environments to those on our early planet.

ACKNOWLEDGMENTS. We thank Roger Buick, Michael Way, Anthony Del Genio, and Mark Chandler, and the two anonymous reviewers for helpful discussions and insightful contributions. This work was supported by NASA Exobiology Program Grant NNX15AL23G awarded to D.C.C., the Simons Collaboration on the Origin of Life Award 511570, and by the NASA Astrobiology Institute's Virtual Planetary Laboratory, Grant NNA13AA93A. J.K.-T. is supported by NASA Headquarters under the NASA Earth and Space Science Fellowship program, Grant NNX15AR63H.

1. Knauth LP (2005) Temperature and salinity history of the Precambrian ocean: Implications for the course of microbial evolution. *Palaeogeogr Palaeoclimatol Palaeoecol* 219:53–69.
2. Knauth LP, Lowe DR (2003) High Archean climatic temperature inferred from oxygen isotope geochemistry of cherts in the 3.5 Ga Swaziland Supergroup, South Africa. *Geol Soc Am Bull* 115:566–580.
3. Fralick P, Carter JE (2011) Neoarchean deep marine paleotemperature: Evidence from turbidite successions. *Precambrian Res* 191:78–84.
4. Gaucher EA, Govindarajan S, Ganesh OK (2008) Palaeotemperature trend for Precambrian life inferred from resurrected proteins. *Nature* 451:704–707.
5. Garcia AK, Schopf JW, Yokobori SI, Akanuma S, Yamagishi A (2017) Reconstructed ancestral enzymes suggest long-term cooling of Earth's photic zone since the Archean. *Proc Natl Acad Sci USA* 114:4619–4624.
6. Robert F, Chaussidon M (2006) A palaeotemperature curve for the Precambrian oceans based on silicon isotopes in cherts. *Nature* 443:969–972.
7. Kasting JF, et al. (2006) Paleoclimates, ocean depth, and the oxygen isotopic composition of seawater. *Earth Planet Sci Lett* 252:82–93.
8. van den Boorn SH, van Bergen MJ, Nijman W, Vroon PZ (2007) Dual role of seawater and hydrothermal fluids in early Archean chert formation: Evidence from silicon isotopes. *Geology* 35:939–942.
9. Hren MT, Tice MM, Chamberlain CP (2009) Oxygen and hydrogen isotope evidence for a temperate climate 3.42 billion years ago. *Nature* 462:205–208.
10. Blake RE, Chang SJ, Lepland A (2010) Phosphate oxygen isotopic evidence for a temperate and biologically active Archaean ocean. *Nature* 464:1029–1032.
11. de Wit MJ, Furnes H (2016) 3.5-Ga hydrothermal fields and diamictites in the Barberton Greenstone Belt-Paleoarchean crust in cold environments. *Sci Adv* 2:e1500368.
12. Sleep NH, Zahnle K (2001) Carbon dioxide cycling and implications for climate on ancient Earth. *J Geophys Res Planets* 106:1373–1399.
13. Charnay B, Hir GL, Fluteau F, Forget F, Catling DC (2017) A warm or a cold early Earth? New insights from a 3-D climate-carbon model. *Earth Planet Sci Lett* 474:97–109.
14. Keller MA, Kampjut D, Harrison SA, Ralser M (2017) Sulfate radicals enable a non-enzymatic Krebs cycle precursor. *Nat Ecol Evol* 1:83.
15. Dora Tang TY, et al. (2014) Fatty acid membrane assembly on coacervate microdroplets as a step towards a hybrid protocell model. *Nat Chem* 6:527–533.
16. Powner MW, Sutherland JD, Szostak JW (2010) Chemoselective multicomponent one-pot assembly of purine precursors in water. *J Am Chem Soc* 132:16677–16688.
17. Konhauser K, Riding R (2012) Bacterial biomineralization. *Fundamentals of Geobiology* (Wiley–Blackwell, Hoboken, NJ), pp 105–130.
18. Knoll AH (2003) Biomineralization and evolutionary history. *Rev Mineral Geochem* 54:329–356.
19. Liu X, et al. (2016) Tracing Earth's O2 evolution using Zn/Fe ratios in marine carbonates. *Geochem Persp Let* 2:24–34.
20. Garvin J, Buick R, Anbar AD, Arnold GL, Kaufman AJ (2009) Isotopic evidence for an aerobic nitrogen cycle in the latest Archean. *Science* 323:1045–1048.
21. Planavsky NJ, et al. (2014) Earth history. Low mid-Proterozoic atmospheric oxygen levels and the delayed rise of animals. *Science* 346:635–638.
22. Grotzinger JP, Kasting JF (1993) New constraints on Precambrian ocean composition. *J Geol* 101:235–243.
23. Buick R, Dunlop J (1990) Evaporitic sediments of early Archaean age from the Warrawoona Group, North Pole, Western Australia. *Sedimentology* 37:247–277.
24. Blättler C, et al. (2017) Constraints on ocean carbonate chemistry and pCO2 in the Archaean and Palaeoproterozoic. *Nat Geosci* 10:41–45.
25. Friend CR, Nutman AP, Bennett VC, Norman M (2008) Seawater-like trace element signatures (REE+ Y) of Eoarchaean chemical sedimentary rocks from southern West Greenland, and their corruption during high-grade metamorphism. *Contrib Mineral Petrol* 155:229–246.
26. Kempe S, Degens ET (1985) An early soda ocean? *Chem Geol* 53:95–108.
27. Sleep NH, Zahnle K, Neuhoff PS (2001) Initiation of clement surface conditions on the earliest Earth. *Proc Natl Acad Sci USA* 98:3666–3672.
28. Stüeken E, Buick R, Schauer A (2015) Nitrogen isotope evidence for alkaline lakes on late Archean continents. *Earth Planet Sci Lett* 411:1–10.
29. Halevy I, Bachan A (2017) The geologic history of seawater pH. *Science* 355:1069–1071.
30. Berner RA (2004) *The Phanerozoic Carbon Cycle: CO2 and O2* (Oxford Univ Press, New York).
31. Walker JC, Hays P, Kasting JF (1981) A negative feedback mechanism for the long-term stabilization of Earth's surface temperature. *J Geophys Res Oceans* 86:9776–9782.
32. Brady PV, Gíslason SR (1997) Seafloor weathering controls on atmospheric CO 2 and global climate. *Geochim Cosmochim Acta* 61:965–973.
33. Coogan LA, Dosso SE (2015) Alteration of ocean crust provides a strong temperature dependent feedback on the geological carbon cycle and is a primary driver of the Sr-isotopic composition of seawater. *Earth Planet Sci Lett* 415:38–46.
34. Berner RA, Caldeira K (1997) The need for mass balance and feedback in the geochemical carbon cycle. *Geology* 25:955–956.
35. Franck S, Kossacki KJ, von Bloh W, Bounama C (2002) Long-term evolution of the global carbon cycle: Historic minimum of global surface temperature at present. *Tellus B Chem Phys Meterol* 54:325–343.
36. Krissansen-Totton J, Catling DC (2017) Constraining climate sensitivity and continental versus seafloor weathering using an inverse geological carbon cycle model. *Nat Commun* 8:15423.
37. Taylor L, Banwart S, Leake J, Beerling DJ (2011) Modeling the evolutionary rise of ectomycorrhiza on sub-surface weathering environments and the geochemical carbon cycle. *Am J Sci* 311:369–403.
38. Moulton KL, West J, Berner RA (2000) Solute flux and mineral mass balance approaches to the quantification of plant effects on silicate weathering. *Am J Sci* 300:539–570.
39. Arthur M, Fahey T (1993) Controls on soil solution chemistry in a subalpine forest in north-central Colorado. *Soil Sci Soc Am J* 57:1122–1130.
40. Krissansen-Totton J, Buick R, Catling DC (2015) A statistical analysis of the carbon isotope record from the Archean to Phanerozoic and implications for the rise of oxygen. *Am J Sci* 315:275–316.
41. Shirey SB, Richardson SH (2011) Start of the Wilson cycle at 3 Ga shown by diamonds from subcontinental mantle. *Science* 333:434–436.
42. Delavault H, Chauvel C, Thomassot E, Devey CW, Dazas B (2016) Sulfur and lead isotopic evidence of relic Archean sediments in the Pitcairn mantle plume. *Proc Natl Acad Sci USA* 113:12952–12956.
43. Moore WB, Webb AAG (2013) Heat-pipe Earth. *Nature* 501:501–505.
44. Foley SF, Buhre S, Jacob DE (2003) Evolution of the Archaean crust by delamination and shallow subduction. *Nature* 421:249–252.
45. Debaille V, et al. (2013) Stagnant-lid tectonics in early Earth revealed by 142 Nd variations in late Archean rocks. *Earth Planet Sci Lett* 373:83–92.
46. Kopparapu RK, et al. (2013) Habitable zones around main-sequence stars: New estimates. *Astrophys J* 765:131.
47. Gough D (1981) Solar interior structure and luminosity variations. *Sol Phys* 74:21–34.
48. Sleep NH (2010) The Hadean-Archaean environment. *Cold Spring Harb Perspect Biol* 2:a002527.
49. Foley BJ (2015) The role of plate tectonic-climate coupling and exposed land area in the development of habitable climates on rocky planets. *Astrophys J* 812:36.
50. Trainer MG, et al. (2006) Organic haze on Titan and the early Earth. *Proc Natl Acad Sci USA* 103:18035–18042.
51. Higgins JA, Schrag DP (2015) The Mg isotopic composition of Cenozoic seawater–Evidence for a link between Mg-clays, seawater Mg/Ca, and climate. *Earth Planet Sci Lett* 416:73–81.
52. Goldblatt C, Zahnle K (2010) Clouds and the faint young sun paradox. *Clim Past Discuss* 6:1163–1207.
53. Som SM, et al. (2016) Earth's air pressure 2.7 billion years ago constrained to less than half of modern levels. *Nat Geosci* 9:448–451.
54. Goldblatt C, et al. (2009) Nitrogen-enhanced greenhouse warming on early Earth. *Nat Geosci* 2:891–896.
55. Nakamura K, Kato Y (2004) Carbonatization of oceanic crust by the seafloor hydrothermal activity and its significance as a CO 2 sink in the early Archean. *Geochim Cosmochim Acta* 68:4595–4618.
56. Shibuya T, et al. (2013) Decrease of seawater CO 2 concentration in the late Archean: An implication from 2.6 Ga seafloor hydrothermal alteration. *Precambrian Res* 236:59–64.
57. Shibuya T, et al. (2012) Depth variation of carbon and oxygen isotopes of calcites in Archean altered upperoceanic crust: Implications for the CO 2 flux from ocean to oceanic crust in the Archean. *Earth Planet Sci Lett* 321:64–73.
58. Kitajima K, Maruyama S, Utsunomiya S, Liou J (2001) Seafloor hydrothermal alteration at an Archaean mid-ocean ridge. *J Metamorph Geol* 19:583–599.
59. Korenaga J (2008) Plate tectonics, flood basalts and the evolution of Earth's oceans. *Terra Nova* 20:419–439.
60. Schwartzman D (2002) *Life, Temperature, and the Earth: The Self-Organizing Biosphere* (Columbia Univ Press, New York).
61. Abbot DS, Cowan NB, Ciesla FJ (2012) Indication of insensitivity of planetary weathering behavior and habitable zone to surface land fraction. *Astrophys J* 756:178.
62. Catling DC, Kasting JF (2017) *Atmospheric Evolution on Inhabited and Lifeless Worlds* (Cambridge Univ Press, Cambridge, UK).

Chapter 7 - Conclusions

"So much universe, and so little time." – Terry Pratchett

The first three chapters of this thesis explored one possible approach to exoplanet life detection, namely the idea of using atmospheric chemical disequilibrium as a generalized sign of life. Chapter 2 presented the most straightforward way of quantifying disequilibrium and applied this to the solar system planets. The modern Earth has by far the largest disequilibrium of the solar system planets due to the coexistence of atmospheric oxygen with nitrogen and water. The coexistence of these three species was then argued to be a more compelling biosignature than oxygen alone because their collective persistence requires continuous replenishment. Chapter 3 then explored possible disequilibrium biosignatures on the early Earth. It was determined that the Archean Earth possessed a large, biogenic disequilibrium due to the coexistence of methane and carbon dioxide in a nitrogen dominated atmosphere with liquid water. The persistence of this combination of species required continuous replenishment of methane, and on the early Earth biological methanogenesis was the source.

Crucially, these chapters also showed that the magnitude of thermodynamic disequilibrium, as measured by available Gibbs free energy, is not in and of itself diagnostic of life. For example, the abiotic disequilibrium on modern Mars is comparable in magnitude to our estimates of the disequilibrium on the inhabited Precambrian Earth (Chapter 3). In fact, the large disequilibrium on modern Mars is a compelling antibiosignature: the disequilibrium between CO and O_2 is maintained by photochemical dissociation. CO is readily consumed by microbes, and so the fact that this uneaten free lunch persists in the martian atmosphere allows the maximum subsurface biomass to be constrained (Sholes et al. 2019). The broader point is that planetary context is important for interpreting any atmospheric disequilibrium. Consideration of reaction kinetics is especially crucial: Given the existence of atmospheric disequilibrium, the next logical questions are what gas fluxes are required to maintain this state and could such fluxes plausibly be produced by known non-biological processes? If the observed disequilibrium cannot be sustained by any known abiotic process, then the argument for biogenicity becomes more compelling.

Chapter 3 provided an example study of disequilibrium kinetics by estimating the methane fluxes required to sustain the CH_4+CO_2 disequilibrium, and it explored whether non-biological processes such as water-rock reactions, impacts, or outgassing could sustain such a disequilibrium. Calculations showed that known abiotic methane production mechanisms could sustain, at most, around 0.1% atmospheric CH_4. Biogenic fluxes on the Archean Earth likely resulted in much higher concentrations of methane, and so this kinetic disequilibrium involving methane is a potentially useful biosignature for Archean Earth-like exoplanets. Chapter 3 also explored other contextual clues that could help disentangle biogenic methane from non-

biological processes. It was argued that the absence of CO would support the biogenicity of CH_4 and CO_2 because it is challenging for non-biological processes to simultaneously produce the most oxidized (CO_2) and reduced (CH_4) forms of carbon without the redox intermediate CO. Additionally, life might be expected to consume any CO. Subsequent work has confirmed that low/absent CO (in the presence of CH_4 and CO_2) is a good indicator of biogenicity, but that the coexistence of CH_4+CO+CO_2 could potentially be explained by either nonbiological CH_4 production or by biomass burning of a terrestrial, photosynthetic biosphere (Schwieterman et al. 2019).

Evidently, further work is needed to investigate these kinetic and contextual considerations. There is already a sizeable literature exploring abiotic oxygen accumulation, including the kinetics of oxygen production and destruction, and possible environmental clues for disentangling biogenic oxygen from false positive scenarios (Domagal-Goldman et al. 2014; Harman et al. 2018; Luger & Barnes 2015; Meadows 2017; Wordsworth & Pierrehumbert 2014). The work in this thesis suggests a similarly detailed exploration for methane plus carbon dioxide disequilibrium biosignatures would be useful. This is especially pertinent since recent work using Xe isotope proxies has revealed that atmospheric CH_4 abundances on the early Earth were likely ~>0.5% (Zahnle et al. 2019), above the threshold we derive for biogenicity. Additionally, Chapters 3 and 4 argued that if life is common in the cosmos then this methane disequilibrium is potentially more common than oxygen biosignatures due to the relative simplicity of methanogenesis and the obstacles to accumulating oxygen rich atmospheres (e.g. Lehmer et al. 2018). Crucially, Chapter 4 showed that anoxic CH_4+CO_2 biosignatures are more easily detectable with the upcoming JWST than oxygen or ozone biosignatures. This suggests that further exploration of this disequilibrium biosignatures, including kinetics, possible false positives, and contextual discriminators, is both necessary and timely.

One of the key conclusions of Chapter 4 is that JWST observations of nearby transiting planets could reveal atmospheres that are strongly suggestive of anoxic biospheres. However, confirmation of biogenicity would probably require follow-up observations with future telescopes. This subject was explored in a National Academies of Sciences Decadal Survey white paper (Krissansen-Totton et al. 2019). This is omitted from this thesis in the interests of brevity, but the key finding is that proposed future telescopes like the Large Ultraviolet Optical Infrared (LUVOIR) survey telescope could provide much stronger CH_4 abundance constraints (and therefore a more compelling case for biogenicity) than JWST.

Motivated by the importance of establishing the planetary context for biosignature interpretation, the second half of this thesis explored the controls on habitability for terrestrial planets. Specifically, the maintenance of habitability on Earth by the carbon cycle was investigated as an analog for the processes that may buffer climate on other terrestrial exoplanets. Fortunately, Earth's geologic record provides data that can be used to constrain the operation of the carbon cycle. In Chapter 5, inverse analyses of Earth's carbon cycle since

100 Ma was presented where pCO_2, temperature, ocean pH, and seafloor weathering proxies were used to constrain unknown parameters.

Three important conclusions emerged. First, the temperature dependence of continental silicate weathering is necessarily much weaker than is commonly assumed in existing carbon cycle models. The inverse analysis reveals the e-folding temperature must be 17-48 K, whereas a range of 5-15 K is typically used. A less efficient continental weathering thermostat allows for a greater role for the seafloor weathering buffer on the early Earth (see chapter 6). Second, the Earth system climate sensitivity, which is defined as the long-term response of mean surface temperature to a CO_2 doubling, is likely high ($5.6^{1.3}_{-1.2}$ K). Third, since 100 Ma, processes unrelated to changes in climate have conspired to approximately double the continental weathering flux and draw down CO_2. Chapter 5 suggested that continental uplift and changing land fraction may be partially responsible. In sum, the analysis validated our carbon cycle model and provided data-driven constraints on the key parameters that dictate how the carbon cycle operates on geological timescales

It is worth noting the conclusions in Chapter 5 have implications for the current anthropogenic perturbation to the carbon cycle. The weaker temperature dependence of continental silicate weathering we derived suggests the time required for recovery from anthropogenic CO_2 injection will be longer than has been previously anticipated (Archer et al. 2009). Additionally, the Earth system climate sensitivity we derived is considerably larger than so-called fast feedback climate sensitivities obtained from GCMs and other atmosphere-ocean models (IPCC 2014). This is consistent with previous paleoclimate analyses (Park & Royer 2011; Royer et al. 2012) and implies that prolonged anthropogenic forcing could result in larger-than-anticipated changes in climate on millennial timescales.

Having validated the carbon cycle model over the last 100 Ma and used proxy data to constrain key carbon cycle parameters, the model was then applied to all Earth history to better understand the climate and ocean chemistry of the Archean Earth (Chapter 6). As anticipated in Chapter 5, an elevated role for seafloor weathering as a climate buffer in the Archean was found to be likely. The combined regulatory effect of continental and seafloor weathering feedbacks buffered the Archean climate to temperate (<40°C) values with slightly acidic to neutral ocean pH. Even with virtually no subaerial land and/or large methane abundances, a hot Archean (>50°C) is unlikely. An alkaline Archean ocean was also excluded.

Applying this understanding of Earth's carbon cycle to other terrestrial exoplanets is the subject of future work. But from the analyses already presented some tentative conclusions can be drawn. The strong temperature dependence of seafloor weathering inferred in Chapter 5 could enhance the habitability of exoplanet waterworlds, rocky planets entirely covered in ocean. Previous studies that omitted the temperature dependence of seafloor weathering concluded that the climate of waterworlds are poorly

buffered against changes in insolation (Abbot et al. 2012). Our quantitative approach to Earth's carbon cycle also highlights the large uncertainties in Earth's climate history. Even with parameters constrained by data from the last 100 Ma, when the model is extended to all of Earth history a broad range of CO_2 and temperature trajectories are possible due to uncertainties in Earth's thermal evolution, continental land fraction, and biogenic enhancements of weathering. For exoplanets, where no geologic data is available, uncertainties in the relevant carbon cycling parameters will be even greater. This suggests that it may be challenging to test the habitable zone concept by looking for a simple inverse relationship between stellar insolation and atmospheric CO_2 (e.g. Bean et al. 2017).

Chapter 8 - References

Note that this reference list excludes citations in reproduced open access Chapters 3, 5, and 6 since these contain their own stand-alone reference lists.

Abbot, D. S., et al. (2012). Indication of insensitivity of planetary weathering behavior and habitable zone to surface land fraction. *The Astrophysical Journal, 756*(2), 178.

Agol, E., et al. (2015). The Center of Light: Spectroastrometric Detection of Exomoons. *The Astrophysical Journal, 812*(1), 5.

Anderson, G. M. (2005). *Thermodynamics of natural systems*: Cambridge University Press.

Anderson, G. M., & Crerar, D. A. (1993). *Thermodynamics in geochemistry: the equilibrium model*: Oxford University Press.

Andrews, D. G. (2010). *An introduction to atmospheric physics*: Cambridge University Press.

Appelo, C. A. J., & Postma, D. (2005). *Geochemistry, groundwater and pollution*: CRC press.

Archer, D. (2005). Fate of fossil fuel CO2 in geologic time. *Journal of Geophysical Research: Oceans, 110*(C9).

Archer, D., et al. (2009). Atmospheric lifetime of fossil fuel carbon dioxide. *Annual Review of Earth and Planetary Sciences, 37*, 117-134.

Arney, G., et al. (2015). *Hazy Archean Earth as an Analog for Hazy Earthlike Exoplanets.* Paper presented at the American Astronomical Society Meeting Abstracts.

Arney, G. N., et al. (2017). Pale orange dots: the impact of organic haze on the habitability and detectability of Earthlike exoplanets. *The Astrophysical Journal, 836*(1), 49.

Arnold, L., et al. (2002). A test for the search for life on extrasolar planets-Looking for the terrestrial vegetation signature in the Earthshine spectrum. *Astronomy & Astrophysics, 392*(1), 231-237.

Arrhenius, S. (1918). *The destinies of the stars*: GP Putnam's Sons.

Aspen Technology Inc., D. (2000). *Aspen Plus: Getting Started Modeling Processes with Electrolytes*. Retrieved from Cambridge, MA:

Bada, J. L., & Miller, S. L. (1968). Ammonium ion concentration in the primitive ocean. *Science, 159*(3813), 423-425.

Baines, K. H., et al. (2014). The Atmospheres of the Terrestrial Planets: Clues to the Origins and Early Evolution of Venus, Earth, and Mars. *Comparative Climatology of Terrestrial Planets*, 137.

Ballard, S., & Johnson, J. A. (2016). The Kepler dichotomy among the M dwarfs: half of systems contain five or more coplanar planets. *The Astrophysical Journal, 816*(2), 66.

Balzhiser, R. E., et al. (1972). *Chemical engineering thermodynamics; the study of energy, entropy, and equilibrium*. Englewood Cliffs, N.J.,: Prentice-Hall.

Barman, T. (2007). Identification of absorption features in an extrasolar planet atmosphere. *The Astrophysical Journal Letters, 661*(2), L191.

Barstow, J. K., et al. (2015). Transit spectroscopy with James Webb Space Telescope: systematics, starspots and stitching. *Monthly Notices of the Royal Astronomical Society, 448*(3), 2546-2561.

Barstow, J. K., & Irwin, P. G. (2016). Habitable worlds with JWST: transit spectroscopy of the TRAPPIST-1 system? *Monthly Notices of the Royal Astronomical Society: Letters, 461*(1), L92-L96.

Batalha, N. E., et al. (2018). Strategies for Constraining the Atmospheres of Temperate Terrestrial Planets with JWST. *The Astrophysical Journal Letters, 856*(2), L34.

Batalha, N. E., et al. (2017). PandExo: a community tool for transiting exoplanet science with JWST & HST. *Publications of the Astronomical Society of the Pacific, 129*(976), 064501.

Bean, J. L., et al. (2017). A statistical comparative planetology approach to the hunt for habitable exoplanets and life beyond the solar system. *The Astrophysical Journal Letters, 841*(2), L24.

Beer, C., et al. (2010). Terrestrial gross carbon dioxide uptake: global distribution and covariation with climate. *Science, 329*(5993), 834-838.

Bekker, A., & Holland, H. D. (2012). Oxygen overshoot and recovery during the early Paleoproterozoic. *Earth And Planetary Science Letters, 317*, 295-304. doi:DOI 10.1016/j.epsl.2011.12.012

Bekker, A., et al. (2008). Fractionation between inorganic and organic carbon during the Lomagundi (2.22-2.1 Ga) carbon isotope excursion. *Earth And Planetary Science Letters, 271*(1-4), 278-291. doi:DOI 10.1016/j.epsl.2008.04.021

Bell, E. A., et al. (2015). Potentially biogenic carbon preserved in a 4.1 billion-year-old zircon. *Proceedings of the National Academy of Sciences, 112*(47), 14518-14521.

Belu, A., et al. (2011). Primary and secondary eclipse spectroscopy with JWST: exploring the exoplanet parameter space. *Astronomy & Astrophysics, 525*, A83.

Benneke, B., & Seager, S. (2012). Atmospheric retrieval for super-Earths: uniquely constraining the atmospheric composition with transmission spectroscopy. *The Astrophysical Journal, 753*(2), 100.

Berner, R. A. (2004). *The Phanerozoic Carbon Cycle: CO2 and O2*. Oxford: Oxford University Press.

Betts, J., & Holland, H. (1991). The oxygen content of ocean bottom waters, the burial efficiency of organic carbon, and the regulation of atmospheric oxygen. *Palaeogeography, Palaeoclimatology, Palaeoecology, 97*(1), 5-18.

Bézard, B., et al. (2002). Carbon monoxide on Jupiter: Evidence for both internal and external sources. *Icarus, 159*(1), 95-111.

Bjerrum, C. J., & Canfield, D. E. (2004). New insights into the burial history of organic carbon on the early Earth. *Geochem. Geophys. Geosys., 5*.

Blandford, R., et al. (2010). Retrieved from

Blaney, D. L., et al. (1988). *Mars: Spectral signatures seen and unseen*. Paper presented at the In Lunar and Planetary Inst., MEVTV Workshop on Nature and Composition of Surface Units on Mars p 25-27 (SEE N88-29654 23-91).

Bolcar, M. R., et al. (2016). *Initial technology assessment for the Large-Aperture UV-Optical-Infrared (LUVOIR) mission concept study.* Paper presented at the Space Telescopes and Instrumentation 2016: Optical, Infrared, and Millimeter Wave.

Botet, R., et al. (1997). Mean-field approximation of Mie scattering by fractal aggregates of identical spheres. *Applied optics, 36*(33), 8791-8797.

Bougher, S. W., et al. (1997). *Venus II--geology, Geophysics, Atmosphere, and Solar Wind Environment* (Vol. 1): University of Arizona Press.

Brandt, T. D., & Spiegel, D. S. (2014). Prospects for detecting oxygen, water, and chlorophyll on an exo-Earth. *Proceedings of the National Academy of Sciences, 111*(37), 13278-13283.

Broecker, W. S. (1970). A boundary condition on the evolution of atmospheric oxygen. *Journal of Geophysical Research, 75*(18), 3553-3557.

Buchner, J., et al. (2014). X-ray spectral modelling of the AGN obscuring region in the CDFS: Bayesian model selection and catalogue. *Astronomy & Astrophysics, 564*, A125.
Burcat, A., & Ruscic, B. (2005). *Third Millennium ideal gas and condensed phase thermochemical database for combustion with updates from active thermochemical tables* (ANL-05/20). Retrieved from Oak Ridge, TN:
Burke, C. J., et al. (2015). Terrestrial planet occurrence rates for the Kepler GK dwarf sample. *The Astrophysical Journal, 809*(1), 8.
Byrd, R. H., et al. (2000). A trust region method based on interior point techniques for nonlinear programming. *Mathematical Programming, 89*(1), 149-185.
Byrd, R. H., et al. (1999). An interior point algorithm for large-scale nonlinear programming. *SIAM Journal on Optimization, 9*(4), 877-900.
Cahoy, K. L., et al. (2010). Exoplanet albedo spectra and colors as a function of planet phase, separation, and metallicity. *The Astrophysical Journal, 724*(1), 189.
Campbell, I. H., & Allen, C. M. (2008). Formation of supercontinents linked to increases in atmospheric oxygen. *Nature Geosci., 1*(8), 554-558.
Canfield, D. E. (2004). The evolution of the Earth surface sulfur reservoir. *Am. J. Sci., 304*(10), 839-861.
Canfield, D. E. (2014). Proterozoic Atmospheric Oxygen. In H. D. Holland & K. K. Turekian (Eds.), *Treatise on Geochemistry* (2 ed., Vol. 6, pp. 197-216). Oxford: Elsevier.
Capone, D. G., et al. (2006). Geochemistry. Follow the nitrogen. *Science (New York, NY), 312*(5774), 708.
Cash, W. (2006). Detection of Earth-like planets around nearby stars using a petal-shaped occulter. *Nature, 442*(7098), 51-53.
Catling, D., & Bergsman, D. (2009). *Using atmospheric composition as a metric for detecting life on habitable planets.* Paper presented at the AGU Fall Meeting Abstracts.
Catling, D., & Bergsman, D. (2010). On detecting exoplanet biospheres from atmospheric chemical disequilibrium. *LPI Contributions, 1538*, 5533.
Catling, D., & Kasting, J. F. (2007). Planetary atmospheres and life. In W. T. Sullivan & J. A. Baross (Eds.), *Planets and Life: The Emerging Science of Astrobiology* (pp. 91-116). Cambridge: Cambridge Univ. Press.
Catling, D. C. (2014). The Great Oxidation Event Transition. In H. D. Holland & K. K. Turekian (Eds.), *Treatise on Geochemistry* (Vol. 6, pp. 177-195). New York: Elsevier.
Catling, D. C. (2015a). Planetary Atmospheres. In G. Schubert (Ed.), *Treatise on Geophysics (2nd Ed.)* (2nd ed., Vol. 10, pp. 429-472). New York: Elsevier.
Catling, D. C. (2015b). Planetary Atmospheres. In G. Schubert (Ed.), *Treatise on Geophysics* (Vol. 10). in press: Elsevier.
Catling, D. C., & Claire, M. W. (2005). How Earth's atmosphere evolved to an oxic state: a status report. *Earth and Planetary Science Letters, 237*(1-2), 1-20.
Catling, D. C., et al. (2005). Why O_2 is required by complex life on habitable planets and the concept of planetary "oxygenation time". *Astrobiology, 5*, 415-438.
Catling, D. C., & Kasting, J. F. (2017). *Atmospheric Evolution on Inhabited and Lifeless Worlds*: Cambridge University Press.
Catling, D. C., et al. (2018). Exoplanet Biosignatures: A Framework for Their Assessment. *Astrobiology, 18*(6), 709-738. doi:10.1089/ast.2017.1737
Catling, D. C., et al. (2001a). Biogenic methane, hydrogen escape, and the irreversible oxidation of early Earth. *Science, 293*, 839-843.

Catling, D. C., et al. (2001b). Biogenic methane, hydrogen escape, and the irreversible oxidation of early Earth. *Science, 293*(5531), 839-843.
Charbonneau, D., et al. (2002). Detection of an extrasolar planet atmosphere. *The Astrophysical Journal, 568*(1), 377.
Charnay, B., et al. (2015). 3D modeling of GJ1214b's atmosphere: vertical mixing driven by an anti-Hadley circulation. *submitted to ApJ.*
Claire, M. W., et al. (2006). Biogeochemical modeling of the rise of oxygen. *Geobiology, 4*(4), 239-269.
Claire, M. W., et al. (2012). The evolution of solar flux from 0.1 nm to 160 μm: quantitative estimates for planetary studies. *The Astrophysical Journal, 757*(1), 95.
Clark, R. N., et al. (2007). USGS digital spectral library splib06a, Digital Data Series 231. from US Geological Survey Reston, VA http://speclab.cr.usgs.gov/spectral.lib06
Cleveland, W. S. (1979). Robust Locally Weighted Regression and Smoothing Scatterplots. *Journal of the American Statistical Association, 74*(368), 829-836. doi:Doi 10.2307/2286407
Cockell, C. S., et al. (2009). Darwin-a mission to detect and search for life on extrasolar planets. *Astrobiology, 9*(1), 1-22.
Conrad, R. (1996). Soil microorganisms as controllers of atmospheric trace gases (H2, CO, CH4, OCS, N2O, and NO). *Microbiological reviews, 60*(4), 609-640.
Conselice, C. J., et al. (2016). The evolution of galaxy number density at z< 8 and its implications. *The Astrophysical Journal, 830*(2), 83.
Cordier, D., et al. (2009). An estimate of the chemical composition of Titan's lakes. *The Astrophysical Journal Letters, 707*(2), L128.
Covey, C., et al. (2013). The greenhouse effect and climate feedbacks. In S. J. Mackwell, A. A. Simon-Miller, J. W. Harder, & M. A. Bullock (Eds.), *Comparative Climatology of Terrestrial Planets*: University of Arizona Press.
Cowan, N. B., & Abbot, D. S. (2014). Water Cycling Between Ocean and Mantle: Super-Earths Need Not be Waterworlds. *arXiv preprint arXiv:1401.0720*.
Cowan, N. B., et al. (2009). Alien maps of an ocean-bearing world. *The Astrophysical Journal, 700*(2), 915.
Cowan, N. B., et al. (2011). Rotational variability of Earth's polar regions: implications for detecting snowball planets. *The Astrophysical Journal, 731*(1), 76.
Cowan, N. B., & Strait, T. E. (2013). Determining reflectance spectra of surfaces and clouds on exoplanets. *The Astrophysical Journal Letters, 765*(1), L17.
Crisp, D. (1990). Infrared radiative transfer in the dust-free Martian atmosphere. *Journal of Geophysical Research: Solid Earth (1978–2012), 95*(B9), 14577-14588.
Crisp, D. (1997). Absorption of sunlight by water vapor in cloudy conditions: A partial explanation for the cloud absorption anomaly. *Geophysical Research Letters, 24*(5), 571-574.
Crow, C. A., et al. (2011). Views from EPOXI: colors in our solar system as an analog for extrasolar planets. *The Astrophysical Journal, 729*(2), 130.
Dahl, T. W., et al. (2010). Devonian rise in atmospheric oxygen correlated to the radiations of terrestrial plants and large predatory fish. *Proc. Nat. Acad. Sci. U.S.A., 107*(42), 17911-17915.
Dalcanton, J., et al. (2015). From Cosmic Birth to Living Earths: The Future of UVOIR Space Astronomy. *arXiv preprint arXiv:1507.04779*.

Davies, G. F. (1998). Topography: a robust constraint on mantle fluxes. *Chemical geology, 145*(3), 479-489.
Davies, P. (1995). *Are we alone?: philosophical implications of the discovery of extraterrestrial life*: Penguin.
de Wit, J., et al. (2016). A combined transmission spectrum of the Earth-sized exoplanets TRAPPIST-1 b and c. *Nature, 537*(7618), 69.
De Wit, J., et al. (2018). Atmospheric reconnaissance of the habitable-zone Earth-sized planets orbiting TRAPPIST-1. *Nature Astronomy, 2*(3), 214.
de Wit, M. J., & Furnes, H. (2016). 3.5-Ga hydrothermal fields and diamictites in the Barberton Greenstone Belt—Paleoarchean crust in cold environments. *Science advances, 2*(2), e1500368.
del Giorgio, P. A., & Duarte, C. M. (2002). Respiration in the open ocean. *Nature, 420*(6914), 379.
Delorme, P., et al. (2013). Direct-imaging discovery of a 12–14 Jupiter-mass object orbiting a young binary system of very low-mass stars. *Astronomy & Astrophysics, 553*, L5.
Delrez, L., et al. (2018). Early 2017 observations of TRAPPIST-1 with Spitzer. *Monthly Notices of the Royal Astronomical Society*.
Deming, D., et al. (2009). Discovery and characterization of transiting super Earths using an all-sky transit survey and follow-up by the James Webb Space Telescope. *Publications of the Astronomical Society of the Pacific, 121*(883), 952.
Deming, D., et al. (2013). Infrared transmission spectroscopy of the exoplanets HD 209458b and XO-1b using the Wide Field Camera-3 on the Hubble Space Telescope. *The Astrophysical Journal, 774*(2), 95.
Des Marais, D. J. (1994). Tectonic control of the crustal organic carbon reservoir during the Precambrian. *Chemical Geology, 114*(3), 303-314.
Des Marais, D. J. (1997). Isotopic evolution of the biogeochemical carbon cycle during the Proterozoic Eon. *Organic Geochemistry, 27*, 185-193.
Des Marais, D. J., et al. (2002a). Remote sensing of planetary properties and biosignatures on extrasolar terrestrial planets. *Astrobiology, 2*(2), 153-181.
Des Marais, D. J., et al. (2002b). Remote sensing of planetary properties and biosignatures on extrasolar terrestrial planets. *Astrobiology, 2*, 153-181.
Des Marais, D. J., et al. (1992). Carbon isotope evidence for the stepwise oxidation of the Proterozoic environment. *Nature, 359*, 605-609.
Devol, A. H. (2008). Nitrogen in the marine environment. In D. G. Capone, D. A. Bronk, M. R. Mulholland, & E. J. Carpenter (Eds.), *Nitrogen in the marine environment* (pp. 263-301): Academic Press.
Dlugokencky, E., et al. (1998). Continuing decline in the growth rate of the atmospheric methane burden. *Nature, 393*(6684), 447-450.
Domagal-Goldman, S., et al. (2015). *A week in the life: an astrobiology-focused strategy for a LUVOIR (Large UV Optical-IR) telescope*. Paper presented at the Astrobiology Science Conference, Chicago.
Domagal-Goldman, S. D., et al. (2008). Organic haze, glaciations and multiple sulfur isotopes in the Mid-Archean Era. *Earth and Planetary Science Letters, 269*(1), 29-40.
Domagal-Goldman, S. D., et al. (2014). Abiotic ozone and oxygen in atmospheres similar to prebiotic Earth. *The Astrophysical Journal, 792*(2), 90.

Driese, S. G., et al. (2011). Neoarchean paleoweathering of tonalite and metabasalt: Implications for reconstructions of 2.69 Ga early terrestrial ecosystems and paleoatmospheric chemistry. *Precambrian Research, 189*(1), 1-17.

Ducrot, E., et al. (2018). The 0.6-4.55$\mu $ m broadband transmission spectra of TRAPPIST-1 planets. *arXiv preprint arXiv:1807.01402*.

Eriksson, G. (1971). Thermodynamics studies of high temperature equilibria. 3. SOLGAS, a computer program for calculating composition and heat condition of an equilibrium mixture. *Acta chemica scandinavica, 25*(7), 2651-&.

Eriksson, G. (1975). Thermodynamic studies of high-temperature equilibria. 12. SOLGASMIX, a computer-program for calculation of equilibrium compositions in multiphase systems. *Chemica Scripta, 8*(3), 100-103.

Estrada, E. (2012). Returnability as a criterion of disequilibrium in atmospheric reactions networks. *Journal of Mathematical Chemistry, 50*(6), 1363-1372.

Evans, T. M., et al. (2013). The deep blue color of HD 189733b: Albedo measurements with Hubble Space Telescope/Space Telescope Imaging Spectrograph at visible wavelengths. *The Astrophysical Journal Letters, 772*(2), L16.

Fallick, A., et al. (2008). The ancient anoxic biosphere was not as we know it *Biosphere Origin and Evolution* (pp. 169-188): Springer.

Fan, J., & Yao, Q. (2003). *Nonlinear time series : nonparametric and parametric methods*. New York: Springer.

Farquhar, J., et al. (2000). Atmospheric influence of Earth's earliest sulfur cycle. *Science, 289*(5480), 756-758.

Farquhar, J., et al. (2007). Isotopic evidence for Mesoarchaean anoxia and changing atmospheric sulphur chemistry. *Nature, 449*(7163), 706-U705. doi:Doi 10.1038/Nature06202

Farquhar, J., et al. (2014). Geologic and Geochemical Constraints on Earth's Early Atmosphere. In H. D. Holland & K. K. Turekian (Eds.), *Treatise on Geochemistry* (Vol. 6, pp. 91-138). Oxford: Elsevier.

Faure, G., & Mensing, T. M. (2005). *Isotopes : principles and applications* (3rd ed.). Hoboken, N.J.: Wiley.

Fegley, B. (2014). Venus. In H. Holland & K. K. Turekian (Eds.), *Treatise on Geochemistry (Second Edition)* (Vol. 2, pp. 127-148).

Feng, Y. K., et al. (2018). Characterizing Earth Analogs in Reflected Light: Atmospheric Retrieval Studies for Future Space Telescopes. *The Astronomical Journal, 155*(5), 200.

Feroz, F., & Hobson, M. (2008). Multimodal nested sampling: an efficient and robust alternative to Markov Chain Monte Carlo methods for astronomical data analyses. *Monthly Notices of the Royal Astronomical Society, 384*(2), 449-463.

Feroz, F., et al. (2009). MultiNest: an efficient and robust Bayesian inference tool for cosmology and particle physics. *Monthly Notices of the Royal Astronomical Society, 398*(4), 1601-1614.

Fischer, D., et al. (2018). The LUVOIR Mission Concept Study Interim Report. *arXiv preprint arXiv:1809.09668*.

Flament, N., et al. (2008). A case for late-Archaean continental emergence from thermal evolution models and hypsometry. *Earth And Planetary Science Letters, 275*(3-4), 326-336. doi:DOI 10.1016/j.epsl.2008.08.029

Foley, B. J. (2015). The role of plate tectonic–climate coupling and exposed land area in the development of habitable climates on rocky planets. *The Astrophysical Journal, 812*(1), 36.
Foreman-Mackey, D. (2016). corner. py: Scatterplot matrices in Python. *The Journal of Open Source Software, 2016*.
Foreman-Mackey, D., et al. (2013). emcee: the MCMC hammer. *Publications of the Astronomical Society of the Pacific, 125*(925), 306.
Fraine, J., et al. (2014). Water vapour absorption in the clear atmosphere of a Neptune-sized exoplanet. *Nature, 513*(7519), 526-529.
Fressin, F., et al. (2013). The false positive rate of Kepler and the occurrence of planets. *The Astrophysical Journal, 766*(2), 81.
Fujii, Y., & Kawahara, H. (2012). Mapping Earth analogs from photometric variability: Spin-orbit tomography for planets in inclined orbits. *The Astrophysical Journal, 755*(2), 101.
Gaidos, E., & Williams, D. (2004). Seasonality on terrestrial extrasolar planets: inferring obliquity and surface conditions from infrared light curves. *New Astronomy, 10*(1), 67-77.
Gaillard, F., et al. (2011). Atmospheric oxygenation caused by a change in volcanic degassing pressure. *Nature, 478*(7368), 229-233.
Gaudi, B. S., et al. (2018). The Habitable Exoplanet Observatory (HabEx) Mission Concept Study Interim Report. *arXiv preprint arXiv:1809.09674*.
Gillon, M., et al. (2017). Seven temperate terrestrial planets around the nearby ultracool dwarf star TRAPPIST-1. *Nature, 542*(7642), 456.
Giuranna, M., et al. (2019). Independent confirmation of a methane spike on Mars and a source region east of Gale Crater. *Nature Geoscience*, 1.
Glein, C. R., & Shock, E. L. (2013). A geochemical model of non-ideal solutions in the methane–ethane–propane–nitrogen–acetylene system on Titan. *Geochimica et Cosmochimica Acta, 115*, 217-240.
Goody, R. M., & Yung, Y. L. (1995). *Atmospheric radiation: theoretical basis*: Oxford university press.
Greene, T. P., et al. (2016). Characterizing transiting exoplanet atmospheres with JWST. *The Astrophysical Journal, 817*(1), 17.
Grenfell, T. C., et al. (1994). Reflection of solar radiation by the Antarctic snow surface at ultraviolet, visible, and near-infrared wavelengths. *Journal of Geophysical Research: Atmospheres (1984–2012), 99*(D9), 18669-18684.
Grimm, S. L., et al. (2018). The nature of the TRAPPIST-1 exoplanets. *Astronomy & Astrophysics, 613*, A68.
Gruber, N. (2008). The marine nitrogen cycle: overview and challenges. *Nitrogen in the marine environment*, 1-50.
Guyon, O., et al. (2005). Exoplanet imaging with a phase-induced amplitude apodization coronagraph. I. Principle. *The Astrophysical Journal, 622*(1), 744.
Guzmán-Marmolejo, A., et al. (2013). Abiotic production of methane in terrestrial planets. *Astrobiology, 13*(6), 550-559.
Haberle, R. M., et al. (2016). Early Mars. In R. M. e. a. Haberle (Ed.), *The Atmosphere and Climate of Mars*: Cambridge Univ. Press, in press.
Halevy, I., & Bachan, A. (2017). The geologic history of seawater pH. *Science, 355*(6329), 1069-1071.

Hamdani, S., et al. (2006). Biomarkers in disk-averaged near-UV to near-IR Earth spectra using Earthshine observations. *Astronomy & Astrophysics, 460*(2), 617-624.
Haqq-Misra, J. D., et al. (2008). A revised, hazy methane greenhouse for the Archean Earth. *Astrobiology, 8*(6), 1127-1137.
Harman, C., & Domagal-Goldman, S. (2018). Biosignature False Positives. In D. H. & J. Belmonte (Eds.), *Handbook of Exoplanets*: Springer.
Harman, C., et al. (2018). Abiotic O2 Levels on Planets around F, G, K, and M Stars: Effects of Lightning-produced Catalysts in Eliminating Oxygen False Positives. *The Astrophysical Journal, 866*(1), 56.
Harman, C., et al. (2015a). Abiotic O_2 Levels on Planets around F, G, K, and M Stars: Possible False Positives for Life? *The Astrophysical Journal, 812*(2), 137.
Harman, C. E., et al. (2015b). Abiotic O2 Levels on Planets around F, G, K, and M Stars: Possible False Positives for Life? . *The Astrophysical Journal, 812:137*.
Hartnett, H. E., et al. (1998). Influence of oxygen exposure time on organic carbon preservation in continental margin sediments. *Nature, 391*(6667), 572-575.
Hayes, J. M. (1994). Global methanotrophy at the Archean-Proterozoic transition. *Early life on Earth, 84*, 220-236.
Hayes, J. M., et al. (1999). The abundance of C-13 in marine organic matter and isotopic fractionation in the global biogeochemical cycle of carbon during the past 800 Ma. *Chemical Geology, 161*(1-3), 103-125. doi:Doi 10.1016/S0009-2541(99)00083-2
Hayes, J. M., & Waldbauer, J. R. (2006a). The carbon cycle and associated redox processes through time. *Philosophical Transactions of the Royal Society B: Biological Sciences, 361*(1470), 931-950.
Hayes, J. M., & Waldbauer, J. R. (2006b). The carbon cycle and associated redox processes through time. *Phil. Trans. R. Soc. B., 361*(1470), 931-950.
Heap, S. R., et al. (2008). *Detecting biomarkers in exoplanetary atmospheres with a Terrestrial Planet Finder.* Paper presented at the SPIE Astronomical Telescopes+ Instrumentation.
Hedelt, P., et al. (2013). Spectral features of Earth-like planets and their detectability at different orbital distances around F, G, and K-type stars. *Astronomy & Astrophysics, 553*, A9.
Hedges, J. I., & Keil, R. G. (1995). Sedimentary organic matter preservation: an assessment and speculative synthesis. *Marine Chemistry, 49*(2), 81-115.
Hegde, S., & Kaltenegger, L. (2013). Colors of extreme exo-Earth environments. *Astrobiology, 13*(1), 47-56.
Hegde, S., et al. (2015). Surface biosignatures of exo-Earths: Remote detection of extraterrestrial life. *Proceedings of the National Academy of Sciences, 112*(13), 3886-3891.
Hinrichs, K. U. (2002). Microbial fixation of methane carbon at 2.7 Ga: Was an anaerobic mechanism possible? *Geochemistry, geophysics, geosystems, 3*(7), 1-10.
Hitchcock, D. R., & Lovelock, J. E. (1967). Life detection by atmospheric analysis. *Icarus, 7*(1), 149-159.
Holland, H. D. (1978). *The Chemistry of the Atmosphere and Oceans*. New York: Wiley.
Holland, H. D. (1984). *The Chemical Evolution of the Atmosphere and Oceans*. Princeton: Princeton University Press.

Holland, H. D. (1994). Early Proterozoic atmospheric change *Early life on Earth* (Vol. Bengtson, S., pp. 237-244). New York: Columbia Univ. Press.
Holland, H. D. (2002). Volcanic gases, black smokers, and the Great Oxidation Event. *Geochim. Cosmochim. Acta, 66*, 3811-3826.
Holland, H. D. (2009). Why the atmosphere became oxygenated: A proposal. *Geochim. Cosmochim. Acta, 73*(18), 5241-5255.
Holser, W. T., et al. (1988). Geochemical cycles of carbon and sulfur. In C. B. Gregor, R. M. Garrels, F. T. Mackenzie, & J. B. Maynard (Eds.), *Chemical Cycles in the Evolution of the Earth* (pp. 105-173). New York: Wiley.
Howard, A. W., et al. (2010). The occurrence and mass distribution of close-in super-Earths, Neptunes, and Jupiters. *Science, 330*(6004), 653-655.
Hren, M., et al. (2009). Oxygen and hydrogen isotope evidence for a temperate climate 3.42 billion years ago. *Nature, 462*(7270), 205-208.
Huguenin, R. L., et al. (1977). Mars: photodesorption from mineral surfaces and its effects on atmospheric stability. *Icarus, 32*(3), 270-298.
Hulburt, E. (1953). Explanation of the brightness and color of the sky, particularly the twilight sky. *JOSA, 43*(2), 113-118.
Hutchinson, G. (1954). The biochemistry of the terrestrial atmosphere. In G. P. Kuiper (Ed.), *The earth as a planet* (Vol. 1, pp. 371). Chicago: The University of Chicago Press.
IPCC. (2014). *Climate change 2013: the physical science basis: Working Group I contribution to the Fifth assessment report of the Intergovernmental Panel on Climate Change*: Cambridge University Press.
Irwin, P. (2009). *Giant Planets of Our Solar System: Atmospheres, Composition, and Structure*: Springer Science & Business Media.
Irwin, P., et al. (2008). The NEMESIS planetary atmosphere radiative transfer and retrieval tool. *Journal of Quantitative Spectroscopy and Radiative Transfer, 109*(6), 1136-1150.
Irwin, P. G., et al. (2014). The transit spectra of Earth and Jupiter. *Icarus, 242*, 172-187.
Jacob, D. (1999). *Introduction to atmospheric chemistry*: Princeton University Press.
Janson, M., et al. (2013). Direct Imaging Detection of Methane in the Atmosphere of GJ 504 b. *The Astrophysical Journal Letters, 778*(1), L4.
Jiang, G., et al. (2010). Organic carbon isotope constraints on the dissolved organic carbon (DOC) reservoir at the Cryogenian–Ediacaran transition. *Earth and Planetary Science Letters, 299*(1), 159-168.
Johnson, J. W., et al. (1992). SUPCRT92: A software package for calculating the standard molal thermodynamic properties of minerals, gases, aqueous species, and reactions from 1 to 5000 bar and 0 to 1000 C. *Computers & Geosciences, 18*(7), 899-947.
Kaltenegger, L., et al. (2010). Deciphering spectral fingerprints of habitable exoplanets. *Astrobiology, 10*(1), 89-102.
Kaltenegger, L., & Traub, W. A. (2009). Transits of Earth-like planets. *The Astrophysical Journal, 698*(1), 519.
Kaltenegger, L., et al. (2007). Spectral evolution of an Earth-like planet. *The Astrophysical Journal, 658*(1), 598.
Karkoschka, E. (1994). Spectrophotometry of the jovian planets and Titan at 300-to 1000-nm wavelength: The methane spectrum. *Icarus, 111*(1), 174-192.
Karkoschka, E. (1998). Methane, Ammonia, and Temperature Measurements of the Jovian Planets and Titan from CCD–Spectrophotometry. *Icarus, 133*(1), 134-146.

Karkoschka, E., & Tomasko, M. G. (2010). Methane absorption coefficients for the jovian planets from laboratory, Huygens, and HST data. *Icarus, 205*(2), 674-694.
Karpov, I. K., et al. (1997). Modeling chemical mass transfer in geochemical processes; thermodynamic relations, conditions of equilibria and numerical algorithms. *American Journal of Science, 297*(8), 767-806.
Kasper, M., et al. (2010). *EPICS: direct imaging of exoplanets with the E-ELT.* Paper presented at the SPIE Astronomical Telescopes+ Instrumentation.
Kasting, J., et al. (2009). *Exoplanet Characterization and the Search for Life.* Paper presented at the Astro2010: The Astronomy and Astrophysics Decadal Survey.
Kasting, J. F. (2013). What caused the rise of atmospheric O-2? *Chemical Geology, 362*, 13-25. doi:DOI 10.1016/j.chemgeo.2013.05.039
Kasting, J. F., & Ackerman, T. P. (1986). Climatic consequences of very high carbon dioxide levels in the Earth's early atmosphere. *Science, 234*(4782), 1383-1385.
Kasting, J. F., et al. (1993a). Mantle redox evolution and the oxidation state of the Archean atmosphere. *J. Geol., 101*, 245-257.
Kasting, J. F., et al. (1979). Oxygen levels in the prebiological atmosphere. *Journal of Geophysical Research: Oceans, 84*(C6), 3097-3107. doi:10.1029/JC084iC06p03097
Kasting, J. F., et al. (2001). A coupled ecosystem-climate model for predicting the methane concentration in the Archean atmosphere. *Origins of Life and Evolution of the Biosphere, 31*(3), 271-285.
Kasting, J. F., et al. (1993b). Habitable zones around main sequence stars. *Icarus, 101*(1), 108-128.
Kaye, J. A., & Strobel, D. F. (1983). HCN formation on Jupiter: The coupled photochemistry of ammonia and acetylene. *Icarus, 54*(3), 417-433.
Kempe, S., & Degens, E. T. (1985). An early soda ocean? *Chemical Geology, 53*(1), 95-108.
Kempton, E. M.-R., et al. (2018). A Framework for Prioritizing the TESS Planetary Candidates Most Amenable to Atmospheric Characterization. *arXiv preprint arXiv:1805.03671, submitted to PASP*.
Khare, B. N., et al. (1984). Optical constants of organic tholins produced in a simulated Titanian atmosphere: From soft X-ray to microwave frequencies. *Icarus, 60*(1), 127-137.
Kharecha, P., et al. (2005). A coupled atmosphere–ecosystem model of the early Archean Earth. *Geobiology, 3*(2), 53-76.
Kiang, N. Y., et al. (2007). Spectral signatures of photosynthesis. II. Coevolution with other stars and the atmosphere on extrasolar worlds. *Astrobiology, 7*(1), 252-274.
Kirschke, S., et al. (2013). Three decades of global methane sources and sinks. *Nature Geoscience, 6*(10), 813-823.
Kleidon, A. (2012). How does the Earth system generate and maintain thermodynamic disequilibrium and what does it imply for the future of the planet? *Philosophical Transactions of the Royal Society A: Mathematical, Physical and Engineering Sciences, 370*(1962), 1012-1040.
Knauth, L. P., & Lowe, D. R. (2003). High Archean climatic temperature inferred from oxygen isotope geochemistry of cherts in the 3.5 Ga Swaziland Supergroup, South Africa. *Geological Society of America Bulletin, 115*(5), 566-580.
Knoll, A., et al. (1986). Secular variation in carbon isotope ratios from Upper Proterozoic successions of Svalbard and East Greenland.

Knoll, A. H. (2008). Cyanobacteria and earth history. *The Cyanobacteria: Molecular Biology, Genomics, and Evolution, 484*.
Knutson, H. A., et al. (2012). 3.6 and 4.5 μm phase curves and evidence for non-equilibrium chemistry in the atmosphere of extrasolar planet HD 189733b. *The Astrophysical Journal, 754*(1), 22.
Kopparapu, R. K., et al. (2013). Habitable zones around main-sequence stars: new estimates. *The Astrophysical Journal, 765*(2), 131.
Korablev, O., et al. (2019). No detection of methane on Mars from early ExoMars Trace Gas Orbiter observations. *Nature*, 1.
Kral, T. A., et al. (1998). Hydrogen consumption by methanogens on the early Earth. *Origins of Life and Evolution of the Biosphere, 28*(3), 311-319.
Krasnopolsky, V. A. (2015). Vertical profiles of H 2 O, H 2 SO 4, and sulfuric acid concentration at 45–75km on Venus. *Icarus, 252*, 327-333.
Krasnopolsky, V. A., & Lefèvre, F. (2013). Chemistry of the Atmospheres of Mars, Venus, and Titan. *Comparative Climatology of Terrestrial Planets, 1*, 231-275.
Krissansen-Totton, J., et al. (2016). On detecting biospheres from chemical thermodynamic disequilibrium in planetary atmospheres. *Astrobiology, 16*(1), 39-67.
Krissansen-Totton, J., et al. (2019). *Atmospheric disequilibrium as an exoplanet biosignature: Opportunities for next generation telescopes*. Astro2020 Science White Paper.
Krissansen-Totton, J., et al. (2018). Disequilibrium biosignatures over Earth history and implications for detecting exoplanet life. *Science advances, 4*(1), eaao5747.
Kump, L. R., & Barley, M. E. (2007). Increased subaerial volcanism and the rise of atmospheric oxygen 2.5 billion years ago. *Nature, 448*(7157), 1033-1036.
Kump, L. R., et al. (2009). Ocean Acidification in Deep Time. *Oceanography, 22*(4), 94-107.
Kuzuhara, M., et al. (2013). Direct imaging of a cold Jovian exoplanet in orbit around the Sun-like star GJ 504. *The Astrophysical Journal, 774*(1), 11.
Laakso, T. A., & Schrag, D. P. (2014). Regulation of atmospheric oxygen during the Proterozoic. *Earth and Planetary Science Letters, 388*, 81-91.
Lacis, A. A., & Oinas, V. (1991). A description of the correlated k distribution method for modeling nongray gaseous absorption, thermal emission, and multiple scattering in vertically inhomogeneous atmospheres. *Journal of Geophysical Research: Atmospheres, 96*(D5), 9027-9063.
Lane, N. (2002). *Oxygen: the molecule that made the world*. Oxford, UK: Oxford University Press.
Langmuir, D. (1997). Aqueous environmental geochemistry: Upper Saddle River, NJ: Prentice Hall.
Lederberg, J. (1965). Signs of life. *Nature, 207*(4992), 9-13.
Léger, A. (2000). Strategies for remote detection of life—DARWIN-IRSI and TPF missions—. *Advances in Space Research, 25*(11), 2209-2223.
Leger, A., et al. (1993). Search for primitive life on a distant planet: relevance of 02 and 03 detections. *Astronomy and Astrophysics, 277*, 309.
Lehmer, O. R., et al. (2018). The Productivity of Oxygenic Photosynthesis around Cool, M Dwarf Stars. *The Astrophysical Journal, 859*(2), 171-178.
Lenton, T. M., et al. (2014). Co-evolution of eukaryotes and ocean oxygenation in the Neoproterozoic era. *Nature Geoscience*.

Levy, H. (1971). Normal atmosphere: Large radical and formaldehyde concentrations predicted. *Science, 173*(3992), 141-143.
Lewis, G. N., & Randall, M. (1923). Thermodynamics and the free energy of chemical substances.
Lewis, J. (2012). *Physics and chemistry of the solar system*: Academic Press.
Li, Y.-H. (2000). *A compendium of geochemistry : from solar nebula to the human brain*. Princeton, N.J.: Princeton University Press.
Line, M. R., & Yung, Y. L. (2013). A Systematic Retrieval Analysis of Secondary Eclipse Spectra. III. Diagnosing Chemical Disequilibrium in Planetary Atmospheres. *The Astrophysical Journal, 779*(1), 3.
Lippincott, E. R., et al. (1967). Thermodynamic equilibria in planetary atmospheres. *The Astrophysical Journal, 147*, 753.
Livengood, T. A., et al. (2011). Properties of an Earth-like planet orbiting a Sun-like star: Earth observed by the EPOXI mission. *Astrobiology, 11*(9), 907-930.
Lodders, K. (2003). Solar system abundances and condensation temperatures of the elements. *The Astrophysical Journal, 591*(2), 1220.
Lodders, K., & Fegley, B. (1998). *The planetary scientist's companion*. New York: Oxford University Press.
Logan, G. A., et al. (1995). Terminal Proterozoic reorganization of biogeochemical cycles. *Nature, 376*(6535), 53-56.
Lorenz, R. D., et al. (2014). A radar map of Titan Seas: Tidal dissipation and ocean mixing through the throat of Kraken. *Icarus, 237*, 9-15.
Lovelock, J. E. (1965). A physical basis for life detection experiments. *Nature, 207*(997), 568-570.
Lovelock, J. E. (1975). Thermodynamics and the recognition of alien biospheres. *Proceedings of the Royal Society of London B: Biological Sciences, 189*(1095), 167-181.
Lovelock, J. E., & Margulis, L. (1974). Atmospheric homeostasis by and for the biosphere: the Gaia hypothesis. *Tellus, 26*(1-2), 2-10.
Lucey, P. G., et al. (1995). Abundance and distribution of iron on the Moon. *Science, 268*(5214), 1150-1153.
Luger, R., & Barnes, R. (2015). Extreme water loss and abiotic O2 buildup on planets throughout the habitable zones of M dwarfs. *Astrobiology, 15*(2), 119-143.
Lunine, J., et al. (1989). Present state and chemical evolution of the atmospheres of Titan, Triton, and Pluto. *Origin and evolution of planetary and satellite atmospheres, 1*, 605-665.
Lwin, Y. (2000). Chemical equilibrium by Gibbs energy minimization on spreadsheets. *International Journal of Engineering Education, 16*(4), 335-339.
Lyons, T. W., et al. (2014). The rise of oxygen in Earth's early ocean and atmosphere. *Nature, 506*(7488), 307-315. doi:Doi 10.1038/Nature13068
Macintosh, B., et al. (2015). Discovery and spectroscopy of the young Jovian planet 51 Eri b with the Gemini Planet Imager. *Science, 350*(6256), 64-67.
Macintosh, B., et al. (2014). First light of the gemini planet imager. *Proceedings of the National Academy of Sciences, 111*(35), 12661-12666.
Mahaffy, P. R., et al. (2013). Abundance and isotopic composition of gases in the martian atmosphere from the Curiosity rover. *Science, 341*(6143), 263-266.

Marcy, G. W., et al. (2014). Occurrence and core-envelope structure of 1–4× Earth-size planets around Sun-like stars. *Proceedings of the National Academy of Sciences, 111*(35), 12655-12660.
Marion, G. M. (2002). A molal-based model for strong acid chemistry at low temperatures (< 200 to 298 K). *Geochimica Et Cosmochimica Acta, 66*(14), 2499-2516.
Marion, G. M., & Kargel, J. S. (2007). *Cold aqueous planetary geochemistry with FREZCHEM: from modeling to the search for life at the limits*: Springer Science & Business Media.
Marois, C., et al. (2008). Direct imaging of multiple planets orbiting the star HR 8799. *Science, 322*(5906), 1348-1352.
Matsuo, T., & Tamura, M. (2010). *Second-earth imager for TMT (SEIT): a proposal and concept Description.* Paper presented at the SPIE Astronomical Telescopes+ Instrumentation.
Mattey, D. P. (1987). Carbon isotopes in the mantle. *Terra Cognita, 7*, 31-37.
McCord, T. B., et al. (1982). Mars- Near-infrared spectral reflectance of surface regions and compositional implications. *Journal of Geophysical Research, 87*, 3021-3032.
Meadows, V. S. (2006). Modelling the diversity of extrasolar terrestrial planets. *Proceedings of the International Astronomical Union, 1*(C200), 25-34.
Meadows, V. S. (2017). Reflections on O2 as a Biosignature in Exoplanetary Atmospheres. *Astrobiology, 17*(10), 1022-1052.
Meadows, V. S., et al. (2018a). The habitability of Proxima Centauri b: environmental states and observational discriminants. *Astrobiology, 18*(2), 133-189.
Meadows, V. S., & Barnes, R. K. (2018). Factors Affecting Exoplanet Habitability. *Handbook of Exoplanets*, 1-24.
Meadows, V. S., & Crisp, D. (1996). Ground-based near-infrared observations of the Venus nightside: The thermal structure and water abundance near the surface. *Journal of Geophysical Research: Planets (1991–2012), 101*(E2), 4595-4622.
Meadows, V. S., et al. (2018b). Exoplanet Biosignatures: Understanding Oxygen as a Biosignature in the Context of Its Environment. *Astrobiology, 18*(6), 1-33. doi:10.1089/ast.2017.1727
Melezhik, V. A., et al. (2013). Huronian-age glaciation. In V. A. e. a. Melezhik (Ed.), *Reading the Archive of Earth's Oxygenation* (Vol. 3, pp. 1059-1109). Berlin: Springer.
Melosh, H. J. (2011). *Planetary surface processes* (Vol. 13): Cambridge University Press.
Menzel, D. H., & Whipple, F. L. (1955). THE CASE FOR H_2O CLOUDS ON VENUS. *Publications of the Astronomical Society of the Pacific, 67*(396), 161-168.
Misra, A., et al. (2015). Transient sulfate aerosols as a signature of exoplanet volcanism. *Astrobiology, 15*(6), 462-477.
Misra, A., et al. (2014). Using dimers to measure biosignatures and atmospheric pressure for terrestrial exoplanets. *Astrobiology, 14*(2), 67-86.
Morley, C. V., et al. (2017). Observing the atmospheres of known temperate Earth-sized planets with JWST. *The Astrophysical Journal, 850*(2), 121.
Morris, B. M., et al. (2018). Possible Bright Starspots on TRAPPIST-1. *The Astrophysical Journal, 857*(1), 39.
Moses, J. I., et al. (2011). Disequilibrium carbon, oxygen, and nitrogen chemistry in the atmospheres of HD 189733b and HD 209458b. *The Astrophysical Journal, 737*(1), 15.
Mudelsee, M. (2010). *Climate time series analysis : classical statistical and bootstrap methods*. Dordrecht ; New York: Springer.

Mulkidjanian, A. Y., et al. (2006). The cyanobacterial genome core and the origin of photosynthesis. *Proceedings of the National Academy of Sciences, 103*(35), 13126-13131.
Nair, H., et al. (1994). A photochemical model of the Martian atmosphere. *Icarus, 111*(1), 124-150.
Nakamura, K., & Kato, Y. (2004). Carbonatization of oceanic crust by the seafloor hydrothermal activity and its significance as a CO2 sink in the Early Archean. *Geochimica Et Cosmochimica Acta, 68*(22), 4595-4618.
NASA. (2013). Cassini images PIA14949 and PIA17170, JPL Photojournal. Retrieved from http://science.nasa.gov/science-news/science-at-nasa/2013/23jul_palebluedot/
Nava-Sedeno, J. M., et al. (2016). Carbon Monoxide and the Potential for Prebiotic Chemistry on Habitable Planets around Main Sequence M Stars. *Astrobiology, 16*(10), 744-754.
Nichita, D. V., et al. (2002). Multiphase equilibria calculation by direct minimization of Gibbs free energy with a global optimization method. *Computers & chemical engineering, 26*(12), 1703-1724.
Och, L. M., & Shields-Zhou, G. A. (2012). The Neoproterozoic oxygenation event: Environmental perturbations and biogeochemical cycling. *Earth-Science Reviews, 110*(1-4), 26-57. doi:DOI 10.1016/j.earscirev.2011.09.004
Oman, L., et al. (2008). Understanding the changes of stratospheric water vapor in coupled Chemistry–Climate Model simulations. *Journal of the Atmospheric Sciences, 65*(10), 3278-3291.
Owen, T. (1980). The search for early forms of life in other planetary systems: future possibilities afforded by spectroscopic techniques *Strategies for the Search for Life in the Universe* (pp. 177-185): Springer.
Park, J., & Royer, D. L. (2011). Geologic constraints on the glacial amplification of Phanerozoic climate sensitivity. *American Journal of Science, 311*(1), 1-26.
Pavlov, A., & Kasting, J. (2002a). Mass-independent fractionation of sulfur isotopes in Archean sediments: strong evidence for an anoxic Archean atmosphere. *Astrobiology, 2*(1), 27-41.
Pavlov, A. A., et al. (2001a). UV shielding of NH3 and O2 by organic hazes in the Archean atmosphere. *Journal of Geophysical Research: Planets (1991–2012), 106*(E10), 23267-23287.
Pavlov, A. A., et al. (2001b). UV shielding of NH3 and O2 by organic hazes in the Archean atmosphere. *Journal of Geophysical Research: Planets, 106*(E10), 23267-23287.
Pavlov, A. A., & Kasting, J. F. (2002b). Mass-independent fractionation of sulfur isotopes in Archean sediments: strong evidence for an anoxic Archean atmosphere. *Astrobiology, 2*, 27-41.
Pearson, D. G., et al. (2003). Mantle samples included in volcanic rocks: Xenoliths and diamonds. In R. W. Carlson (Ed.), *Treatise on Geochemistry - Volume 2: The Mantle and Core* (Vol. 2, pp. 171-276). Amsterdam: Elsevier.
Perry, R. H., et al. (2008). *Perry's chemical engineers' handbook* (8th ed.). New York: McGraw-Hill.
Pierrehumbert, R., & Gaidos, E. (2011). Hydrogen greenhouse planets beyond the habitable zone. *The Astrophysical Journal Letters, 734*(1), L13.
Pilson, M. E. (2012). *An Introduction to the Chemistry of the Sea*: Cambridge University Press.

Planavsky, N. J., et al. (2014a). Evidence for oxygenic photosynthesis half a billion years before the Great Oxidation Event. *Nature Geoscience*.
Planavsky, N. J., et al. (2014b). Evidence for oxygenic photosynthesis half a billion years before the Great Oxidation Event. *Nature Geoscience, 7*(4), 283.
Planavsky, N. J., et al. (2010). The evolution of the marine phosphate reservoir. *Nature, 467*(7319), 1088-1090.
Pohorille, A., & Pratt, L. (2012). Is water the universal solvent for life? *Origins of Life and Evolution of Biospheres, 42*(5), 405-409.
Pont, F., et al. (2008). Detection of atmospheric haze on an extrasolar planet: the 0.55–1.05 μm transmission spectrum of HD 189733b with the Hubble Space Telescope. *Monthly Notices of the Royal Astronomical Society, 385*(1), 109-118.
Postman, M., et al. (2009). Advanced Technology Large-Aperture Space Telescope (ATLAST): a technology roadmap for the next decade. *arXiv preprint arXiv:0904.0941*.
Prausnitz, J. M., et al. (1999). *Molecular thermodynamics of fluid-phase equilibria*: Pearson Education.
Prinn, R., et al. (2001). Evidence for substantial variations of atmospheric hydroxyl radicals in the past two decades. *Science, 292*(5523), 1882-1888.
Prinn, R. G., & Barshay, S. S. (1977). Carbon monoxide on Jupiter and implications for atmospheric convection. *Science, 198*(4321), 1031-1034.
Rackham, B. V., et al. (2018). The transit light source effect: false spectral features and incorrect densities for M-dwarf transiting planets. *The Astrophysical Journal, 853*(2), 122.
Rakov, V. A., & Uman, M. A. (2007). *Lightning: physics and effects*: Cambridge University Press.
Rameau, J., et al. (2013). Discovery of a probable 4-5 Jupiter-mass exoplanet to HD 95086 by direct imaging. *The Astrophysical Journal Letters, 772*(2), L15.
Rauer, H., et al. (2011). Potential biosignatures in super-Earth atmospheres: I. Spectral appearance of super-Earths around M dwarfs. *Astronomy and Astrophysics, 529*.
Reinhard, C. T., et al. (2017). False negatives for remote life detection on ocean-bearing planets: Lessons from the early Earth. *Astrobiology, 17*(4), 287-297.
Robinson, T. D. (2011). Modeling the infrared spectrum of the Earth-Moon system: Implications for the detection and characterization of Earthlike extrasolar planets and their moonlike companions. *The Astrophysical Journal, 741*(1), 51.
Robinson, T. D., & Catling, D. C. (2014a). Common 0.1 bar tropopause in thick atmospheres set by pressure-dependent infrared transparency. *Nature Geoscience, 7*(1), 12.
Robinson, T. D., & Catling, D. C. (2014b). Common 0.1 bar tropopause in thick atmospheres set by pressure-dependent infrared transparency. *Nat. Geosci., 7*(1), 12-15.
Robinson, T. D., et al. (2014). Detection of ocean glint and ozone absorption using LCROSS Earth observations. *The Astrophysical Journal, 787*(2), 171.
Robinson, T. D., et al. (2010). Detecting oceans on extrasolar planets using the glint effect. *The Astrophysical Journal Letters, 721*(1), L67.
Robinson, T. D., et al. (2011). Earth as an extrasolar planet: Earth model validation using EPOXI Earth observations. *Astrobiology, 11*(5), 393-408.
Robinson, T. D., et al. (2015). Characterizing Rocky and Gaseous Exoplanets with 2-meter Class Space-based Coronagraphs: General Considerations. *PSAP, in press*.
Rodler, F., & López-Morales, M. (2014). Feasibility studies for the detection of O2 in an Earth-like exoplanet. *The Astrophysical Journal, 781*(1), 54.

Rothman, D. H. (2014). *Earth's carbon cycle: a mathematical perspective*. Paper presented at the Current Events Bulletin, American Mathematical Society, Joint Mathematics Meeting, Baltimore, MD.
Rothman, D. H., et al. (2003). Dynamics of the Neoproterozoic carbon cycle. *Proc. Nat. Acad. Sci. USA, 100*, 8124-8129.
Rothman, L., et al. (2013). The HITRAN database: 2012 edition. *J Quant Spectrosc Radiat Transfer*.
Rothman, L. S., et al. (2009). The HITRAN 2008 molecular spectroscopic database. *Journal of Quantitative Spectroscopy and Radiative Transfer, 110*(9-10), 533-572.
Rowe, J. F., et al. (2006). An upper limit on the albedo of HD 209458b: direct imaging photometry with the MOST satellite. *The Astrophysical Journal, 646*(2), 1241.
Royer, D., et al. (2012). Geobiological constraints on Earth system sensitivity to CO2 during the Cretaceous and Cenozoic. *Geobiology, 10*(4), 298-310.
Rugheimer, S., et al. (2015). Effect of UV radiation on the spectral fingerprints of Earth-like planets orbiting M stars. *The Astrophysical Journal, 809*(1), 57.
Rushby, A. J., et al. (2018). Long-Term Planetary Habitability and the Carbonate-Silicate Cycle. *Astrobiology, 18*(5), 469-480.
Sagan, C. (1994). *Pale blue dot: A vision of the human future in space*: Random House.
Sagan, C., & Mullen, G. (1972). Earth and Mars: Evolution of atmospheres and surface temperatures. *Science, 177*(4043), 52-56.
Sagan, C., et al. (1993). A search for life on Earth from the Galileo spacecraft. *Nature, 365*(6448), 715-721.
Sanromá, E., et al. (2013). On the effects of the evolution of microbial mats and land plants on the Earth as a planet. Photometric and spectroscopic light curves of paleo-Earths. *The Astrophysical Journal, 766*(2), 133.
Sanromá, E., et al. (2014). Characterizing the Purple Earth: Modeling the Globally Integrated Spectral Variability of the Archean Earth. *The Astrophysical Journal, 780*(1), 52.
Scalo, J. M. (1986). The stellar initial mass function. *Fundamentals of Cosmic Physics, 11*, 1-278.
Schiaparelli, G. (1899). Observations of the Planet Mars.'. *Science, 9*(227), 633-637.
Schidlowski, M. (1988). A 3,800-million-year isotopic record of life from carbon in sedimentary rocks. *Nature, 333*, 313-318.
Schidlowski, M., et al. (1979). Carbon isotope geochemistry of the 3.7× 10< sup> 9</sup>-yr-old Isua sediments, West Greenland: implications for the Archaean carbon and oxygen cycles. *Geochimica Et Cosmochimica Acta, 43*(2), 189-199.
Schidlowski, M., et al. (1976). Carbon isotope geochemistry of Precambrian Lomagundi carbonate province, Rhodesia. *Geochim. Cosmochim. Acta, 40*(4), 449-455.
Schopf, J. W., & Klein, C. (1992). *The Proterozoic Biosphere: A Multidisciplinary Study*: Cambridge University Press.
Schrag, D. P., et al. (2013). Authigenic Carbonate and the History of the Global Carbon Cycle. *SCIENCE, 339*(6119), 540-543. doi:DOI 10.1126/science.1229578
Schwartzman, D., & Volk, T. (2004). Does life drive disequilibrium in the biosphere. *Scientists Debate Gaia: The Next Century*, 129-135.
Schwieterman, E., et al. (2015a). Nonphotosynthetic pigments as potential biosignatures. *Astrobiology, 15*(5), 341-361.

Schwieterman, E. W., et al. (2016). Identifying planetary biosignature impostors: spectral features of CO and O4 resulting from abiotic O2/O3 production. *The Astrophysical Journal Letters, 819*(1), L13.
Schwieterman, E. W., et al. (2019). Rethinking CO Antibiosignatures in the Search for Life Beyond the Solar System. *The Astrophysical Journal, 874*(1), 9.
Schwieterman, E. W., et al. (2015b). Detecting and Constraining N2 Abundances in Planetary Atmospheres Using Collisional Pairs. *The Astrophysical Journal, 810*(1), 57.
Seager, S. (2013). Exoplanet habitability. *Science, 340*(6132), 577-581.
Seager, S. (2014). The future of spectroscopic life detection on exoplanets. *Proceedings of the National Academy of Sciences, 111*(35), 12634-12640.
Seager, S., & Bains, W. (2015). The search for signs of life on exoplanets at the interface of chemistry and planetary science. *Science Advances, 1*(2), e1500047.
Seager, S., et al. (2013). A biomass-based model to estimate the plausibility of exoplanet biosignature gases. *The Astrophysical Journal, 775*(2), 104.
Seager, S., et al. (2015). *Exo-S: Starshade Probe-Class Exoplanet Direct Imaging Mission Concept Final Report*. Retrieved from Pasadena, California:
Seager, S., & Deming, D. (2010). Exoplanet Atmospheres. *Annual Review of Astronomy and Astrophysics, 48*, 631-672.
Seager, S., et al. (2012). An astrophysical view of Earth-based metabolic biosignature gases. *Astrobiology, 12*(1), 61-82.
Seager, S., et al. (2005). Vegetation's red edge: a possible spectroscopic biosignature of extraterrestrial plants. *Astrobiology, 5*(3), 372-390.
Segura, A., et al. (2005). Biosignatures from Earth-like planets around M dwarfs. *Astrobiology, 5*(6), 706-725.
Segura, A., et al. (2003). Ozone concentrations and ultraviolet fluxes on Earth-like planets around other stars. *Astrobiology, 3*(4), 689-708.
Shields-Zhou, G., & Och, L. (2011). The case for a Neoproterozoic Oxygenation Event: Geochemical evidence and biological consequences. *GSA Today, 21*, 4-11. doi:10.1130/GSATG102A.1
Shields, A. L., et al. (2013). The effect of host star spectral energy distribution and ice-albedo feedback on the climate of extrasolar planets. *Astrobiology, 13*(8), 715-739.
Shields, G., & Veizer, J. (2002). Precambrian marine carbonate isotope database: Version 1.1. *Geochem. Geophys. Geosys., 3*.
Shirey, S. B., et al. (2013). Diamonds and the Geology of Mantle Carbon. *Carbon in Earth, 75*, 355-421. doi:DOI 10.2138/rmg.2013.75.12
Sholes, S. F., et al. (2019). A Maximum Subsurface Biomass on Mars from Untapped Free Energy: CO and H2 as Potential Antibiosignatures. *Astrobiology*.
Shumway, R. H., & Stoffer, D. S. (2011). *Time series analysis and its applications : with R examples* (3rd ed.). New York: Springer.
Sillén, L. G. (1966). Regulation of O2, N2 and CO2 in the atmosphere; thoughts of a laboratory chemist. *Tellus, 18*(2-3), 198-206.
Simon, D. (2001). Kalman Filtering. *Embedded Systems Programming, 14*(6), 72-79.
Simoncini, E., et al. (2013). Quantifying drivers of chemical disequilibrium: theory and application to methane in the Earth's atmosphere. *Earth System Dynamics, 4*(2), 317-331.

Sing, D. K., et al. (2016). A continuum from clear to cloudy hot-Jupiter exoplanets without primordial water depletion. *Nature, 529*(7584), 59.
Sleep, N. (2005a). Dioxygen over geological time. *Metal ions in biological systems, 43*, 49.
Sleep, N. H. (2005b). Dioxygen over geological time. *Metal ions in biological systems, biogeocehmical cycles of elements Sigel A, Sigel H, Sigel RKO, 43*, 49-73.
Sleep, N. H., & Zahnle, K. (2001). Carbon dioxide cycling and implications for climate on ancient Earth. *J. Geophys. Res., 106*, 1373-1399.
Smirnov, A., et al. (2008). Abiotic ammonium formation in the presence of Ni-Fe metals and alloys and its implications for the Hadean nitrogen cycle. *Geochem Trans, 9*(5).
Snellen, I., et al. (2013). Finding extraterrestrial life using ground-based high-dispersion spectroscopy. *The Astrophysical Journal, 764*(2), 182.
Spergel, D., et al. (2015). Wide-Field InfrarRed Survey Telescope-Astrophysics Focused Telescope Assets WFIRST-AFTA 2015 Report. *arXiv preprint arXiv:1503.03757*.
Spiegel, D. S., et al. (2010). Models of Neptune-mass exoplanets: Emergent fluxes and albedos. *The Astrophysical Journal, 709*(1), 149.
Stapelfeldt, K., et al. (2015). *Exo-C Imaging Nearby Worlds: Exoplanet Direct Imaging: coronograph probe mission study Final Report*. Retrieved from Pasadena, California:
Stevenson, K. B., et al. (2010). Possible thermochemical disequilibrium in the atmosphere of the exoplanet GJ 436b. *Nature, 464*(7292), 1161-1164.
Stüeken, E. E., et al. (2012). Contributions to late Archaean sulphur cycling by life on land. *Nature Geoscience, 5*(10), 722-725.
Sudarsky, D., et al. (2005). Phase functions and light curves of wide-separation extrasolar giant planets. *The Astrophysical Journal, 627*(1), 520.
Sudarsky, D., et al. (2000). Albedo and reflection spectra of extrasolar giant planets. *The Astrophysical Journal, 538*(2), 885.
Suissa, G., & Kipping, D. (2018). TRAPPIST-1e Has a Large Iron Core. *arXiv preprint arXiv:1804.10618, accepted to RNAAS*.
Summers, D. P., et al. (2012). Abiotic nitrogen fixation on terrestrial planets: Reduction of NO to ammonia by FeS. *Astrobiology, 12*(2), 107-114.
Sun, X. L., & Turchyn, A. V. (2014). Significant contribution of authigenic carbonate to marine carbon burial. *Nature Geoscience, 7*(3), 201-204. doi:Doi 10.1038/Ngeo2070
Sundquist, E. T. (1991). Steady-State and Non-Steady-State Carbonate Silicate Controls on Atmospheric Co2. *Quaternary Science Reviews, 10*(2-3), 283-296. doi:Doi 10.1016/0277-3791(91)90026-Q
Tashiro, T., et al. (2017). Early trace of life from 3.95 Ga sedimentary rocks in Labrador, Canada. *Nature, 549*(7673), 516.
Thomazo, C., et al. (2009). Methanotrophs regulated atmospheric sulfur isotope anomalies during the Mesoarchean (Tumbiana Formation, Western Australia). *Earth And Planetary Science Letters, 279*(1-2), 65-75. doi:DOI 10.1016/j.epsl.2008.12.036
Tian, F., et al. (2014). High stellar FUV/NUV ratio and oxygen contents in the atmospheres of potentially habitable planets. *Earth and Planetary Science Letters, 385*, 22-27.
Tinetti, G., et al. (2005). Disk-averaged synthetic spectra of Mars. *Astrobiology, 5*(4), 461-482.
Tinetti, G., et al. (2006). Detectability of planetary characteristics in disk-averaged spectra II: synthetic spectra and light-curves of earth. *Astrobiology, 6*(6), 881-900.
Tolfo, F. (1977). A simplified model of aerosol coagulation. *Journal of Aerosol Science, 8*(1), 9-19.

Traub, W. A. (2003a). *The colors of extrasolar planets.* Paper presented at the Scientific Frontiers in Research on Extrasolar Planets.
Traub, W. A. (2003b). *Extrasolar planet characteristics in the visible wavelength range.* Paper presented at the Earths: DARWIN/TPF and the Search for Extrasolar Terrestrial Planets, Heidelberg, Germany.
Turbet, M., et al. (2018). Modeling climate diversity, tidal dynamics and the fate of volatiles on TRAPPIST-1 planets.
Ulanowicz, R. E., & Hannon, B. (1987). Life and the production of entropy. *Proceedings of the Royal society of London. Series B. Biological sciences, 232*(1267), 181-192.
Van Kranendonk, M. J., et al. (2008). Geological setting of Earth's oldest fossils in the ca. 3.5 Ga Dresser Formation, Pilbara Craton, Western Australia. *Precambrian Research, 167*(1-2), 93-124.
Venot, O., et al. (2013). The nitrogen chemistry in hot Jupiters atmosphere *The Early Evolution of the Atmospheres of Terrestrial Planets* (pp. 67-83): Springer.
Vidal-Madjar, A., et al. (2003). An extended upper atmosphere around the extrasolar planet HD209458b. *Nature, 422*(6928), 143-146.
Walas, S. M. (1985). *Phase equilibria in chemical engineering*. Boston: Butterworth.
Walker, J. C., et al. (1981). A negative feedback mechanism for the long-term stabilization of Earth's surface temperature. *Journal of Geophysical Research: Oceans (1978–2012), 86*(C10), 9776-9782.
Walther, J. V. (2009). *Essentials of geochemistry*: Jones & Bartlett Publishers.
Warren, S. G., et al. (2002). Snowball Earth: Ice thickness on the tropical ocean. *Journal of Geophysical Research: Oceans (1978–2012), 107*(C10), 31-31-31-18.
Webb, W. A. (1957). On the rejection of the Martian canal hypothesis. *The Scientific Monthly, 85*(1), 23-28.
Wedepohl, K. H. (1995). The composition of the continental crust. *Geochimica et Cosmochimica Acta, 59*(7), 1217-1232.
Weiss, M. C., et al. (2016). The physiology and habitat of the last universal common ancestor. *Nature Microbiology, 1*(9), 16116.
White, W. B., et al. (1958). Chemical equilibrium in complex mixtures. *The Journal of Chemical Physics, 28*(5), 751-755.
Wolf, E. T. (2017). Assessing the habitability of the TRAPPIST-1 system using a 3D climate model. *The Astrophysical Journal Letters, 839*(1), L1.
Wolfe, J. M., & Fournier, G. P. (2018). Horizontal gene transfer constrains the timing of methanogen evolution. *Nature ecology & evolution, 2*(5), 897.
Wordsworth, R., & Pierrehumbert, R. (2014). Abiotic oxygen-dominated atmospheres on terrestrial habitable zone planets. *The Astrophysical Journal Letters, 785*(2), L20.
Wordsworth, R. D., et al. (2011). Gliese 581d is the first discovered terrestrial-mass exoplanet in the habitable zone. *The Astrophysical Journal Letters, 733*(2), L48.
Yan, F., et al. (2015). High-resolution transmission spectrum of the Earth's atmosphere-seeing Earth as an exoplanet using a lunar eclipse. *International Journal of Astrobiology, 14*(02), 255-266.
Yang, X., et al. (2014). A relatively reduced Hadean continental crust and implications for the early atmosphere and crustal rheology. *Earth and Planetary Science Letters, 393*, 210-219.

Young, G. M., et al. (1998). Earth's oldest reported glaciation: physical and chemical evidence from the Archean Mozaan Group (~ 2.9 Ga) of South Africa. *The Journal of geology, 106*(5), 523-538.

Younglove, B., & Ely, J. F. (1987). Thermophysical properties of fluids. II. Methane, ethane, propane, isobutane, and normal butane. *Journal of Physical and Chemical Reference Data, 16*(4), 577-798.

Yung, Y. L., & DeMore, W. B. (1999). *Photochemistry of planetary atmospheres* (Vol. 1). New York: Oxford University Press.

Zahnle, K., et al. (2006). The loss of mass-independent fractionation in sulfur due to a Palaeoproterozoic collapse of atmospheric methane. *Geobiology, 4*(4), 271-283.

Zahnle, K., et al. (2011). Is there methane on Mars? *Icarus, 212*(2), 493-503.

Zahnle, K., et al. (2008). Photochemical instability of the ancient Martian atmosphere. *Journal of Geophysical Research: Planets (1991–2012), 113*(E11).

Zahnle, K. J. (1986). Photochemistry of methane and the formation of hydrocyanic acid (HCN) in the Earth's early atmosphere. *Journal of Geophysical Research: Atmospheres, 91*(D2), 2819-2834.

Zahnle, K. J., et al. (2013). The rise of oxygen and the hydrogen hourglass. *Chemical Geology, 362*, 26-34.

Zahnle, K. J., et al. (2019). Strange messenger: A new history of hydrogen on Earth, as told by Xenon. *Geochimica et Cosmochimica Acta, 244*, 56-85.

Zerkle, A. L., et al. (2012). A bistable organic-rich atmosphere on the Neoarchaean Earth. *Nature Geoscience, 5*(5), 359-363.

Zhang, X., et al. (2012). Sulfur chemistry in the middle atmosphere of Venus. *Icarus, 217*(2), 714-739.

Zhang, Z., et al. (2018). The Near-Infrared Transmission Spectra of TRAPPIST-1 Planets b, c, d, e, f, and g and Stellar Contamination in Multi-Epoch Transit Spectra. *arXiv preprint arXiv:1802.02086, submitted AAS journals*.

Zugger, M. E., et al. (2010). Light scattering from exoplanet oceans and atmospheres. *The Astrophysical Journal, 723*(2), 1168.

Appendix I – Supplementary materials to Chapters 2 and 4

Appendix 2-A: Gas phase Gibbs minimization

This section describes the methodology used to find gas phase equilibrium using Gibbs free energy minimization. We provide the Matlab code that implements this methodology on the website of the first author (JKT). Recall that for a gas phase system, the equilibrium state has mole fraction abundances, $\bar{n}_i$, that minimize equation (5) in Chapter 2. Temperature dependent standard Gibbs free energies of formation, $\Delta_f G^\circ_{i\,(T,\mathrm{P}_r)}$, were calculated from enthalpies and entropies of formation retrieved from NASA's thermodynamic database (Burcat & Ruscic 2005). We used the 2009 version of this database (available here http://www.grc.nasa.gov/WWW/CEAWeb/ or http://garfield.chem.elte.hu/Burcat/NEWNASA.TXT). The database provides 10 coefficients for each gaseous species (sometimes multiple sets of 10 coefficients are specified for different temperature ranges). The enthalpies and entropies of formation are calculated from these coefficients using the following empirically fitted expressions:

$$\Delta_f H^\circ_{i\,(T,\mathrm{P}_r)} / RT = -a_1 T^{-2} + a_2 \ln(T)/T + a_3 + a_4 T/2 + a_5 T^2/3 + a_6 T^3/4 + a_7 T^4/5 + a_9/T \quad \text{(AI-1)}$$

$$\Delta_f S^\circ_{i\,(T,\mathrm{P}_r)} / R = -a_1 T^{-2}/2 - a_2/T + a_3 \ln(T) + a_4 T + a_5 T^2/2 + a_6 T^3/3 + a_7 T^4/4 + a_{10} \quad \text{(AI-2)}$$

Here, $a_{1\text{–}10}$ are the coefficients from the NASA database (the 9th coefficient is unused). Enthalpies and entropies are combined to calculate the Gibbs free energy of formation:

$$\Delta_f G^\circ_{i\,(T,\mathrm{P}_r)} = \Delta_f H^\circ_{i\,(T,\mathrm{P}_r)} - T\Delta_f S^\circ_{i\,(T,\mathrm{P}_r)} \quad \text{(AI-3)}$$

Note that there are several different conventions for Gibbs free energies of formation (see for instance Anderson and Crerar (1993, p154)). The different conventions produce equivalent equilibrium results, but it is important to use Gibbs energies of the same convention within any given calculation. The NASA database provides Gibbs free energies of formation according to the Berman-Brown convention (e.g. Anderson and Crerar (1993, p156)), but we convert these to standard free energies of formation in our Matlab code.

In the expression for Gibbs energy, equation (5) in Chapter 2, temperature dependent fugacity coefficients, γ_{fi}, were calculated using the Soave equation as described in Walas (1985, p146):

$$\ln\left(\gamma_f\right)=\frac{B_i}{B}\left(Z-1\right)-\ln\left(Z-B\right)+\frac{A}{B}\left[\frac{B_i}{B}-\frac{2}{a\alpha}\sum_j n_j\left(a\alpha\right)_{ij}\right]\ln\left(1+\frac{B}{Z}\right) \quad \text{(AI-4)}$$

Here, Z is the smallest real solution to the cubic, $f(Z)=Z^3-Z^2+\left(A-B-B^2\right)Z-AB=0$. The other terms and variables are defined by the following set of equations:

$$\begin{aligned}
&A=\left(a\alpha\right)P/R^2T^2 \qquad B=bP/RT\\
&B_i=b_iP/RT \qquad a\alpha=\sum_i\sum_j n_in_j\left(a\alpha\right)_{ij}\\
&\left(a\alpha\right)_{ij}=\left(1-k_{ij}\right)\sqrt{\left(a_i\alpha_i\right)\left(a_j\alpha_j\right)}\\
&a_i=0.42747\,R^2T_{ci}^2/P_{ci}\\
&b_i=0.08664\,RT_{ci}/P_{ci} \qquad b=\sum_i n_ib_i\\
&\alpha_i=\left[1+\left(0.480+1.574\omega_i-0.176\omega_i^2\right)\left(1-T_{ci}^{0.5}\right)\right]^2
\end{aligned} \quad \text{(AI-5)}$$

In this set of equations, n_i is the number of moles of the *i*-th species, *R* is the universal gas constant, and *P* and *T* are the pressure and temperature of the system, respectively. T_{ci} is the critical temperature of the *i*-th species and P_{ci} is the critical pressure of the *i*-th species. Finally, ω_i is the acentric factor of the *i*-th species and k_{ij} is a binary interaction parameter for species *i* and *j*. All the other variables and terms are computable from these basic parameters. Critical temperatures, critical pressures, and acentric factors for gaseous species were obtained from Perry et al. (2008, section 2-136). To investigate the importance of binary interaction parameters, we performed some sensitivity tests using the simple gaseous system described in Lwin (2000). In this system, H_2O and CH_4 are reacted to equilibrium to form CO, CO_2 and H_2 at high temperature (1000 K) and pressure (90 bar). We performed these tests at high temperature and pressure because this is the regime where departure from ideal behavior is the most significant. The inclusion of binary interaction parameters had a small effect on the fugacity coefficients and a negligible effect (<1%) on the overall change in Gibbs energy of the system. Consequently, in the equations above we assumed k_{ij}=0 for every pair of molecules. The close agreement between our numerical Gibbs free energy calculations, which don't include binary interaction parameter, and the Aspen Plus calculations, which do include binary interaction parameters, is further confirmation that ignoring binary interaction parameters is justified.

Given the Gibbs energies of formation and fugacity coefficients for all species, the Gibbs energy expression, equation (5), can be computed and minimized. We used an interior points method implemented using

Matlab's *fmincon* function to minimize $\Delta G_{(T,P)}$. The n_i that minimize $\Delta G_{(T,P)}$ and satisfy the atom conservation constraint (equation (6)) define the equilibrium state.

Appendix 2-B: Gibbs energy proof

Here, we demonstrate that the minimum of equation (4) is identical to the minimum of equation (5) in Chapter 2. The standard Gibbs free energy of formation for a compound is the change in Gibbs energy with formation of one mole from its constituent elements in their standard states (i.e. the most stable elemental form at standard conditions, usually taken usually taken as 25°C and 1 atm for most databases (Anderson 2005, p. 211; Anderson & Crerar 1993, p. 154)):

$$\Delta_f G^{\circ}_{i\,(T,\mathrm{P}_r)} \equiv G^{\circ}_{i\,(T,\mathrm{P}_r)} - \sum_{elements=j} \nu_{ji} G^{\circ}_{j(T,\mathrm{P}_r)} \qquad \text{(AI-6)}$$

Recall that ν_{ji} is the number of atoms of element *j* per molecule of species *i*, and $G^{\circ}_{j(T,P_r)}$ is the standard partial molar Gibbs free energy of gas *j* at reference pressure P_r and temperature *T*. The other variables are defined in the Chapter 2. Substitution yields the following expression:

$$\begin{aligned}
\Delta G_{(T,P)} &= \sum_i n_i (\Delta_f G^{\circ}_{i\,(T,\mathrm{P}_r)} + RT \ln(P_i \gamma_{fi})) \\
&= \sum_i n_i (G^{\circ}_{i\,(T,\mathrm{P}_r)} - \sum_{elements=j} \nu_{ji} G^{\circ}_{j(T,\mathrm{P}_r)} + RT \ln(P n_i \gamma_{fi} / n_T)) \qquad \text{(AI-7)} \\
&= G_{(T,\mathrm{P})} - \sum_i \sum_{elements=j} n_i \nu_{ji} G^{\circ}_{j(T,\mathrm{P}_r)} = G_{(T,\mathrm{P})} - \sum_{elements=j} G^{\circ}_{j(T,\mathrm{P}_r)} \sum_i n_i \nu_{ji}
\end{aligned}$$

The last line uses equation (4) to substitute for $G_{(T,\mathrm{P})}$.

It is often assumed that $G^{\circ}_{j(T,\mathrm{P}_r)} = 0$ for the elements, thereby establishing that $\Delta G_{(T,P)} = G_{(T,\mathrm{P})}$. However, this assumption is incorrect (Anderson & Crerar 1993, p. 147). Instead, the Gibbs free energy of formation for elements equals zero, $\Delta_f G^{\circ}_{i\,(T,\mathrm{P}_r)} = 0$ if species *i* is an element. Consequently, equations (4) and equation (5) are not identical $\left(\Delta G_{(T,P)} \neq G_{(T,\mathrm{P})}\right)$, but they do have the same minimum. This can be seen by considering the second term on the last line of equation (AI-7). Conservation of atoms ensures that this term is a constant; refer to equation (6) if this is not immediately clear. Since this term is a constant, minimizing $G_{(T,\mathrm{P})}$ is equivalent to minimizing $\Delta G_{(T,P)}$. Note also that because $G_{(T,\mathrm{P})}$ and $\Delta G_{(T,P)}$ only differ by a constant, then differences in Gibbs energies between two states will be the same regardless of which form is used. This establishes that using equation (7) to calculate our metric of available Gibbs energies is equivalent to using equation (8).

Appendix 2-C: Multiphase calculations

This section describes the methodology used to find multiphase equilibrium using Gibbs free energy minimization. Recall that for a multiphase system, the equilibrium state is the mole fraction abundances, $\bar{n}_i$, that minimize the expression in equation (9) in the Chapter 2. Temperature and pressure dependent standard Gibbs free energies of formation were calculated from the SUPCRT database (Johnson et al. 1992). Gibbs free energies of formation for aqueous species are given by the following expression (Walther 2009, p704):

$$\begin{aligned}
&\Delta_f G^{\circ}_{i\,(T,\mathrm{P})} = \Delta_f G^{\circ}_{i\,(T_r,\mathrm{P}_r)} - \Delta_f S^{\circ}_{i\,(T_r,\mathrm{P}_r)}\left(T - T_r\right) - c_1\left[T\ln\left(\frac{T}{T_r}\right) - T + T_r\right] \\
&+ a_1\left(P - P_r\right) + a_2\ln\left(\frac{\Psi + P}{\Psi + P_r}\right) \\
&- c_2\left\{\left[\left(\frac{1}{T-\theta}\right) - \left(\frac{1}{T_r-\theta}\right)\right]\left(\frac{\theta - T}{\theta}\right) - \frac{T}{\theta^2}\ln\left[\frac{T_r\left(T-\theta\right)}{T\left(T_r-\theta\right)}\right]\right\} \\
&+ \left(\frac{1}{T-\theta}\right)\left[a_3\left(P - P_r\right) + a_4\ln\left(\frac{\Psi + P}{\Psi + P_r}\right)\right] \\
&+ \omega_{P,T}\left(\frac{1}{\varepsilon_{P,T}} - 1\right) - \omega_{P_r,T_r}\left(\frac{1}{\varepsilon_{P_r,T_r}} - 1\right) + \omega_{P_r,T_r}Y_{P_r,T_r}\left(T - T_r\right)
\end{aligned} \qquad \text{(AI-8)}$$

Where:

$\Delta_f G^{\circ}_{i\,(T,\mathrm{P})}$ = Gibbs free energy of formation for the *i*-th species.

$\Delta_f G^{\circ}_{i\,(T_r,\mathrm{P}_r)}$ = Gibbs free energy of formation for the *i*-th species at the reference temperature and pressure (from SUPCRT database)

$\Delta_f S^{\circ}_{i\,(T_r,\mathrm{P}_r)}$ = Entropy of formation at the reference temperature and pressure

T = Temperature of the system

T_r = Reference temperature (298 K)

P = Pressure of the system

P_r = Reference pressure (1 bar)

c_1, c_2, a_{1-4} = species specific coefficients (from the SUPCRT database)

Ψ = Solvent pressure parameter (2600 bar)

θ = Solvent temperature parameter (228 K)

$\omega_{P,T}$ = Born coefficient

ω_{P_r,T_r} = Born coefficient at the reference temperature and pressure (from the SUPCRT database)

$\varepsilon_{P,T}$ = Dielectric constant of water.

ε_{P_r,T_r} = Dielectric constant of water at the reference temperature and pressure (78.47)

Y_{P_r,T_r} = Born derivative equation (- 5.81 × 10^{-5} K^{-1})

The Born coefficients have a small effect on the overall Gibbs energy of formation. For neutral species, $\omega_{P_r,T_r} = \omega_{P,T}$. In other cases, these two terms are nearly equal, and will approximately cancel each other. Thus, we simplified the Gibbs energy of formation expression by dropping these two terms:

$$\begin{aligned}
\Delta_f G^{\circ}_{i\,(T,\mathrm{P})} &= \Delta_f G^{\circ}_{i\,(T_r,\mathrm{P}_r)} - \Delta_f S^{\circ}_{i\,(T_r,\mathrm{P}_r)}\left(T - T_r\right) - c_1\left[T\ln\left(\frac{T}{T_r}\right) - T + T_r\right] \\
&+ a_1\left(P - P_r\right) + a_2\ln\left(\frac{\Psi + P}{\Psi + P_r}\right) \\
&- c_2\left\{\left[\left(\frac{1}{T-\theta}\right) - \left(\frac{1}{T_r-\theta}\right)\right]\left(\frac{\theta - T}{\theta}\right) - \frac{T}{\theta^2}\ln\left[\frac{T_r\left(T-\theta\right)}{T\left(T_r-\theta\right)}\right]\right\} \\
&+ \left(\frac{1}{T-\theta}\right)\left[a_3\left(P - P_r\right) + a_4\ln\left(\frac{\Psi + P}{\Psi + P_r}\right)\right] \\
&+ \omega_{P_r,T_r} Y_{P_r,T_r}\left(T - T_r\right)
\end{aligned} \qquad \text{(AI-9)}$$

This expression is used to calculate the Gibbs free energies of formation for all the aqueous species in our multiphase equilibrium code.

Activity coefficients for aqueous species, γ_{ai} in equation (9), were approximated using the Truesdell-Jones equation (Langmuir 1997, p140):

$$\ln(\gamma_{ai}) = \frac{-0.5092 z_i^{\,2}\sqrt{I}}{1+0.3283 a_i \sqrt{I}} + b_i I \qquad \text{(AI-10)}$$

Here, $I = \frac{1}{2}\sum_j m_j z_j^2$ is the ionic strength of the solution, where m_j is the molality of the *j*-th species and z_j is the charge of the *j*-th species. The variables a_i and b_i are species-specific thermodynamic coefficients that were obtained from Langmuir (1997). The Truesdell-Jones equation is only an approximation, but it is known to be accurate for solutions up to 2 molal (Langmuir 1997, p. 142). Because the Earth's ocean has an ionic strength of 0.7 molal, and the dissolution of nitrate and hydrogen by reaction to equilibrium does not increase this very much (see table 7), the Truesdell-Jones equation provides accurate activity coefficients in our calculations. Sensitivity analysis also reveals that the available Gibbs free energy of the Earth is fairly insensitive to the activity coefficients of the major aqueous species. However, the available Gibbs energy of the Earth's atmosphere-ocean system is quite sensitive to water activity. Consequently, rather than use the Truesdell-Jones approximation above, the activity coefficient for water was calculated rigorously using a simplified form of the Pitzer equations (Marion & Kargel 2007):

$$\phi = 1 + \frac{2}{\sum_i m_i}\left\{\frac{-0.3915 I^{3/2}}{1+1.2 I^{1/2}} + \sum_{all}\sum_{pairs} m_c m_a \left(B_{ca}^{\phi} + Z C_{ca}\right)\right\} \qquad \text{(AI-11)}$$

Here, ϕ is the osmotic coefficient and can be related to the activity coefficient of water, γ_{aw} in equation (9), by the following expression:

$$\ln(\gamma_{aw}) = -\phi \sum_i m_i / 55.50844 \qquad \text{(AI-12)}$$

The double summation in equation (AI-11) is over all unique pairs of anions and cations in solution (no double counting). The other variables in equation (AI-11) are defined as follows:

m_i = molality of the *i*-th species

m_a = molality of the anion

m_c = molality of the cation

I = ionic strength of the solution (defined above)

$$Z = \sum_i m_i \left|z_i\right|$$

$$B_{MX} = B_{MX}^{(0)} + B_{MX}^{(1)} \exp\left(-\alpha_1 I^{1/2}\right) + B_{MX}^{(2)} \exp\left(-\alpha_2 I^{1/2}\right)$$

$\alpha_1 = 2.0\ kg^{0.5}mol^{-0.5}, \alpha_2 = 0\ kg^{0.5}mol^{-0.5}$ for all binary systems except 2:2 electrolytes

$\alpha_1 = 1.4\ kg^{0.5}mol^{-0.5}, \alpha_2 = 12\ kg^{0.5}mol^{-0.5}$ for 2:2 electrolytes

$B_{MX}^{(0)}, B_{MX}^{(1)}, B_{MX}^{(2)}, C_{MX}$ are species-specific binary interaction parameters that were obtained from Appelo and Postma (2005) and Marion (2002). The form of the Pitzer equation described above is a simplification of the complete expression; we have ignored cation-cation and anion-anion interactions, neutral solute parameters, and triple particle parameters since these terms will be small for Earth's ocean. Temperature dependencies were also ignored since, in absolute Kelvin, the temperature of the ocean is close to the reference temperature of 298 K. The activity coefficient of water was calculated using these equations at every iteration in our multiphase Gibbs free energy minimization calculations.

Finding the equilibrium state for multiphase systems is more challenging than for single-phase gaseous systems. The Matlab function *fmincon* was once again used to implement the optimization, but this time we provided the analytic gradient for the Gibbs energy function in equation (9) from differentiation, as follows:

$$\frac{1}{RT}\frac{\partial \Delta G_{(T,P)}}{\partial n_i} = \begin{cases} \dfrac{\Delta_f G^{\circ}_{i\,(T,\mathrm{P})}}{RT} + \ln\left(\gamma_{aw}\right) + \ln\left(\dfrac{n_i}{n_{aq}}\right) - \dfrac{n_i}{n_{aq}} - \dfrac{n_{aq}}{n_i} + 2 & \alpha = water \\ \dfrac{\Delta_f G^{\circ}_{i\,(T,\mathrm{P})}}{RT} + \ln\left(\dfrac{n_i}{n_\alpha}\right) + \ln\left(\gamma_{fi}\right) & \alpha = gas \\ \dfrac{\Delta_f G^{\circ}_{i\,(T,\mathrm{P})}}{RT} + \ln\left(55.5084\right) + \ln\left(\gamma_{ai}\right) + \ln\left(\dfrac{n_i}{n_{aq}}\right) - \ln\left(\dfrac{n_w}{n_{aq}}\right) - \dfrac{n_w}{n_{aq}} + 1 & \alpha = aqueous \end{cases} \quad \text{(AI-13)}$$

The terms in this expression are defined in the methods section. We assumed that the activity coefficients were, to first order, independent of molar abundances.

Proving *fmincon* with an analytic gradient ensured more rapid and reliable convergence. For multiphase Gibbs energy minimization problems there is no guarantee that the local minima equal the global minimum (Nichita et al. 2002). Consequently, we implemented a simple global minimum search by iterating over an ensemble of random initial conditions. The vast majority of runs converged to the same minimum; only occasionally would an optimization run converge to another, less optimum, minimum or simply not

converge. This gives us confidence that the consensus minimum was in fact the true global minimum. Semi-analytic calculations and Aspen Plus results also validate our multiphase Gibbs energy minimization result.

Appendix 2-D: Semi-analytic calculations

Here, we describe the methodology for our semi-analytic calculation using equilibrium reactions in the atmospheres of Jupiter and Earth as examples. The reactions chosen for the semi-analytic calculations for the other atmospheres are also listed at the end.

Jupiter

In Jupiter's atmosphere, the key available redox couples suggest that there are two important reactions that contribute to chemical disequilibrium:

$$3H_2(g) + HCN(g) \rightleftharpoons CH_4(g) + NH_3(g) \qquad \text{(AI-14)}$$

$$3H_2 + CO \rightleftharpoons CH_4 + H_2O \qquad \text{(AI-15)}$$

We begin with reaction (AI-14). The Gibbs energy of this reaction is given by (e.g. Anderson and Crerar (1993, p238)):

$$\Delta_r G = \Delta_r G^\circ + RT\ln(Q) = \Delta_r G^\circ + RT\ln\left(\frac{a_{CH_4}a_{NH_3}}{a_{H_2}{}^3 a_{HCN}}\right) \qquad \text{(AI-16)}$$

The activity of each species *i* is denoted by a_i, the temperature of Jupiter's atmosphere at 1 bar is *T*=165 K, *R* is the universal gas constant, and *Q* is the reaction quotient. From equation (AI-14) the Gibbs energy of the reaction, $\Delta_r G$, is the change in Gibbs energy of the system per 3 moles of H_2 and 1 mole of HCN that are converted to CH_4 and NH_3. The standard free energy of the reaction, $\Delta_r G^\circ$, represents the value of this quantity when the activities of all species equals unity. In this case, taking *T* = 165 K and P_r = 1 bar,

$$\begin{aligned}\Delta_r G^\circ &= \Delta_f G^\circ_{CH_4(T,P_r)} + \Delta_f G^\circ_{NH_3(T,P_r)} - 3\Delta_f G^\circ_{H_2(T,P_r)} - \Delta_f G^\circ_{HCN(T,P_r)} \\ &= -6.025\times10^4 + -2.88021\times10^4 - 3\times0 - 1.27374866\times10^5 \text{ J/mol} \\ &= -2.1643\times10^5 \text{ J/mol}\end{aligned} \qquad \text{(AI-17)}$$

where we have substituted the appropriate Gibbs free energies of formation for each species computed at 165 K using the database and methodology of Appendix A. Gibbs free energies of formation were taken from the same thermodynamic databases as those used for the Gibbs energy minimization calculations.

Reaction (AI-14) is in equilibrium when the left hand side of equation (AI-16) is zero. We solve for this equilibrium by making the following substitution:

$$\Delta_r G(x) = \Delta_r G^\circ + RT \ln\left(\frac{\left[P\left(n_{CH_4} + x\right)/\mathrm{n}_T \right]\left[P\left(n_{NH_3} + x\right)/\mathrm{n}_T \right]}{\left[P\left(n_{H_2} - 3x\right)/\mathrm{n}_T \right]^3 \left[P\left(n_{HCN} - x\right)/\mathrm{n}_T \right]} \right) \quad \text{(AI-18)}$$

Here, n_i is the observed moles for each species, n_T is the total number of moles, P is the pressure, and x is the number of moles that have reacted. We solve for x to find the equilibrium abundances for each species. Note that since we are performing this calculation at P=1 bar in Jupiter's atmosphere, and since we are using mixing ratios for the number of moles (n_T = 1) the equation (AI-18) can be simplified:

$$\Delta_r G(x) = \Delta_r G^\circ + RT \ln\left(\frac{\left(n_{CH_4} + x\right)\left(n_{NH_3} + x\right)}{\left(n_{H_2} - 3x\right)^3 \left(n_{HCN} - x\right)} \right) \quad \text{(AI-19)}$$

By setting $\Delta_r G(x) = 0$ this equation can be rearranged to give the following polynomial:

$$\left(n_{H_2} - 3x\right)^3 \left(n_{HCN} - x\right) \exp\left(-\frac{\Delta_r G^\circ}{RT} \right) - \left(n_{CH_4} + x\right)\left(n_{NH_3} + x\right) = 0 \quad \text{(AI-20)}$$

This polynomial in x is solved numerically. The equilibrium is the smallest real solution since the reaction will proceed to this point. In this case this solution is $x_{eqm}=3.6\times10^{-9}$. This solution equals the initial mixing ratio of HCN (table 3), which implies that reaction (AI-14) goes to completion when Jupiter's atmosphere is reacted to equilibrium.

To calculate the change in Gibbs energy change associated with this reaction going to completion we calculate the integral:

$$\begin{aligned} &\int_{x=0}^{x=3.6\times10^{-9}} \Delta_r G(x')/n_T dx' = \int_{x=0}^{x=3.6\times10^{-9}} \Delta_r G(x') dx' \\ &= \int_{x=0}^{x=3.6\times10^{-9}} \left[\Delta_r G^\circ + RT \ln\left(\frac{\left(n_{CH_4} + x'\right)\left(n_{NH_3} + x'\right)}{\left(n_{H_2} - 3x'\right)^3 \left(n_{HCN} - x'\right)} \right) \right] dx' = 7.5137\times10^{-4}\ J/mol \end{aligned} \quad \text{(AI-21)}$$

The same methodology can be repeated for reaction (AI-15).

$$\Delta_r G = \Delta_r G^\circ + RT \ln(Q) = \Delta_r G^\circ + RT \ln\left(\frac{a_{CH_4} a_{H_2O}}{a_{H_2}{}^3 a_{CO}} \right) \quad \text{(AI-22)}$$

In this case the standard free energy of the reaction computed at T = 165 K is $\Delta_r G^\circ = -1.68862\times10^5$ J/mol. Substituting activities for x and simplifying yields the equation:

$$\Delta_r G(x) = \Delta_r G^\circ + RT\ln\left(\frac{\left(n_{CH_4}+x\right)\left(n_{H_2O}+x\right)}{\left(n_{H_2}-3x\right)^3\left(n_{CO}-x\right)}\right) \qquad \text{(AI-23)}$$

Next, the Gibbs energy of the reaction is set to zero and terms are rearranged to obtain the polynomial:

$$\left(n_{H_2}-3x\right)^3\left(n_{CO}-x\right)\exp\left(-\frac{\Delta_r G^\circ}{RT}\right)-\left(n_{CH_4}+x\right)\left(n_{H_2O}+x\right)=0 \qquad \text{(AI-24)}$$

The solution to this polynomial is $x_{eqm}=1.6\times10^{-9}$ which indicates that CO is depleted and this reaction also goes to completion. The change in Gibbs free energy associated with this reaction is given by:

$$\int_{x=0}^{x=1.6\times10^{-9}} \Delta_r G(x)dx = 2.8068\text{e-}04\times10^{-4}\ \text{J/mol} \qquad \text{(AI-25)}$$

Finally, we sum together the Gibbs energy changes from these two reactions to obtain an approximation of the available Gibbs energy in Jupiter's atmosphere:

$$\Phi \approx 7.5137\times10^{-4} + 2.8068\text{e-}04\times10^{-4} = 0.001032\ \text{J/mol} \qquad \text{(AI-26)}$$

This compares to 0.001032 J/mol using the numerical model (Chapter 2, table 3), so the semi-analytic approximation is good to 4 significant figures in this instance.

Earth (atmosphere-ocean):

Next, we describe our semi-analytic calculations for the Earth atmosphere-ocean system. These calculations were used to obtain the "semi-analytic approximation" values in table 8 and table 9. Firstly, we consider the Gibbs energy associated with the equation:

$$2N_2(g)+5O_2(g)+2H_2O(l) \rightleftharpoons 4H^+(aq)+4\,\mathrm{NO_3^-}(aq) \qquad \text{(AI-27)}$$

The Gibbs energy of this reaction is given by:

$$\Delta_r G = \Delta_r G^\circ + RT\ln(Q) = \Delta_r G^\circ + RT\ln\left(\frac{a_{H^+}{}^4 a_{NO_3^-}{}^4}{a_{N_2}{}^2 a_{O_2}{}^5 a_{H_2O}{}^2}\right) \qquad \text{(AI-28)}$$

The activity of each species *i* is denoted by a_i, the average temperature of Earth's atmosphere at the surface is T=288.15 K, R is the universal gas constant, and Q is the reaction quotient. From equation (AI-27) the

Gibbs energy of the reaction, $\Delta_r G$, is the change in Gibbs energy of the system per 2 moles of N_2, 5 moles of O_2, and 2 moles of $H_2O_{(l)}$ that are converted to hydrogen ions and nitrate. The standard free energy of the reaction, $\Delta_r G^\circ$, represents the value of this quantity when the activities of all species equals unity. In this case, with T = 288.15 K and P = P $_r$= 1 bar:

$$\begin{aligned}\Delta_r G^\circ &= 4\Delta_f G^\circ_{H^+(T,\mathrm{P})} + 4\Delta_f G^\circ_{NO_3^-(T,\mathrm{P})} - 2\Delta_f G^\circ_{H_2O_{(l)}(T,\mathrm{P}_r)} - 5\Delta_f G^\circ_{O_2(T,\mathrm{P}_r)} - 2\Delta_f G^\circ_{N_2(T,\mathrm{P}_r)} \\ &= 4\times 0 + 4\times -1.09164\times 10^5 - 2\times -2.387764\times 10^5 - 5\times 0 - 2\times 0 \text{ J/mol} \\ &= 4.0897\times 10^4 \text{ J/mol}\end{aligned} \quad \text{(AI-29)}$$

Gibbs free energies of formation were taken from the same thermodynamic databases as those used for the Gibbs energy minimization calculations. Reaction (AI-27) is in equilibrium when the left hand side of equation (AI-28) is equal to zero. We solve for this equilibrium by making the following substitution:

$$\Delta_r G(x) = \Delta_r G^\circ + RT \ln\left(\frac{\left[\gamma_{H^+}\left(n_{H^+}+4x\right)/M_{ocean}\right]^4\left[\gamma_{NO_3^-}\left(n_{NO_3^-}+4x\right)/M_{ocean}\right]^4}{\left[P\left(n_{N_2}-2x\right)/n_T\right]^2\left[P\left(n_{O_2}-5x\right)/n_T\right]^5 {a_{H_2O}}^2}\right) \quad \text{(AI-30)}$$

The activities of aqueous species are given by their molalities multiplied by an activity coefficient. Here, M_{ocean} =1.3802×10^{21} kg is the mass of the Earth's ocean, n_i is the observed moles for each species, n_T = 1.7560×10^{20} is the total number of moles of air (all gases) in the atmosphere, P=1.013 bar is the mean sea-level pressure, and x is the number of moles that have reacted. We solve for x to find the equilibrium abundances for each species. By setting the left hand side of equation (AI-30) to zero, assuming that the activity of water equals 1, and that the activity coefficients of all other species are 1, we obtain the following polynomial in x:

$$\left(\frac{P}{n_T}\right)^7\left(n_{N_2}-2x\right)^2\left(n_{O_2}-5x\right)^5 \mathrm{e}^{-\frac{\Delta_r G^\circ}{RT}} = \left(\frac{1}{{M_{ocean}}^8}\right)\left(n_{H^+}+4x\right)^4\left(n_{NO_3}+4x\right)^4 \quad \text{(AI-31)}$$

This polynomial is solved numerically. The equilibrium is the smallest real solution since the reaction will proceed to this point. In this case this solution is x_{eqm}= 6.05586×10^{18}. This solution does not equal the initial mixing ratio of O_2, which implies that reaction does not go all the way to completion.

To calculate the change in Gibbs energy change associated with reaction (AI-27) going to equilibrium we calculate the integral:

$$\Delta G_1 = \int_{x=0}^{x=6.055\times 10^{18}} \Delta_r G(x)/n_T \, dx = 1051 \text{ J/mol} \quad \text{(AI-32)}$$

This is how the "semi-analytic approximation" value in row 1, table 9 was calculated.

Next, we consider the Gibbs energy changes associated with the following carbon-bearing reactions:

$$H^+ + HCO_3^- \rightleftharpoons H_2O_{(l)} + CO_{2(g)} \qquad \text{(AI-33)}$$

$$2H^+ + CO_3^{-2} \rightleftharpoons H_2O_{(l)} + CO_{2(g)} \qquad \text{(AI-34)}$$

The Gibbs energy of reaction (AI-33), the first dissociation of carbonic acid, is given by:

$$\Delta_r G = \Delta_r G^\circ + RT\ln(Q) = \Delta_r G^\circ + RT\ln\left(\frac{a_{H_2O_{(l)}} a_{CO_{2(g)}}}{a_{H^+} a_{HCO_3^-}}\right) \qquad \text{(AI-35)}$$

The method for calculating the Gibbs energy change for this reaction is identical to that described above, and so we simply list the key equations:

$$\begin{aligned}\Delta_r G^\circ &= \Delta_f G^\circ_{H_2O_{(l)}(T,\mathrm{P_r})} + \Delta_f G^\circ_{CO_{2(g)}(T,\mathrm{P_r})} - \Delta_f G^\circ_{H^+(T,\mathrm{P})} - 5\Delta_f G^\circ_{HCO_3^-(T,\mathrm{P})} \\ &= 4.7475\times10^4 \text{ J/mol, with } T = 288 \text{ K and P = P}_\mathrm{r} = 1 \text{ bar}\end{aligned} \qquad \text{(AI-36)}$$

$$0 = \Delta_r G(x) = \Delta_r G^\circ + RT\ln\left(\frac{\left[P\left(n_{CO_2}+x\right)/n_T\right]a_{H_2O}}{\left[\gamma_{H^+}\left(n_{H^+}-x\right)/M_{ocean}\right]\left[\gamma_{HCO_3^-}\left(n_{HCO_3^-}-x\right)/M_{ocean}\right]}\right) \qquad \text{(AI-37)}$$

Crucially, n_{H^+} is not the observed H^+ abundance but is instead the equilibrium abundance from reaction (AI-27); it is the acidification of the ocean from dissolved nitrate that drives the change in carbon species (see Chapter 2). Simplifying to obtain polynomial in *x*:

$$\left(n_{H^+}-x\right)\left(n_{HCO_3^-}-x\right)\exp\left(\frac{-\Delta_r G^\circ}{RT}\right) = {M_{ocean}}^2 P\left(n_{CO_2}+x\right)/n_T \qquad \text{(AI-38)}$$

The physically relevant solution is $x_{eqm} = 2.3951\times10^{18}$. The Gibbs energy change for the reaction can thus be calculated:

$$\Delta G_2 = \int_{x=0}^{x=2.44\times10^{18}} \Delta_r G(x)/n_T dx = 520 \text{ J/mol} \qquad \text{(AI-39)}$$

Repeating this procedure for equation (AI-34), the second dissociation of carbonic acid, yields $\Delta G_3 = 152$ J/mol. The contributions from all three reactions can be summed to approximate the total available Gibbs energy for the Earth atmosphere-ocean system (assuming water activity equals 1):

$$\Phi \approx \Delta G_1 + \Delta G_2 + \Delta G_3 = 1724 \text{ J/mol} \qquad \text{(AI-40)}$$

This is how the value for the "semi-analytic approximation" in tables 8 and 9 was calculated. There is no straightforward way to extend this semi-analytic method to include changes in water activity, hence the discrepancy between semi-analytic and numerical values.

This procedure was repeated to approximate the available Gibbs energy for the Solar System planets. The key redox reactions chosen for these calculations are as follows:

Mars:

$$2CO + O_2 \rightleftharpoons 2CO_2 \quad \text{(AI-41)}$$

$$2NO \rightleftharpoons N_2 + O_2 \quad \text{(AI-42)}$$

$$2O_3 \rightleftharpoons 3O_2 \quad \text{(AI-43)}$$

$$2H_2 + O_2 \rightleftharpoons 2H_2O \quad \text{(AI-44)}$$

In Mars' case all these reactions go to completion.

Venus:

$$H_2S + CO_2 \rightleftharpoons H_2O + OCS \quad \text{(AI-45)}$$

$$3CO + SO_2 \rightleftharpoons 2CO_2 + OCS \quad \text{(AI-46)}$$

$$2CO_2 + S \rightleftharpoons SO_2 + 2CO \quad \text{(AI-47)}$$

$$H_2 + S \rightleftharpoons H_2S \quad \text{(AI-48)}$$

In Venus' case, reactions (AI-47) and (AI-48) go to completion whereas reactions (AI-45) and (AI-46) reach equilibria where the reactants are not entirely depleted.

Earth (atmosphere only):

$$CH_4 + 2O_2 \rightleftharpoons 2H_2O + CO_2 \quad \text{(AI-49)}$$

$$2H_2 + O_2 \rightleftharpoons 2H_2O \quad \text{(AI-50)}$$

$$2CO + O_2 \rightleftharpoons 2CO_2 \quad \text{(AI-51)}$$

$$2N_2O \rightleftharpoons 2N_2 + O_2 \quad \text{(AI-52)}$$

All of these reactions proceed to completion in the Earth's case.

Titan:

$$C_2H_6 + H_2 \rightleftharpoons 2CH_4 \quad \text{(AI-53)}$$

$$C_2H_2 + 3H_2 \rightleftharpoons 2CH_4 \quad \text{(AI-54)}$$

Both of these reactions proceed to completion.

Uranus:

$$C_2H_6 + H_2 \rightleftharpoons 2CH_4 \quad \text{(AI-55)}$$

$$C_2H_2 + 3H_2 \rightleftharpoons 2CH_4 \quad \text{(AI-56)}$$

$$CO + 3H_2 \rightleftharpoons CH_4 + H_2O \quad \text{(AI-57)}$$

All three reactions proceed to completion.

Appendix 2-E: Multiphase calculations in Aspen Plus

To validate our multiphase Matlab calculations, we used Aspen Plus to calculate chemical and phase equilibrium for the Earth atmosphere-ocean system. Figure E1 shows the Aspen Plus flowsheet. The observed state was partitioned into vapor and liquid phases, and fed into the RGIBBS reactor as two separate streams. RGIBBS is a module in Aspen Plus that can calculate equilibrium abundances using Gibbs free energy minimization. The resultant mixed stream was fed into a Flash2 phase separator and partitioned into equilibrium vapor abundances and liquid abundances. Without the phase separator the equilibrium results were unphysical, and the resultant Gibbs energy change was inaccurate. We used a calculator block to determine the Gibbs energy change between the two input streams and two output streams. Calculator blocks were necessary to compute the Gibbs energy of the initial and equilibrium states with sufficient precision to calculate the Gibbs energy change accurately (otherwise the default output did not provide enough significant figures).

To check that our results were robust we used the setup of figure E1 to calculate the equilibrium state using two different Aspen Plus electrolyte models, the Electrolyte Non-Random Two Liquid (ELECNRTL) model the PITZER model. Henry's Law components were used for all gaseous species except water. The equilibrium abundances from both models were very similar. The overall Gibbs energy change of the Earth atmosphere-ocean system was 2348 J/mol for the ELECNRTL model and 2205 J/mol for the PITZER model. It is unsurprising that there are slight differences between the two models since they use different equations of state and different thermodynamic property models. Both agree with our own numerical Gibbs energy minimization to within 6%.

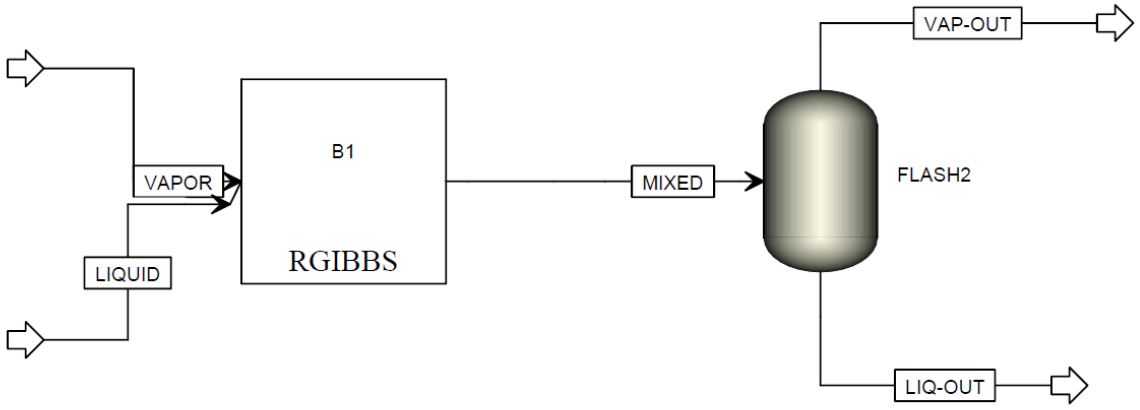

Figure E1: Aspen Plus flowsheet for multiphase calculations.

Appendix 4-A: Energy-limited carbon monoxide consumption

This section calculates likely steady-state CO abundances in Archean Earth-like atmospheres assuming biological CO consumption uses the available free energy. The two relevant metabolisms are specified by the following equations:

$$CO + H_2O \rightarrow CO_2 + H_2 \quad \text{(AI-58)}$$

$$CO_2 + 4H_2 \rightarrow CH_4 + 2H_2O \quad \text{(AI-59)}$$

Since we are considering planets with CH_4+CO_2 biosignatures, methanogenesis (equation (AI-59)) is present by assumption. The net result of these two metabolisms is:

$$4CO + 2H_2O \rightarrow CH_4 + 3CO_2 \quad \text{(AI-60)}$$

Given this net reaction and assumed CH_4 and CO_2 abundances, the CO abundance at which the net biological reaction proceeds at the limit of thermodynamic viability can be calculated. The biosphere will draw down atmospheric CO to this level assuming metabolic activity is not limited by the availability of other substrates or nutrients (see below).

Following Kral et al. (1998) and Kasting et al. (2001), we conservatively assume the reaction (AI-60) is no longer thermodynamically viable when the Gibbs energy yield equals the Gibbs energy required to synthesize four moles of ATP (4 moles of CO are oxidized in reaction (AI-58)). In other words, we are solving the following equation:

$$\Delta G_{4\,ATP} = \Delta G_0 + RT \ln\left(\frac{p\mathrm{CH_4} \times \left(p\mathrm{CO_2}\right)^3}{\left(p\mathrm{CO}\right)^4}\right) \quad \text{(AI-61)}$$

Here, $\Delta G_{4\,ATP}$ =-142 kJ/mol is the change in Gibbs energy required to synthesize 4 mol of ATP, ΔG_0 = -227.2 kJ/mol is the Gibbs energy of the reaction at standard conditions (calculated using code and databases described in Krissansen-Totton et al. (2016)), R=8.314 J/mol/K is the gas constant, T=300 K is surface temperature, and pCH_4, pCO_2, and pCO are gas partial pressures (in bar). Note that the activity of water is unity since water is not supply limited at the surface of habitable planets. For the Archean Earth-like planets in our paper pCH_4=0.005 bar and pCO_2=0.05 bar. Solving this equation yields pCO = 6×10^{-6} bar. This is almost certainly an overestimate of the energy-limited CO abundance because chemoautotrophic metabolisms are known to metabolize at free energies less than the amount required for ATP synthesis (Conrad 1996). For example, methanogenesis can be supported by less than half the Gibbs energy yield

from ATP synthesis (Conrad 1996), and so adopting a more realistic value of $\Delta G_{2\ ATP}$ on the left hand side of equation (AI-61) yields pCO = 5×10^{-9} bar.

Is it reasonable to assume biological CO-consumption would be energy limited? Harman et al. (2015a) modeled the photochemical production of CO in Earth-like atmospheres and found steady-state CO surface deposition fluxes of up to 5×10^{11} molecules/cm^2/s (1.3×10^{14} mol C/yr) were required to balance photochemical production around M-dwarfs. The carbon throughput on Earth's terrestrial biosphere is around 10^{16} mol/yr (Beer et al. 2010), whereas the primary ocean productivity is around 4×10^{15} mol C/yr (del Giorgio & Duarte 2002). Consequently, any CO-consuming biosphere need only be a few percent as productive as Earth's biosphere to draw down atmospheric CO. The only other substrate in the CO-consuming reaction, water, would not be limiting on the surfaces of habitable planets by assumption. Biospheres may exist that are so severely nutrient-limited that photochemically-produced CO accumulates despite CO consumption. However, based on the above considerations we expect biological CO drawdown to be the norm rather than the exception on inhabited worlds.

Appendix 4-B: Alternative radius formulation and radius-abundance degeneracy

In Chapter 4 the planet radius parameter used in our retrievals was defined as the solid-body radius. Here, we repeat our nominal Archean Earth-like NIRSpec prism retrieval (Fig. 2) where the radius parameter now represents the 1 mbar radius. This approach is more typical of retrievals of giant planet atmospheres, and it ensures radius and surface pressure are independent. By defining the radius as the 1 mbar radius the degeneracy between gas abundances and radius are more clearly revealed than when using surface radius, which is anticorrelated with surface pressure (Fig. 2).

The results are shown in Fig. A1. The joint distributions for radius and gas abundances now show a tight anticorrelation because if the the 1 mbar radius is increased then the abundances of absorbing gases must be decreased to produce the same transit heights. However, the marginal distributions for gas abundances are virtually identical to Fig. 2 because we are merely changing the basis vector that describes our atmosphere.

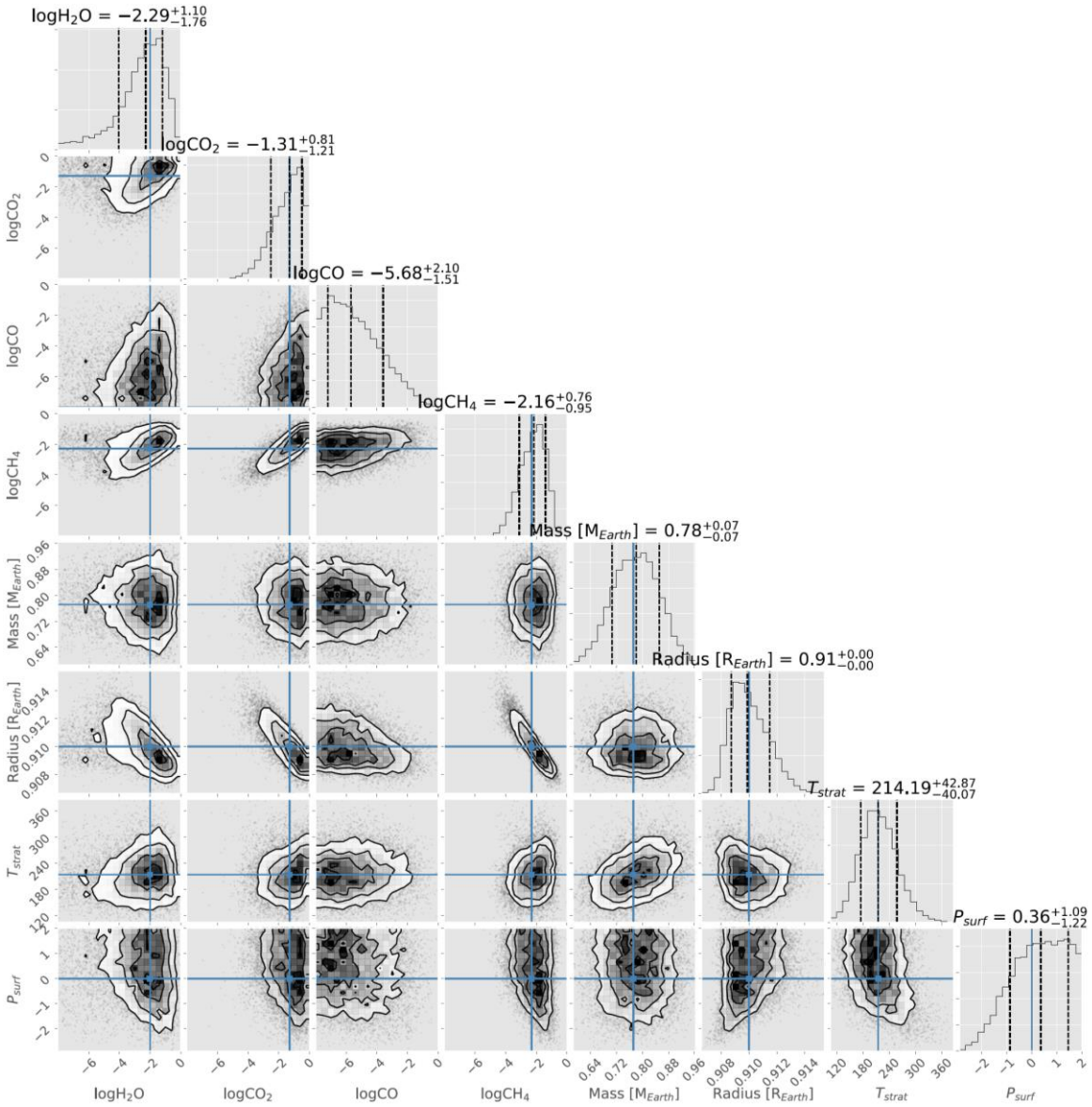

Fig. A1: Same as Fig. 2 except in this retrieval the planet radius parameter represents the 1 mbar radius rather than the solid-body (surface) radius. The joint distributions between radius and gas abundances now show a clear anti-correlation, but the marginal distributions for gas abundances are unchanged.

.

Appendix II - Is the Pale Blue Dot unique? Optimized photometric bands for identifying Earth-like exoplanets

Portions of this appendix were originally published in collaboration with Edward W. Schwieterman, Benjamin Charnay, Giada Arney, Tyler D. Robinson, Victoria Meadows, David C. Catling in The Astrophysical Journal (Krissansen-Totton et al. (2016), Is the Pale Blue Dot unique? Optimized photometric bands for identifying Earth-like exoplanets. The Astrophysical Journal 817 (1), 31)

Abstract

The next generation of ground and space-based telescopes will image habitable planets around nearby stars. A growing literature describes how to characterize such planets with spectroscopy, but less consideration has been given to the usefulness of planet colors. Here, we investigate whether potentially Earth-like exoplanets could be identified using UV-visible-to-NIR wavelength broadband photometry (350-1000 nm). Specifically, we calculate optimal photometric bins for identifying an exo-Earth and distinguishing it from uninhabitable planets including both Solar System objects and model exoplanets. The color of some hypothetical exoplanets – particularly icy terrestrial worlds with thick atmospheres – is similar to Earth's because of Rayleigh scattering in the blue region of the spectrum. Nevertheless, subtle features in Earth's reflectance spectrum appear to be unique. In particular, Earth's reflectance spectrum has a 'U-shape' unlike all our hypothetical, uninhabitable planets. This shape is partly biogenic because O_2-rich, oxidizing air is transparent to sunlight, allowing prominent Rayleigh scattering, while ozone absorbs visible light, creating the bottom of the 'U'. Whether such uniqueness has practical utility depends on observational noise. If observations are photon limited or dominated by astrophysical sources (zodiacal light or imperfect starlight suppression), then the use of broadband visible wavelength photometry to identify Earth twins has little practical advantage over obtaining detailed spectra. However, if observations are dominated by dark current then optimized photometry could greatly assist preliminary characterization. We also calculate the optimal photometric bins for identifying extrasolar Archean Earths, and find that the Archean Earth is more difficult to unambiguously identify than a modern Earth twin.

Introduction

Voyager 1's iconic image of the pale blue dot vividly illustrates the isolation and fragility of the Earth (Sagan 1994). However, the image also shows that hints of Earth's uniqueness are visible at great distances. In both *Voyager's* image, and in more recent reincarnations such as the *Cassini* portrait (NASA 2013), the pale blue color of Earth sets it apart from any other planet in our Solar System. In this study we explore the extent to which Earth's color is unique, and evaluate whether color photometry can be used to identify Earth-like planets around other stars.

In recent years, exoplanets have been directly imaged using ground-based telescopes (Delorme et al. 2013; Kuzuhara et al. 2013; Macintosh et al. 2015; Marois et al. 2008; Rameau et al. 2013), and in some cases characterized using photometry (Janson et al. 2013; Kuzuhara et al. 2013). Current instrumentation is limited to imaging young Jovian planets with large planet-star separations. These are still glowing with their heat of formation, which improves the planet/star contrast ratio (Macintosh et al. 2014).

However, starlight suppression technologies such as an internal coronagraph (e.g. Guyon et al. 2005; Stapelfeldt et al. 2015) or an external occulter (e.g. Cash 2006; Seager et al. 2015) could enable large-aperture future telescopes to directly image terrestrial exoplanets. In the near-term, the 2.4m WFIRST-AFTA telescope, identified as the top priority for NASA Astrophysics in the last Astronomy Decadal Survey (Blandford et al. 2010) and slated for launch in 2024, may be capable of performing the first space-based direct imaging of super-Earth planets around a small number of the very nearest stars (Spergel et al. 2015). Using the telescope/instrument noise model of Robinson et al. (2015), a 2m-class coronagraphic telescope like WFIRST-AFTA could image an Earth around a solar twin to a SNR=5 in V-band in 17 hr at 3 pc, and 76 hr at 5 pc, although this would require observing at roughly an order of magnitude below the 10^{-9} raw contrast, and so post-processing would be required.

The next generation large-aperture space-based telescopes concepts currently under consideration for the 2020 Decadal Survey, such as HabEx, a 4-6m-class dedicated exoplanet telescope; and the proposed, more ambitious 8-12m-class general purpose Advanced Technology Large-Aperture Space Telescope (ATLAST) (Postman et al. 2009), and High Definition Space Telescope (HDST) (Dalcanton et al. 2015), if selected for development, would be designed to be even more capable of direct imaging and spectral characterization of terrestrial exoplanets in the habitable zone. The Robinson et al. (2015) model for a 4m-class coronagraphic telescope, with a raw contrast of 10^{-10} and assuming an inner working angle of $2\lambda/D$, gives 2.8 hr and 8.3 hr integration times to reach SNR=5 in V-band for an Earth around Solar twin at 3pc and 5pc respectively. For a target system at a distance of 10 pc, a 4m-class telescope can make a V-band detection in 42 hr, while a 12-m class telescope would only require 4 hr. These initial designs and calculations suggest that obtaining photometry of Earth-like planets will be readily achievable with the planned next generation telescopes.

Similarly, on the ground, the next generation 40 m-class European Extremely Large Telescope (E-ELT) has identified taking images of Earth-like exoplanets as its highest scientific priority for the telescope, and the instrumentation plan includes an ambitious and powerful planetary camera and spectrograph for this purpose (https://www.eso.org/sci/facilities/eelt/instrumentation/, see also Kasper et al. (2010)). The Thirty Meter Telescope (TMT) may also be capable of directly imaging planets in the habitable zone around M-dwarfs (Matsuo & Tamura 2010).

Once potentially habitable exoplanets are directly imaged they may then be characterized by spectroscopy. A growing literature details how the atmospheric composition and surface properties of habitable exoplanets could be observationally constrained (e.g. Cockell et al. 2009; Des Marais et al. 2002a; Kaltenegger et al. 2010; Livengood et al. 2011; Robinson et al. 2010; Tinetti et al. 2006), including the possible detection of atmospheric and surface biosignatures (e.g. Kiang et al. 2007; Robinson et al. 2014; Sagan et al. 1993; Seager et al. 2012; Seager et al. 2005; Segura et al. 2003). However, for the first generation of telescopes capable of directly imaging terrestrial exoplanets, observing time devoted to exoplanets will likely be limited. The integration time required to detect an exo-Earth is significantly shorter than the time required to characterize an exo-Earth with a high-resolution spectrum. Consequently, only a handful of terrestrial exoplanets will initially be fully characterized. It would be advantageous if an initial photometric survey could identify exoplanets worthy of further characterization so telescope time can be used more judiciously. Of particular interest is whether habitable, terrestrial exoplanets can be identified using photometry alone, or whether there are photometric false positives for habitable exoplanets.

Color has been invaluable in the study of stars using the Hertzsprung-Russell diagram, but despite this precedent there is a sparse literature discussing terrestrial exoplanet characterization using photometry. Traub (2003a, 2003b) argued that planetary color might be sufficient for complete characterization and classification. Traub (2003b) used observational and modeled spectra of the Solar System planets, the Moon, and Titan to produce red and blue reflectivities on a color-color plot. It was argued that Earth occupies a unique position in red-blue color-color space. Crow et al. (2011) performed a more comprehensive analysis of the colors of Solar System bodies using photometric observations from EPOXI and other spacecraft, and also concluded that Earth occupies a unique space in red-blue color-color space compared to other Solar System bodies. However, Crow et al. (2011) did not consider exoplanets and used fixed red and blue bands, unlike the optimization we explore in this work.

Why is Earth a pale blue dot? Rayleigh scattering is strongest at short wavelengths and in transparent atmospheres without visible-light absorbers. Because Earth has a thick and largely transparent N_2-dominated atmosphere it has strong reflectance in the blue (<450 nm) due to Rayleigh scattering (Crow et al. 2011). The ocean contributes a small amount to Earth's blueness, but it is predominately a Rayleigh scattering effect (Cowan et al. 2011; Crow et al. 2011). The Earth is pale blue rather than deep blue because white clouds enhance reflectivity at all visible wavelengths and thus reduce the relative intensity of the Rayleigh tail. Earth's reflectance spectrum is shown in Fig. 1a. Additionally, Earth's spectrum is upward sloping between 600 nm and 900 nm due to the reflectivity of continents, which includes some vegetation (red edge) component (Arnold et al. 2002; Seager et al. 2005; Tinetti et al. 2006). Earth's spectrum also has a slight U-shape due to the combined effect of Rayleigh scattering, upward sloping continental reflectivity,

and ozone absorption in the Chappuis bands around 600 nm (Hamdani et al. 2006). The effect of the O_3 Chappuis bands can be seen on a daily basis. At twilight, a clear sky at the horizon would be more yellowish were it not for O_3 absorbing orange and yellow light, thereby producing a deep blue sky (Hulburt 1953). Chappuis bands ozone absorption is also a prominent features in Earth's transmission spectrum (Yan et al. 2015).

Crow et al. (2011) demonstrated that Solar System planets and moons without thick atmospheres are easily distinguished from Earth because their reflectance spectra are dominated by surface absorption and scattering. Both the Moon and Mars are strongly reflective in the red due to space weathering (Lucey et al. 1995) and the presence of iron oxides (Crow et al. 2011), respectively (see Fig. 1b). Uranus and Neptune are blue due to Rayleigh scattering, albeit to a lesser extent than Earth as a result of upper atmospheric hazes (see spectra in Fig. 1d). However, Uranus and Neptune are distinguishable from Earth on a color-color plot since they are much less reflective in the red due to methane absorption. Blueness from Rayleigh scattering is suppressed in the other Solar System bodies with thick atmospheres due to the presence of optical absorbers. This can be seen in the spectra of Jupiter, Saturn, Titan, and Venus in Fig. 1b and 1c.

Earth possesses this unique color in part due to biology. Photodissociation reactions in Earth's O_2-rich atmosphere generate ozone (O_3), and O_3 absorption at <340 nm generates excited oxygen, $O(^1D)$ (e.g. review by Catling 2015a). In the presence of water, excited oxygen readily reacts to produce hydroxyl radicals via the following reaction (Levy 1971):

- $$H_2O + O(^1D) \rightarrow 2OH \qquad \text{(AII-1)}$$

These hydroxyl radicals are highly reactive and oxidize sulfur species such as H_2S, OCS, and dimethyl sulfate to form sulfate aerosols, which rain out of the atmosphere. Additionally, hydroxyl radicals oxidize reduced species such as CO, CH_4, and other hydrocarbons to form CO_2 and H_2O (Catling 2015a). The net result is that haze-forming species are destroyed, thereby maintaining a clear atmosphere.

In the absence of biogenic O_2, hydroxyl abundance would be low, and so an optically absorbing haze could accumulate, particularly at high altitudes above the air where rainfall operates. Furthermore, the O_3 absorbs in the Chappuis bands, as mentioned above, which, in combination with Rayleigh scattering and continental reflectivity, gives Earth a unique U-shaped spectrum from UV through visible wavelengths. Note that this requires both oxygen-producing life and an active hydrological cycle to produce the necessary hydroxyl radicals.

The diversity of planetary environments within the Solar System is limited, and so to determine whether habitable Earth-like planets occupy a unique position in color space we must consider possible exoplanet spectra. Due to the limitations of current instrumentation, reflectance spectra can only be obtained for

transiting hot Jupiters in secondary eclipse, as has been done for HD209458b (Rowe et al. 2006) and HD189733b (Evans et al. 2013). Even in these cases, the error bars on reflectivity measurements are very large, and so we do not consider these observations in this study. For example, in the case of HD18933b, the mean reflectivity from 450-570 nm is within error of zero, and so the uncertainty in the reflectivity ratio with 450-570 nm in the denominator is effectively infinite.

In the absence of well-constrained observations, we must rely upon atmospheric models to determine the likely colors of exoplanets. There have been numerous attempts to generate plausible reflectance spectra of exoplanets. Sudarsky et al. (2000) modeled the reflectance spectra of gas giants by specifying composition and applying a radiative-transfer model that incorporated condensables. Five distinct giant planet classes were identified on the basis of temperature. Spiegel et al. (2010) modeled the atmospheres of Neptune-sized exoplanets using a similar methodology, and also demonstrated that planet-star separation (temperature) has a strong effect on color because the presence of both highly reflective condensables and short-wave absorbers is temperature dependent. Cahoy et al. (2010) modeled extrasolar Jupiter and Neptune analogs for a range of star-planet separations, viewing phases, and metallicities. They concluded that viewing phase may have strong effect on Jovian reflectance spectra, which can make photometric characterization challenging.

The colors of terrestrial exoplanets have also been modeled with special attention given to the possible surface spectra of terrestrial exoplanets. For instance Sanromá et al. (2013) modeled the reflectance spectra of Earth-like planets with different continental surfaces such as desert, microbial mats, and vegetation, and Sanromá et al. (2014) calculated Archean Earth spectra for coastal areas dominated by purple bacteria. Hegde and Kaltenegger (2013) and Hegde et al. (2015) also described reflectance spectra for different surface features including extremophiles. However, the neglect of an atmosphere in Hegde and Kaltenegger (2013) means that the reflectance spectra and their derived broadband colors are not what would be observed remotely. Schwieterman et al. (2015a) measured the reflectance spectra of a diverse range of microorganism colonies and found that a halophile world might be remotely identifiable. Meadows (2006) and Kaltenegger et al. (2007) modeled the evolution of Earth's reflectance spectrum from the Archean to the present as an analog for exoplanet observations. Fig. 1e shows a selection of model exoplanet spectra.

Despite this abundance of model spectra, there has not been a systematic study of exoplanet reflectance spectra to determine the extent to which terrestrial planets can be distinguished from giant planets on the basis of color, or the extent to which Earth-like "pale blue dots" occupy a unique location in color-color space taking into account possible false positives. In this study we use both model and observed reflectance spectra to explore the locations of planets in color-color space. Specifically, we calculate the optimal photometric bands for identifying Earth-like exoplanets and distinguishing them from uninhabitable

planets. Our sample of uninhabitable planets is not intended to be exhaustive, but the model and observed spectra we consider are broadly representative of the types of planets that could be mistaken for habitable Earth-like planets, based on current knowledge. We also consider the prospects for identifying extrasolar Archean Earths using photometry. Finally, we compare the relative telescope integration time required to identify an exo-Earth using color to the time required to obtain a spectrum.

Methods

Reflectance spectra

The visible reflectance spectra used in this study were obtained from a variety of sources and are summarized in Table 1. Here, we describe in detail how model reflectance spectra were generated and where observed spectra were sourced.

For most Solar System objects, we used spectral observations from spacecraft and ground-based telescopes. Reflectance spectra for Jupiter, Saturn, Uranus, Neptune and Titan were obtained from Karkoschka (1998), and reflectance spectra for Callisto, Io, Europa and Ganymede were obtained from Karkoschka (1994). All of these spectra are full phase or very close to full phase (<7°).

The model reflectance spectra used in this study were generated using the Spectral Mapping Atmospheric Radiative Transfer Model (SMART). SMART is a one-dimensional, plane-parallel, line-by-line, multiple-scattering radiative transfer model developed by D. Crisp (Crisp 1997; Meadows & Crisp 1996). SMART takes as input vertical profiles of temperature, pressure, gas mixing ratios, and aerosol optical depths. With these inputs SMART calculates the monochromatic optical properties of each layer. Line absorption cross-sections are calculated with a program called Line-by-Line Absorption Coefficients (LBLABC), which determines the absorption coefficients of spectrally active given a line list database (Crisp 1997; Meadows & Crisp 1996). Because we leverage many existing spectra from the literature, the older HITRAN 2008 (Rothman et al. 2009) line lists were used to calculate the absorption coefficients for the spectrally absorbing gases in our model atmospheres except where stated otherwise. Throughout this work, when calculating gaseous absorption coefficients with LBLABC, a line cutoff of 1000 cm^{-1} is used. The gas absorption cross-sections determined by LBLABC are read in by SMART and multiplied by the gas mixing ratios and layer thicknesses to determine the normal-incidence gas extinction optical depths. The total extinction at each layer and each hyperfine spectral grid point is calculated by combining the gas extinction optical depths with those calculated for Rayleigh scattering and aerosols. We used a single solar zenith angle of 60 degrees for all runs, which approximates the illumination observed in a planetary disk average during an observation at quadrature phase (Segura et al. 2005). We assume the surfaces in this model are Lambertian reflectors, which is an approximately true assumption for the Earth at non-crescent phase angles (Robinson et al. 2010).

Earth spectra were obtained from Robinson *et al.* (2014; 2011). We used a validated 3D Earth model since this enabled us to explore how Earth's reflectance spectrum changes with phase. Validated (1D) model spectra were also used for Mars, Venus, and the Moon (Robinson et al. 2011). The disk-averaged Mars surface albedo spectrum was the same as that used in Crisp (1990) and was constructed from data obtained from McCord et al. (1982) and Blaney et al. (1988)

A coupled 1D photochemical-climate model was used to generate self-consistent ancient Earth atmospheres, both with and without haze, that are best estimates of those that existed in the Archean Eon (4.0-2.5 Ga). The radiative-convective climate portion of the model is based on the code developed originally by Kasting and Ackerman (1986) and updated most recently to study habitable zone boundaries (Kopparapu et al. 2013).

The photochemical portion of the coupled code originated in Kasting et al. (1979) and has since been modified extensively, including in a study that examined the potential for hazes to exist in the atmosphere of early Earth (Zerkle et al. 2012) using the mean field approximation for fractal particle scattering (Botet et al. 1997). The photochemical model includes 200 plane-parallel layers with a layer spacing of 0.5 km up to an altitude of 100 km. The abundances of chemically active species in each layer are calculated by solving mass and flux continuity equations using a reverse-Euler method. Outputs from this coupled model (haze particle density, the temperature profile, gas mixing ratios) are input into SMART to generate spectra. Haze refractive indices are taken from Khare et al. (1984).

The Archean Earth may have had a hydrocarbon haze in its atmosphere during some intervals (Domagal-Goldman et al. 2008; Pavlov et al. 2001a; Zerkle et al. 2012). This fractal hydrocarbon haze thickness scales with increasing CH_4 relative to CO_2 (Haqq-Misra et al. 2008). Our hazy Archean simulations have 1% CO_2, below a recent paleosol upper limit (Driese et al. 2011) for 2.7 Ga. A CH_4/CO_2 ratio of 0.2 generates a substantial haze in the coupled photochemical-climate model. A thicker haze, with larger particles, may be possible at a higher CH_4/CO_2 ratio or a hotter atmosphere because the particle coagulation timescale depends on temperature (Tolfo 1977). For this thicker haze scenario, we use a spectrum with $CH_4/CO_2 = 1$. For the purposes of this study, the $CH_4/CO_2 = 0.2$ spectrum is considered a "thin" haze compared to the "thick" haze of large particles generated by $CH_4/CO_2 = 1$. The solar constant in these simulations is scaled to 2.7 Ga and includes a wavelength-dependent scaling that corrects for solar evolution (Claire et al. 2012). The haze-free Archean Earth atmosphere was assumed to have 50% clear skies, 25% high cloud (8.5km), and 25% low cloud (1.5 km), which is a cloud parameterization used for the modern Earth (Robinson et al. 2011). Hazy spectra include the same cloud parameterization along with global coverage by hydrocarbons. A full description of the methodology used to generate Archean Earth atmospheres can be found in Arney

et al. (2015). Note that HITRAN 2012 (Rothman et al. 2013) was used to generate Archean Earth absorption coefficients.

To investigate the diversity of colors of giant planets, we included a number of model spectra of giant exoplanets and sub-Neptunes. Giant planet reflectance spectra were obtained from Sudarsky et al. (2000). Sudarsky et al. (2000) and Sudarsky et al. (2005) define five classes of giant planets based on temperature. Class 1 giant planets are cool (<150 K) and highly reflective due to ammonia clouds, class 2 planets are warmer (250 K) and reflective due to water clouds, class 3 and 4 planets are warmer still (≥350K and 900-1500 K respectively) and strongly absorbing due to alkali absorption bands and the absence of condensable species in the upper atmosphere, and class 5 planets are the hottest (>1500 K) and highly reflective due to silica and iron clouds. The bulk compositions of all five classes are assumed to be the same; what determines any giant planet's class is its planet-star separation (i.e. temperature). The effects of metallicity on reflectance spectra are relatively minor compared to the effects of temperature (Cahoy et al. 2010). We only consider class 1 and 2 giant planets in this study since higher temperature gas giants would necessarily be well interior to the inner edge of the habitable zone and thus easily distinguishable from habitable worlds on the basis of orbital distance.

NASA's *Kepler* mission has revealed that Super-Earths and sub-Neptunes are common (Fressin et al. 2013; Howard et al. 2010; Marcy et al. 2014). To better sample the diversity of exoplanet colors we generated a number of plausible sub-Neptune reflectance spectra based on a planet with the same mass ($6.6\,m_{\oplus}$) and radius ($2.4\,R_{\oplus}$) as GJ1214b, but with a stellar insolation of 2000 W/m^2. Reflectance spectra were generated for a cloud free H_2 dominated atmosphere with solar elemental abundances and a H_2 dominated atmosphere with 100x solar metallicity (solar nebula atomic abundances from Lodders (2003)). Each atmosphere was assumed to be in chemical equilibrium, and the temperature pressure profiles were obtained using the 1D version of the Generic LMDZ GCM (Charnay et al. 2015; Wordsworth et al. 2011). We also computed the reflectance spectra for a sub-Neptune with a pure steam atmosphere (water clouds were neglected). Note that HITRAN 2012 (Rothman et al. 2013) was used to generate sub-Neptune absorption coefficients.

The model spectra for the giant planets and sub-Neptunes described above are unrealistic because they assume that each atmosphere is in chemical equilibrium and so they do not include the effects of photochemical hazes. In our Solar System, both Jupiter and Saturn possess photochemical hazes that affect their color by suppressing Rayleigh scattering (Crow et al. 2011). Sudarsky et al. (2000) and Spiegel et al. (2010) considered the effects of adding photochemical hazes to their giant planet models, and we used the hazy class 1 giant planet reflectance spectra from Sudarsky et al. (2000) in this study. The model spectra

for giant planets and sub-Neptunes used in this study are speculative because currently few observational constraints exist for the reflectance spectra of exoplanets.

To simulate the color of a snowball Earth we used reflectance spectra for snow and blue ice surfaces from Warren et al. (2002) and Grenfell et al. (1994), as cited in Shields et al. (2013). We assumed an Earth-like atmosphere above these surfaces, and computed the resultant reflectance spectra for both a 100% snow and 100% blue ice planet. We also computed the reflectance spectra for an Earth-like atmosphere above a 100% kaolinite surface. These three spectra can be considered as end-member cases for a dusty snowball Earth. In our color-color plots we assume that a triangle region bounded by these three spectra encompasses the possible colors of a snowball Earth (see results section).

Optimization algorithm

For the purposes of this paper, we define a habitable planet as a terrestrial planet within its star's habitable zone (Kasting et al. 1993b; Kopparapu et al. 2013). Firstly, we consider the color of Earth and all uninhabitable planets, where the latter set includes gas and ice giants, hydrogen dominated and thick steam atmosphere sub-Neptunes, permanent snowballs, and all Solar System bodies excluding Earth. Table 1 indicates which planets are assumed to be uninhabitable. We refer to this set of uninhabitable planets as potential false positives, and we seek the photometric bins that optimally separate Earth from this set of false positives in color-color space such that probable exo-Earths can be easily identified by photometric observations.

The reflectivity of a planet, $R_{[a,b]}$, is defined as the mean reflectivity in the wavelength range *a* to *b* (in nm). In the simplest case, we seek three photometric bins $\{[a_1,b_1],[a_2,b_2],[a_3,b_3]\}$ which maximally separate Earth from false positives in color-color space, where $[a_i,b_i]$ denotes the wavelength range (in nm) of the ith photometric bin. Given these three bins, the reflectance spectra of every planet is calculated for each bin, and the planet can be plotted in color-color space, where color axes are defined as the reflectivity ratios $R_{[a_3,b_3]} / R_{[a_2,b_2]} = R_{red} / R_{green}$ and $R_{[a_1,b_1]} / R_{[a_2,b_2]} = R_{blue} / R_{green}$. Note that whenever reporting optimizations involving three bins, we typically use "red" to label the color of the longest wavelength bin, "blue" for the shortest wavelength bin, and "green" for the intermediate bin. These "red", "green", and "blue" labels may not correspond to the true colors of the bin. We use reflectivity ratios rather than absolute reflectivity because radius-albedo degeneracy will typically preclude the accurate measurement of absolute reflectivity from direct imaging alone.

We applied the optimization algorithm Constrained Optimization by Linear Approximation (COBYA) in Python to determine the set of photometric bins that maximizes Earth's separation from false positive

planets, subject to constraints ensuring non-overlapping bins that fit within the visible spectrum and are at least 100 nm wide (unless stated otherwise). The quantity that was maximized was the Pythagorean distance between Earth and the nearest false positive neighbor in color-color space. The optimization problem can be formally posed as follows:

$$\underset{a_1,a_2,a_3,b_1,b_2,b_3}{\textit{maximize}} \quad f\left(a_1,a_2,a_3,b_1,b_2,b_3\right) =$$

$$- \quad \min\left(\sqrt{\left[\left(R_{[a_1,b_1]}/R_{[a_2,b_2]}\right)_{Earth}-\left(R_{[a_1,b_1]}/R_{[a_2,b_2]}\right)_j\right]^2+\left[\left(R_{[a_3,b_3]}/R_{[a_2,b_2]}\right)_{Earth}-\left(R_{[a_3,b_3]}/R_{[a_2,b_2]}\right)_j\right]^2}\right)$$

$$\textit{subject to} \quad \left\{\lambda_{\min}<a_1\right\},\left\{b_3<\lambda_{\max}\right\},\left\{a_i+m<b_i\right\},\left\{b_i<a_{i+1}\right\}, \quad i=1,2,3$$

(AII-2)

Here, *j* is a member of the set of false-positive (uninhabitable) planets (see Table 1). The smallest wavelength used to form photometric bins, $\lambda_{\min}$, is typically 350 nm in our analysis. Similarly, $\lambda_{\max}=1000$ nm is the maximum allowable wavelength used to construct photometric bins. The minimal photometric bin width, *m*, is typically taken to be 100 nm unless stated otherwise. The first and second inequality constraints ensure that all three photometric bins fit into the desired spectral range (350-1000 nm). The third inequality constraint enforces the minimum bin size, and the fourth inequality constraint ensures that bins do not overlap.

The function to be maximized in (AII-2) is not convex, and so local maxima are not guaranteed to be the global maximum. Consequently, we implemented a brute force global optimization search by iterating the COBYA algorithm over 2000 randomized initial conditions and selecting the best solution as the global maximum. Repeat calculations consistently produced the same answer, thereby establishing that this optimization algorithm with 2000 iterations successfully computes the global maximum.

This methodology assumes three photometric bins with “red”/”green” and “blue”/”green” axes, but extension to three or four bins with generalized axes was also done for comparison. Rather than force the horizontal axis to be “red”/”green” and the vertical axis to be “blue”/”green” reflectivity ratios, the optimization algorithm can be modified to allow for any combination of bins on each axis (e.g. $R_{[a_i,b_i]}/R_{[a_k,b_k]}$ and $R_{[a_l,b_l]}/R_{[a_n,b_n]}$). In other words, calculations with generalized axes do not force the numerator (denominator) on the vertical axis to be the shortest (middle) wavelength bin, and do not force the numerator (denominator) on the horizontal axis to be the longest (middle) wavelength bin.

Results

Identifying exo-Earths

The color-color plot with optimized bins for separating Earth from false positives is shown in Fig. 2. The blue circle shows the Earth's position in color-color space (at quadrature), and the remaining symbols are the set of uninhabitable false positives. Some false positives are directly labeled and some are labeled in the legend, depending on available space. Earth is the only planet in the set we considered where both the "blue"/"green" and "red"/"green" ratios are appreciably bigger than 1. The wavelength ranges for the three optimal bins that define the reflectivity axes are 431-531 nm, 569-693 nm, 770-894 nm, and Earth is separated from its nearest neighbor (Callisto with a 0.75 bar N_2 atmosphere) by a distance of 0.32 in color-color space. The implications of the dimensionless separation are discussed below. A complete list of all the false positives in Fig. 2 is available in Table 1.

The red shaded region in Fig. 2 denotes the possible range of colors for a snowball Earth planet. This region encloses linear combinations of blue ice, snow, and kaolinite (dust) to represent spectra for a dirty snowball, as described in the methods section. The snowball false positive is assumed to possess an Earth-like atmosphere with clear skies. If clouds are added to the snowball then it moves slightly closer to Earth in color-color space. No false positives from our sample of planets occupy the exact same region of color-color space as the Earth (Fig. 2).

Many of the false positives we considered are models of icy worlds with relatively thick atmospheres. For instance, we computed the reflectance spectra for hypothetical exoplanets with surface spectra from Callisto, Europa, Ganymede, and Io, overlain by thick nitrogen atmospheres with surface pressures ranging 0.5-2 bar. Additionally, we computed the reflectance spectra for a hypothetical exoplanet with a Mars-like surface spectrum and a thick atmosphere of either N_2 or CO_2. Finally, we modeled thick atmospheres overlying kaolinite, CO_2 ice, and a gray surface to represent the possible diversity of icy worlds. Unless stated otherwise we assumed 250 K isothermal atmosphere for all icy planet models because this temperature is consistent with a frozen, uninhabitable surface, but is not so different from habitable conditions that it would be easily distinguishable on the basis of semi-major axis. Note however that the temperature does not affect the spectrum, only the implied atmospheric mass. These planets represent uninhabitable false positives that could plausibly be found beyond the outer edge of the habitable zone (semi-major axis may initially be unknown for planets discovered by direct imaging surveys). They were included in this study because the strong Rayleigh scattering from their thick, clear atmospheres, in combination with relatively flat or upward sloping surface spectra makes them similar in color to Earth. Some of these false positive spectra are shown in Fig. 3b and 3c.

Earth is separated from all the false positives due to the unique U-shape of its spectrum. Fig. 3a shows the Earth's reflectance spectrum superimposed on the optimal photometric bins that define the axes in Fig. 2. Here, it can be seen that the optimization algorithm picked bins that capture the U-shape of the Earth's spectrum. As described in the introduction, the high reflectivity in the blue is largely attributable to Rayleigh scattering, whereas the upward sloping shape of the spectrum between 600 and 900 nm is attributable to the reflectivity of continents, which includes some vegetation (red edge) component. (Tinetti et al. 2006). Reduced reflectivity around 600 nm due to ozone absorption in the Chappuis bands also contributes to the U-shape. This can be seen in Fig. 3a where we plot Earth's spectrum without ozone alongside Earth's spectrum with ozone. Ozone absorption is responsible for the bottom of the U-shape, and without ozone Earth would occupy a somewhat different position in color-color space.

If the optimization calculation is repeated - but the icy false positives are excluded - then the separation between Earth and its closest (non icy false positive) neighbor increases. This is shown in Fig. 4 where the separation between Earth and its nearest neighbor (a Class 1 giant, i.e. cool with ammonia clouds) in color-color space is 0.53. Here, the wavelength ranges for the three optimal bins that define the reflectivity axes are 350-450 nm, 593-693 nm, and 879-992 nm. This set of photometric bins does a better job of separating Earth from the non-icy bodies than the photometric bins in Fig. 2. However, if these revised photometric bins were used to identify potential exo-Earths then any exo-Earth would be indistinguishable from uninhabitable icy worlds. Fig. 4 shows that with these photometric bins Earth occupies the same region in color-color space as a planet with a 2 bar CO_2 atmosphere overlying Mars' surface or a planet with a 0.75 bar N_2 atmosphere overlying Callisto's surface. Even a planet with a gray (flat) surface spectrum and a 1-2 bar clear N_2 atmosphere is very similar in color to Earth. In short there are many ways to make a quasi pale blue dot that is not habitable.

For the purposes of characterizing exo-Earths, it is beneficial to allow gaps between photometric bins. For example, if the optimization algorithm is modified to disallow gaps between bins by enforcing the additional constraint, $\{b_i = a_{i+1}\}$, then the optimal separation between Earth and its nearest neighbor is reduced to 0.27 (not shown).

In addition to considering the forced "red"/"green" and "blue"/"green" axes in Fig. 2 and 4, we also optimized the separation between Earth and false-positive neighbors in color-color space with generalized axes. In other words, we allowed the optimization algorithm to consider all possible combinations of reflectivity ratios for use on the horizontal axis and vertical axis of color-color space. Fig. 5 shows the optimal separation between Earth and its nearest neighbor using generalized axes and three photometric bins. In this case the three bins that define the axes are 579-679 nm ("yellow"), 797-897 nm ("red"), and

898-999 nm ("far red"), and the color-color space axes for this optimal separation are $R_{[797,897]} / R_{[579,679]}$ and $R_{[797,897]} / R_{[898,999]}$. Here, Earth is separated from its nearest neighbor (Mars) by 0.40 in color-color space; this is a marginal improvement over the separation using "red"/"green" and "blue"/"green" axes. The vast majority of planets have a $R_{[797,897]} / R_{[898,999]}$ ratio of approximately 1, but Earth is closer to 1.5 due to strong water absorption around 940 nm. Thus, although generalized axes do a slightly better job of separating the Earth from uninhabitable planets than the forced "red"/"green" and "blue"/"green" axes, Earth is separated due to the presence of water (a habitability feature) and not specifically biogenic features of its spectrum. If the calculation is repeated using four photometric bins rather than three, then the optimal separation is 0.38 (not shown). This demonstrates there are no added benefits to using four photometric bins rather than three photometric bins to identify exo-Earths.

We also investigated optimizing Earth's separation from false-positive planets in a 3-dimensional color space, and by modifying the separation criteria to be optimized. Examples of the latter included maximizing the mean or median separation between Earth and all its neighbors, maximizing the separation to the nearest neighbor scaled by the mean difference between all pairs of planets, and fitting a linear regression to all planets and maximizing Earth's residual. None of these approaches were improvements over the simple criteria applied in figures 2, 4 and 5.

The effect of phase

All the model spectra so far in this study represent observations during quadrature, which is the most probable viewing geometry for directly imaged exoplanets. Fig. 6 shows the probability distribution of apparent phase for the direct imaging of an exoplanet with a random inclination and position in its orbit. This was calculated by repeatedly sampling uniform distributions of inclination and position in orbit, and calculating the resultant phase as viewed by a distant observer. Disk-averaged quadrature observations do not exist for many Solar System objects, and so we were forced to use full phase observations in these cases. It is beyond the scope of this study to model the 3D phase-dependent photometry for every planet we considered. However, it is possible to explore the effects of phase for some planets to see how this affects our conclusions.

A validated 3D Earth model was used to generate Earth's reflectance spectrum (see methods), and so the effect of phase on Earth's position in color-color space can be explored. Fig. 7 is identical to Fig. 2 (Earth optimally separated from all false positives), except that we have plotted four blue symbols for the Earth representing full, quadrature, gibbous, and crescent phases. Evidently, viewing phase does not have a large effect on Earth's color – all four phases are clearly separated from the uninhabitable false positives in color-color space. This is a general result that is not dependent on the specific photometric bins used.

Cahoy et al. (2010) used an albedo spectral model with detailed scattering calculations to compute the reflectance spectra of Jupiter and Neptune analogs as a function of orbital phase. In this model the emergent flux is integrated over the planet's surface to capture spatially-dependent scattering behavior. It is found that the Jupiter analog – a 3x solar metallicity Jovian at 0.8 AU with an atmosphere in chemical equilibrium – has the most phase variability in its reflectance spectrum. The Jovian model spectra from figure 12 of Cahoy et al. (2010) are plotted in color-color space in our Fig. 7 to show an extreme example of phase-dependent color. Here, the "blue"/"green" ratio decreases dramatically as phase angle increases. This is analogous to the sunset effect: at large phase angles (crescent phase), the mean path length through the atmosphere is large, and so blue light is preferentially scattered out of the observer's beam.

The effect of clouds

The clouds for the Earth spectra used in our analyses are parametrized based on the comparison of *EPOXI* Earth observations to the 3D Earth model (Robinson et al. 2011). Exo-Earths could have different levels of cloudiness to the modern Earth, and so the effects of cloudiness on color need to be evaluated. We investigated the dependence of Earth's color on cloud fraction and height by computing a 1D Earth spectrum for five different cases: 100% low level stratocumulus cloud (1.5 km, optical depth 10), 100% medium-level alto-stratus clouds (3.9 km, optical depth 10), 100% high level cirrus clouds (8.5 km, optical depth 10), clear skies, and clear skies with a 100% ocean surface. These end-member cases are plotted in color-color space in Fig. 7. The blue shaded region spans the range of colors possible for different levels of cloudiness. We find that 100% cloud cover at any height moves the Earth closer to the icy false positives in color-color space. This is unsurprising because 100% cloud cover eliminates all contributions from the surface reflectance spectrum, which is responsible for the upward sloping shape in the red portion of Earth's spectrum. Additionally, 100% cloud cover reduces the average path length in the atmosphere, which diminishes the blueness due to Rayleigh scattering. This explains why the 'clear skies with a 100% ocean surface' end-member is bluer than all the other Earth spectra, although the ocean surface itself also contributes to the blueness (Crow et al. 2011). The position of the clear sky Earth shows the redness of the vegetated continental surface compared to the ocean.

Minimum bin size

There is a trade-off between optimal color-color separation and photometric bin sizes. Reducing the minimal bin size (m) will result in larger optimal separations between Earth and its nearest neighbor because narrower, more diagnostic regions of the spectra can be targeted. However, reducing the minimal bin size will reduce the photon flux in each bin, thereby increasing the integration time required to separate the Earth from its nearest neighbor to any desired level of precision. To investigate the effect of minimum bin size, we repeated the Earth-separating optimization and varied the minimum bin size from 50 nm to 150

nm. This is shown in Fig. 8 where the optimal separation between Earth and its nearest neighbor is plotted as a function of minimum bin size. Reducing the minimum bin size does not improve the optimal separation much. For a minimum bin size of 50 nm, the optimal separation between Earth and its nearest neighbor is 0.39. This is only 20% larger than the optimal separation for 100 nm minimum bins (0.32). The minimum bin size must be decreased to 30 nm before the nearest neighbor separation increases markedly to 1.10 (not shown).

Identifying extrasolar Archean Earths

If the Archean Earth is plotted in color-color space using the three photometric bins that optimally separate the modern Earth, then it is clear that the Archean Earth is difficult to identify (Fig. 7). For example, the hazy Archean Earth could be mistaken for a gas giant or Titan-like exoplanet, whereas the non-hazy Archean Earth could be mistaken for a Mars-like exoplanet with a thick atmosphere. This demonstrates the potential for false negatives: planets that appear to be uninhabitable based on photometry, but could in fact be revealed as habitable using high resolution spectroscopy.

To try to distinguish Archean Earths, we repeated the optimal separation calculations described above with the Archean Earth as the subject. Specifically, we repeated the calculations four times to represent four plausible Archean Earth scenarios: thick-haze with high methane (1% mixing ratio), thin-haze with low methane (0.2% mixing ratio), non-hazy with high methane (1% mixing ratio), and non-hazy with low methane (0.2% mixing ratio). Note that although the modern Earth is included in the figures that follow, we only attempted to separate the Archean Earth from the set of false positives: the modern Earth is merely plotted as a reference.

It is extremely difficult to uniquely identify the hazy Archean Earth using photometry alone. Fig. 9a shows the thin-haze Archean Earth optimally separated from all potential false-positives using the "red"/"green" and "blue"/"green" axes. Here, the optimal photometric bins are 350-535 nm ("blue"), 780-893 nm ("green"), and 900-1000 nm ("red"), and the Archean Earth is separated from its nearest neighbor, Jupiter, by only 0.20 in color-color space (note that the scaling of the horizontal axis is bigger than the vertical axis). Modifying the optimization algorithm to allow for generalized axes improves the optimal separation slightly, but tends to place the Archean Earth in a non-unique region of color-color space. For example Fig. 9b shows the thick haze Archean Earth optimally separated from all false-positives using generalized three-bin axes. In this case, the optimal photometric bins are 350-450 nm ("blue"), 572-853 nm ("green"), and 853-953 nm ("red") with corresponding axes $R_{[572,853]} / R_{[350,450]}$ and $R_{[572,853]} / R_{[853,953]}$. The separation between the Archean Earth and its nearest neighbor is 0.44, but Fig. 9b shows that it is positioned between

Jupiter and Saturn; it is easy to imagine an intermediate gas giant that could be conflated with the thick-hazed Archean Earth using these photometric bins.

It is also difficult to identify the non-hazy Archean Earth using photometry. For example Fig. 9c shows the high methane non-hazy Archean Earth optimally separated from all false positives using generalized reflectivity axes with three photometric bins. The optimal photometric bins are 350-450 nm ("blue"), 504-625 nm ("green"), and 879-991 nm ("red") with corresponding axes $R_{[879,991]} / R_{[504,625]}$ and $R_{[350,450]} / R_{[879,991]}$. The separation between the Archean Earth and its nearest neighbor (100% snow) is 1.47. Although this separation is comparatively large, the extent to which the non-hazy Archean Earth occupies a unique position in color-color space is once again unclear; for example, an intermediate between Jupiter and Uranus (or the sub-Neptune model) could potentially occupy the same region in color-color space. If the calculations are repeated for 4 photometric bins, or for the low methane (2000 ppmv) non-hazy Archean Earth case then similar results are obtained (not shown). In short, the non-hazy Archean Earth can be separated from false positives, but it does not occupy a unique region in color-color space. We did not consider the oxygenated Proterozoic Earth because previous work shows that its spectrum is similar to the modern Earth (Kaltenegger et al. 2007; Meadows 2006). However, the Chappuis bands - and therefore their contribution to Earth's unique U-shape - are not visible in both Proterozoic and Archean Earth spectra. This suggests that for most of Earth's history, it was more difficult to photometrically distinguish from uninhabitable planets than the modern Earth.

Detectability considerations

Using optimized photometric bins, we have shown that (modern) Earth can be separated from false positives in color-color space by around 0.3-0.4 in a particular dimensionless color-color space. Furthermore, there is reason to believe that Earth occupies a unique region in color-color space due to the U-shape of its spectrum from far UV to near-IR. Whether or not this unique color has any utility depends on how difficult it is to constrain color through photometric observations. Rather than calculate the necessary telescope integration time required to identify an exo-Earth, we calculate a dimensionless ratio of the integration time required to identify an exo-Earth using photometry relative to the integration time required to obtain a spectrum of the same exo-Earth. This ratiometric approach does not require any explicit assumptions about telescope parameters or a detailed noise model, and so the results will apply to any future telescope.

Specifically, we wish to compare the telescope integration time required to separate Earth from its nearest false positive with 5σ precision to the integration time required to obtain a spectrum with signal-to-noise of 5. Fig. 10 shows a zoomed-in version of Fig. 2, which highlights the important parameters for this calculation. We seek the integration time that ensures the separation distance, S_d, between exo-Earth and

the nearest neighbor is five times larger the uncertainty in this separation, σ_s. The separation distance is given by $S_d = \sqrt{x^2 + y^2}$, where $x = R_{red}/R_{green\ Earth} - R_{red}/R_{green\ Neighbor}$ is the distance between Earth and its nearest neighbor along the horizontal axis, and $y = R_{blue}/R_{green\ Earth} - R_{blue}/R_{green\ Neighbor}$ is the distance between Earth and its nearest neighbor along the vertical axis. The uncertainty in the total separation is given by:

- $$\sigma_S = \sqrt{\left(\frac{\partial S_d}{\partial x}\sigma_x\right)^2 + \left(\frac{\partial S_d}{\partial y}\sigma_y\right)^2} = \sqrt{\frac{x^2\sigma_x{}^2 + y^2\sigma_y{}^2}{x^2 + y^2}} \qquad \text{(AII-3)}$$

- where σ_x and σ_x are the uncertainties in x and y, respectively.

- The reflectivity measurements R_{blue}, R_{green} and R_{red} will each have an associated observational uncertainty, σ_{blue}, σ_{green} and σ_{red}, respectively (for an exo-Earth). These can be recast in terms of the signal-to-noise (S/N) reciprocal for each photometric bin ($\sigma_{blue} / R_{blue} = (N/S)_{blue}$ etc.). Assuming there is no uncertainty in the position of the nearest neighbor, the rules of error propagation then allow us to express the S_d/σ_S ratio as follows, using equation (AII-3):

-
$$\frac{S_d}{\sigma_S} = \frac{x^2 + y^2}{\left(x^2\sigma_x{}^2 + y^2\sigma_y{}^2\right)^{1/2}}$$

$$= \frac{\left(x^2 + y^2\right)}{\sqrt{x^2\left(\left(R_{red}/R_{green}\right)_{Earth}\sqrt{\left(\frac{N}{S}\right)_{red}{}^2 + \left(\frac{N}{S}\right)_{green}{}^2}\right)^2 + y^2\left(\left(R_{blue}/R_{green}\right)_{Earth}\sqrt{\left(\frac{N}{S}\right)_{blue}{}^2 + \left(\frac{N}{S}\right)_{green}{}^2}\right)^2}}$$

(AII-4)

The noise-to-signal (N/S) for each photometric bin will be a monotonically decreasing function of the telescope integration time, which is in turn dependent on the stellar spectrum, Earth's wavelength dependent reflectivity, external noise sources such as exozodiacal dust, and various telescope parameters. For simplicity, we will assume that N/S for all three bins is the same for any given integration time i.e. $N/S = (N/S)_{red} = (N/S)_{green} = (N/S)_{blue}$. This is approximately true since neither stellar flux nor

Earth's albedo varies greatly across the visible spectrum. By making this assumption and substituting in the values from Fig. 10 we have:

$$\frac{S}{\sigma_S} = \frac{\left(0.31^2 + 0.079^2\right)}{\sqrt{0.31^2\left(1.25\sqrt{2\left(\frac{N}{S}\right)^2}\right)^2 + .079^2\left(1.27\sqrt{2\left(\frac{N}{S}\right)^2}\right)^2}} = 0.181\left(\frac{S}{N}\right) \quad \text{(AII-5)}$$

Since we wish to separate Earth to 5σ the signal-to-noise in each individual photometric bin must be $S/N = 5/0.181 = 27.6$. Incidentally, this implies that photometric observations must be accurate to within 1/27.6 ≈ 4% to separate Earth from uninhabitable planets to 5σ.

We consider two endmember cases for the noise source in direct imaging telescope observations. Firstly, we assume the signal-to-noise is dominated by astrophysical noise such as zodiacal light, imperfectly suppressed starlight, or is photon limited. The signal-to-noise for any such observation is given by:

$$S/N = \frac{F_{Planet}\,t}{\sqrt{F_{Planet}\,t + F_{Zodiacal}\,t + F_{null}\,t}} = \frac{F_{Planet}}{\sqrt{F_{Planet} + F_{Zodiacal} + F_{null}}}\sqrt{t} \quad \text{(AII-6)}$$

Here F_{Planet} is the photon flux from the planet in the wavelength range being observed, $F_{Zodiacal}$ is the exo-zodiacal and zodiacal photon flux in the wavelength range being observed, F_{null} is the unsuppressed starlight in the wavelength range being observed, and t is the integration time.

The integration time required, t_{color}, to obtain a S/N of 27.6 in each 100 nm reflectivity bin (and therefore separate Earth from its nearest neighbor by 5σ) will be given as follows, using equation (AII-6):

$$27.6 = S/N = \frac{F_{Planet}}{\sqrt{F_{Planet} + F_{Zodiacal} + F_{null}}}\sqrt{t_{color}} \quad \text{(AII-7)}$$

This photometry integration time should be compared to the integration time required to obtain a $S/N = 5$ spectrum with 10 nm bins. In effect, we are comparing the time required to photometrically separate the Earth to 5σ precision to the time required to constrain the reflectivity at every point in a spectrum with the same level of precision. We chose 10 nm bins to achieve a moderate spectral resolution of 70 at 700 nm (λ/Δλ=700/10=70). The integration time required to obtain such a spectrum, $t_{spectrum}$, is given by:

$$5 = S/N = \frac{F_{Planet}'}{\sqrt{F_{Planet}' + F_{Zodiacal}' + F_{null}'}} \sqrt{t_{spectrum}} \qquad \text{(AII-8)}$$

Since the spectral bins (10 nm wide) are 10 times smaller than the photometric bins (>100 nm wide), then it will be approximately true that all fluxes decrease by a factor of 10. In other words $10F_X' = F_X$ for all the fluxes in equation (AII-8). By combining equations (AII-7) and (AII-8) we arrive at the result:

$$t_{spectrum} \approx 0.33 t_{color} \qquad \text{(AII-9)}$$

This demonstrates that *if observational noise is dominated by astrophysical sources then the integration time required to separate Earth from the nearest false positive to 5σ is comparable to, or even greater than, the integration time required to obtain a 10 nm spectrum with a signal-to-noise of 5.*

This is a counter-intuitive result. We would normally expect photometric characterization to take less telescope time than obtaining a spectrum. However, differences in color between Earth and the nearby false-positives are subtle, and so relatively long integration times are required to resolve this difference. Additionally, because the color-color space is defined by reflectivity ratios, with an observational uncertainty in both the numerator and denominator, error propagation dictates that individual photometric observations need to be quite precise to accurately place Earth in color-color space. This is reflected in the fact that the S/N in each photometric bin needs to be 27.6 to ensure the color-color space separation signal-to-noise of 5.

If we repeat the detectability calculation but assume a separation of 0.5 between Earth and its nearest neighbor then we find $t_{spectrum} \approx 0.8 t_{color}$. This shows that even if we ignore all the possible icy false positives (i.e. Fig. 4), separating Earth from other false positives using optimal photometric bins still takes about the same amount of telescope time as obtaining a spectrum. It should also be noted that changing the minimum bin size does not affect this conclusion since, as demonstrated above in Fig. 8, optimal separation is only weakly dependent on minimum bin size. Additionally, if we consider the integration time required to separate Earth from all false positives to only 3σ, compared to the integration time required to obtain a 10 nm spectrum with S/N of 5, then we find $t_{spectrum} \approx 0.9 t_{color}$. For a separation of 2σ we find $t_{spectrum} \approx 2 t_{color}$.

For the first generation of coronagraph-equipped space telescopes capable of imaging habitable exoplanets (e.g. WFIRST-AFTA or Exo-C) the dominant noise source will be dark current in the detector (Robinson

et al. 2015). For this second scenario, we replace equation (AII-6) with the following signal-to-noise expression:

$$S/N = \frac{F_{Planet}}{\sqrt{F_{Dark}}}\sqrt{t} \qquad \text{(AII-10)}$$

Here, F_{Dark} is the dark current count rate. Robinson et al. (2015) estimates that for an integral field spectrometer, the dark current flux in spectroscopic observations will be six times that for photometric observations. This is because the critical sampling of each spectral element over two pixels in the dispersion direction on the CCD is multiplied by the perpendicular spread of the spectrum across roughly three pixels in width. We therefore have:

$$\begin{aligned} t_{spectrum} &= \left(\frac{(S/N)_{spectrum}\sqrt{F_{Dark-spectrum}}/F_{Planet}'}{(S/N)_{color}\sqrt{F_{Dark-color}}/F_{Planet}} \right)^2 t_{color} \\ &= \left(\frac{5\sqrt{6F_{Dark-color}}/F_{Planet}'}{27.6\sqrt{F_{Dark-color}}/10F_{Planet}'} \right)^2 t_{color} \\ &= 6\left(\frac{50}{27.6} \right)^2 t_{color} \approx 20 t_{color} \end{aligned} \qquad \text{(AII-11)}$$

Thus, *if observational noise is dominated by dark current then the integration time required to separate Earth from the nearest false positive to 5σ is twenty times less than the integration time required to obtain a 10 nm spectrum with a signal-to-noise of 5.* This indicates that photometry could be practically applied to identify probable Earth-like planets for spectroscopic follow-up if observational noise is dominated by dark current.

Discussion

Although the set of uninhabitable false positive planets considered in this study is extensive, it is not intended to be exhaustive. Exotic surface mineralogy or other pathological scenarios could potentially produce spectra that mimic Earth's apparently unique spectrum. For example, a growing literature investigates hypothetical scenarios whereby atmospheric oxygen could accumulate in the absence of life. If these false-positive scenarios are realistic, then some planets may occupy a similar region in color-color space to Earth. Kasting et al. (1993b) argued that a runaway greenhouse on a planet interior to the habitable zone, or the photochemical production of oxygen on a frozen Mars-like planet exterior to the habitable zone, could result in detectable levels of oxygen. These false-positives could eventually be distinguished on the basis of semi-major axis and the absence of water vapor, but a photometric survey may not

discriminate these variables. Wordsworth and Pierrehumbert (2014) and Luger and Barnes (2015) outline scenarios whereby water loss on otherwise habitable planets could result in the accumulation of atmospheric oxygen. Once again, these scenarios could eventually be distinguished through a lack of non-condensable gases and subtle pressure-sensitive spectral features (Misra et al. 2014; Schwieterman et al. 2015b), respectively, but photometry alone could not differentiate these false positives. Domagal-Goldman et al. (2014), Tian et al. (2014) and Harman et al. (2015b) also investigated oxygen false positives within the habitable zone. Harman et al. (2015b) concluded that it is extremely difficult to produce false positive oxygen around G and F stars through photochemistry alone, but that abiotic oxygen could accumulate around K and M stars if surface sinks, such as reactions with dissolved ferrous iron or CO, are small. In short, the variety and plausibility of false-positive oxygen accumulation is still under discussion. For this reason, planet color is not a means of definitive characterization, but rather an indicator that certain objects are sufficiently interesting to justify more extensive observations. In this way, planet color could be incorporated into the observing strategy for future direct imaging missions (see below).

It could be asked whether the false-positive model planets used in this study – especially the icy worlds that are most similar in color to Earth – are realistic objects. Firstly we consider the Mars-like false positives: planets with a Mars-like surface and a thick CO_2 or N_2 atmosphere. There is no strong reason to believe that such objects are unlikely to exist. In fact, it has been argued that Mars may have had a thick CO_2 atmosphere early in its history due to greater levels of volcanic outgassing (e.g. review by Haberle et al. 2016).

It is less clear whether exoplanets with an icy surface like that of Callisto or Europa could form with a thick, pure N_2 atmosphere. The only example of an icy body with a thick N_2 atmosphere in the Solar System is Titan, and in this case the presence of atmospheric methane causes an optical haze that completely changes the disk-averaged reflectance spectrum. Titan's atmospheric CH_4 is completely destroyed by photodissociation on a timescale of 30-100 m.y., and so either it is being replenished by a subsurface reservoir or we are observing Titan at a special time in its history (Lunine et al. 1989). In the latter case, there would have been times in Titan's history when its atmosphere was more similar to our icy false positives. Even if it is not possible for icy bodies to form with thick, pure N_2 atmospheres, we can envisage a scenario whereby a terrestrial planet with an N_2 atmosphere formed interior to the snow line, then later migrated outwards. Since the planet would be too warm to preserve subsurface methane clathrates in its original location, post-migration there would be no subsurface reservoir to replenish CH_4 lost to photodissociation and subsequent hydrogen escape. Additionally, any liquid water would freeze out post-migration resulting in an icy surface. Thus, it is possible to imagine an icy body with a relatively thick, pure N_2 atmosphere after atmospheric CH_4 has been depleted. Such a planet might be observed to reside outside

the traditional habitable zone (through time-dependent photometry or existing transit or radial velocity data), but the potential photometric similarity to modern Earth cautions us against permissive interpretations of planet colors in the extended habitable zones that have recently been proposed (Pierrehumbert & Gaidos 2011; Seager 2013).

Although we have treated the Earth and the Moon separately in this analysis, direct imaging missions will not separately resolve exo-Earths from companion satellites, and will instead obtain a combined spectrum. This could have an effect on an exo-Earth's position in color-color space. Robinson (2011) showed that in the infrared the presence of the Moon has a significant effect on the combined Earth-Moon emission spectrum. However, in the visible, the presence of the Moon should not have a large effect on the Earth's color. The radii and average albedos for the Earth and The Moon are 6400 km and 0.3, and 1700 km and 0.1, respectively. This implies that at full phase the radiance of The Moon is approximately $\left(1700^2 \times 0.1\right) / \left(6400^2 \times 0.3\right) = 2\%$ that of Earth. In addition, the Moon's spectrum is relatively flat and featureless, and so we would not expect the Moon to have a large effect on the combined Earth-Moon color. Of course, exo-Earths with larger, higher-albedo companions could be considerably different in color, and so the possibility for false negatives cannot be completely ignored. However, although the exoplanet-exomoon system is unresolved, if the time- and wavelength-dependent positional variation of the center of light of the combined exoplanet-exomoon system can be measured, then the exoplanet and exomoon spectrum could be disentangled (Agol et al. 2015).

Implications for observing strategies and telescope design

There are numerous scenarios whereby uninhabitable exoplanets could appear very similar in color to Earth. Even with optimized photometric bins the distinction between Earth and these uninhabitable exoplanets is subtle. For 2-meter class direct imaging space telescopes such as WFIRST-AFTA, Exo-C or Exo-S, exoplanet observations will mostly be dominated by dark noise (Robinson et al. 2015). In this scenario, photometric identification of exo-Earths will require much shorter integration times than spectroscopic characterization. However, for these 2-meter class telescopes it will only be possible to image potentially habitable terrestrial planets around a small number of nearby stars, and so doing a photometric survey of habitable planets will not be possible.

For the next generation of large-aperture ($\sim$10 m) space telescope such as ATLAST/LUVOIR, the utility of photometric surveys will depend strongly on dark current. If dark current dominates the observational noise, then photometric characterization could be readily incorporated into an observing strategy, such as that for ATLAST/LUVOIR described by Domagal-Goldman et al. (2015). For example, after preliminary observations have characterized the system architecture and determined if any planets are in the habitable

zone, the next step would be to obtain broadband photometry (100 nm bins) of any potentially habitable planets. The optimal bins from Fig. 2, 3 and 7 (431-531 nm, 569-693 nm, 770-894) could be used to identify probable exo-Earths for spectroscopic follow-up. In this scenario optimized photometry would be a valuable tool for preliminary characterization.

Alternatively, if astrophysical noise dominates ATLAST/LUVOIR observations, then the integration times required to separate Earth from uninhabitable positives using optimal photometric bins are comparable to the integration times required to obtain a spectrum. Thus there is little advantage in using visible wavelength photometry first, before spectroscopy, to identify potential Earth-like planets for spectroscopic follow-up. Instead, color could be calculated from a low-resolution spectrum and used as an additional piece of information to evaluate whether higher-resolution spectral observations are justified. For example, after preliminary observations have characterized the system the next step would be to obtain low-resolution spectra (e.g. 50 nm bins, S/N=5) of any potentially habitable planets. These observations would be insufficient to photometrically separate Earth from false positives unambiguously – in fact, they would separate Earth from its nearest neighbor by only 1.3σ in color-color space. However, this crude color information still constrains the region in color-color space the exoplanet occupies, and hence it could be used in combination with suggestive absorption features in the spectrum (such as water absorption) to evaluate whether a high resolution spectrum should be obtained, or whether the telescope should move on to its next target. It may be preferable to use the optimal photometric bins in Fig. 4 for this purpose (350-450 nm, 593-693 nm, and 879-992 nm). This is because the purpose of these photometric observations is not to definitively identify exo-Earths, but rather identify potentially Earth-like planets for higher-resolution spectroscopic follow-up. The Fig. 4 bins have the advantage of better-separating Earth from all false positives except the icy bodies with thick atmospheres, which is appropriate given the coarseness of the spectrum (there will be large uncertainties in color-color position). Additionally, it may be possible to distinguish icy bodies from Earth-like planets with a low-resolution spectrum from the presence or absence of water vapor absorption.

Optimal wavelength range

In the original Earth-separating optimization with all false positives included (Fig. 2) we found that despite allowing the optimization to consider all photometric bins between 350 nm and 1000 nm, the solution only uses bins between 431 nm and 894 nm. This suggests that extending the wavelength capabilities of a direct imaging telescope beyond this range is not necessary to uniquely identify potential Earth-like planets with photometry (note however that extending wavelength to 1000 nm is highly desirable for spectroscopy because it provides access to the 940 nm water vapor band, which is critical for assessing habitability).

This conclusion does not hold if we accept the possibility of icy false positives (Fig. 4). In this case, if the wavelength range available for photometric bins is made smaller, then the optimal bins do not separate Earth as clearly as the 350-1000 nm case ($\lambda_{min} = 350, \lambda_{max} = 1000$). For instance, if the photometric bins are restricted to 450-1000 nm range then the Earth is only separated from its neighbor by a distance of 0.34 in color-color space (not shown), compared to 0.53 for the full wavelength range in Fig. 4. The separation is poor because the restricted wavelength range does not fully capture Earth's exceptional shortwave reflectivity due to Rayleigh scattering. In the absence of icy false positives, shortwave reflectivity is the most diagnostic feature of Earth's spectrum. If an intermediate wavelength range is applied ($\lambda_{min} = 400, \lambda_{max} = 1000$) then the separation between Earth and its nearest neighbor is 0.47. This suggests that telescopes with a minimum wavelength of 400 nm receive most of the benefits of short wavelength photometric characterization. Currently, the direct imaging mission proposals Exo-C and Exo-S are planned to operate from 450-1000 nm and 400-1000 nm respectively (Seager et al. 2015; Stapelfeldt et al. 2015), whilst the WFIRST-AFTA coronograph will operate between 430-970 nm with spectrometry restricted to 600-970 nm (Spergel et al. 2015). The HDST concept has a minimum wavelength range of 100-2000 nm (Dalcanton et al. 2015), whereas the similar ATLAST concept has a 110-2500 nm wavelength range (Postman et al. 2009).

We have not explored the utility of photometry shortward of 350 nm. This is because the model spectra we generated are unreliable in the UV due to incomplete line lists and absorption cross sections. However, UV photometry could be useful for identifying exo-Earths due to strong ozone absorption at $\lambda<320$ nm. This has been previously noted by Heap et al. (2008), who argued that Hartley band (ozone absorption) is a promising biosignature in the UV. However, it should be noted that recent photochemical modeling has shown that O_3 is much easier to produce abiotically in a terrestrial planet atmosphere than O_2 (Domagal-Goldman et al. 2014; Harman et al. 2015b), thus complicating the interpretation of an O_3 signature. An upper wavelength limit of 1000 nm was used in this study because this is the upper wavelength limit for near-term direct imaging missions, and because the spectra available in the literature are typically truncated at around 1000 nm. However, the utility of photometry longward of 1000 nm could also be explored in future work.

Conclusions

- Icy bodies with thick N_2 atmospheres or Mars-like surfaces with thick N_2 or CO_2 atmospheres are very similar in color to the Earth. The thick atmospheres of these uninhabitable, quasi pale blue dots mimic the blue reflectance of Earth's Rayleigh scattering.

- However, the U-shape of Earth's spectrum from the far-UV to the near IR is unlike any known uninhabitable planet or our model uninhabitable planets, and at least partly biogenic in origin. The optimal photometric bins for separating Earth from uninhabitable planets exploit this feature of Earth's spectrum. The wavelength ranges of these bins are 431-531 nm, 569-693 nm, 770-894 nm (Fig. 2, 3 and 7).
- The utility of broadband photometry for identifying exo-Earths depends strongly on the primary source of observational noise. If observations are photon limited or dominated by astrophysical noise (e.g. zodiacal light or imperfect starlight suppression) then the telescope integration time required to identify Earth's unique color is comparable to - or even greater than - the integration time required to obtain a moderate resolution (R~70) spectrum. In this scenario there is little advantage to using visible wavelength photometry first, before spectroscopy, to identify potential Earth-like planets for spectroscopic follow-up.
- However, if observational noise is dominated by dark current comparable to those of present detectors, then the telescope integration time required to identify Earth's unique color is ~20 times shorter than the integration time required to obtain a moderate resolution (R~70) spectrum. In this scenario optimized photometric bins could be used to identify probable exo-Earths for spectroscopic follow-up.
- Extrasolar Archean Earths are extremely difficult to uniquely identify using visible broadband photometry. Additionally, the unique, biogenic shape of Earth's spectrum has only been present during the Phanerozoic (0.5-0 Ga). This implies that for the majority of its history Earth would be challenging to uniquely identify using photometry alone.

Tables and Figures

Table 1: This table lists all the planet spectra used in this study. The bolded rows represent the set of uninhabitable false positives, and the italicized rows are the subset of icy false positives referred to in the main text. The color-color plot symbols for each planet are specified. Note that these are consistent across all figures in this study. The source of each spectrum – either a citation or SMART model output – is also listed. All spectra are observed at quadrature unless otherwise stated.

Planet/Moon	**Notes**	**Symbol**	**Source for spectrum**
Earth quadrature phase	This Earth spectrum was used in all optimization calculations.	Blue circle	Validated 3D Earth model and SMART
Earth full phase		Blue diamond	Validated 3D Earth model and SMART

Earth gibbous phase		Blue star	Validated 3D Earth model and SMART
Earth crescent phase		Blue downward triangle	Validated 3D Earth model and SMART
The Moon		**Black circle**	**Validated 1D model and SMART**
Mars		**Red circle**	**Validated 1D model and SMART**
Venus		**Black circle**	**Validated 1D model and SMART**
Jupiter	**Full phase**	**Black circle**	***Karkoschka (1998)***
Saturn	**Full phase**	**Black circle**	***Karkoschka (1998)***
Uranus	**Full phase**	**Black circle**	***Karkoschka (1998)***
Neptune	**Full phase**	**Black circle**	***Karkoschka (1998)***
Titan	**Full phase**	**Black circle**	***Karkoschka (1998)***
Io	**Full phase**	**White circle**	***Karkoschka (1994)***
Callisto	**Full phase**	**Cyan circle**	***Karkoschka (1994)***
Ganymede	**Full phase**	**Purple circle**	***Karkoschka (1994)***
Europa	**Full phase**	**Green circle**	***Karkoschka (1994)***
Giant planet class I	**Full phase**	**Black circle**	***Sudarsky et al. (2000)***
Giant planet class II	**Full phase**	**Black circle**	***Sudarsky et al. (2000)***
Giant type I with haze	**Full phase**	**Black circle**	***Sudarsky et al. (2000)***
Sub-Neptune thick H_2 atmosphere	**6.6 $m_\oplus$ and 2.4 $R_\oplus$ with 2000 W/m^2 insolation and solar metallicity**	**Black circle**	**SMART**
Sub-Neptune thick H_2 atmosphere high metallicity	**6.6 $m_\oplus$ and 2.4 $R_\oplus$ with 2000 W/m^2 insolation 100x and solar metallicity**	**Black circle**	**SMART**
Sub-Neptune thick H_2O atmosphere	**6.6 $m_\oplus$ and 2.4 $R_\oplus$ with 2000 W/m^2 insolation**	**Black circle**	**SMART**
Snow	**100% snow-covered planet with clear sky Earth-like atmosphere**	**Black circle**	***SMART, surface spectrum from Shields et al. (2013)***
Blue ice	**100% blue ice-covered planet with clear sky Earth-like atmosphere**	**Black circle**	***SMART, surface spectrum from Shields et al. (2013)***

Kaolinite	**100% kaolinite covered planet with clear sky Earth-like atmosphere**	**Black circle**	***SMART, surface spectrum from Clark et al. (2007)***
Callisto 0.5 bar N_2	***250 K isothermal atmosphere.***	***Cyan upward triangle***	***SMART, surface spectrum from Karkoschka (1994)***
Callisto 0.75 bar N_2	***“***	***Cyan star***	***SMART, surface spectrum from Karkoschka (1994)***
Callisto 1 bar N_2	***“***	***Cyan square***	***SMART, surface spectrum from Karkoschka (1994)***
Callisto 2 bar N_2	***“***	***Cyan downward triangle***	***SMART, surface spectrum from Karkoschka (1994)***
Europa 0.5 bar N_2	***“***	***Green upward triangle***	***SMART, surface spectrum from Karkoschka (1994)***
Europa 1 bar N_2	***“***	***Green square***	***SMART, surface spectrum from Karkoschka (1994)***
Europa 2 bar N_2	***“***	***Green downward triangle***	***SMART, surface spectrum from Karkoschka (1994)***
Ganymede 0.5 bar N_2	***“***	***Purple downward triangle***	***SMART, surface spectrum from Karkoschka (1994)***
Ganymede 2 bar N_2	***“***	***Purple square***	***SMART, surface spectrum from Karkoschka (1994)***
Io 0.5 bar N_2	***“***	***White square***	***SMART, surface spectrum from Karkoschka (1994)***
Gray 0.2 bar N_2	***Gray surface has albedo of 0.27. 250 K isothermal atmosphere.***	***Gray square***	***SMART***
Gray 1.2 bar N_2	***“***	***Gray downward triangle***	***SMART***
Gray 2 bar N_2	***“***	***Gray diamond***	***SMART***
Mars 0.5 bar N_2	***250 K isothermal atmosphere.***	***Red pentagon***	***SMART***
Mars 2 bar N_2	***“***	***Red leftward triangle***	***SMART***
Mars 5 bar N_2	***“***	***Red rightward triangle***	***SMART***
Mars 0.5 bar CO_2	***“***	***Red upward triangle***	***SMART***
Mars 1 bar CO_2	***“***	***Red square***	***SMART***
Mars 1.5 bar CO_2	***“***	***Red star***	***SMART***

Mars 5 bar CO_2	***“***	***Red downward triangle***	***SMART***
Kaolinite 1 bar CO_2	***“***	***Lime downward triangle***	***SMART, surface spectra from Clark et al. (2007)***
CO_2 ice 1 bar N_2	***180 K isothermal atmosphere for consistency***	***Lime upward triangle***	***SMART, surface spectra from Tinetti et al. (2005)***
Archean Earth no haze, high (1E-2) CH_4	50% clear skies, 25% med cloud, 25% low cloud	Yellow circle	SMART
Archean Earth no haze, low (2E-3) CH_4	“	Yellow star	SMART
Archean Earth with thick haze (1E-2 CH_4)	“	Yellow upward triangle	SMART
Archean Earth with thin haze (2E-3 CH_4)	“	Yellow leftward triangle	SMART
Earth with clear skies	Surface chosen to be linear mix of Ocean (65.6%), Kaolinite (5.5%), Grass (13.6%), Conifers (4%) and snow (11.3%) to match 24-hour averaged 3D model.	Blue pentagon	SMART
Earth 100% clear skies over ocean		Blue upward triangle	SMART
Earth with 100% low cloud		Blue rightward triangle	SMART
Earth with 100% mid cloud		Blue leftward triangle	SMART
Earth with 100% high cloud		Blue square	SMART
Jovian phase=0	3x solar metallicity with atmosphere in chemical equilibrium at 0.8 AU	Green star	Cahoy et al. (2010)
Jovian phase=70	“	Green star	Cahoy et al. (2010)
Jovian phase=90	“	Green star	Cahoy et al. (2010)
Jovian phase=120	“	Green star	Cahoy et al. (2010)
Jovian phase=140	“	Green star	Cahoy et al. (2010)
Jovian phase=150	“	Green star	Cahoy et al. (2010)

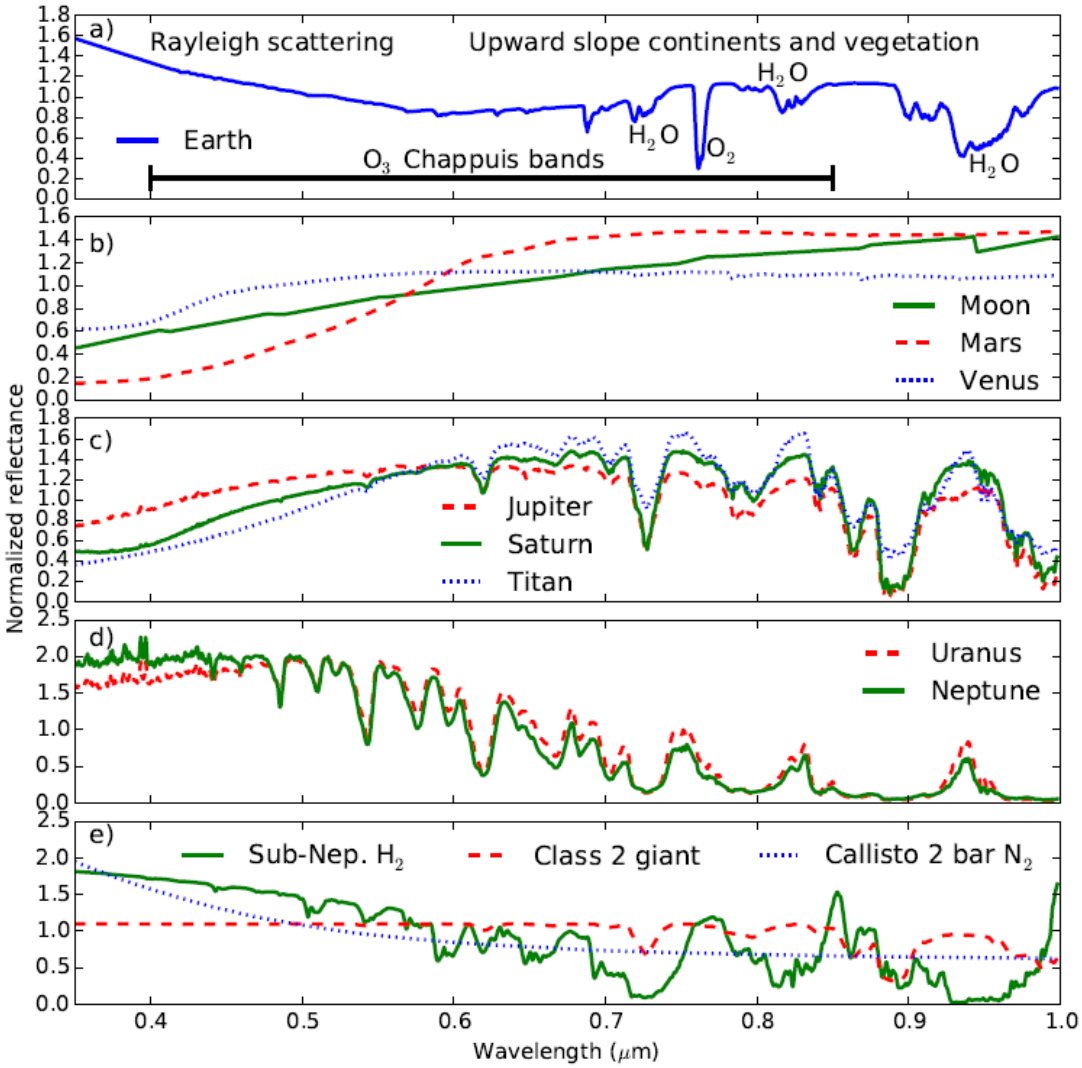

Figure 1: Reflectance spectra of Solar System objects and exoplanet models. (a) Earth is a pale blue dot due to strong Rayleigh scattering at short wavelengths. The spectrum is upward sloping from 600-900 nm due to continental reflectivity and the vegetation red edge. This, in combination with ozone absorption at 600 nm, gives the spectrum an overall U-shape. The black bar shows the width of the Chappuis ozone absorption bands (Andrews 2010). In contrast, objects with little or no atmosphere and a basaltic crust (Mars and the Moon in (b)) have an upward sloping spectrum. (c) Shows how Rayleigh scattering is suppressed in planets with optical hazes (see also Venus in (b)). (d) Demonstrates that Uranus and Neptune have qualitatively different spectra to Earth despite also being highly reflective in the blue. (e) Shows a selection of model exoplanet spectra including a sub Neptune, a giant planet, and an icy planet with a thick N_2 atmosphere. The references and descriptions for these spectra are described in full in the main text.

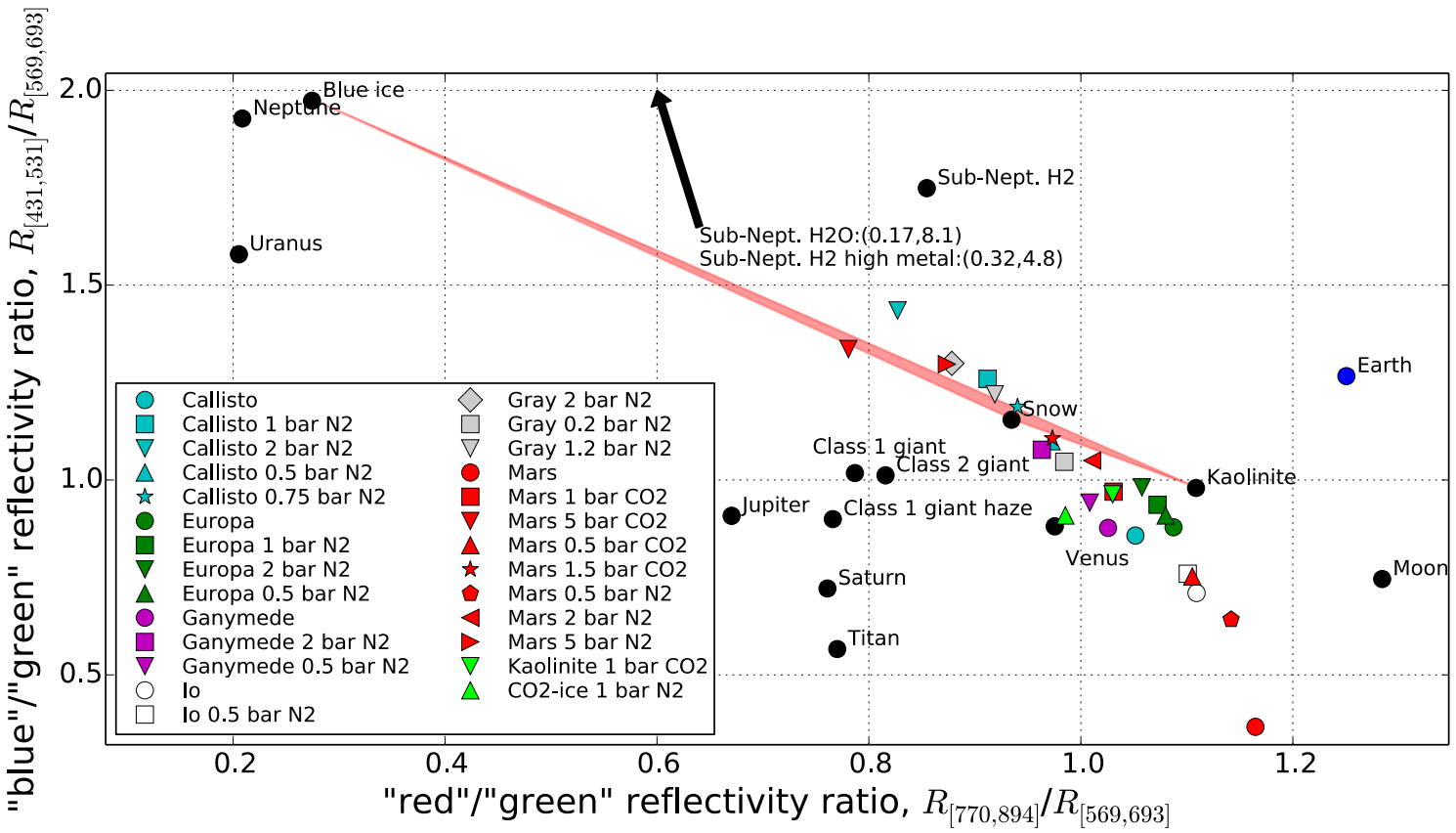

Figure 2: The Earth (blue circle) and all the uninhabitable planets (other symbols) – including both Solar System objects and exoplanet models – are plotted in color-color space, optimized to separate the Earth from its nearest neighbor. The horizontal axis is the mean reflectivity in the "red" bin (770-894 nm) divided by mean reflectivity in the "green" bin (569-693 nm), and the vertical axis is mean reflectivity in the "blue" bin (431-531 nm) divided by mean reflectivity in the "green" bin (569-693 nm). Earth's nearest neighbor is a Callisto with a 0.75 bar N_2 atmosphere, separated by 0.32 units (dimensionless). Note that the scaling of the horizontal axis is bigger than the vertical axis. The arrow denotes two sub-Neptune models that fall beyond the axis limits of this figure, and the red shaded region represents the range of colors possible for a snowball Earth planet (see main text). The Earth occupies a unique region in color-color space because of the U-shape of its reflectance spectrum: it is unusually blue for its level of redness and so both the "red"/"green" and "blue"/"green" reflectivities are appreciably greater than 1. The set of uninhabitable planets in this figure is described in full the main text and in Table 1.

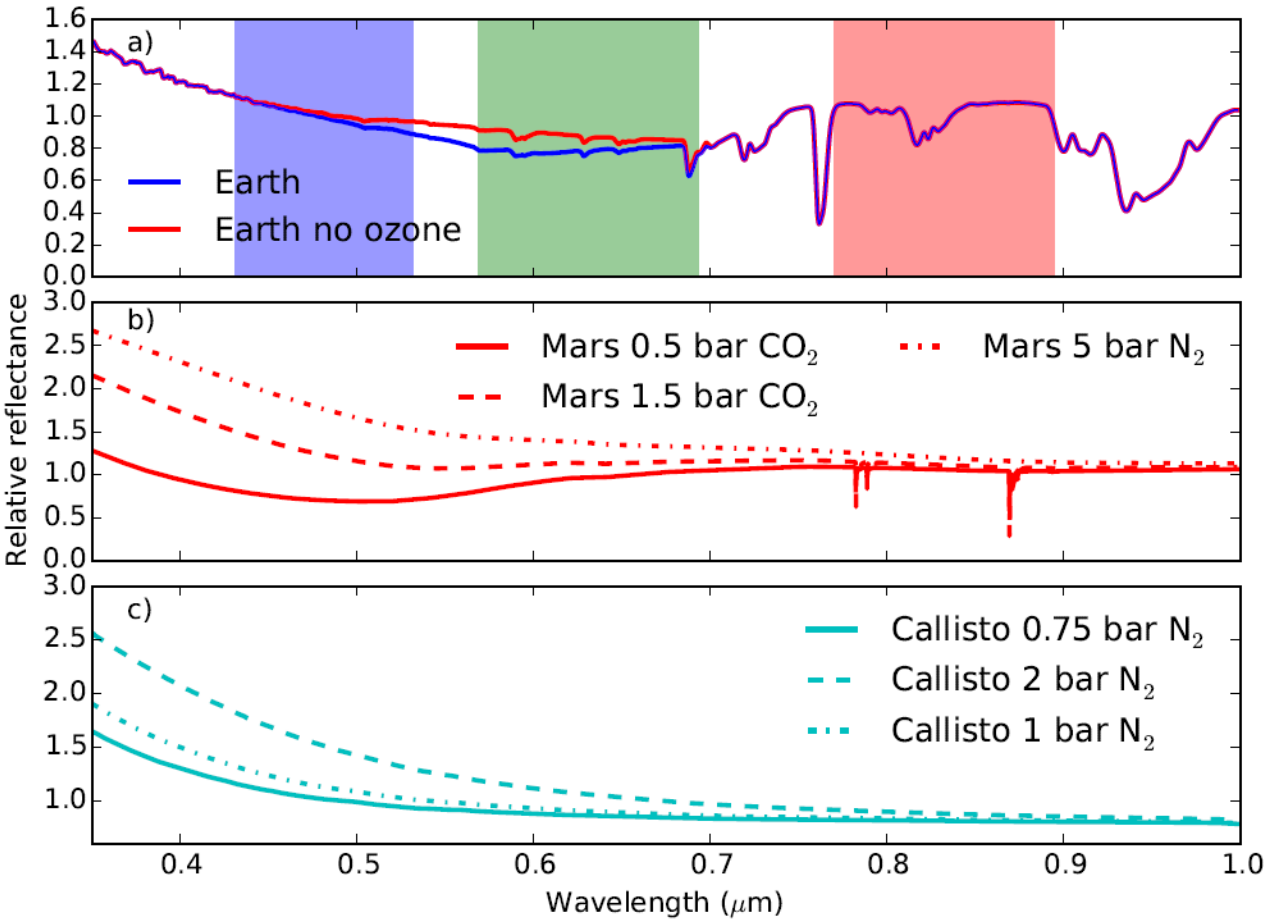

Figure 3: (a) shows Earth's reflectance spectrum (at quadrature) superimposed on the three optimal photometric bins from Fig. 2. These are the bins that maximize the separation between Earth and the nearest uninhabitable false-positive in color-color space. Note how the photometric bins highlight the U-shape of Earth's spectrum. For comparison we also plot Earth's spectrum without ozone to highlight how ozone absorption contributes to the unique U-shape. (b) Shows the reflectance spectra for a Mars-like surface with a thick atmosphere, and (c) shows reflectance spectra for Callisto with a thick N_2 atmosphere. These uninhabitable planets are mostly blue in color, but they don't have the same U-shape spectra as Earth, and so they are distinguishable using the optimal bins in (a).

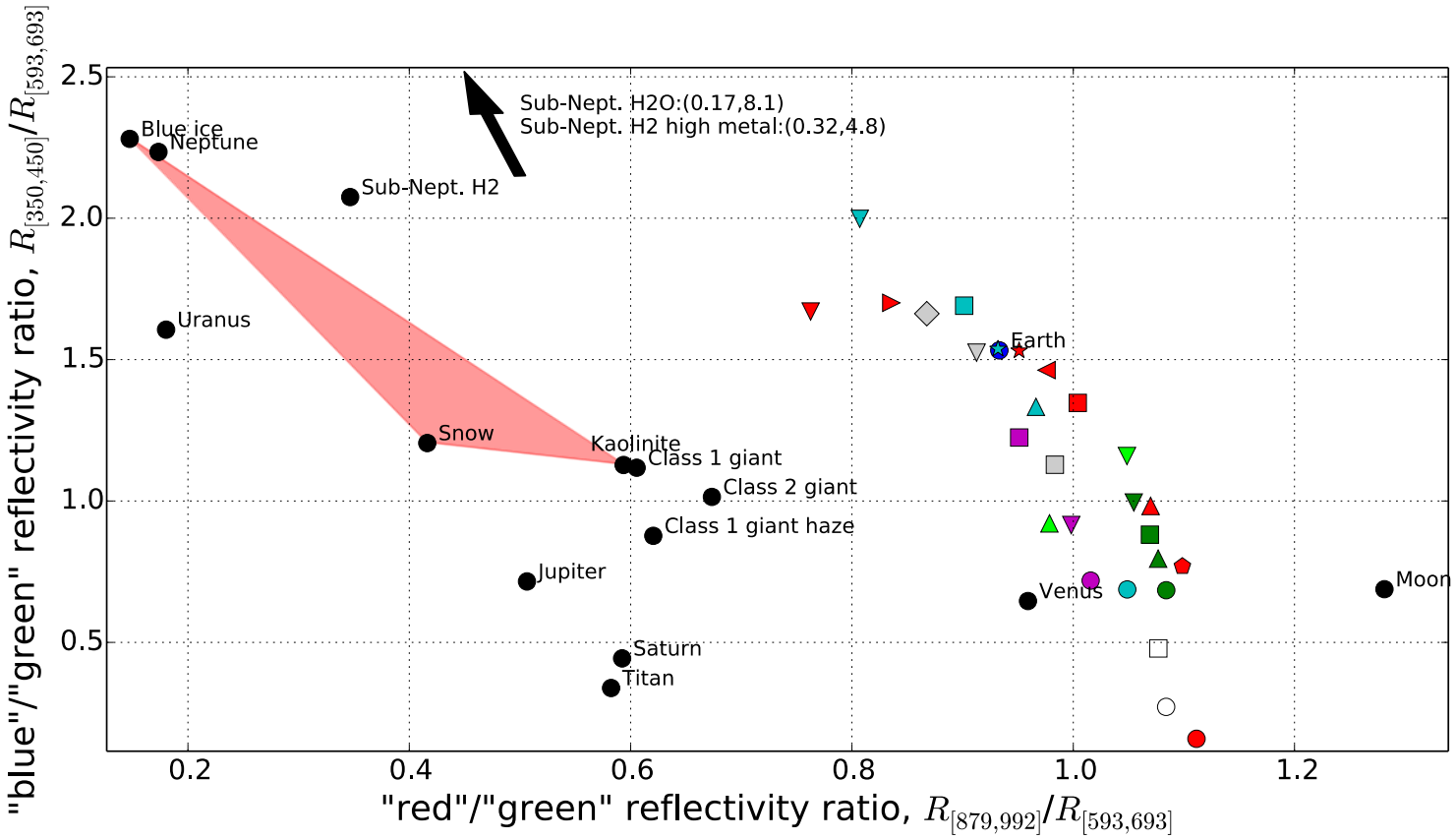

Figure 4: Here the Earth (blue circle) is optimally separated from all uninhabitable planets *except* for the icy false positives. Any planet with a circle symbol is included in the optimization calculation, whereas planets with other symbols (icy false positives) are not included. The legend is identical to that of Fig. 2. The horizontal axis is the mean reflectivity in the "red" bin (879-992 nm) divided by mean reflectivity in the "green" bin (593-693 nm), and the vertical axis is mean reflectivity in the "blue" bin (350-450 nm) divided by mean reflectivity in the "green" bin (593-693 nm). These photometric bins are optimized to maximize the separation between Earth and its nearest non-icy neighbor, a Class 1 giant (see text), and in this case the separation is 0.53. The arrow denotes two sub-Neptune models that fall beyond the axis limits of this figure, and the red shaded region represents the range of colors possible for a snowball Earth planet (see main text). Although Earth is better separated from non-icy false positives than in Fig. 2, it occupies the same region of color-color space as many icy bodies. In particular, Earth is identical in color to Mars with a 1.5 bar CO_2 atmosphere and Callisto with a 0.75 bar N_2 atmosphere using these photometric bins.

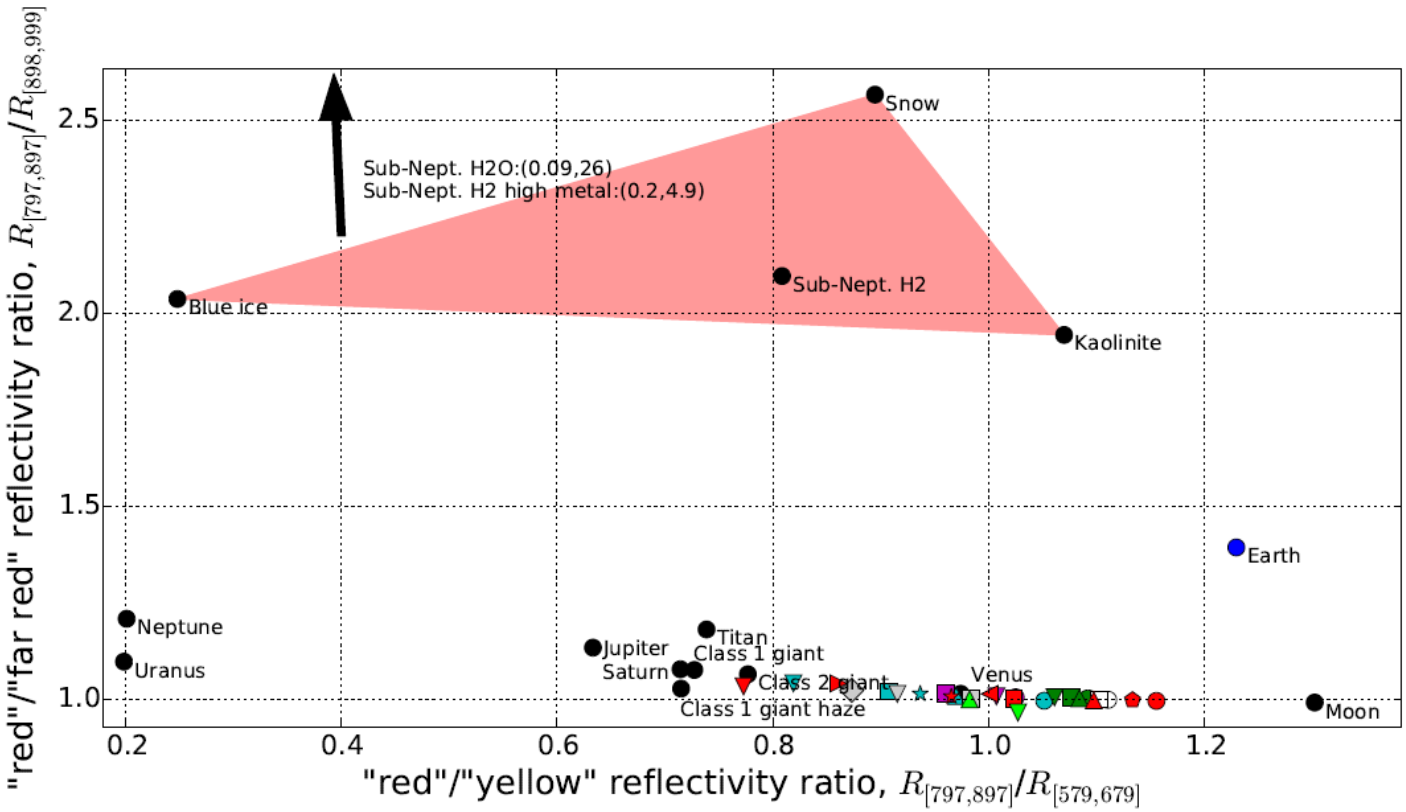

Figure 5: Here the Earth is optimally separated from all uninhabitable planets. Rather than enforce "red"/"green" and "blue"/"green" axes as in Fig. 2 and 4, in this figure the optimization algorithm considered all possible combinations of reflectivity ratios with three photometric bins. The three bins that define the axes are 579-679 nm ("yellow"), 797-897 nm ("red"), and 898-999 nm ("far red"), and the color-color space axes for this optimal separation are $R_{[797,897]} / R_{[579,679]}$ and $R_{[797,897]} / R_{[898,999]}$. The separation between Earth and its nearest neighbor (Mars) is 0.40. The arrow denotes two sub-Neptune models that fall beyond the axis limits of this figure, and the red shaded region represents the range of colors possible for a snowball Earth planet (see main text). The Earth has an unusually large ratio of $R_{[797,897]} / R_{[898,999]}$ due to water vapor absorption in its atmosphere (940 nm band).

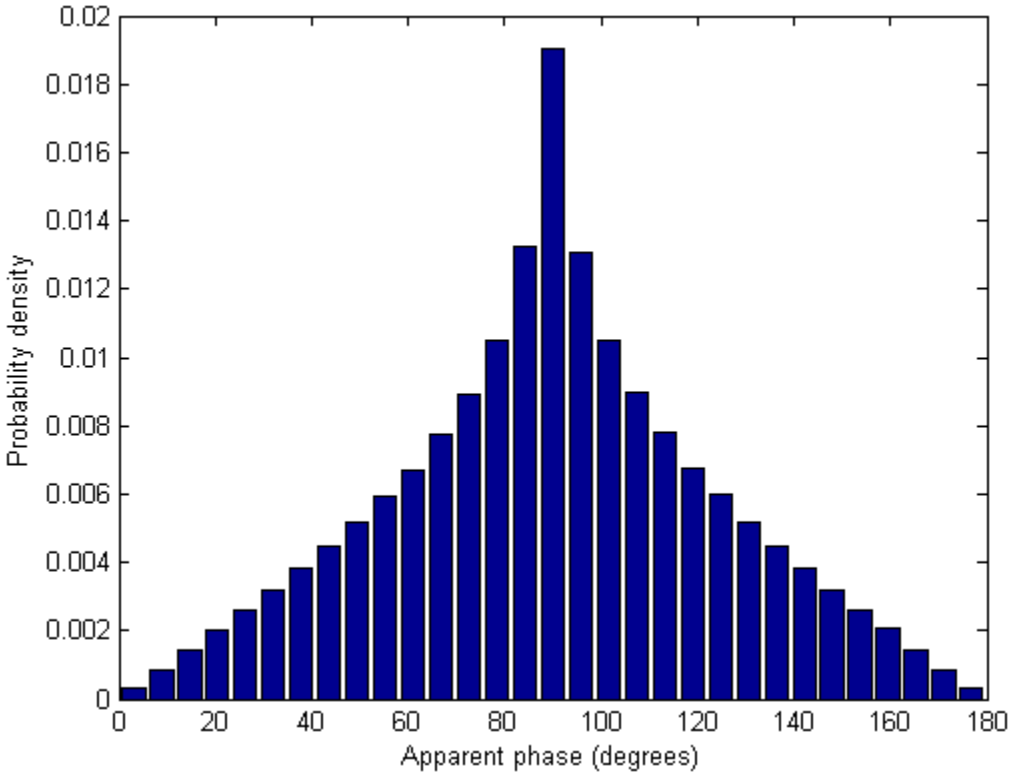

Figure 6: Probability distribution of the apparent phase for an exoplanet with a random position in its orbit and a random orbital inclination relative to the observer. This was calculated by repeatedly sampling uniform distributions of inclination and position in (a circular) orbit, and calculating the resultant phase as viewed by a distant observer. Quadrature (90 degrees) is the most likely apparent phase because planets with orbits inclined zero degrees relative to the Earth will always appear in quadrature. In practice, the distribution will be truncated at the edges due to inner working angle constraints.

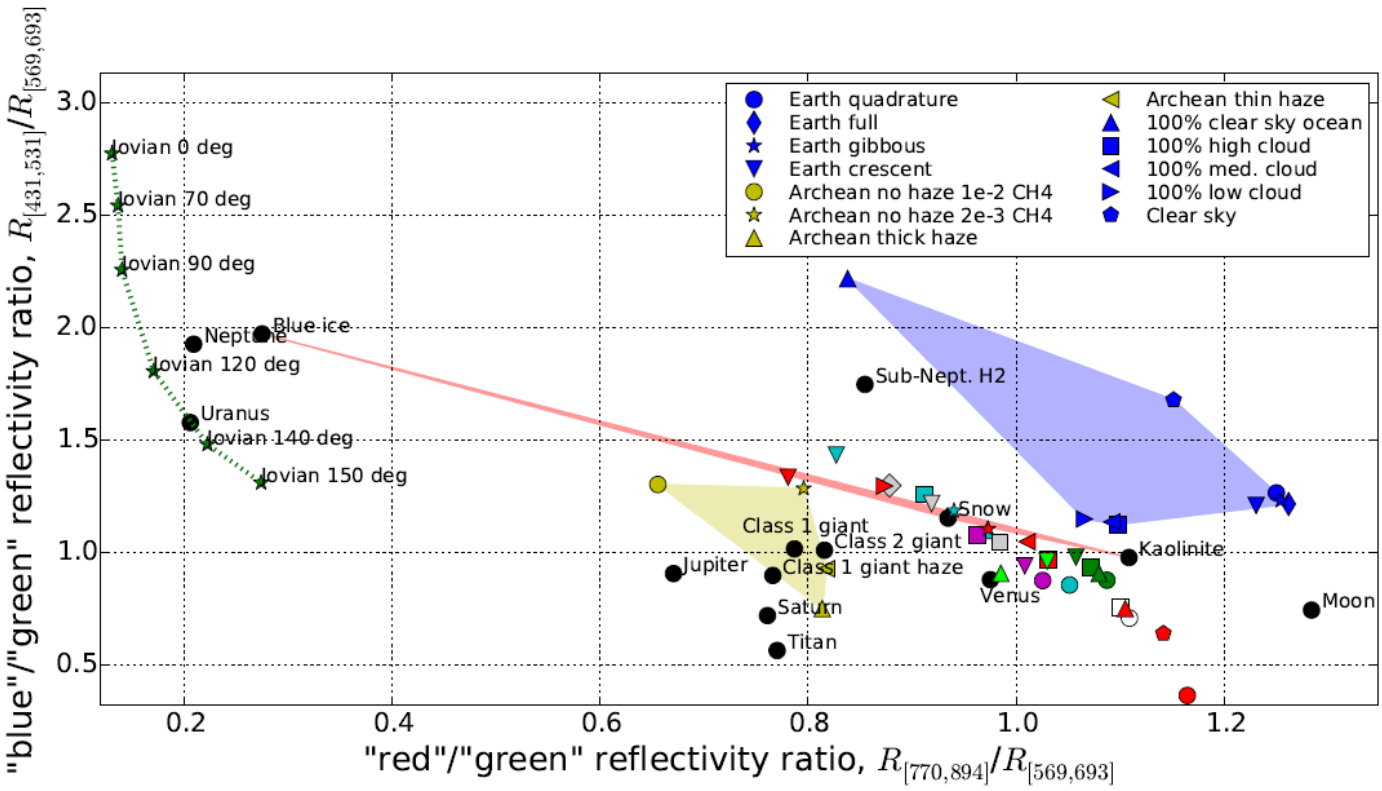

Figure 7: This figure is identical to Fig. 2 (including the legend) except a number of additional model planets have been added to illustrate the effects of phase, clouds, and haze. Note that these additional models are not optimally separated from Earth, but are instead merely plotted on top of the results from Fig. 2. The Earth in quadrature, gibbous, crescent and full phases (blue symbols) occupy very similar points in color-color space, indicating that phase does not have a large effect on the apparent color of Earth-like planets. However, phase can have a large effect on Jovian planets, as shown by the phase variation along the green dotted line. The reflectance spectra for this Jovian planet at 0.8 AU were obtained from Cahoy *et al.* (2010). To explore the effect of cloudiness on Earth's spectrum we have plotted Earth with 100% low, medium and high level cloud, in addition to a clear-sky Earth and a clear-sky Earth with a 100% ocean surface (blue symbols). The blue shaded region bounds these endmembers. Evidently, increased levels of cloudiness could make the Earth appear more similar in color to uninhabitable icy planets. Finally, we have plotted four Archean Earth spectra: thin haze, thick haze, no haze low methane, and no haze high methane (yellow symbols). The shaded yellow region represents the range of possible colors for the Archean Earth. Clearly, if these photometric bins were used to identify potentially habitable planets, then an exo-Archean Earth could be mistaken for a gas giant or Titan-like exoplanet.

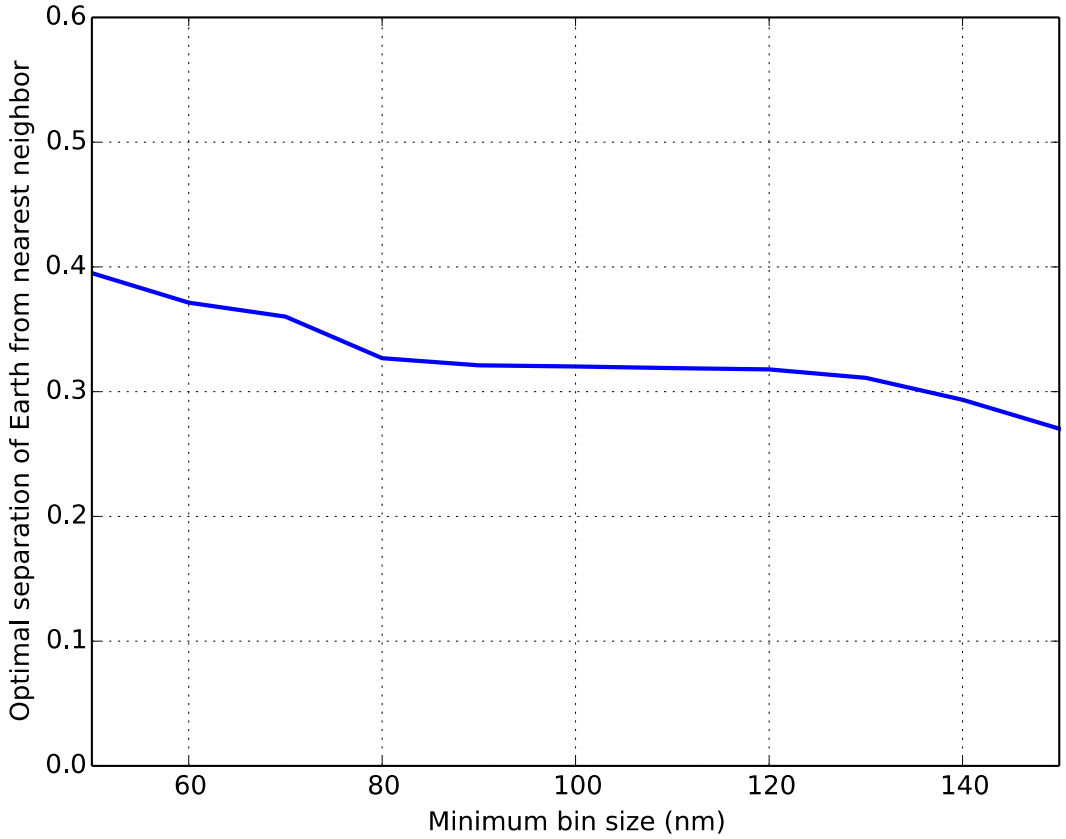

Figure 8: Optimal separation between Earth and its nearest uninhabitable neighbor (all false positives included) as a function of the minimum bin size constraint. Changing the minimum bin size does not have a dramatic effect on how well Earth can be separated.

9a

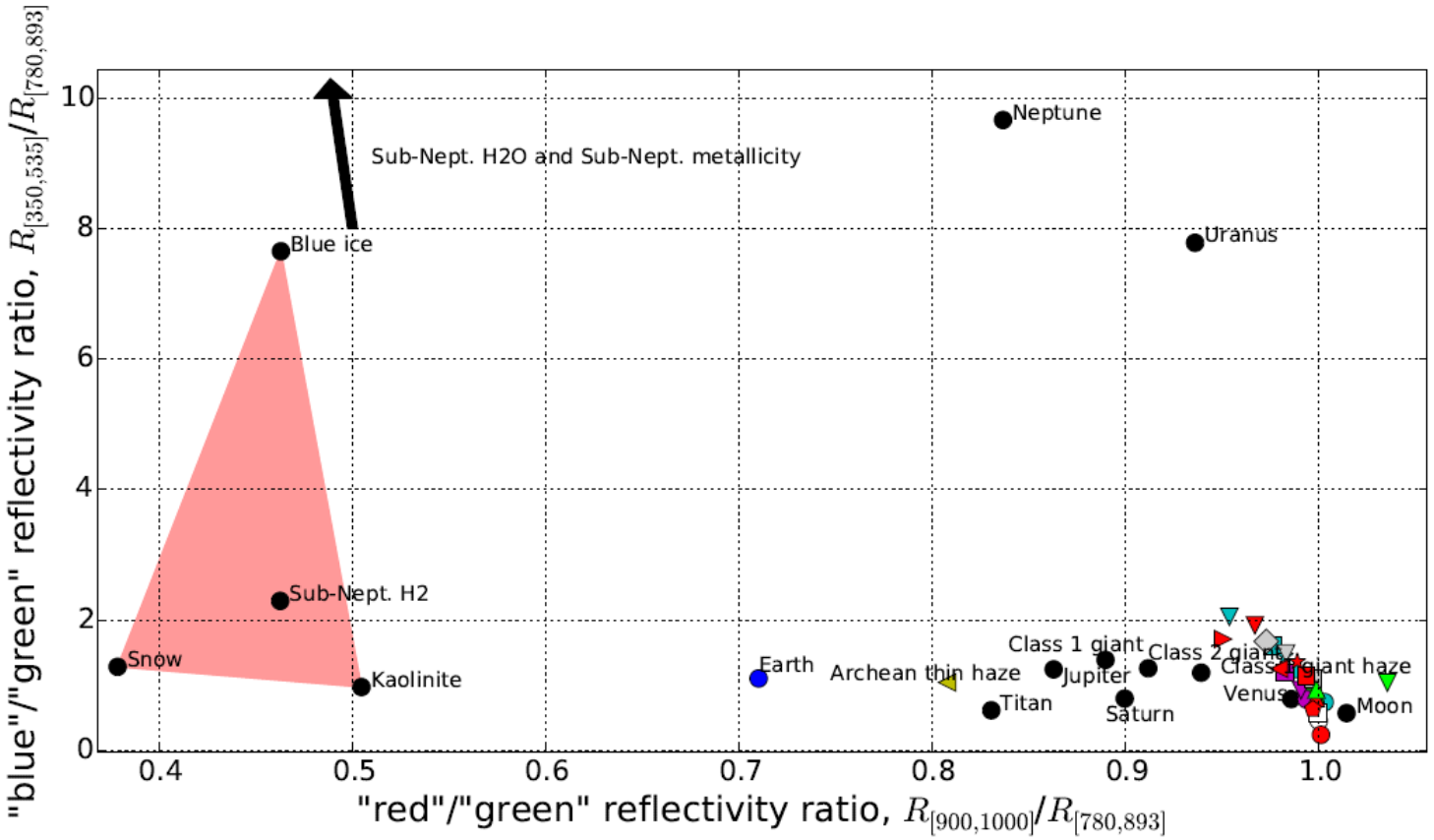
Sub-Nept. H2O and Sub-Nept. metallicity
Neptune
Uranus
Blue ice
Sub-Nept. H2
Snow
Kaolinite
Earth
Archean thin haze
Titan
Class 1 giant
Jupiter
Saturn
Class 2 giant
Venus
Moon
"blue"/"green" reflectivity ratio, $R_{[350,535]}/R_{[780,893]}$
"red"/"green" reflectivity ratio, $R_{[900,1000]}/R_{[780,893]}$

9b

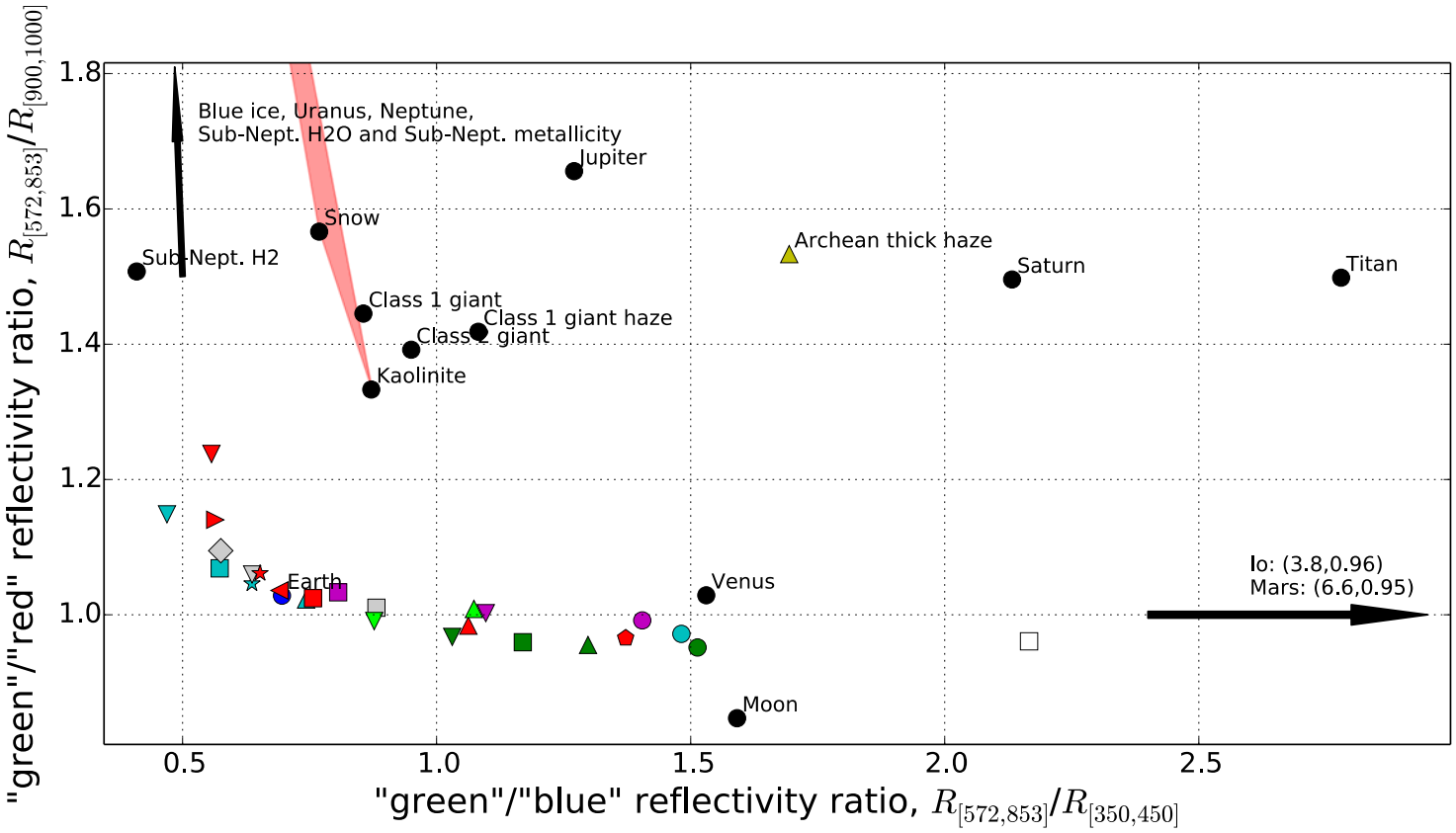
Blue ice, Uranus, Neptune,
Sub-Nept. H2O and Sub-Nept. metallicity
Jupiter
Snow
Sub-Nept. H2
Archean thick haze
Saturn
Titan
Class 1 giant
Class 1 giant haze
Class 2 giant
Kaolinite
Earth
Venus
Moon
Io: (3.8,0.96)
Mars: (6.6,0.95)
"green"/"red" reflectivity ratio, $R_{[572,853]}/R_{[900,1000]}$
"green"/"blue" reflectivity ratio, $R_{[572,853]}/R_{[350,450]}$
1.8
1.6
1.4
1.2
1.0
0.5
1.0
1.5
2.0
2.5

9c

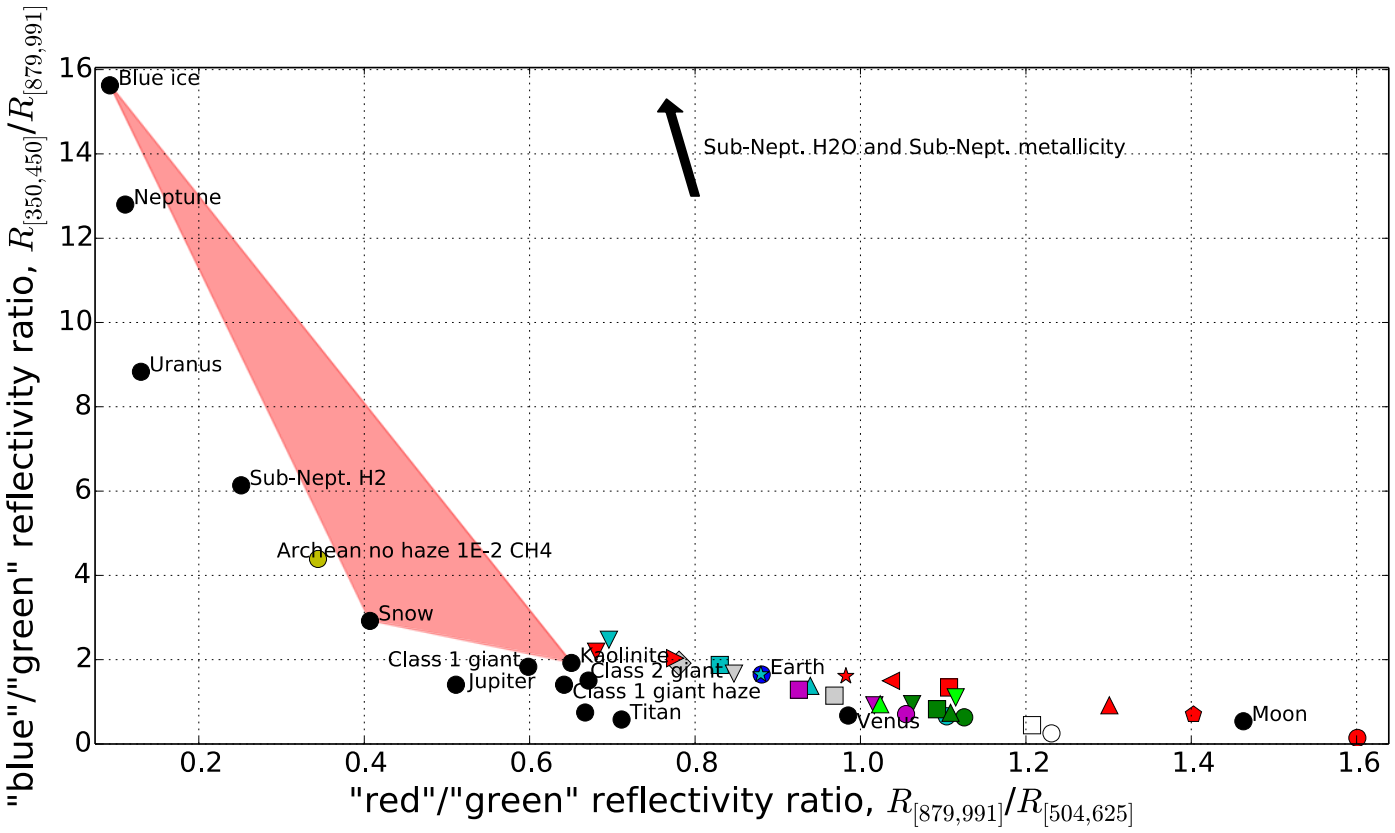

Figure 9: Here the Archean Earth has been optimally separated from all false positives. The legend is the same as Fig. 2, and the modern Earth is plotted for reference in each subfigure. (a) optimally separates the thin-haze Archean Earth from all false positives using “red”/”green” and “blue”/”green” reflectivity axes. The separation between the Archean Earth (left pointing yellow triangle) and its nearest neighbor, Jupiter, is only 0.20 (note that the scaling of the horizontal axis is bigger than the vertical axis). (b) optimally separates the thick-haze Archean Earth (upward pointing yellow triangle) from all false positives using generalized axes with three photometric bins. In this case the separation between the Archean Earth and its nearest neighbor is somewhat improved (0.44), but the Archean Earth does not occupy a unique region in color-color space since intermediates between Jupiter and Saturn are plausible. Finally, (c) optimally separates the non-hazy Archean Earth with high methane (yellow circle) from all false positives using generalized axes and three photometric bins. Once again the optimal separation is comparatively large (1.47), but the Archean Earth does not occupy a unique region in color-color space.

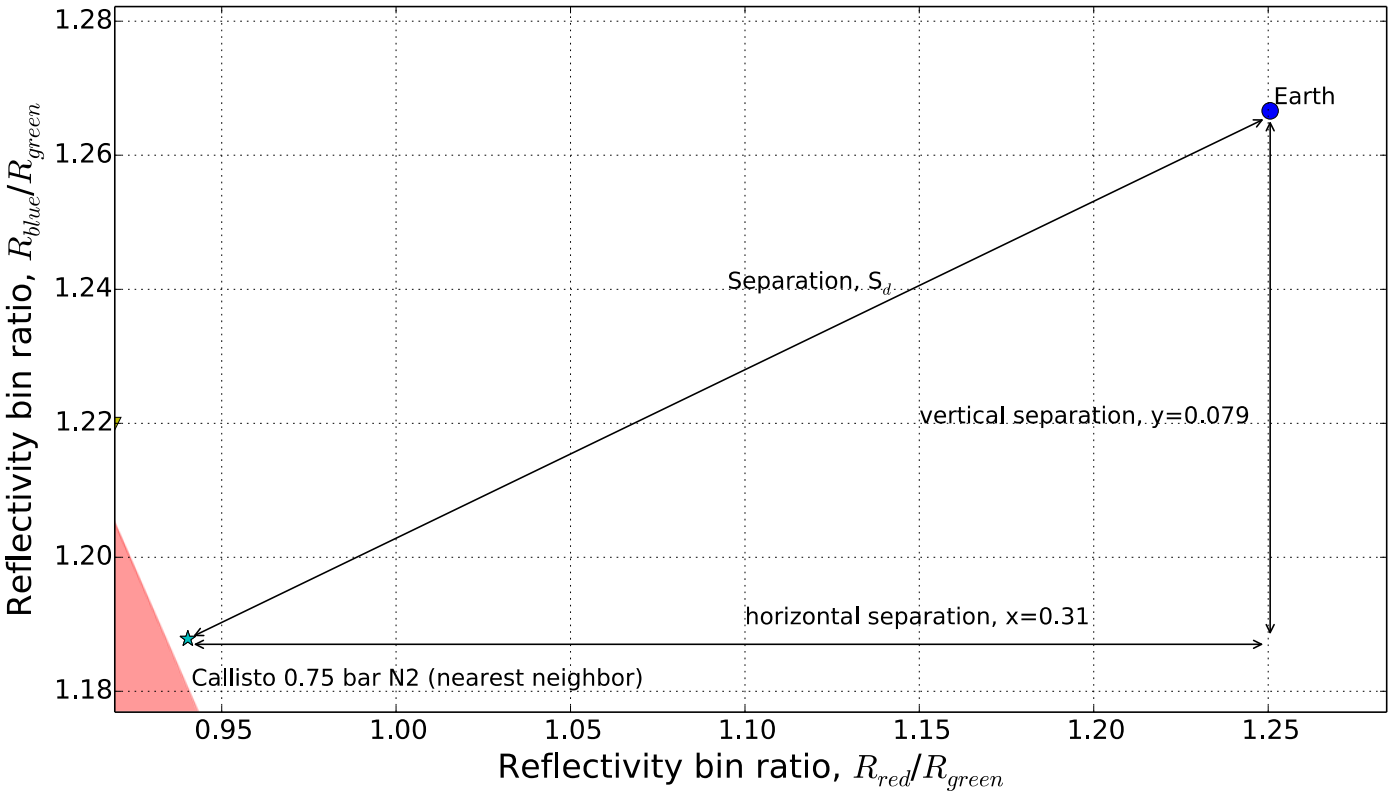

Figure 10: A zoomed in version of Fig. 2 illustrating the key parameters in the detectability calculations.

Appendix III - A statistical analysis of the carbon isotope record from the Archean to Phanerozoic and implications for the rise of oxygen

Portions of this appendix were originally published in collaboration with Roger Buick and David Catling in The American Journal of Science (Krissansen-Totton et al. (2015), A statistical analysis of the carbon isotope record from the Archean to Phanerozoic and implications for the rise of oxygen, American Journal of Science, 315 (4), 275-316.).

Abstract

Organic and inorganic carbon isotope records reflect the burial of organic carbon over geological timescales. Permanent burial of organic carbon in the crust or mantle oxidizes the surface environment (atmosphere, ocean and biosphere) by removing reduced carbon. It has been claimed that both organic and inorganic carbon isotope ratios have remained approximately constant throughout Earth's history, thereby implying that the flux of organic carbon burial relative to the total carbon input has remained fixed and cannot be invoked to explain the rise of atmospheric oxygen *(Catling et al. 2001a; Holland 2002, 2009; Kump et al. 2009; Rothman 2014; Schidlowski 1988)*. However, the opposite conclusion has been drawn from the same carbon isotope record (Bjerrum & Canfield 2004; Des Marais et al. 1992). To test these opposing claims, we compiled an updated carbon isotope database and applied both parametric and non-parametric statistical models to the data to quantify trends and mean-level changes in fractional organic carbon burial with associated uncertainties and confidence levels.

We first consider a conventional mass-balance model where carbon input to surficial reservoirs is balanced by burial of sedimentary carbonates and organic carbon. For this model, statistical analysis implies fractional organic burial has increased over Earth history by a factor of 1.5 relative to organic burial at 3.6 Ga, with the 95% confidence interval ranging from factors of 1.2 to 2.0. An increase in organic burial by a factor of 1.2 cannot explain the rise of oxygen, whereas an increase by a factor of 2 could conceivably explain the rise of oxygen. There is, however, a highly significant and well constrained increase in organic burial from the Proterozoic to the Phanerozoic.

We also analyze changes in the difference between carbonate and organic carbon isotopic ratios over Earth history. There is a statistically significant increase in this difference from the early to late Archean, possibly caused by increased biological fractionation due to methanotrophic recycling. This transition is consistent with the evolution of oxygenic photosynthesis at 2.8 Ga or earlier.

Finally, we explore how these conclusions change if we modify the traditional mass balance model to include other carbon cycle fluxes, specifically ocean crust carbonatization and authigenic carbonates. Because the size of these fluxes has a large, poorly constrained range, our statistical analysis with this

uncertainty implies that the carbon isotope record does not constrain the history of organic burial at all. However, it remains possible that the magnitude of these additional processes has been inconsequential throughout geologic time, in which case conclusions from the conventional model would be valid.

Introduction

Explaining the oxygenation of Earth's atmosphere and oceans is a great unsolved problem in Earth and planetary science. Its solution would enrich our understanding of the co-evolution of life and the environment because abundant atmospheric oxygen sustains virtually all macroscopic multicellular life on Earth (Catling et al. 2005). Moreover, understanding the 2.4 Ga rise of oxygen and subsequent increases on Earth (e.g. Lyons et al. 2014) may inform the search for life on exoplanets because abundant atmospheric O_2 or O_3 is a potential biosignature that may be detectable with next-generation large-aperture telescopes (Des Marais et al. 2002b).

Multiple lines of geological evidence suggest that atmospheric oxygen levels have increased dramatically over Earth's history (Farquhar et al. 2014). In particular, mass independent fractionation of sulfur isotopes indicates that atmospheric oxygen was $\leq 10^{-5}$ of present atmospheric levels during the Archean. Then around 2.4 Ga, a transition led to levels of oxygen exceeding 10^{-3} to 10^{-2} of present atmospheric levels (Farquhar et al. 2007; Holland 1994; Pavlov & Kasting 2002b). Atmospheric oxygen is believed to have remained relatively low for the next billion years until the Neoproterozoic when oxygen levels increased again (Shields-Zhou & Och 2011). Geochemical indicators suggest that this, in turn, was possibly followed by a further increase in the Devonian associated with the colonization of the land by vascular plants (Dahl et al. 2010).

Although it is widely accepted that atmospheric oxygen has increased over Earth history, the precise causes of this increase are debated (e.g. Catling 2014; Kasting 2013; Lyons et al. 2014 for recent reviews). Evidently oxygen source fluxes exceeded oxygen sink fluxes at times during Earth's history; the 2.4 Ga rise, in particular, established a new balance with a permanently oxygenated atmosphere.

There are two broad categories of explanations for the Paleoproterozoic oxic transition: 1) the oxygen source flux permanently increased due to enhanced organic carbon burial (Campbell & Allen 2008) including the possibility that organics were preferentially subducted into the mantle (Hayes & Waldbauer 2006b), and 2) the oxygen sink flux permanently decreased. Hypotheses for the latter include changes in the redox state of volcanic gases due to mantle redox evolution (Kasting et al. 1993a), a transition from subaerial to submarine volcanism (Gaillard et al. 2011; Kump & Barley 2007), or a change in carbon or sulfur recycling (Holland 2009). Alternatively, a change in the redox state of low temperature crustal

volatiles has been proposed due to hydrogen escape oxidizing the crust (Catling et al. 2001a; Claire et al. 2006; Zahnle et al. 2013).

The geological carbon cycle is linked to the oxygen source flux. Earth's atmospheric oxygen is produced almost exclusively by photosynthesis, which can be stoichiometrically approximated by the following:

$$CO_2 + H_2O \rightarrow CH_2O + O_2 \quad \text{(AIII-1)}$$

However the oxygen produced during photosynthesis doesn't constitute a net source of atmospheric oxygen unless it is coupled with the burial of organic matter. In the absence of organic burial, biogenic oxygen merely re-oxidizes organic matter during respiration, reversing equation (AIII-1), and there is no net change in atmospheric oxygen. Thus the burial rate of organic carbon equals the rate of oxygen production, and hypotheses that invoke an increased source flux to explain the rise of oxygen necessarily invoke enhanced organic burial as the mechanism. The long-term behavior of the geological carbon cycle is thereby directly related to atmospheric oxygen. It is the majority opinion that the evolution of oxygenic photosynthesis preceded the rise of atmospheric oxygen by at least several hundred million years (Catling 2014). Note that if anoxygenic photosynthesis was the source of Archean organic matter then the burial of organic carbon does not add molecular oxygen to that atmosphere. However, anoxygenic photosynthesis still produces an oxidized product (such as ferric iron), and so the burial of organic carbon still implies net oxidation of the surface reservoir.

The factors that control organic carbon burial are complex and not fully understood. All else being equal, enhanced biological productivity will result in greater deposition of organic matter in sediments. However, only a small fraction of the organic matter deposited in sediments becomes permanently buried (Hedges & Keil 1995). Instead, most sedimentary organic matter is remineralized to carbon dioxide by microbial metabolisms. Biological productivity and the remineralization fraction are potentially influenced by a variety of geological and biological factors such as tectonic context (Des Marais 1994), sedimentation rates (Betts & Holland 1991), oxygen exposure time in sediments (Hartnett et al. 1998), and evolutionary innovations (Logan et al. 1995).

Fortunately, the carbon isotope record provides a window into the geological carbon cycle through deep time (Broecker 1970). A conventional approach, pioneered by Schidlowski and others (Schidlowski 1988; 1979), assumes that the geological carbon cycle is in steady state over long timescales, or more specifically that (i) the carbon input into surficial reservoirs (atmosphere, oceans and biosphere) is balanced by the burial of carbonates plus organic carbon, and (ii), that the isotopic ratio of carbon inputs equals the average isotopic composition of burial outputs. Taken together these assumptions yield the conservation equation:

$$\delta^{13}C_{in} = f_{org}\delta^{13}C_{org} + (1 - f_{org})\delta^{13}C_{carb} \quad \text{(AIII-2)}$$

Here, $\delta^{13}C_{in}$ is the isotopic abundance of the outgassed carbon inputs, f_{org} is the fraction of the total carbon buried that is buried as organic carbon, and $\delta^{13}C_{org}$ and $\delta^{13}C_{carb}$ are the isotopic abundances of the buried organic and carbonate carbon respectively. Standard isotopic notation is $\delta^{13}C = 1000 \times \left(R_{sample} - R_{std}\right) / R_{std}$ where R_{sample} is the $^{13}C / {}^{12}C$ ratio of the sample, and R_{std} is the $^{13}C / {}^{12}C$ ratio of the Pee Dee Belemnite standard (Faure & Mensing 2005 p. 620,705). Oxygenic photosynthesis preferentially fixes isotopically light carbon, and so the two carbon sinks are isotopically distinct with $\delta^{13}C_{org}$ approximately 20-30‰ lower than $\delta^{13}C_{carb}$. Rearranging equation (AIII-2) yields an expression for f_{org} as a function of the isotopic abundances of the inputs and outputs:

$$f_{org} = \frac{(\delta^{13}C_{in} - \delta^{13}C_{carb})}{(\delta^{13}C_{org} - \delta^{13}C_{carb})} \quad \text{(AIII-3)}$$

Peridotititc xenoliths, mantle-derived basalts, and carbonatites suggest that $\delta^{13}C_{in}$ has remained unchanged throughout Earth's history (Holser et al. 1988; Mattey 1987; Pearson et al. 2003). Shirey et al. (2013) found that 72% of mantle diamonds have $\delta^{13}C$ values that fall within -5±1‰ (measurements outside this range can be explained by recycled crustal material), and so a constant value of $\delta^{13}C_{in} = -5‰$ is assumed in this study. Consequently, by measuring $\delta^{13}C_{org}$ and $\delta^{13}C_{carb}$ over time, the history of f_{org} can be reconstructed. If the absolute rate of total carbon burial can be independently constrained, then f_{org} can be used to infer an absolute oxygen source function through Earth's history. Note that the assumption of constant $\delta^{13}C_{in}$ may not be valid on timescales less than a few hundred million years because preferential weathering of carbonates or organics could modulate the isotopic ratio of riverine carbon input, even if the carbon outgassed remains at -5‰. However over timescales greater than the rock cycle we can expect the average isotopic value of riverine inputs to equal that of outgassed carbon.

The validity of the steady state assumption is generally accepted. Sundquist (1991) explored a time-dependent model of the carbonate-silicate cycle which yielded response times to perturbations of less than 1 million years. This is consistent with an ocean residence time of around 200 ky; the short response time of the ocean reservoir suggests the steady state approximation is valid. Rothman et al. (2003) explicitly modeled the dynamics of the geological carbon cycle and discovered that under certain conditions response times of 10-100 million years are possible. However, on longer timescales the steady state approximation

can be expected to hold. Any long-duration imbalance in the carbon cycle would deplete or swamp the surface reservoir of carbon or induce large secular changes in isotopic composition.

The carbonate and organic carbon isotope records over Earth history are shown in figure 1. An apparent steady average of both $\delta^{13}C_{org}$ and $\delta^{13}C_{carb}$ has led many authors to conclude that f_{org} has remained approximately constant throughout Earth's history (Catling et al. 2001a; Holland 2002, 2009; Kump et al. 2009; Rothman 2014; Schidlowski 1988). A value of f_{org} around 0.2 is derived if $\delta^{13}C_{org} \approx -25‰$, $\delta^{13}C_{carb} \approx 0‰$ and $\delta^{13}C_{in} \approx -5‰$ are assumed in equation (AIII-3). If f_{org} had been constant, this would imply that secular changes in fractional organic burial - and by extension changes in the oxygen source flux - cannot explain the rise of oxygen. Instead, decreases in one or more oxygen sinks must be responsible for the oxidation of Earth's atmosphere and oceans.

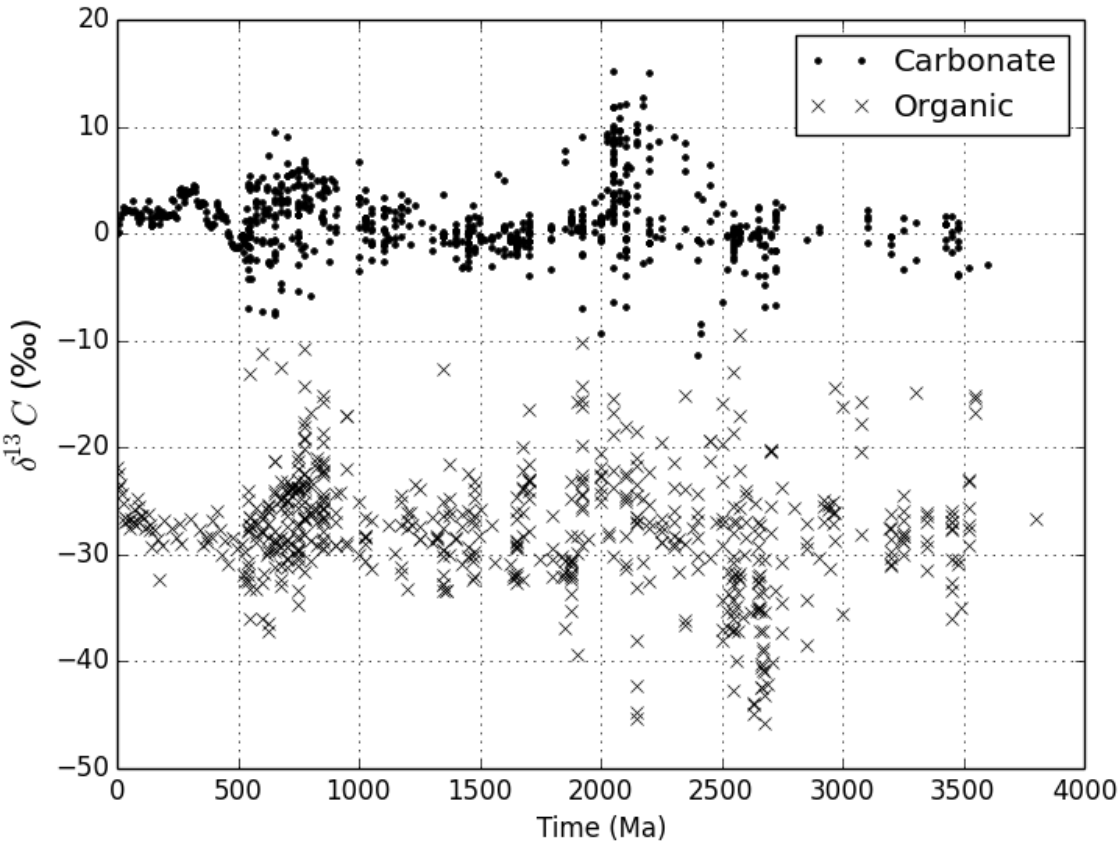

Figure 1: Carbonate (dots) and organic (crosses) carbon isotope data used in this study. Each data point represents the average per formation per author per lithology. Data exclude lacustrine environments, heavily metamorphosed samples and banded iron formations (see section 2). 13,381 individual carbonate isotope measurements and 4,236 organic isotope measurements were averaged to produce the Precambrian data in this figure (see main text for Phanerozoic data). The method of averaging is described in section 2.

However, this interpretation of the constancy of the carbon isotope record is not universal. For instance, Des Marais et al. (1992) incorporated the effects of post-depositional isotopic changes and argued that the carbon isotope record from 2.6 Ga indicates an increase in f_{org} of sufficient magnitude to explain the Paleoproterozoic rise of oxygen. Similarly, Bjerrum and Canfield (2004) suggested that Archean ocean crust carbonatization sequestered light carbon, such that f_{org} could have increased substantially over Earth history as carbonatization declined. Schrag et al. (2013) argued that interpreting fluctuations in the carbon isotope record as changes in f_{org} may be incorrect if a sizeable portion of marine carbonate is authigenic in origin. Authigenic carbonates are isotopically distinct from allogenic (sedimentary) carbonates because the carbon that constitutes authigenic carbonates is primarily remineralized organic matter (Schrag et al. 2013).

Even without considering post-depositional alteration of isotopic ratios or additional carbonate sinks there is considerable scatter in the carbon isotope record. In fact it is not obvious whether or not sizeable secular trends or changes in f_{org} could be hidden beneath the noise. Here, we present a rigorous statistical analysis to examine whether secular trends or changes exist in the history of f_{org}.

The carbon isotope time series data are not evenly spaced, do not necessarily have Gaussian noise, and may possess autocorrelation i.e. a memory of previous states that effectively diminishes the number of independent data points. Thus it is unclear which statistical model best captures the secular changes, noise structure, and temporal autocorrelation of the carbon cycle data. Consequently, our approach is to employ and compare a variety of statistical techniques, both parametric and non-parametric, to ensure robust conclusions. Loosely speaking, parametric techniques assume the data are described by simple functions and distributions, whereas non-parametric techniques make minimal assumptions about the functional form of the data. Section 2 outlines the selection and filtering of carbon isotope data used in this study. Section 3.1 is a non-technical summary of our methods for readers primarily interested in understanding the results and their implications. Sections 3.2 and 3.3 discuss the statistical methods in more detail. Section 3.2 describes the parametric approach, using mean-differencing and linear regressions to evaluate changes in f_{org}. We employ a variety of noise models to characterize the temporal autocorrelation and uncertainty in the data. In section 3.3 we describe an ensemble of non-parametric smoothing techniques used to derive a best estimate of f_{org} over time. Section 4 presents and compares the results from these parametric and non-parametric methodologies. In addition to analyzing f_{org} we also analyze $\varepsilon = \delta^{13}C_{carb} - \delta^{13}C_{org}$ through time. This parameter primarily depends on biological fractionation of carbon with respect to inorganic carbon in seawater and so gives insight into the origin of oxygenic photosynthesis. In section 5, we introduce a

modified mass balance equation that includes isotopically distinct sinks such as ocean crust carbonatization and authigenic carbonates. We redo parts of our statistical analysis using this new model. Finally, section 6 discusses the implications of our results for the rise of oxygen, and key conclusions are summarized in section 7.

Isotope Data

We compiled carbon isotope data for both sedimentary carbonates and organic carbon over Earth history back to the early Archean. Carbonate data were taken primarily taken from Shields and Veizer (2002), but were updated with recent data in the literature. Organic carbon data were taken primarily from Schopf and Klein (1992) and references therein, supplemented using recent results in the literature. Rather than report individual isotope measurements, our database uses averaged carbon isotope values; each entry in the database is the mean isotopic value per formation per author or study per lithology. This averaging is appropriate for the statistical tests we employ in this study because all these tests involve additional averaging or binning of adjacent data points; whether or not data is pre-averaged doesn't change the results appreciably. Where known to be inaccurate, radiometric dates were updated from the literature, and if radiometric dates were unavailable for a given study, then approximate dates were obtained from linear interpolation between dated formations. Spreadsheets containing our dataset are available in the online supplementary materials. The density of Precambrian isotope measurements does not change drastically with time, except for the Archean where there is a scarcity of both organic and carbonate measurements (see supplementary spreadsheet).

The carbon isotope data were also filtered to exclude sediments from non-marine settings, authigenic settings like banded iron formations, or heavily metamorphosed settings. Non-marine sediments were excluded because the steady state mass-balance model relies on carbon-bearing sediments being sourced from an isotopically homogeneous reservoir that reflects the well-mixed global average. This is true for carbon sediments deposited in the Earth's oceans since the typical mixing time in the oceans (~500-1000 years) is small compared to the timescale for sedimentary rock formation. However, the well-mixed assumption doesn't hold for isolated lacustrine environments where isotopic values are potentially variable and may not reflect the global average. Banded iron formations and highly metamorphosed sediments were excluded due to the potential for post-depositional changes in isotopic composition. This filtering is likely imperfect, but it is better than using all carbon isotope data indiscriminately. For completeness we repeated our data analysis on the original unfiltered data and these results are reported only in the supplementary materials, except where they differed notably from the filtered data analysis.

Since multiple authors often report isotopic ratios for the same formation, and since many geological formations are of similar ages, there are often multiple isotopic values per radiometric date in our data.

Standard regression techniques and smoothing algorithms cannot be applied to data with multiple dependent variable values per independent variable value. Consequently, data were binned into 10 million year averages prior to all statistical analyses. Analyses were repeated using 20 million year bins and unique-date bins; results were generally robust to these changes unless stated otherwise. More fundamentally, repeat sampling of the same formation does not constitute independent measurements of globally averaged isotopic ratios in a given geological timescale. Instead it merely refines our knowledge of the globally averaged isotopic ratio at a specific date, rather than improving our knowledge of the mean-level ratio over a larger span of time. Thus binning same-date isotope measurements before applying statistical tests is justified on both pragmatic and theoretical grounds.

Because of the relatively abundant Phanerozoic data, rather than swamp our data set with recent data we used pre-binned data from Hayes et al. (1999) to characterize Phanerozoic carbon isotope values. Where possible, data analyses were repeated excluding the Phanerozoic data to test whether results were robust to the exclusion of this qualitatively different data set.

Ideally we would filter organic carbon data using H/C ratios to remove or correct samples with appreciable diagenetic modification (e.g. Des Marais 1997; Schopf & Klein 1992). However H/C ratios are not available for the majority of organic carbon isotope data and so this filtering is not possible. The statistical effects of diagenetic modification are considered briefly in appendix B.4, and are shown not to be important influences on secular trends.

Statistical Methodologies

Non-technical summary of methods

The carbon isotope data have various features that make them difficult to analyze: they are unevenly spaced in time, serially correlated in time, and there is uncertainty in the nominal radiometric dates. In light of these difficulties we have applied a broad ensemble of statistical techniques to test specific hypotheses about fractional organic burial, and only report conclusions that are robust irrespective of the methodology.

Our methods address three questions about the isotope data:

(i) What is the history of fractional organic burial and biological fractionation over Earth history? In other words, what are $f_{org}(t)$ and $\varepsilon(t)$ with uncertainties? We apply three different smoothing algorithms: locally weighted scatterplot smoothing (LOWESS), kernel regression and Kalman smoothing. These algorithms are each used to estimate $\delta^{13}C_{org}$ and $\delta^{13}C_{carb}$ as functions of time, with uncertainty. The isotope functions are then combined to obtain $f_{org}(t)$ and $\varepsilon(t)$ with uncertainties.

(ii) What is the overall change in fractional organic burial over Earth history with uncertainty? We calculate the linear trend in $\delta^{13}C_{carb}$ and $\delta^{13}C_{org}$ over Earth history, and then combine these to get the linear trend in f_{org} over Earth history. This trend is compared with the null hypothesis that f_{org} has remained constant over Earth history (trend of zero). This analysis is repeated with various assumptions about the correlation structure of data (simple ordinary leased squares (OLS) regression, classical generalized least squares (GLS) regression and bootstrap GLS). Essentially we ask the question under what conditions (if any) can the null hypothesis of no change in f_{org} be rejected, and is this conclusion robust to methodology. The start and end points of the trend line in f_{org} can also be used to calculate the absolute and relative increase in f_{org} over Earth history. The relative increase in f_{org} over Earth history is an important quantity for the history of atmospheric oxygen, as explained in the discussion section. We also fit trends to the smoothed curves and check the non-parametric results (i) against parametric results (ii).

(iii) What is the change in f_{org} and ε between key geological time periods? For instance how much does f_{org} change from the early Archean to late Archean, the Archean to the Proterozoic, and the Proterozoic to Phanerozoic? Here, we are testing the null hypothesis that there has been no change in fractional organic burial between these periods, and we quantify any changes that do occur with uncertainties. This analysis is repeated using different methods that make different assumptions about the temporal correlation of data, and only results robust to choice of methodology are reported.

Parametric Methods

Time series data are often not directly amenable to classical statistical techniques because the data may be correlated in time, as previously mentioned, and thus cannot be treated as independent. To properly characterize uncertainties and perform meaningful statistical tests, temporal autocorrelation must first be accounted for. In our parametric analysis, autocorrelation in the data is explicitly modeled as a first order autoregressive (AR(1)) stationary noise process (see below). Linear regressions and mean differences between two different time periods are then calculated within this autocorrelation framework, and the results are compared to classical statistical techniques where data are assumed to be independent in time.

Autocorrelational model

Characterizing the autocorrelation in unevenly spaced data is challenging since time series theory is predominately designed for evenly spaced data. Traditionally, unevenly spaced data are converted to evenly spaced data using linear interpolation. However, if this approach were applied to the carbon isotope data

then it would introduce significant bias because the spacing is extremely varied. Instead, we adopt an AR(1) stationary noise model for the unevenly spaced data as described by Mudelsee (2010):

- $$X_{noise}(1) = \varepsilon_{N(0,1)}(1) \quad \text{(AIII-4)}$$

- $$X_{noise}(i) = X_{noise}(i-1) \times \exp\{-(t(i)-t(i-1))/\tau\} + \varepsilon_{N(0,1-\exp\{-2[t(i)-t(i-1)]/\tau\})}(i) \quad \text{(AIII-5)}$$

Here $i = 1,...,n$, n is the number of data points, and $\varepsilon_{N(0,1)}$ is a random variable from the standard normal distribution with a mean of 0 and standard deviation of 1. Intuitively, at any given time step the noise term $X_{noise}(i)$ is equal to Gaussian noise ε_N plus the previous noise term $X_{noise}(i-1)$, weighted by some autocorrelation parameter, $\exp\{-(t(i)-t(i-1))/\tau\}$, with a magnitude that depends on the time difference between $X_{noise}(i)$ and $X_{noise}(i-1)$. Evidently for closely spaced data the autocorrelation will dominate and consecutive noise terms will be similar, whereas distantly spaced data will approach random noise. AR(1) denotes the noise model is an autoregressive model of order 1. Each noise term is dependent on the previous noise term, but not the 2nd or 3rd previous noise terms, as would be the case for AR(2) and AR(3) models. The persistence time τ is the e-folding time that describes how rapidly autocorrelation falls off as spacing is increased. For time series data $\{t(i), x(i)\}_{i=1}^{n}$ the persistence time τ can be found by minimizing the sum of the squares:

- $$S(\tau) = \sum_{i=2}^{n} [x_{noise}(i) - x_{noise}(i-1) \times \exp\{-[t(i)-t(i-1)]/\tau\}]^2 \quad \text{(AIII-6)}$$

Note that we have switched to lower case notation to refer to the actual data, as opposed to upper case notation for the general model. Given this noise model, bootstrapping algorithms can be applied to generate confidence intervals for variables of interest such as the mean change in fractional organic burial over Earth history.

The application of this model to regression analysis assumes that the carbon isotope record can be described as a secular background trend plus autocorrelated noise. The noise in the data consists of measurement noise along with process noise such as local environmental conditions, diagenetic changes and rock cycle feedbacks. Specifically, we would expect the carbon cycle to have memory on timescales less than the ~200 million year rock cycle (Holland 1978) since this is the time it takes to weather away carbonates and organic carbon on the continents. The presence of some degree of autocorrelation in these various noise processes is confirmed by non-zero τ values in our analysis, and thus the use of an autocorrelation model rather than treating all data as independent is appropriate. The specific choice of an AR(1) model as opposed to higher order autoregressive moving average models is pragmatic; higher order models do not exist for unevenly spaced data (Mudelsee 2010). Furthermore, the AR(1) model is preferable because it is a correct embedding

of a continuous process in time, unlike higher order models which have no continuous analog (Mudelsee 2010).

Regression analysis

The regression analysis method can be summarized as follows. A linear regression is performed for both organic carbon isotope data and carbonate isotope data. These regression results, with corresponding uncertainties, are then combined to calculate f_{org}. Following Mudelsee (2010) we incorporate non-stationarity (i.e. a change in mean with time) into the model as follows:

$$X(i) = X_{trend}(i) + X_{noise}(i) \times V \qquad \text{(AIII-7)}$$

Here $X_{trend}(i)$ is (in this case) a linear trend, $X_{noise}(i)$ is the noise term from the AR(1) stationary noise model above (eqs (AIII-4) and (AIII-5)), and V is the magnitude of the noise, which is taken to be an unknown constant for simplicity.

Three different approaches were used to calculate the linear regression for the carbon isotope data:

I) Ordinary Least Squares (OLS) fit, with no temporal autocorrelation model. This method treats data as independent in time. This is the ubiquitous technique of "simple linear regression."

II) Classical Generalized Least Squares (GLS) fit. The algorithm for this method is provided in appendix A.1. The basic idea is to provide an initial guess for τ and V, compute the GLS fit along with the uncertainties in fit parameters, and then use these outputs to re-calculate τ and V with a new GLS fit, and repeat until the fitted parameters converge. The GLS fit is an extension of an OLS regression that accounts for AR(1) autocorrelation by preferentially weighting more spaced (less autocorrelated) data points and assuming Gaussian distributions for all uncertainties.

III) Bootstrap GLS. The basic idea is to first perform the classical GLS regression (method II) to estimate the trend, and then subtract the trend from the data to obtain *correlated* residuals. The best-fit τ is then used to perform a weighted differencing to obtain *uncorrelated* residuals. The uncorrelated residuals are resampled with replacement, and the previous operation is inverted to retrieve resampled *correlated* residuals. These correlated residuals are added back to the GLS trend line, and the GLS regression is performed again. Best fit parameters (intercept and gradient) are stored, and the resampling is repeated to build up a probability distribution for each parameter and hence uncertainties. The algorithm for this method is described in appendix A.2.

Each method is performed independently for carbonate and organic carbon data, thereby bootstrapping distributions for the gradient and intercept for each data set. These distributions are in turn sampled to obtain

a realization of $f_{org}(t)$. Finally, a linear regression through this $f_{org}(t)$ realization is performed, and this process is repeated to build up a distribution for the trend in f_{org}. The trend in f_{org} with uncertainty can then be compared to the null hypothesis of zero trend to determine if there is a statistically significant change in fractional organic burial over Earth history.

Mean difference analysis

It is known independently of carbon isotope data that there have been transitional periods in Earth's redox-history whereby atmospheric oxygen has increased dramatically, the Great Oxidation Event (GOE) at ~2.4 Ga (Catling 2014; Farquhar et al. 2014) and the second rise of oxygen in the Neoproterozoic (Och & Shields-Zhou 2012). Changes in Earth's biogeochemical cycles accompanied these redox transitions, and consequently there are sizeable carbon isotope excursions during these transitional periods, the precise causes of which are debated (Canfield 2014; Melezhik et al. 2013). Given that the residence time of O_2 against geologic sinks is relatively short (~2 m.y.), for isolated changes in organic carbon burial to permanently increase steady state atmospheric oxygen, the mean f_{org} of non-transitional periods must change, i.e. the average f_{org} prior to a rise of oxygen must be less than the mean f_{org} after the rise of oxygen. Hence calculating the mean difference between two non-transitional regions in the carbon isotope record provides a method to test whether f_{org} has permanently increased, and whether this can quantitatively explain oxygen increases. The mean difference approach is complimentary to regression analysis.

The mean difference method can be summarized as follows. The "mean level" was calculated for different subsections of organic carbon and carbonate isotope data. These mean levels were determined by a variety of methods such as a simple arithmetic mean or a best fit GLS regression where the regression line was flat because gradient of zero was imposed. The mean levels of different subsections of the data were then compared as described below. The probability distributions for organic and carbonate subsections were also sampled to determine if f_{org} had changed between different time intervals. Figure 2 illustrates the general methodology.

Two different approaches were used to calculate and compare mean levels for the carbon isotope data:

I) Student's t-test. Firstly, two non-transitional intervals of interest were defined, e.g. 1.8-1.0 Ga and 3.8-2.5 Ga (fig. 2). The means and standard errors of the carbon isotope data in each interval were calculated, assuming Gaussian distributions, and then the means of each region were quantitatively compared using the Student's t-test. This approach will overstate the

significance of differences in mean-levels since it does not account for temporal autocorrelation; however it provides a useful comparison with other methods.

II) a) Bootstrap "flat" GLS regression. Firstly we adopted the autocorrelation model described in section 3.2.1. This model was used to describe the noise, and the bootstrap GLS regression was used to find the mean level for each subsection of the data (gradient specified as zero). The resulting mean-level probability distributions for each subsection of the data were then sampled to make statistical comparisons between different subsections of the data. The approach is essentially identical to the algorithm used to perform the bootstrap GLS regression above, except that in equation (AIII-7), $X_{trend}(i)$ is replaced by the constant mean-level X_{mean}, and the regression algebra is modified accordingly since we are only solving for one parameter (mean-level) as opposed to two (gradient and intercept). For completeness the full algorithm is described in appendix A.3.

b) Identical to IIa) except that persistence times, τ, were fitted to each interval individually rather than fitting the persistence time to the entire data set.

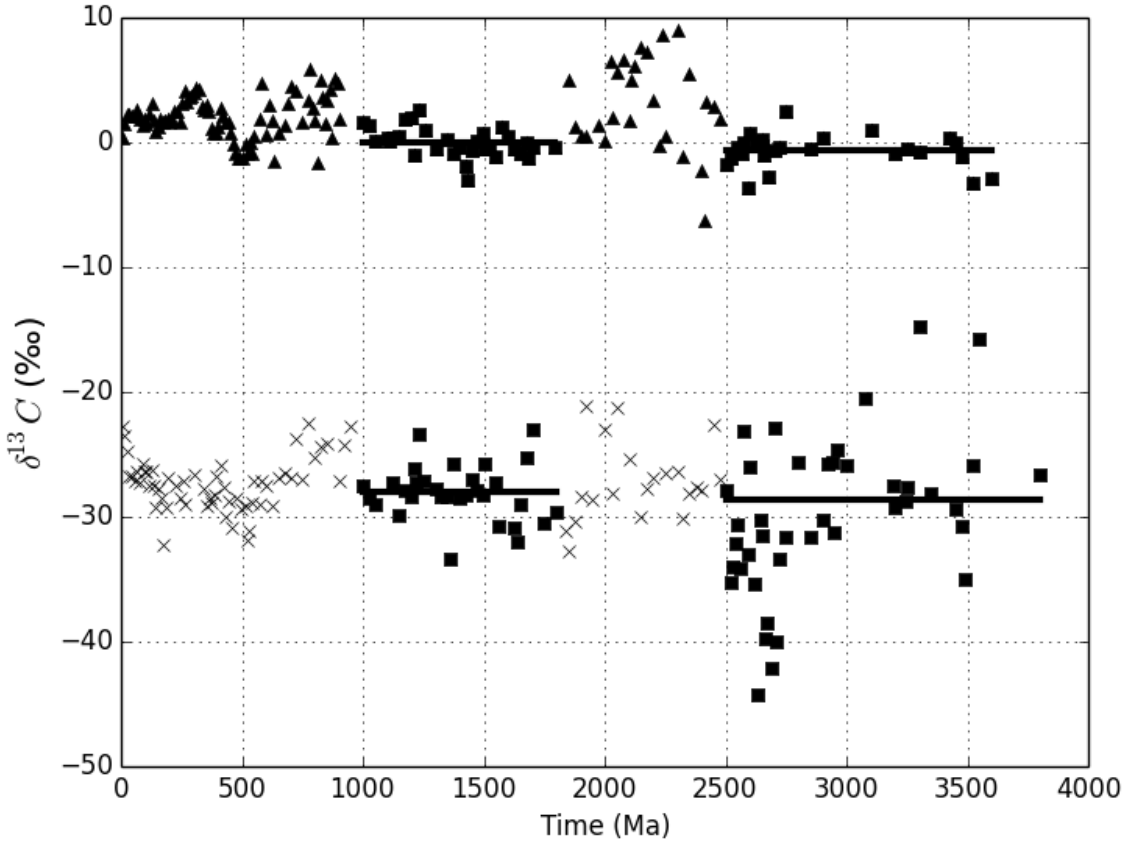

Figure 2: Binned carbonate (triangles) and organic carbon isotopes (crosses) illustrating the mean-difference methodology. Two regions of interest are defined (1.8-1.0 Ga and 3.8-2.5 Ga) and data in these

regions, highlighted by squares, are fitted with a zero-gradient regression to determine mean values. A black horizontal line denotes the mean value in each region. This process is repeated for resampled data to build up distribution for mean values (and f_{org}) within each interval of interest.

The mean difference methods were used to calculate probability distributions for the mean-level of organic carbon (or carbonate) isotopes for two different intervals of the data. Given these probability distributions, we determined whether the organic carbon (or carbonate) mean-level had changed by sampling from the resulting distributions and building a probability distribution for the difference between the two intervals. To determine whether f_{org} from two different intervals was different, the organic and carbonate isotope distributions in each intervals were sampled, realizations of f_{org} were calculated, and a f_{org} distribution was created for each of the two subsections. The two f_{org} distributions corresponding to different intervals of time were then sampled and differenced to determine if there was a statistically significant change in f_{org} between the two intervals. In other words, here we were testing the null hypothesis that the two f_{org} distributions have the same mean. The difference between carbonate and organic carbon isotopic ratios, ε, was also calculated using the same approach.

Four pairs of intervals were chosen for mean level comparison:

a) The late Archean (2.8-2.5 Ga) and the early Archean (3.8-2.8 Ga). This division was chosen to investigate possible changes in $\delta^{13}C_{org}$ and ε associated with proposed methanotrophic recycling of carbon during the late Archean (Hayes & Waldbauer 2006b; Thomazo et al. 2009).
b) The "boring billion" Proterozoic (1.8-1.0 Ga) and the Archean (3.8-2.5 Ga). This division was chosen to investigate changes in steady-state organic burial following the Great Oxidation Event (excluding the 2.2-2.06 Ga Lomagundi excursion of very positive $\delta^{13}C_{carb}$ (Bekker et al. 2008; Schidlowski et al. 1976)).
c) The "boring billion" Proterozoic (1.8-1.0 Ga) and the early Archean (3.8-2.8 Ga). This division was also chosen to compare pre-GOE and post-GOE steady state organic burial, but excludes the late Archean excursion because of ostensible methanotrophic recycling of carbon.
d) The Phanerozoic (0.54-0 Ga) and the "boring billion" Proterozoic (1.8-1.0 Ga). This division was chosen to examine increased steady-state organic burial following the Neoproterozoic Oxygenation Event (Och & Shields-Zhou 2012).

Non parametric methods

To complement the parametric models, carbon isotope data were also analyzed using a variety of non-parametric smoothing algorithms to ensure robust conclusions. In particular, the change in f_{org} over Earth history from the parametric analyses above was compared to the same change in f_{org} from non-parametric smoothing. Smoothing algorithms also reveal $f_{org}(t)$ with uncertainties; this is potentially useful for quantifying carbon cycle excursions and validating or parameterizing geological carbon cycle models.

We applied three smoothing methods to the carbon isotope data: locally weighted scatterplot smoothing (LOWESS), kernel regression, and Kalman smoothing. LOWESS is a standard non-parametric smoothing algorithm often applied to unevenly spaced time series data. It utilizes a moving window approach where the bandwidth of the window is a fixed fraction of the total number of data points. For each data point $\{t(i), x(t(i))\}$ a quadratic is fitted to all the data pairs within the surrounding window (each point is weighted by its distance from the center of the window). The smoothed estimate, $\bar{x}(t)$, is the value of the fitted polynomial evaluated at t. Each data point is then re-weighted by its residual and the procedure is repeated to ensure outliers are discounted. The only free parameter in the LOWESS algorithm is the smoothing bandwidth, i.e. the fraction of data points used for each polynomial fit. Various heuristic methods exist for selecting an optimal bandwidth; we adopted "leave-out-one cross-validation". The LOWESS algorithm and the cross-validation procedure are described in full in Cleveland (1979). Uncertainties in the smoothed curve were generated by bootstrapping: the residuals from each fit were repeatedly resampled and added back to the smoothed curve to generate an ensemble of smoothed curves.

The second smoothing method adopted is Kernel regression using the Nadaraya-Watson estimator (Fan & Yao 2003). This is a moving-average scheme that estimates the conditional expectation value of the dependent variable with a Gaussian weighting function. The bandwidth of the weighting function is a free parameter, and this was once again optimized using leave-out-one cross validation. Uncertainties were generated by bootstrap resampling and refitting. Both LOWESS and Kernel regression algorithms are standard functions in the statsmodels module for python, the programming language that was used for these analyses. We provide the python code used to perform this smoothing analysis as supplementary material, and they are mirrored on the website of the senior author (DCC).

The third smoothing method adopted is the Kalman smoother (Shumway & Stoffer 2011). We implemented a local level state-space model whereby the state of the system at time t, x_t, represents the globally averaged isotopic ratio and evolves stochastically according to:

- $$x_{t+1} = x_t + w_t \quad \text{(AIII-8)}$$

Here, w_t is the process noise which is interpreted as representing real changes in the carbon cycle. It is a normally distributed random variable with a mean of zero and unknown variance. The Kalman smoother represents imperfect observations of the isotope record with:

- $$y_t = x_t + z_t \quad \text{(AIII-9)}$$

Here, y_t is the observed isotope value and z_t is a normally distributed random variable with a mean of zero and unknown variance. z_t is interpreted as the measurement noise, which is any source of noise that causes a difference between observed $\delta^{13}C$ values and the true globally averaged $\delta^{13}C$ values at the time of deposition. Possible sources of measurement noise include preservation or sampling biases and diagenetic modifications. A Gaussian distribution is justified on the grounds that there are many sources of error and that therefore the Central Limit Theorem applies. The Kalman smoother fits this model to the data using a Bayesian framework, optimizing the variance of both the process noise and the measurement noise. Equation (AIII-9) can be modified to account for missing observations in otherwise evenly spaced data. This allows unevenly spaced data to be analyzed using the Kalman smoother; carbon isotope data were averaged into 10 my bins and the empty bins were taken to be missing observations (the analyses were repeated using 50 my bins with negligible difference in results). Equation (AIII-8) was also modified to include a variable trend term to improve the fit provided by a simple random walk.

Strictly speaking the Kalman smoother is a parametric model. However it is useful for comparison with non-parametric smoothers because of its theoretical optimality. It can be shown that the Kalman smoother provides estimates of the state vector with expectation values that match the true expectation values and minimize variance (Simon 2001). The Kalman smoother was implemented using the KFAS package in the statistical freeware 'r' (where KFAS documentation provides information on algorithms). Uncertainties in smoothed curves were generated using KFAS simulations of the best fit state-space parameters; an ensemble of smoothed curves was generated to obtain confidence intervals.

Results

All the results reported in this section assume that the carbon cycle is in steady state. This means that the isotopic composition of outgassed carbon into the surficial reservoir is constant (-5‰), and that the simple mass balance representation of the carbon cycle in equation (AIII-2) is valid.

History of organic burial and biological fractionation over time

The carbonate and organic $\delta^{13}C$ time series were smoothed independently using all three smoothing techniques and the resulting ensemble of curves were sampled to produce a distribution of smoothed f_{org} curves. Figures 3A and 3B show smoothed carbonate and organic carbon curves, respectively, for all three smoothers with 95% confidence intervals. The three different smoothing techniques produce consistent results. The smoothed carbonate curve(s) provide confirmation of positive $\delta^{13}C_{carb}$ excursions in the Paleoproterozoic (the Lomagundi excursion) and Neoproterozoic. The smoothed organic curves are relatively constant within uncertainties except for the negative excursion around 2.7 Ga.

Figure 3C shows the smoothed f_{org} curves from the three smoothing algorithms with 95% confidence intervals. Once again the three algorithms produce congruent results. The Kalman smoother produces slightly larger uncertainties - especially in the Archean - since it incorporates a scheme for missing data and has a more robust method of error calculations than mere resampling of residuals. Neoproterozoic and Paleoproterozoic excursions in the carbonate data appear as pulses of organic burial in the smoothed f_{org} reconstruction. Outside of these excursions the smoothed curves suggest that there is little change in steady-state f_{org} from the Archean to the "boring billion", but that there is an increase in f_{org} from the Proterozoic to the Phanerozoic. These changes in steady-state f_{org} are quantified in section 4.3 below.

The sensitivity of the smoothed f_{org} curves to different assumptions was briefly investigated. It makes no difference whether the LOWESS and kernel regression uncertainties are generated by simple resampling and refitting (effectively a white noise model), or by applying the autoregressive noise model described in section 3.2; smoothed f_{org} curves and confidence intervals are virtually identical in both cases. This suggests that there is no autocorrelation in the post-smoothing noise which justifies the application of the white-noise approach. Rather than assuming a constant variance noise model we also fitted a LOWESS curve to the squared residuals and scaled the noise terms accordingly to better capture the changes in variance over time. This is a somewhat *ad hoc* approach, but arguably better captures the fact that carbon isotope measurements are well constrained in the Phanerozoic compared to the Proterozoic and Archean. Modifying the uncertainties in this way increases the mean-value and confidence intervals for the total change in f_{org} over Earth history, but once again the differences are slight.

Introducing uncertainty in the independent variable also does not change the smoothed results appreciably. Gaussian time-scale noise with a standard deviation of 100 m.y. was added to the data and new uncertainties

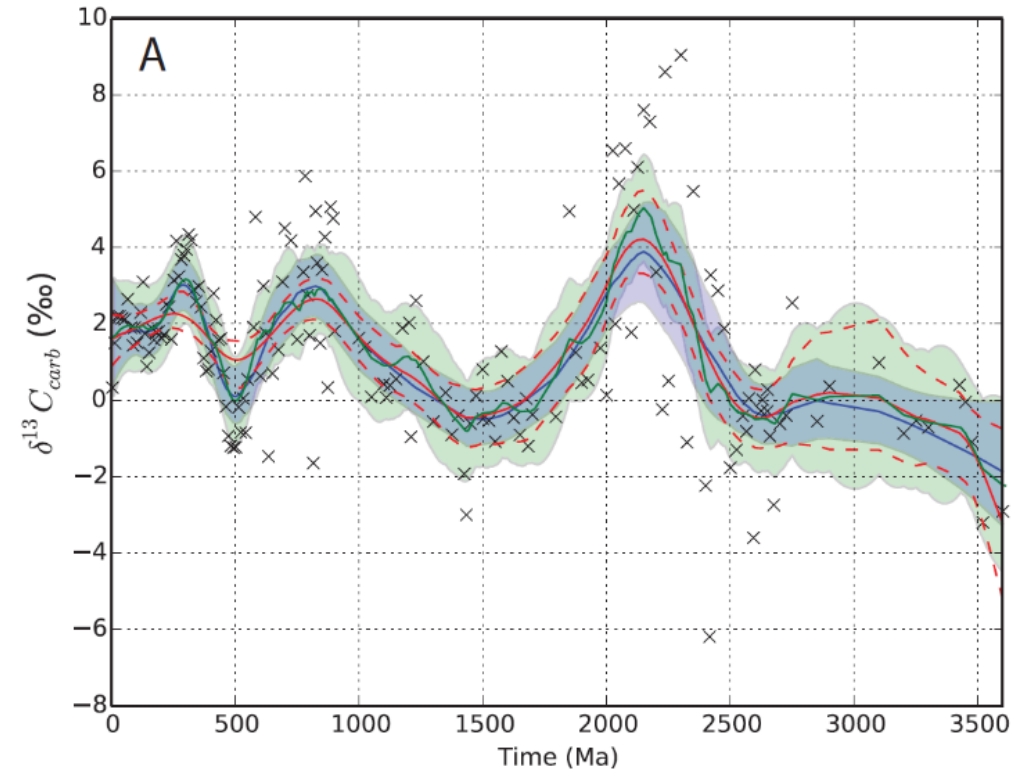
A
10
8
6
4
2
0
−2
−4
−6
−8
$\delta^{13}C_{carb}$ (‰)
0
500
1000
1500
2000
2500
3000
3500
Time (Ma)

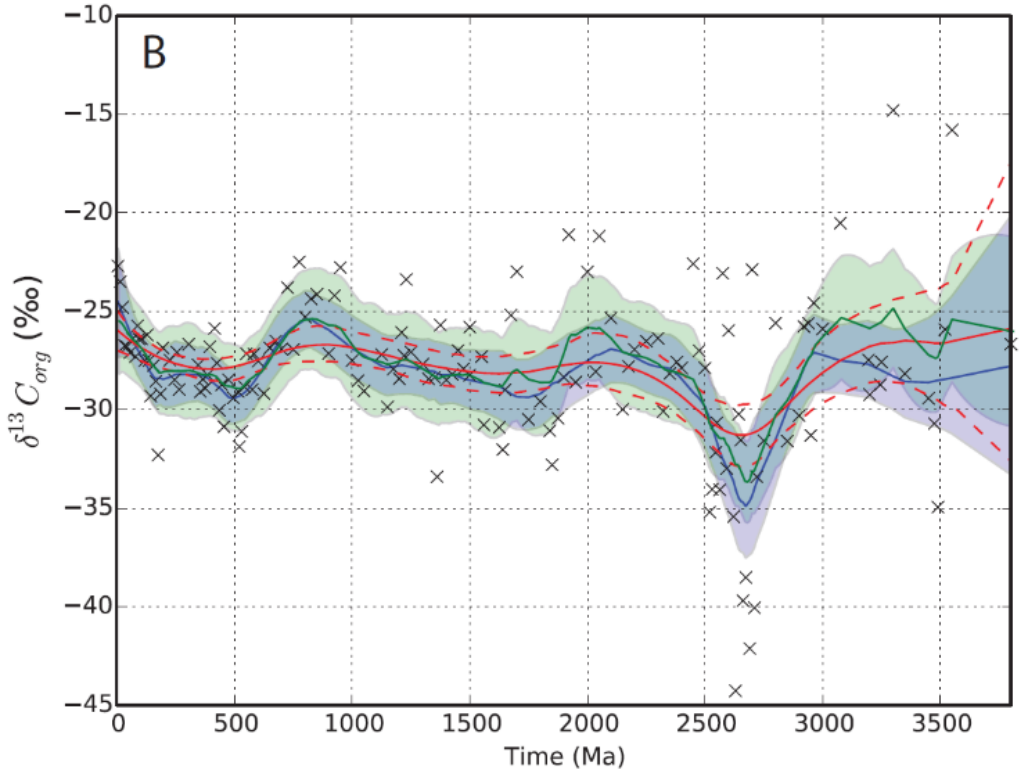
B
−10
−15
−20
−25
−30
−35
−40
−45
$\delta^{13}C_{org}$ (‰)
0
500
1000
1500
2000
2500
3000
3500
Time (Ma)

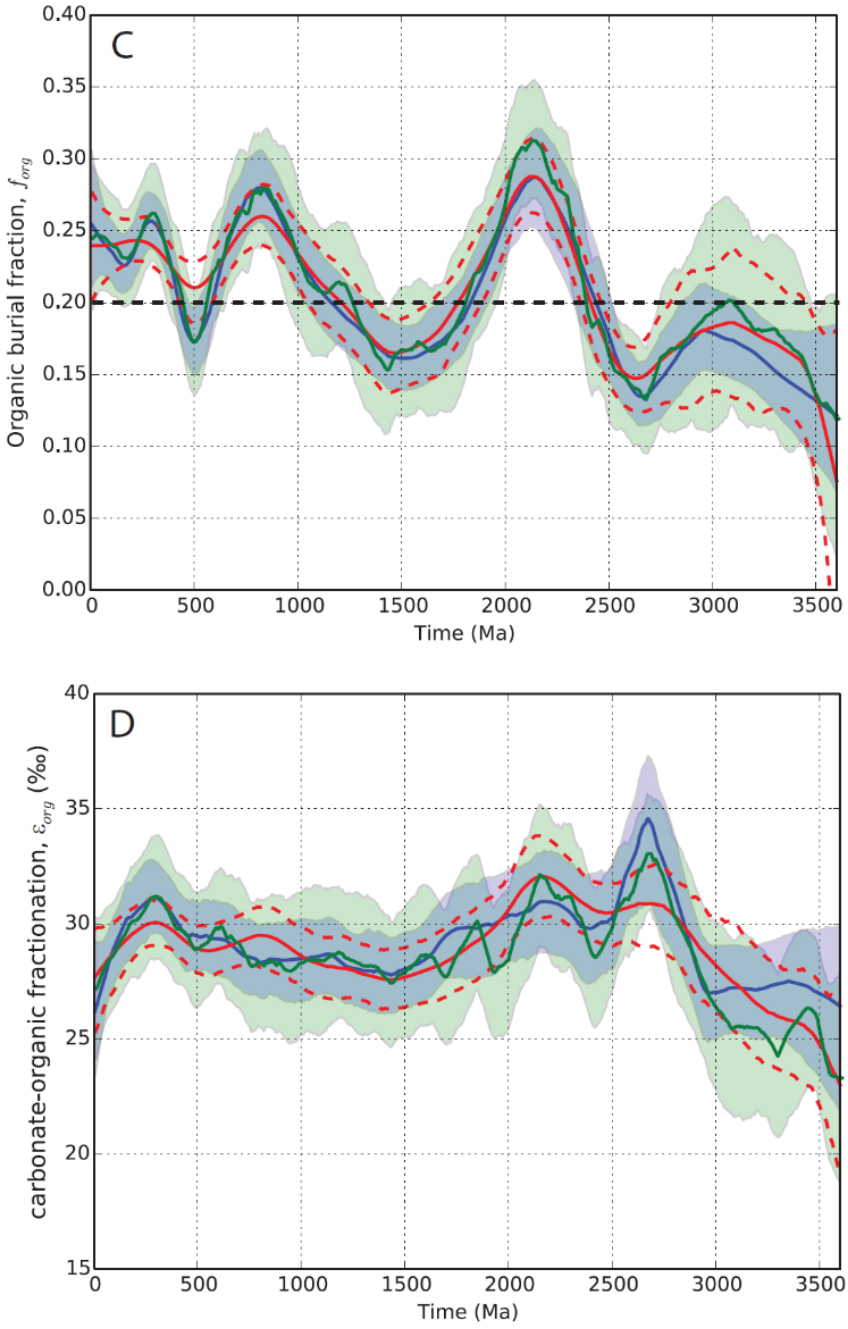

Figure 3: LOWESS and Kernel regression smoothed curves are denoted by blue and red solid lines respectively, with 95% confidence denoted by blue shading and red dashed lines, respectively. The Kalman smoother curve is the green solid line, with 95% confidence shown with green shading. A) Shows carbonate results with binned (10 my) carbonate data denoted by black crosses, B) shows organic results with binned (10 my) organic data denoted by black crosses, C) shows the resulting curves, and D) shows the resulting ε curves. The black dashed line in C) shows the previously accepted canonical value for fractional organic burial of 0.2.

were generated by bootstrapping as described in section 4.2.2. This damped the f_{org} fluctuations slightly but otherwise had not effect. Finally, excluding Phanerozoic data from the analysis did not change the results appreciably.

Our reconstruction of f_{org} over Earth history, with uncertainties, could be used as input for (or validation of) dynamical models of the rise of oxygen. We have included the python scripts used to generate the smoothed curves as supplementary material.

Figure 3D shows the smoothed ε curve over Earth history (where $\varepsilon = \delta^{13}C_{carb} - \delta^{13}C_{org}$). The difference, ε, is largely determined by biological fractionation during carbon fixation and subsequent pathways of remineralization of organic carbon, although changes in climate or carbon dioxide abundance could result in small variations in ε (Hayes 1994). Compared to the fractional organic burial record, there has been comparatively less variation in the fractionation between organic and inorganic carbon. Visually, it appears as though there is an increase in fractionation from the early Archean to late Archean, followed by a decline in fractionation from the late Archean to the Paleoproterozoic and no further significant changes through to the Phanerozoic. These results are quantified in section 4.3.

Total change in fractional organic burial over Earth history

Here, rather than estimating f_{org} as a function of time we calculate the overall change in f_{org} over Earth history. This is achieved by fitting a linear regression to both the carbonates and organics, and multiplying the consequent slope in f_{org} by the duration of the rock record. This absolute change in f_{org} can be compared to the fitted f_{org} value at 3.6 Ga to get the relative increase over Earth history, which equals the fitted modern value of f_{org} divided by the fitted 3.6 Ga value of f_{org}. This quantity is useful for determining whether increases in organic burial can explain the transition from an anoxic to oxic atmosphere, as explored in section 6.

Regression analyses suggest that fractional organic burial increased over Earth history, but the magnitude of this increase has a large spread centered around 1.5 (increase relative to 3.6 Ga). Tables 1 and 2 show the results for the three parametric regression methods outlined in section 3.2.2. The bootstrap GLS regression leads us to conclude with 95% confidence that the increase in f_{org} over Earth history is between 0.008 (factor of 1.04 increase relative to 3.6 Ga) and 0.139 (factor of 2.10 increase relative to 3.6 Ga). This is a very large confidence interval: the lower bound would constitute a negligible increase in the oxygen source flux, whereas the upper bound would approximately double the source flux. The probability

distribution for the change in f_{org} over Earth history from the GLS bootstrap is shown in figure 4. Even if we ignore autocorrelation and assume the carbon isotope data are temporally independent (OLS) then the 95% confidence interval still ranges from a factor of 1.19 to 1.99 increase in f_{org} relative to 3.6 Ga. The low p-values for the change in f_{org} merely indicate that f_{org} probably hasn't decreased given this carbon cycle model. This result, that a wide spread of possible f_{org} increases are possible, is robust to data selection and filtering. If the analysis is repeated but Phanerozoic data is excluded, then the uncertainty in the change in f_{org} increases (GLS bootstrap 95% confidence interval ranges from a factor of 0.96 to 2.5 change relative to 3.6 Ga). If the analysis is repeated for unfiltered carbon isotope data then the GLS bootstrap 95% confidence interval for the increase in f_{org} extends from 1.02 to 2.43 relative to 3.6 Ga. Tables showing the analysis results for different data selection criteria and filtering are available in appendix B.

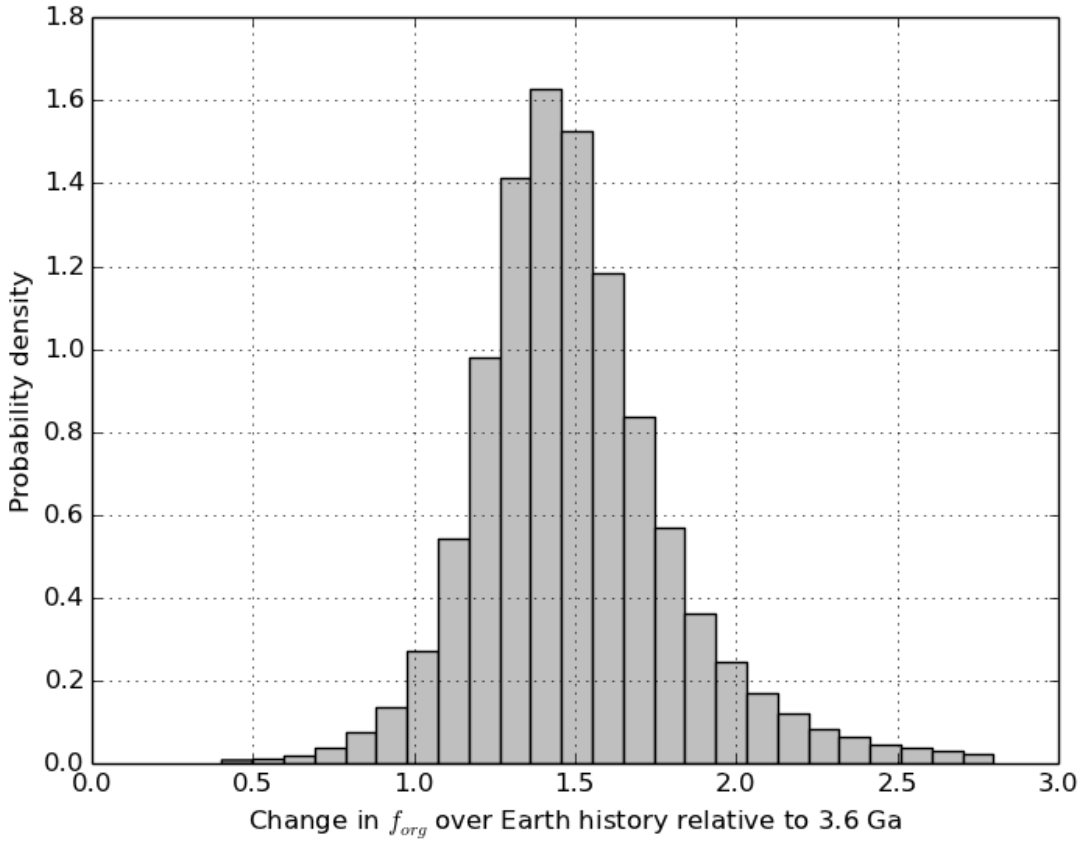

Fig. 4: Probability distribution for the change in the fraction of carbon buried as organics, , over Earth history (relative to 3.6 Ga) from the bootstrap GLS regression.

Introducing autocorrelation does not dramatically change the results compared to a simple OLS regression, thereby indicating that there is minimal autocorrelation in the carbon isotope data. The confidence intervals

are slightly wider for the GLS results, but OLS regression analysis is sufficient to provide a similar answer. However, it was necessary to run GLS fits to prove this.

Comparison with smoothing algorithms

In order to directly compare the results from the regression analyses in section 3.2 with the smoothing algorithms in section 3.3, the change in f_{org} over Earth history (with confidence intervals) was calculated for each of the smoothing techniques. This was achieved by taking the ensemble of f_{org} curves from each of the smoothing algorithms and producing a corresponding ensemble of linear regressions. Thus a distribution for the linear change in f_{org} over Earth history was obtained and compared with equivalent parametric results.

These results are summarized in table 2 (rows 4-6). Both the smoothing algorithms and the parametric regression techniques produce a similar f_{org} change over Earth history (factor of 1.5 increase relative to 3.6 Ga) with similar 95% confidence intervals (approximately 1.2 to 2.0 relative to 3.6 Ga). The consistently low p-values suggest that some positive increase in f_{org} has probably occurred, but it is clear from the confidence intervals that the magnitude of this increase is poorly constrained. The parametric regression techniques generally produce larger uncertainties than the smoothing techniques; this is unsurprising since the smoothing of data reduces extremes compared to unsmoothed linear regressions.

Timescale uncertainty

In the analysis above we assumed that there were no uncertainties in the carbon isotope sample ages. This assumption is unrealistic. Although the radiometric ages of dated strata are tightly constrained, the stratigraphic distance between datable layers and carbon-bearing layers is often large, and thus interpolation is necessary, thereby introducing considerable uncertainty in ages. Errors in the database are also likely to exist and introduce further uncertainty in nominal ages. Rather than attempt the task of estimating the uncertainty in the radiometric age for every point in the carbon isotope database, time-axis uncertainty was introduced by adding Gaussian noise to each radiometric date, and then bootstrapping over many different realizations of the time-uncertain data to generate probability distributions for parameters of interest. Adding noise in this way is undoubtedly an oversimplification because some samples have well constrained ages, whereas other samples have uncertainties of tens to hundreds of millions of years. However this approach provides some indication of the sensitivity of the results to uncertainties in the formation ages. The alterations to the algorithms made to account for timescale uncertainty are described in appendix A.4.

Because the choice for the width of the Gaussian used to introduce noise to the time values is unclear, the analysis was repeated for a range of Gaussian widths. Figure 5 shows the change in f_{org} over Earth history (relative to 3.6 Ga) as a function of t_{noise}, where t_{noise} is the standard deviation of the Gaussian (in millions of years) used to add uncertainty to the nominal ages of carbon isotope samples. Evidently, adding a small amount of noise to the nominal carbon isotope ages causes a sharp increase in the uncertainty in the f_{org} change with GLS bootstrapping. This is because for $t_{noise} = 0$ there are many closely spaced observations due to preservation biases, which imply low τ values, a larger effective sample size, and therefore smaller uncertainties in the final parameters. However when t_{noise} is increased there are fewer closely spaced observations, the τ estimate is larger, effective sample sizes are smaller, and final uncertainties are larger. The initial sharp increase in bootstrap GLS confidence intervals as t_{noise} increases perhaps suggests that the true autocorrelation is low, and that by adding time-axis noise we are artificially introducing autocorrelation by increasing the spacing between data points.

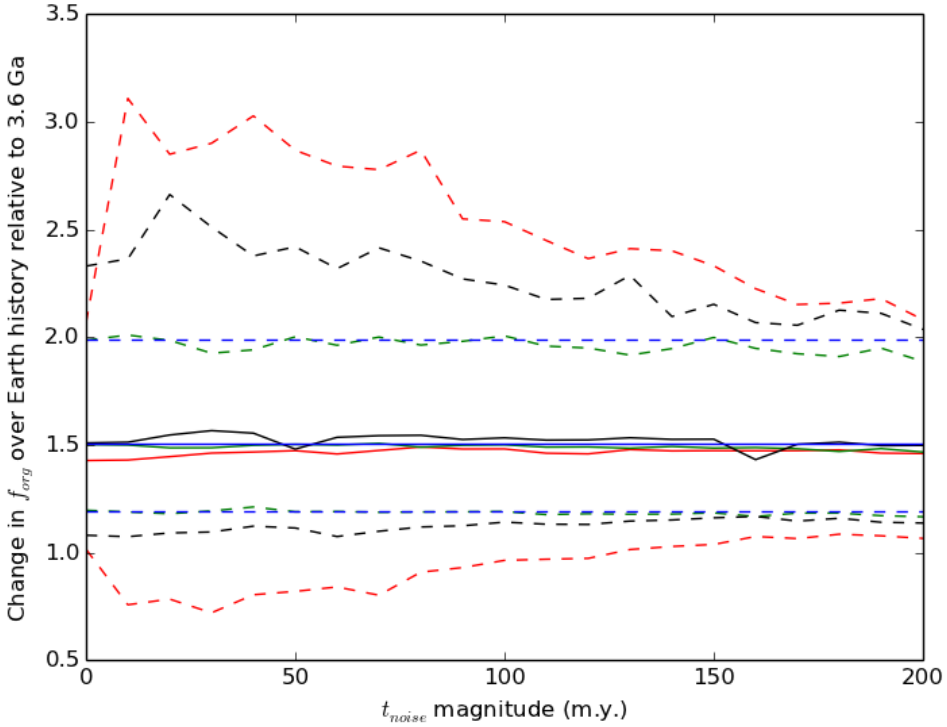

Fig. 5: Change in over Earth history relative to 3.6 Ga as a function of t_{noise}, where t_{noise} is the standard deviation of the Gaussian (in millions of years) used to add uncertainty to the nominal ages of carbon isotope samples. Solid lines are median changes and dashed lines denote 95% confidence intervals for different methods. Median rather than mean changes are used to reduce fluctuations due to extreme increases or decreases. The blue line is a reference line that shows the OLS regression result, which does not account for timescale uncertainty in any way. The green line is the OLS regression modified to account

for timescale uncertainty (method I, section 3.2.2), the black line is the classical GLS regression modified to account for timescale uncertainty (method II, section 3.2.2), and the red line is the GLS bootstrap regression modified to account for timescale uncertainty (method III, section 3.2.2).

As t_{noise} is increased further, the autocorrelation is destroyed entirely and the uncertainties converge toward the OLS confidence interval. A similar decay in uncertainties is visible in the classical GLS confidence intervals (though the initial sharp increase is absent for reasons that are unclear). For reasonable t_{noise} magnitudes the mean value for the change in f_{org} is constant. This indicates that it is only the autocorrelation structure that is being altered by adding time-scale uncertainty. However, for very large values of t_{noise} the mean change in f_{org} does approach zero as we would expect (not shown).

Unsurprisingly, the confidence interval for the OLS, zero time-uncertainty reference case (blue line) is essentially identical to the OLS regression confidence interval that incorporates time-uncertainty (green line). Again, this indicates that adding t_{noise} does not change the confidence intervals due to changes in the data points themselves, but rather it changes the autocorrelation structure of the data.

Change in f_{org} and ε between key geological time periods

Table 3 shows the results of mean difference comparisons between the four intervals defined in section 3.2.3. For each sub-table, the first six rows give the mean level with standard error for two time intervals and three different methods. The seventh to ninth rows give the mean difference between the two intervals for the three methods, and the tenth to twelfth rows give the corresponding p-values for the mean level differences (the null hypothesis being that there is no difference between mean levels). The analysis is reported separately for organic carbon isotopes, carbonate isotopes, f_{org} and ε (four columns).

We also directly compared the mean-difference results from the parametric analyses in section 3.2.3 to the smoothing analysis. We adopted a heuristic method for comparing the mean-difference between two sections of smoothed data since the number of independent measurements is unknown. For a given time interval the distribution for the mean-level was obtained from the ensemble of (means of) smoothed curves within that interval. Complete tables comparing mean-difference results from both parametric analyses and smoothing analyses are available in appendix B.3. Key results are briefly summarized here.

Early Archean to late Archean

Both the Student's t-test and the GLS bootstrap regression indicate a significant decrease in $\delta^{13}C_{org}$ from the early Archean to the late Archean (Table 3A). This result is robust to the precise date chosen to divide

the early and late Archean; the difference is statistically significant for any division date between 2.7 and 3.0 Ga. The mean difference between the early and late Archean is maximized when the division is placed at 2.78 or 2.90 Ga, where the former correlates with a change in sulfur cycling (Stüeken et al. 2012) and the latter roughly coincides with a glaciation episode (Young et al. 1998).

Despite the decline in $\delta^{13}C_{org}$ there is no statistically significant decrease in f_{org} from the early Archean to the late Archean. This is confirmed by both the parametric methods above and smoothing analysis (table B.4a appendix). There is, however, a statistically significant increase in ε by about 6‰ from the early to late Archean. This change is apparent in figure 3D, and has also been quantified by mean-difference analysis as shown in table 3A. These results suggest that changes in the carbon isotope record from the early to late Archean are best explained by changes in biological fractionation between inorganic and organic carbon, and not by changes in fractional organic burial.

Archean to Proterozoic

There is a marginally significant increase in f_{org} from the Archean (3.8-2.5 Ga) to the Proterozoic (1.8-1.0 Ga), although the magnitude of the increase is not well constrained by either the Student's t-test or the GLS bootstrap regression (Table 3B). The mean (absolute) increase in fractional organic burial from the Archean to the Proterozoic is ~0.03, with the 95% confidence interval ranging from approximately 0 and 0.05. Smoothing analysis also confirms this result (table B.4b). One way of testing whether f_{org} increased from the Archean to the Proterozoic is to exclude the late Archean and to difference only the early Archean and the Proterozoic (Table 3C). This is because, as established above, there is a marked decrease in $\delta^{13}C_{org}$ in the late Archean plausibly due to methanotrophic-recycling. When only the early Archean is considered, there is clearly no statistically significant difference between pre-GOE f_{org} and post-GOE f_{org}. Smoothing analysis confirms this result (table B.4c). However, the 95% confidence interval for the change in f_{org} between these two levels is quite large in absolute terms, and so sizeable changes in f_{org} could exist buried within the noise.

There is no statistically difference in ε between the Archean and the Proterozoic. However, this is only because the low values of ε in the early Archean cancel out the high values in the late Archean. If the late Archean and Proterozoic are compared, we find that there is a statistically significant decrease in ε to levels marginally greater than the early Archean (not shown). This is consistent with figure 3D.

Proterozoic to Phanerozoic

Both mean difference analysis (table 3D) and smoothing analysis (table B.4d) indicate that there is a statistically significant and well-constrained increase in f_{org} from the Proterozoic to the Phanerozoic. The mean absolute increase in f_{org} from the Proterozoic to the Phanerozoic is ~0.04 with a 95% confidence interval ranging from approximately 0.03 to 0.065. In short, the carbon isotope record suggests that there is a real increase in organic burial temporally correlated with the Neoproterozoic rise of oxygen. This challenges the widely held belief that the carbon isotope record doesn't support secular changes in organic carbon burial. It is unclear as to whether there is a change in ε from the Proterozoic to Phanerozoic; the different methods reported in table 3D produce conflicting results.

All the mean-difference results described above are robust to changes in data binning and filtering. If unfiltered carbon isotope data are used, then all the key results above are unchanged, except that there appears to be a statistically significant (albeit poorly constrained) increase in f_{org} from the early to late Archean. If only non-unique valued data points are binned (as opposed to 10 m.y. bins) then the key results are also unchanged, though there is some variation in confidence intervals and p-values (not shown). Adding noise to the time-axis increases the size of the confidence intervals for the mean-level change in f_{org} by approximately a factor of 2 (not shown).

Results summary

Trend analysis implies that f_{org} increased over Earth history and that the null hypothesis of constant f_{org} can be rejected. However, the magnitude of this increase has a large range. The simplest regression, OLS, which does not account for timescale uncertainty or autocorrelation, gives a mean change in f_{org} over Earth history of 1.5 (relative to 3.6 Ga), with a broad 95% confidence interval that ranges from 1.19 to 1.99 (relative to 3.6 Ga). Accounting for autocorrelation and/or timescale uncertainty widens this confidence interval. There is, however, a statistically significant increase in fractional organic burial from the Proterozoic to the Phanerozoic, and a significant increase in ε from the early Archean to late Archean which is not accompanied by a change in f_{org}. The analysis above assumes that the carbon cycle is in steady state, that the isotopic composition of outgassed carbon into the surficial reservoir is constant (-5‰), and that the simple mass balance representation of the carbon cycle in equation (AIII-2) is valid. In the next section we explore how these results change when we consider a more complex carbon cycle model.

Complex mass balance model

The mass-balance model used to calculate f_{org} in the analysis above is a simplification of the geological carbon cycle with only two isotopically distinct carbon burial sinks: organic and carbonate sediments. However, in practice there are at least two other distinct sinks, which may or may not be important: the burial of authigenic carbonates and carbonate burial via oceanic crust carbonatization (OCC). Authigenic carbonates are isotopically distinct from allogenic (sedimentary) carbonates because their carbon is primarily remineralized organic matter (Schrag et al. 2013). Oceanic crust carbonates are potentially isotopically distinct from sedimentary carbonates because the sedimentary carbonates mostly form near the surface (above the carbonate compensation depth), whereas oceanic crust carbonatization occurs at depth or below the sea floor. If there is an isotopic gradient in the dissolved inorganic carbon from the surface to the sea floor, then the two carbonate sinks will be distinct (Bjerrum & Canfield 2004). The question arises as to whether a more complex isotopic mass balance could change our results.

We can consider a modified version of the mass-balance model (eq (AIII-2)), which includes the additional isotopically distinct carbonate sinks described above. The new mass-balance equation is given by:

$$\delta^{13}C_{in} = f_{org}\delta^{13}C_{org} + (1-\alpha-\beta)(1-f_{org})\delta^{13}C_{carb} + \underbrace{\alpha(1-f_{org})\delta^{13}C_{ac}}_{authigenic\ \ fraction} + \underbrace{\beta(1-f_{org})\delta^{13}C_{OCC}}_{ocean\ crust\ \ fraction} \quad \text{(AIII-10)}$$

Here, $\delta^{13}C_{org}$ is the isotopic ratio of organic matter, $\delta^{13}C_{carb}$ is isotopic ratio of allogenic (non authigenic sedimentary) carbonates, $\delta^{13}C_{OCC} = \delta^{13}C_{carb} + \Delta S$ is the isotopic ratio of oceanic crust carbonates, and ΔS is the difference in dissolved inorganic carbon isotopic ratio between the surface ocean and the seafloor. Also, f_{org} is the fraction of carbon buried as organic carbon, α is the fraction of inorganic carbon deposited as authigenic carbonates, β is the fraction of inorganic carbon deposited during OCC, and $\delta^{13}C_{ac}$ is the isotopic ratio of authigenic carbonates. We also introduce an apparent carbonate isotopic abundance, $\delta^{13}C_{carb}^{AP}$:

$$\delta^{13}C_{carb}^{AP} = \frac{(1-\alpha-\beta)\delta^{13}C_{carb} + \alpha\delta^{13}C_{ac}\lambda}{(1-\alpha-\beta)+\alpha\lambda} \quad \text{(AIII-11)}$$

This is the isotopic composition we observe in buried carbonates, which is some weighted mixture of true allogenic carbonates and authigenic carbonates. The fraction of authigenic carbonate that are preserved in the observable rock record, λ, accounts for the fact that even though authigenic burial may be large, it might not be apparent from the isotope record if allogenic carbonates are preferentially preserved. The

range of λ is from zero to one. The denominator in equation (AIII-11) is simply the sum of the weightings to ensure normalization.

By solving these equations (5.1) and (5.2) we obtain fractional organic burial,

$$f_{org} = \frac{\delta^{13}C_{in} - (1-\alpha-\beta)\delta^{13}C_{carb} - \beta(\Delta S + \delta^{13}C_{carb}) - \alpha\delta^{13}C_{ac}}{\delta^{13}C_{org} - (1-\alpha-\beta)\delta^{13}C_{carb} - \beta(\Delta S + \delta^{13}C_{carb}) - \alpha\delta^{13}C_{ac}} \qquad \text{(AIII-12)}$$

where $\delta^{13}C_{carb} = \lambda\alpha(\delta^{13}C^{AP}_{carb} - \delta^{13}C_{ac})/(1-\alpha-\beta) + \delta^{13}C^{AP}_{carb}$ is the actual isotopic value in sedimentary carbonates only, not what is observed.

We investigated how the results of the smoothing analysis changed using this more complex carbon cycle model. The model contains five free parameters that are currently uncertain: α, λ, $\delta^{13}C_{ac}$, β, and ΔS. However it is possible to perform bootstrapping over geologically plausible parameter ranges to reconstruct probabilistic f_{org} histories. The ensemble of $\delta^{13}C^{AP}_{carb}$ and $\delta^{13}C_{org}$ curves from the LOWESS analysis in section 4.1 were used as inputs. To reconstruct f_{org} over Earth history, probability distributions for the five unknown parameters were specified and sampled along with the ensemble of smoothed curves for $\delta^{13}C^{AP}_{carb}$ and $\delta^{13}C_{org}$ to obtain a smoothed estimate of $f_{org}(t)$ with confidence intervals.

Our choice of parameter ranges is based on literature data. The difference between dissolved inorganic carbon isotopes in surface and seafloor water, ΔS, was taken to be a uniform distribution between -2‰ (modern) and 0‰. There is some evidence from seafloor basalts for constant $\delta^{13}C$ with depth in the Archean ocean (Nakamura & Kato 2004), i.e. $\Delta S \approx 0‰$, but the depth of the ocean floor carbonate used to infer this is not well constrained and so large ΔS values cannot be excluded. However, a conservative parameter range was chosen to demonstrate that a large sea floor to surface isotopic gradient is not required to considerably magnify uncertainties in f_{org}. The fraction of carbonates deposited via OCC, β, was taken to be a linear function from some unknown initial Archean value (0.3-0.9 uniform distribution) to the known present value, 0.0. The initial OCC fraction depends strongly on the composition of the Archean seafloor and our chosen parameter range is derived from theoretical estimates by Sleep and Zahnle (2001). It is not yet known whether authigenic carbonates are quantitatively important in the interpretation of the carbon isotope record. It has been argued that the fraction of authigenic carbonates was greater at some times in Earth's history than today (Schrag et al. 2013), although even the modern fraction of authigenic carbonates is not well constrained (Sun & Turchyn 2014). If there is a preservation bias against authigenic carbonates then the conventional mass balance model will not correctly predict f_{org} from the isotope record, and hence the need for the complex mass balance model described above. We are (mostly) agnostic as to whether

authigenic carbonates are quantitatively important, and simply vary the model parameters describing authigenic carbonates across plausible ranges (loosely speaking from 'authigenic carbonates negligible' to 'authigenic carbonates quantitatively important'). The fraction of authigenic carbonates, α, and the preservation rate of authigenic carbonates, λ, cannot be independently estimated from the isotope record since the carbonate time series is a product of both of these parameters. Heuristic lower bounds can arguably be put on α and λ by inspection of the isotope record; no more than ~10% of Archean data lie below the bulk-Earth composition of -5‰, although this observation does not constrain each parameter individually. Authigenic fraction α was taken to be a linear function from 0-0.3 (uniform distribution) in the Archean to 0.07-0.20 (uniform distribution) at the present. The modern value was taken from Sun and Turchyn (2014) and the Archean upper limit was an arbitrary cut-off chosen to ensure the allogenic carbonate fraction was generally non-zero (zero or near-zero allogenic carbonates is unphysical). In the absence of strong constraints the preservation fraction, λ, was sampled from a uniform distribution from 0.1-1.0. The authigenic isotopic abundance was set to a constant value of $\delta^{13}C_{ac}$=-23‰ which is the approximate modern value for organic carbon sediments (later it will be shown that results are insensitive to assumptions about $\delta^{13}C_{ac}$).

Figure 6 shows $f_{org}(t)$ with 95% confidence intervals given the parameter choices specified above. The smoothed LOWESS curve from figure 3C (simple carbon cycle model) with 95% confidence intervals is also plotted for comparison. The confidence intervals from the new model are much larger; this illustrates the capacity for uncertainties in carbon cycle processes to greatly magnify the uncertainties in organic burial. The mean linear change in f_{org} over Earth history was also evaluated using the model parameters described above and found to be a factor of 1.15 (relative to 3.6 Ga), with 95% confidence ranging from 0.29 to 2.44.

Naturally the precise parameter ranges we have chosen are somewhat arbitrary; the result above is more illustrative than definitive. It demonstrates that unless the five carbon cycle parameters can be meaningfully constrained then the carbon isotope record does not constrain either the direction or the magnitude of the change in organic burial over Earth history. The confidence interval for f_{org} in the Archean nominally extends to zero organic burial. Of course, zero organic burial is impossible since we know kerogenous sediments exist from the Archean, but this result indicates that very low fractional organic burial in the Archean cannot be entirely excluded. Alternatively, this result may indicate that the ranges we have chosen for the parameters are too generous. Whatever the explanation, the probability distributions for the change in f_{org} over Earth history have long tails extending to factors of 4 or more (see below). The sensitivity of

the uncertainty in f_{org} changes to different parameter assumptions is explored in appendix C and key findings are summarized in table 4. The remainder of this section can be skipped without loss of continuity by readers not interested in this sensitivity analysis.

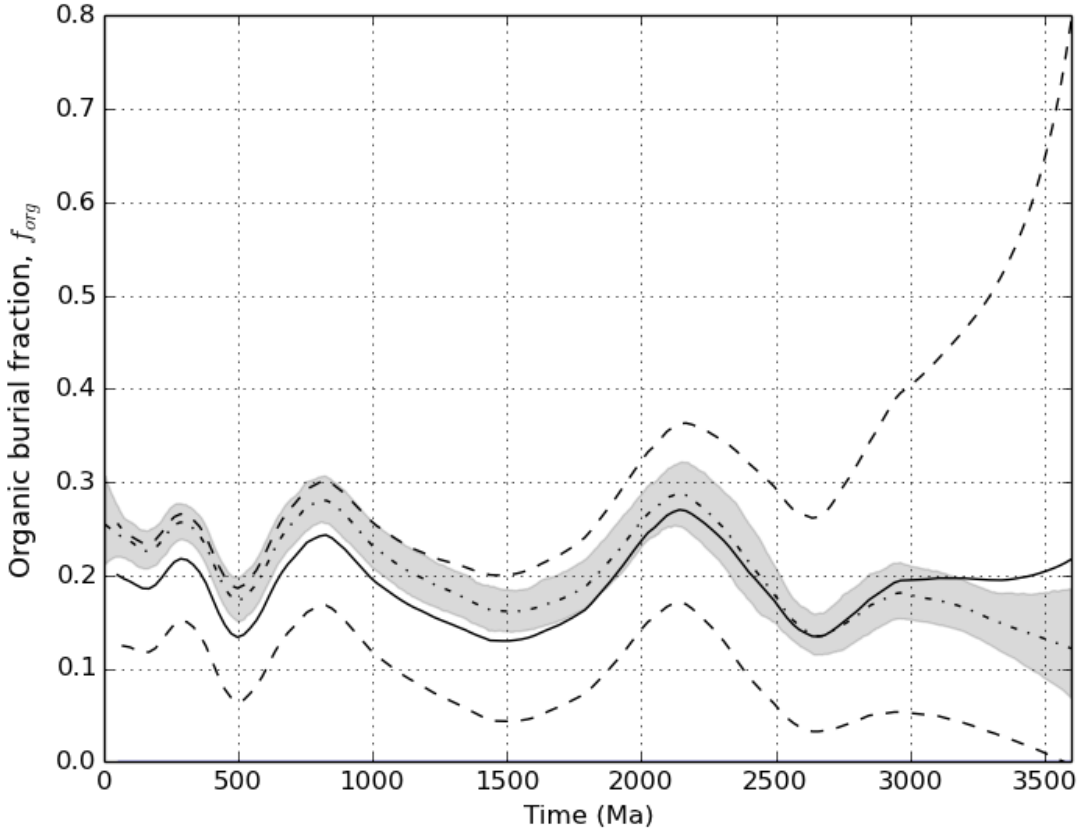

Figure 6: Smoothed f_{org} (solid line) with 95% confidence intervals (dashed lines) from the updated carbon cycle model and parameter distributions described in the main text. Smoothed f_{org} from the simple carbon cycle model using LOWESS (section 4.1) is denoted by the dot-dash line for comparison, with 95% confidence intervals shaded grey.

In table 4, each row represents one set of parameter choices, and the final two columns give the change in f_{org} over Earth history (both absolute and relative) given these parameter distributions and the ensemble of smoothed LOWESS curves for $\delta^{13}C_{org}$ and $\delta^{13}C_{carb}^{AP}$ from section 4.1. The first row (italicized) denotes the "best-estimate" parameter choices that generated figure 6. The 13th row (also italicized) denotes the parameter choices for the simple carbon cycle model that generated the smoothed LOWESS curve in figure 3C (and repeated in fig. 6). Rows 2 to 13 explore the sensitivity of the results to different parameter assumptions; where parameters have been changed from their original values in row 1 they are highlighted in bold.

In general we see that the large uncertainty in the change-in- f_{org} over Earth history is not attributable to any one parameter. In all cases except when Archean OCC fraction is low (rows 5 and 8), neither the sign nor magnitude of the change-in- f_{org} over Earth history is determinable from the carbon isotope data. The authigenic preservation parameter λ has a sizeable impact on the change-in- f_{org} confidence intervals (rows 2-4). Thus any geological observations or theoretical arguments that constrain this parameter would greatly refine our knowledge of the geological carbon cycle. Similarly, constraining the inorganic carbonate fractions α (authigenic carbonates) and β (OCC) would also dramatically reduce the uncertainty in organic burial changes (rows 5-8). Determining the magnitude of the Archean ocean isotope gradient would also be desirable, though this is of secondary importance since it seems to only extend the tail of the change-in- f_{org} distribution. Finally, the precise value for the isotopic composition of authigenic carbonates $\delta^{13}C_{ac}$ doesn't influence uncertainties very much so long as it is approximately equal to that of organic carbon.

Discussion

The precise extent to which secular changes in f_{org} of differing magnitudes can explain the rise of oxygen is beyond the scope of this study. However by considering absolute fluxes we can draw some conclusions. In steady state the total O_2 oxygen source flux (in $\text{Tmol}\,O_2/\text{yr}$ where one $\text{Tmol}=10^{12}\ \text{mol}$) due to the burial of organic matter is given by:

$$F_{O_2.carbon} = f_{org}(F_{total.carbon.burial}) = f_{org}(F_{volc+meta.CO_2} + F_{weather.CO_2}) \qquad \text{(AIII-13)}$$

Here $F_{volc+meta.CO_2}$ is the carbon outgassed into the surficial reservoir (Tmol C/yr) from volcanic and metamorphic processes, and $F_{weather.CO_2}$ is the carbon released into the surficial reservoir (Tmol C/yr) from the weathering of carbonates and organic carbon sediments. The combined term in the brackets is the total source flux of carbon into the surface reservoir, which we assume to equal total carbon burial, $F_{total.carbon.burial}$. In the discussion that follows the carbon cycle is always assumed to be in steady state.

A useful metric to conceptualize the rise of oxygen is the dimensionless K_{OXY} parameter, which is defined as the ratio of the oxygen source flux to fast and efficient oxygen sinks. The parameter excludes hydrogen escape, which is a small relative flux at the oxic transition, and oxidative weathering, which increases only afterwards (Claire et al. 2006; Kasting 2013). Thus, we specify K_{OXY} as:

$$K_{OXY} = (F_{O_2.carbon} + F_{O_2.\text{other}}) / F_{reduced} \qquad \text{(AIII-14)}$$

Here $F_{O_2.\text{other}}$ is the flux of oxygen from the burial of other reduced species such as sulfide and iron(II) oxide, and $F_{reduced}$ is the flux of outgassed reductants from volcanic and metamorphic processes in O_2 consuming equivalents ($\text{Tmol}\,O_2/\text{yr}$). The utility of K_{OXY} is illustrated by the biogeochemical model of Claire et al. (2006) of the Great Oxidation Event. In the Archean, fast and efficient oxygen sinks overwhelm the oxygen source flux from organic burial. This implies that $K_{OXY} < 1$ and that the atmosphere was anoxic. An approximate steady state was maintained by the escape of hydrogen to space. However, if the source flux increases or the sink flux decreases then atmospheric oxygen may accumulate (until oxidative weathering provides a negative feedback). If $K_{OXY} > 1$ then the oxygen source flux dominates fast and efficient oxygen sinks and the resulting atmosphere is oxic. For instance, in Claire et al. (2006) f_{org} is held constant over Earth history; the transition to an oxic state is caused by the escape of hydrogen to space, which causes a secular decline in reduced metamorphic and volcanic outgassing fluxes ($F_{reduced}$) due to the gradual oxidation of the crust. Cerium anomalies in zircons suggest that the Earth's crust has in fact become more oxidized over time; Yang et al. (2014) suggest that this oxidation proceeded until 3.6 Ga but the exact duration is uncertain due to noise in the data, and the trend seemingly continues into the late Archean. Also, inventories of total O2 equivalents in the crust that include ocean, atmosphere, sediments, and oxidized hard rocks (igneous and metamorphic) show 1.7-2.3 times as much O2 as organic carbon (Catling et al. 2001a; Hayes & Waldbauer 2006b; Sleep 2005a).

The Great Oxidation Event occurs when K_{OXY} transitions from being less than unity to greater than unity. Today, $K_{OXY} \approx 6$, which indicates an oxic atmosphere (Claire et al. 2006; Kasting 2013). Kasting (2013) adopted K_{OXY} as a simple means of exploring the capacity of different hypotheses to explain the Great Oxidation Event: K_{OXY} was calculated for different assumptions about source/sink fluxes in the Archean (relative to modern fluxes) to see if such changes are capable of implying $K_{OXY} < 1$ in the Archean. If the conjectured fluxes in the Archean do not ensure $K_{OXY} < 1$, then the hypothesis cannot explain the Great Oxidation Event since they would predict that Earth always had an oxic atmosphere.

We adopt the approach of Kasting (2013) to explore whether changes in f_{org} can explain the rise of oxygen. For the modern day fluxes, let us take $F_{O_2.carbon} = 10 \pm 3.3\,\text{Tmol}\,O_2/\text{yr}$, $F_{O_2.\text{other}} = 5.15 \pm 1.4\,\text{Tmol}\,O_2/\text{yr}$, and $F_{reduced} = 2.4 \pm 1.8\,\text{Tmol}\,O_2/\text{yr}$ from Holland (2002). Note that our numbers are slightly different to previous studies because there is an error in the stoichiometric coefficients in row 2, Table A2 of Holland (2002), which has propagated through the literature. Using corrected flux values we find $K_{OXY}(\text{modern}) = (10 + 5.15)/2.4 = 6.3$ with a 95% confidence interval from 3.3 to 22.3. Thus even if we take

the lower end of the 95% confidence interval of $K_{OXY}(\text{modern})$ and generously assume that $F_{O_2.\text{other}}$ scales with f_{org} in the same way that $F_{O_2.carbon}$ scales, then a doubling of f_{org} over Earth history – the upper bound of the 95% confidence interval from our statistical analysis – implies that $K_{OXY}(Archean) = 0.5 \times 3.3 \geq 1$. Evidently a secular increase in organic burial cannot on its own explain the Great Oxidation Event. This is consistent with the mean-difference analysis that indicated no statistically significant difference between f_{org} in the early Archean and middle Proterozoic. The only caveat on this result is that exceptionally large changes in f_{org} (increases by a factor of a few) are not completely ruled out with the more complicated carbon cycle model in section 5.

However, merely changing f_{org} and holding all other fluxes constant is an unrealistic scenario. The total volcanic outgassing on the early Earth was probably 3-5 times larger than the present flux due to greater heat flow from the interior (Sleep & Zahnle 2001). The overall effect on K_{OXY} of elevated carbon outgassing - and therefore total burial - is partially offset by the corresponding increase in reductant outgassing. However if we assume $F_{volc+meta.CO_2}$ and $F_{reduced}$ are scaled by the same amount for a given increase in total outgassing, then there is still a change in K_{OXY} since presumably $F_{weather.CO_2}$ does not have the same scaling. Additionally, the input of carbon from organic weathering would have been lower in the Archean due to diminished oxidative weathering in anoxic conditions and carbonate weathering may have also been lower if continental size was smaller. Thus total organic and carbonate weathering, $F_{weather.CO_2}$, was likely lower in the Archean than today (Bekker & Holland 2012; Flament et al. 2008).

To explore whether changes in f_{org} could explain the rise of oxygen given these more realistic flux assumptions we calculated an Archean K_{OXY} using the following expression: f_{org}

$$K_{OXY}(\text{Archean}) = \frac{f_{org} F_{total.carbon.burial} + F_{O_2.\text{other}}}{MF_{reduced}} = \frac{f_{org}(MF_{volc+meta.CO_2} + WF_{weather.CO_2}) + F_{O_2.\text{other}}}{MF_{reduced}} \quad \text{(AIII-15)}$$

Here M (dimensionless) is the total outgassing in the Archean relative to modern levels, and W (dimensionless) is the weathering of carbonate and organic sediments in the Archean as a fraction of the modern flux. Given that the total modern carbon burial rate is ~50 Tmol C/yr (Berner 2004; Holland 2002), and that the carbon cycle is in steady state, this implies $F_{volc+meta.CO_2} + F_{weather.CO_2} = 50$ Tmol C/yr . Furthermore, since $F_{volc+meta.CO_2}$ must equal the silicate weathering rate (modern value ~10 Tmol C/yr), we partitioned the

modern carbon source fluxes by $F_{volc+meta.CO_2} = 10$ Tmol C/yr and $F_{weather.CO_2} = 40$ Tmol C/yr. All other variables were unchanged from their modern values.

Figure 7 shows Archean K_{OXY} as a function of M and W assuming a doubling of f_{org} over Earth history. We observe that for low Archean weathering fluxes and higher total outgassing rates, there are regions of parameter space with Archean $K_{OXY} < 1$, thus implying that a doubling of f_{org} over Earth history could explain the rise of oxygen. For instance if $M = 2$ then the Archean carbonate and organic weathering flux, W, must be less than 0.31 to ensure an anoxic Archean atmosphere ($K_{OXY} < 1$). Note that it is possible for M to increase and W to decrease because the weathering term only includes carbonate and organic weathering and not silicate weathering; the carbon cycle is in steady state by assumption. In contrast, if the increase in f_{org} over Earth history is only 1.2 relative to 3.6 Ga, the lower limit of our 95% confidence interval, then there is no region in this parameter space with $K_{OXY} < 1$. The inability of a factor of 1.2 increase in f_{org} to explain the rise of oxygen is not because the integrated O_2 imbalance is too small (it is not), but rather because such a modest change in the oxygen source flux would imply an oxic Archean atmosphere unless Archean O_2 sink fluxes were larger than today. This illustrates that given the uncertainty in f_{org} over Earth history it is difficult to evaluate whether changes in f_{org} constitute an important contribution to the rise of oxygen when other fluxes are changing. This uncertainty arises from noise inherent to the isotope record, and not from uncertainty in our interpretations. Similar conclusions are obtained if we consider changes in the reductant flux in combination with f_{org} increases. This result ignores the sizeable uncertainties in the modern fluxes, and unrealistically assumes that the burial flux from sulfides and iron(II) oxide has remained constant, although similar results are obtained if the burial flux from other reduced species scales with f_{org}, or if $F_{O_2.\text{other}} = 0$ in the Archean.

Evidently to make progress we require better constraints on the absolute O_2 source and sink fluxes through time, which includes the contribution to carbon input from the weathering flux of carbonates and organics on the early Earth (equation 6.1). The weight percent of organic carbon and carbonates in modern, globally averaged sedimentary rocks is consistent with $f_{org} \approx 0.2$ (Li 2000). This suggests that organic content could be used to inform total burial rates through time. However the rock record is too incomplete to provide global averages for the weight percent of organic carbon in Precambrian sedimentary rocks. The weight percent of organics in Archean and Proterozoic shales is within a factor of 2-3 of that of Phanerozoic shales (Holland 1984). From our organic carbon data set, the weight percent organic content of Archean sedimentary rocks (3.59%) is indistinguishable from that of Proterozoic sedimentary rocks (3.56%), and

Lyons et al. (2014) showed the cumulative distribution of total organic content in organic rich Archean sedimentary rocks is identical to that of Neogene rocks. Thus assuming that sedimentation rates have not changed markedly this would imply the total rate of organic carbon burial also hasn't changed dramatically. However it is difficult to be quantitative about this constraint given the absence of globally averaged sedimentary rock organic content for the Archean; modest changes in the total burial flux of less than an order of magnitude probably cannot be ruled out by sedimentary organic concentrations. Even these modest changes in absolute fluxes could have dramatic implications for the surficial redox balance. Figure 7 and the discussion above demonstrate that relatively small changes in carbonate and organic weathering (or total outgassing) can affect whether changes in fractional organic burial can trigger surface oxidation. Thus, even if the conventional mass balance model of the carbon cycle is accepted, the redox implications of the carbon isotope record will be ambiguous until these absolute fluxes are more tightly constrained.

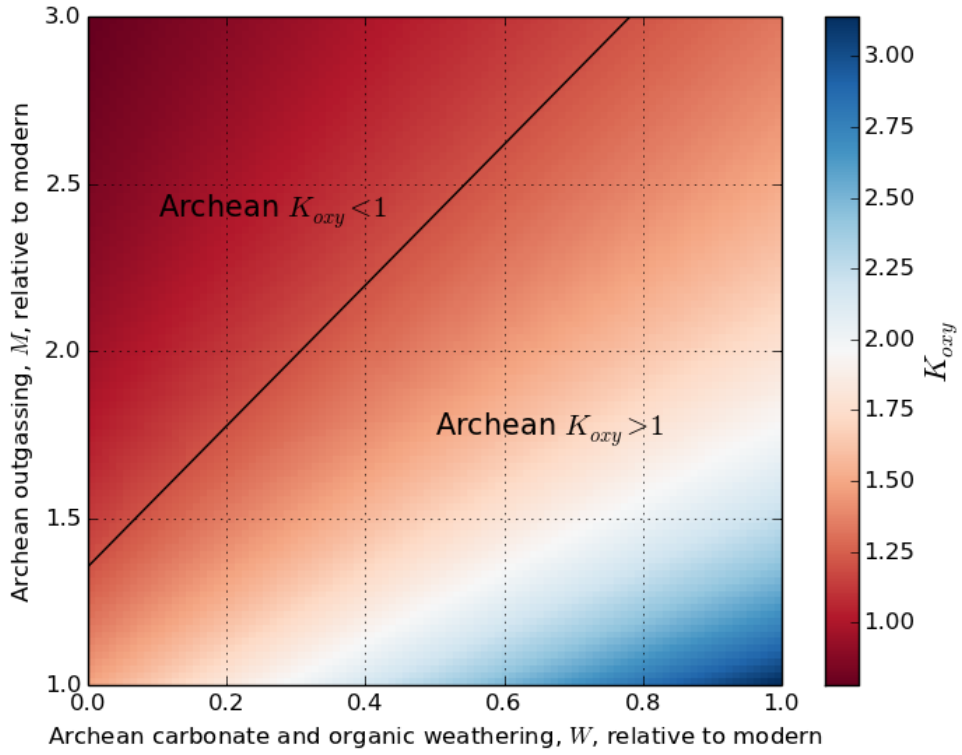

Figure 7: Archean K_{OXY} as a function of Archean carbonate plus organic weathering plotted as a fraction, W, of the modern flux, and total Archean outgassing plotted as a scalar multiple, M, of the modern flux. This plot assumes a doubling of f_{org} from the Archean to the modern Earth. The black line denotes $K_{OXY} = 1$, the cross-over from anoxic to oxic atmospheres. Regions above the line predict an anoxic Archean atmosphere and could potentially explain the rise of oxygen ($K_{OXY} < 1$), whereas regions below the line predict an oxic Archean atmosphere and cannot explain the rise of oxygen ($K_{OXY} > 1$). If the same figure is plotted for a factor of 1.2 increase in f_{org} over Earth history, then Archean $K_{OXY} > 1$ everywhere.

Our analysis also neglects the oxygen source flux from other biogeochemical cycles. Microbial reduction of sulfate and subsequent burial of sulfide is a sizeable source of oxygen on the modern Earth (Berner 2004; Holland 2002). The rise of oxygen could be better understood if fluxes of sulfur were constrained, but this is challenging because unlike the carbon cycle, the sulfur cycle is not in mass balance through the Proterozoic and so sulfur isotopes are of less utility for determining fractional sulfide burial (Canfield 2004).

Although the carbon isotope record is too noisy to determine whether changes in organic burial can explain the transition from an anoxic to oxic atmosphere, our analysis does indicate a permanent increase in organic burial coincident with the Neoproterozoic rise of oxygen. This is broadly consistent with previous analyses of the carbon isotope record (Des Marais et al. 1992; Jiang et al. 2010), and with mineralogical, tectonic and biological arguments for enhanced Neoproterozoic organic burial (Lenton et al. 2014). For instance, elevated phosphorus delivery (Planavsky et al. 2010), the breakup of the supercontinent Rodinia (Knoll et al. 1986) and biological innovations (Logan et al. 1995) have all been suggested as possible explanations for enhanced organic burial in the Neoproterozoic. Naturally, this increase in fractional organic burial from the Proterozoic to the Phanerozoic is not necessarily the cause of the Neoproterozoic rise of oxygen. We have not quantitatively evaluated whether this enhanced organic burial that could explain the Neoproterozoic rise of oxygen, or even whether the timing is consistent with it being a cause or effect of the rise. Laakso and Schrag (2014)'s model of the Neoproterozoic rise of oxygen implicates an increase in fractional organic burial, and is thus qualitatively consistent with the carbon isotope record. However, their model requires changes in fractional organic burial well in excess of the upper limit of our confidence interval for the change in fractional organic burial from the Proterozoic to the Phanerozoic (assuming the conventional mass balance model is correct).

Our analysis suggests that changes in the carbon isotope record from the early to late Archean are best explained by changes in biological fractionation between inorganic and organic carbon, and not by changes in fractional organic burial, given that the latter is not statistically significant. This is consistent with previous studies that attributed strongly negative late Archean $\delta^{13}C_{org}$ values to the recycling of organic carbon by methanotrophs (Hayes 1994; Hayes & Waldbauer 2006b; Hinrichs 2002). In anoxic sediments, isotopically depleted methane produced by fermentation is converted to biomass by methanotrophs; the resultant organic carbon may be extremely depleted relative to carbonates, with $\delta^{13}C_{org}$ as low as -60‰ (Hayes 1994). Our analysis also indicates that ε declined from the late Archean to the Proterozoic, which suggests methanotrophic recycling was pushed deep into the sediments due to increasingly oxidizing conditions following the great oxidation event (Fallick et al. 2008; Hayes 1994). Methanotrophy requires

either molecular oxygen or oxygen-derived electron acceptors such as sulfates (Hinrichs 2002). There would have been some abiotically produced sulfate in the Archean atmosphere due to photochemical oxygen production in the upper atmosphere. However, the low partial pressure of oxygen makes this abiotic source an unlikely electron acceptor for the apparent pulse of methanotrophy observed in the globally integrated carbon isotope record. It is more likely that oxygenic photosynthesis produced the abundant electron acceptors that enabled methanotrophic recycling in the late Archean. This ostensible menthanotrophic transition occurs at 2.8 Ga which suggests the evolutionary origin of oxygenic photosynthesis is at least this ancient. This statistical argument supports molybdenum isotope analysis which also indicates an early origin of oxygenic photosynthesis (Planavsky et al. 2014a).

Conclusions

- Analyses invoking a conventional carbon isotope mass balance model imply that fractional organic burial, f_{org}, has increased over Earth history by around 0.08 (factor of 1.5 increase relative 3.6 Ga), but with a large 95% confidence interval extending from about 0.03 to 0.13 (factor of 1.2-2.0 increase relative to 3.6 Ga).

- The carbon isotope record does not constrain the history of organic burial well enough to evaluate whether changes in fractional organic burial can explain the rise of oxygen. Uncertainties in absolute fluxes such as total outgassing and the weathering of carbonates and organics, coupled with uncertainties in the fractional organic burial change imply that the carbon isotope record neither supports nor negates the hypothesis that secular changes in organic burial were responsible for the oxidation of the surface environment.

- There is a well constrained and permanent increase in organic burial temporally correlated with the Neoproterozoic oxygenation event.

- Analysis of the difference between carbonate and organic carbon isotope ratios, ε, implies a statistically significant increase in ε from the early to late Archean. This shift is consistent with enhanced biological fractionation due to methanotrophic recycling, which in turn could indicate that oxygenic photosynthesis evolved 2.8 Ga or earlier.

- All of the conclusions above are derived assuming a conventional mass balance model of the carbon cycle. When authigenic carbonates and ocean crust carbonatization are included in a more complex carbon cycle model, the utility of the carbon isotope record for reconstructing the fractional burial of organic carbon is dramatically limited. If these processes are important, then the various parameters describing the burial of allogenic, authigenic and carbonatization carbonates (see section 5) must be independently determined and specified before the carbon isotope record can be used to constrain the history of organic burial and oxygen production

Appendix A: Algorithms

A.1) Classical Generalized Least Squares (GLS) fit algorithm.

This is the algorithm for method II in the main text. This algorithm closely follows Mudelsee (2010), Chapter 4, p122. We start with either the carbonate or organic carbon isotope time series data, $\{t(i), x(i)\}_{i=1,\ldots,n}$ where t is time and x is the carbon isotope value for point i.

1) Make an initial guess for the persistence time, τ, and the variability in the noise, V. These variables are defined in the main text.

2) Calculate the covariance matrix, $\mathbf{C}$:

- $$C(i,j) = V^2 \times \exp(-|t(i) - t(j)| / \tau) \qquad \text{(AIII-16)}$$

Here $i = 1,\ldots n \quad j = 1,\ldots n$ index the n data points in the time series, and $t(i)$ is the radiometric age of the i th carbon isotope data point.

3) Perform the GLS regression:

- $$\mathbf{B} = \left(\mathbf{T}^T \mathbf{C}^{-1} \mathbf{T}\right)^{-1} \mathbf{T}^T \mathbf{C}^{-1} \mathbf{x} \qquad \text{(AIII-17)}$$
- Where $\mathbf{B} = \begin{pmatrix} B_0 \\ B_1 \end{pmatrix}$, $\mathbf{x} = \begin{pmatrix} x(1) & \ldots & x(n) \end{pmatrix}^T$ and $\mathbf{T} = \begin{pmatrix} 1 & \ldots & 1 \\ t(1) & \ldots & t(n) \end{pmatrix}^T$
- Here $x(i)$ is the i th carbon isotope value, corresponding to time $t(i)$. B_0 and B_1 are the fitted linear regression parameters, intercept and gradient, respectively. Superscript T denotes matrix transpose.
- 4) Update V using the GLS parameters:
- $$V = \sum_{k=1}^{n} \left(x(k) - B_1 \times t(k) - B_0\right)^2 \Big/ (n-2) \qquad \text{(AIII-18)}$$
- Use equation (AIII-16) to update the covariance matrix using the new V. The new autocorrelated residuals $r(i)$ can be found using:
- $$r(i) = \left(x(i) - B_1 \times t(i) - B_0\right) / V \qquad \text{(AIII-19)}$$

$r(i)$ is the fitted $X_{noise}(i)$ in equation (3.4) in the main text. Substitute $r(i)$ into equation (3.3) in the main text and minimize the sum of the squares to find the best-fit τ.

5) Perform GLS regression on the original data (step 3) but using the new fitted parameters, τ, V and $C(i,j)$. Repeat steps 3-5 until converged, i.e. B_0 and B_1 are not changing after each iteration. The B_0 and

B_1 obtained at convergence are the best-fit regression parameters. The variance in these parameters (Gaussian uncertainties by assumption) is given by:

- $$\mathrm{Var}(\mathbf{B}) = \left(\mathbf{T}^T V^{-1} \mathbf{T}\right)^{-1} \quad \text{(AIII-20)}$$

A.2) GLS bootstrap algorithm

This is the algorithm for method III, section 3.2.2 in the main text. This algorithm closely follows Mudelsee (2010), Chapter 4, p. 123. We start with either the carbonate or organic carbon isotope time series data, $\{t(i), x(i)\}_{i=1,\ldots,n}$.

1) Perform steps 1-5 from method II.

2) For convenience define the autocorrelation parameter:

- $$\hat{a}(i) = \exp(-[t(i) - t(i-1)] / \tau) \quad \text{(AIII-21)}$$

Convert correlated residuals, $r(i)$, (eq (AIII-19)) to uncorrelated, $\varepsilon(i)$, as follows:

- $$\varepsilon(i) = \left(r(i) - r(i-1) \times \hat{a}(i)\right) \times (1 - \hat{a}(i)^2)^{-0.5} \quad \text{(AIII-22)}$$
- 3) Center on zero mean to obtain uncorrelated white noise residuals:
- $$\overline{x}_{noise}(i) = \varepsilon(i) - \sum_{i=2}^{n} \varepsilon(i) / (n-1) \quad \text{(AIII-23)}$$

4) Resample (with replacement) from these white noise residuals.

- $$\{\overline{x}_{noise}(i)\} \rightarrow \{\overline{x}^*_{noise}(i)\} \quad \text{(AIII-24)}$$

5) Invert step 2 to obtain resampled correlated residuals, $r^*(i)$:

- $$r^*(i) = \hat{a}(i) \times r^*(i-1) + \overline{x}^*_{noise}(i) \times (1 - \hat{a}(i)^2)^{-0.5} \quad \text{(AIII-25)}$$

6) Add the best-fit gradient from step 1 to resampled correlated residuals in step 5:

- $$\overline{x}^*(i) = B_0 + B_1 \times t(i) + V \times r^*(i) \quad \text{(AIII-26)}$$

7) Calculate GLS regression for $\overline{x}^*(i)$ using τ, V and $C(i, j)$ obtained from step 1. The gradient and intercept from this final fit are added to the probability distributions for these parameters. Return to step 4 and resample again until the probability distributions converge.

The GLS code was verified by artificially setting the persistence time, τ, to 0.0001 to check that GLS and OLS confidence intervals converged. Additionally, classical GLS and GLS bootstrap produce identical results for AR(1) test data.

A.3) Mean difference algorithm

This is the algorithm for method II, section 3.2.3 in the main text. This algorithm is virtually identical to Algorithm (A.1) above, except that a zero gradient is imposed on the regression.

1) Define two intervals of interest for comparison (e.g. 1.8-1.0 Ga and 3.8-2.5 Ga), and choose either the organic or carbonate data set, $\{t(i), x(i)\}_{i=1,\ldots,n}$. For the data points in each interval do the following:

2) Make an initial guess for the persistence time τ and the variability in the noise V. Calculate the covariance matrix, $\mathbf{C}$, as before:

- $$C(i, j) = V^2 \times \exp(-|t(i) - t(j)| / \tau) \qquad \text{(AIII-27)}$$

3) Calculate the GLS regression where the only fitted parameter is the mean level (gradient specified as zero).

- $$\mathbf{B} = \left(\mathbf{T}^T \mathbf{C}^{-1} \mathbf{T}\right)^{-1} \mathbf{T}^T \mathbf{C}^{-1} \mathbf{x} \qquad \text{(AIII-28)}$$

Here $\mathbf{B} = (B_0)$ is the fitted mean level, $\mathbf{x} = (x(1) \quad \ldots \quad x(n))^T$ and $\mathbf{T} = (1 \quad \ldots \quad 1)^T$

4) Use the best fit mean-level, B_0, to update the variability term (AIII-29) and then the covariance matrix (AIII-27).

- $$V = \sum_{k=1}^{n} \left(x(k) - B_0\right)^2 / (n - 2) \qquad \text{(AIII-29)}$$

5) Find the correlated residuals:

- $$r(i) = \left(x(i) - B_0\right) / V \qquad \text{(AIII-30)}$$

6) Update the persistence time τ by substituting the correlated residuals into equation (3.3) in the main text, setting $x_{noise}(i) = r(i)$.

7) Calculate the GLS regression with the original data using the new fitted parameters, τ, V and $C(i, j)$. Repeat steps 3-7 until convergence i.e. B_0 unchanging after each iteration.

8) Given the best-fit mean-level, correlated residuals and variability term, perform the following:

a) Define the autocorrelation parameter:

$$\hat{a}(i) = \exp(-[t(i) - t(i-1)] / \tau)$$

b) Calculate uncorrelated residuals

$$\varepsilon(i) = \left(r(i) - r(i-1) \times \hat{a}(i)\right) \times (1 - \hat{a}(i)^2)^{-0.5}$$

c) Center on zero mean to obtain uncorrelated white noise residuals:

$$\overline{x}_{noise}(i) = \varepsilon(i) - \sum_{i=2}^{n} \varepsilon(i) / (n-1)$$

d) Resample uncorrelated residuals

$$\{\overline{x}_{noise}(i)\} \rightarrow \{\overline{x}^*_{noise}(i)\}$$

e) Invert step (8b) to obtain resampled correlated residuals, $r^*(i)$:

$$r^*(i) = \hat{a}(i) \times r^*(i-1) + \overline{x}^*_{noise}(i) \times (1 - \hat{a}(i)^2)^{-0.5}$$

f) Add the best-fit mean-level from step 7 to the resampled correlated residuals in step (8e):

$$\overline{x}^*(i) = B_0 + V \times r^*(i)$$

g) Calculate the GLS regression for $\overline{x}^*(i)$ using the τ, V and $C(i, j)$ obtained from step 7. The mean-level from this final fit is added to the probability distribution for this parameter. Return to step (8d) and resample again to build up the probability distribution.

A.4) Modifications to algorithms to account for timescale uncertainty

Here we briefly summarize the modifications made to methods I, II and III in section 3.2.2 (algorithms A.1 and A.2 above) to account for timescale uncertainty. See section 4.2.2 in the main text for an explanation of timescale uncertainty.

I) To adapt OLS regression to timescale uncertainty we took a heuristic approach. The Gaussian distributions for each regression parameter were sampled for each time-uncertain realization to generate an overall probability distribution for each parameter.

II) Gaussian noise was added to time values prior to step 1 and carbon isotope values were re-ordered accordingly. Gaussian distributions obtained at step 5 are sampled, and the algorithm was repeated for different time-uncertainty realizations to generate an overall uncertainty distribution for each parameter.

III) Gaussian noise was added to time values prior to step 1 and carbon isotope values were re-ordered accordingly. At step 7, rather than return to step 4 to resample carbon isotope values, we instead returned to step 1, added Gaussian noise to the original time values, and repeat the entire algorithm to generate probability distributions for regression parameters (this is computationally intensive).

For mean difference methods (section 3.2.3, Algorithm A.3 above), the algorithms were modified to account for time-scale uncertainty in a way identical to how the regression algorithm was modified. Gaussian noise was added to the time values at the start of the algorithm, and for each iteration these were resampled and the entire algorithm was repeated.

Appendix B: Additional Results

B.1) Sensitivity of regression results to data selection and filtering assumptions

Table B.1 gives the change in f_{org} over Earth history from parametric analysis methods if the Phanerozoic data are excluded. Table B.2 compares the change in f_{org} over Earth history from both parametric and non-parametric smoothing methods for filtered (all results in main text) and unfiltered data. Data filtering is described in section 2 in the main text. Generally speaking, the effect of filtering is to reduce the mean change in f_{org} over Earth history. This is unsurprising since by filtering we are excluding extreme values from unrepresentative and/or non-primary samples (e.g. lacustrine settings, BIFs etc.). Confidence intervals from unfiltered data are generally larger, and the change in f_{org} over Earth history is even less well constrained, which is also unsurprising for the same reasons.

B.2) Sensitivity of mean-difference results to filtering

Table B.3 summarizes the mean-difference result for unfiltered data using parametric methods. These results are analogous to table 3 in the main text. In general, there are only minor difference between the unfiltered results below and the filtered results in the main text.

B.3) Mean difference results from smoothing analysis and comparison with parametric results

Table B.4 compares the (filtered data) mean-difference results for non-parametric smoothing methods and parametric regression techniques. The non-parametric smoothing analysis was performed using a white noise model with zero timescale uncertainty, 10 my binning and 10,000 iterations bootstrapping. These results are summarized in section 4.3 in the main text.

B.4) Sensitivity of results to diagenetic modification of organics

The effects of non-random diagenetic modification of organic carbon were briefly investigated. Des Marais et al. (1992) corrected organic carbon data using H/C ratios as a proxy for diagenetic modification; older samples generally show more evidence for diagenetic modification and so this correction results in an increasing trend in $\delta^{13}C_{org}$ compared to the uncorrected data. H/C ratios are unavailable for the majority of new data, and so the effects of diagenetic modification were investigated by artificially adding a trend to

the organic carbon isotope series of -2‰ over Earth history. This had the effect of marginally increasing the change in f_{org} over Earth history given the simple carbon cycle model (e.g. factor of 1.76 increase with confidence interval 1.47 to 2.13 compared to a factor of 1.64 increase confidence interval 1.32 to 2.04 for uncorrected LOWESS smoothing). Similarly, using the updated carbon cycle model with standard parameters and the -2‰ correction for diagenetic changes does not modify the f_{org} increase over Earth history greatly (e.g. factor of 1.23 increase with confidence interval 0.3 to 2.61 compared to a factor of 1.15 increase with confidence interval 0.29 to 2.44 for uncorrected data). However it should be noted that this *ad hoc* correction does not fully replicate the corrections made for diagenetic modifications in Des Marais et al. (1992) where extremely low H/C ratio samples are discarded, in addition to correcting those that remained.

Appendix C: Sensitivity analysis for complex carbon cycle model

This section reports the sensitivity of the complex carbon cycle results in section 5 to different assumptions about parameter ranges. If authigenic carbonates are ignored ($\alpha = 0$) then decreasing OCC over time (decreasing $\beta(t)$) will result in an increase in f_{org} if there is a non-zero isotopic gradient in the oceans, ΔS (Bjerrum & Canfield 2004). However, the magnitude of the f_{org} increase is slight for $\Delta S = -2$ ‰.

If the OCC fraction is ignored ($\beta = 0$) and preservation of authigenics is imperfect relative to allogenic carbonates ($\lambda < 1$) then decreasing the authigenic fraction over time will also result in an increasing f_{org}. This can be understood as follows: if $\lambda = 1$ then f_{org} is unchanged compared to the simple two-sink model since there is effectively no isotopically distinct carbonate sink that isn't being captured by the well-mixed isotope record. However if $\lambda < 1$ and the authigenic fraction was larger in the past, then the true $\delta^{13}C$ of all carbonates that were buried in the past must have been lower than the isotope record suggests (the further back in time we go, the greater the amount of isotopically light carbonates that aren't captured in the geological record). This implies that f_{org} was lower in the past than the simple two-sink model would suggest, and has in fact been increasing over time. The magnitude of this effect is small for λ close to 1, but increases substantially for small λ.

When both OCC and authigenic carbonates are considered together, their effects on the history of f_{org} are more complex and counterintuitive. In particular, if there is some non-zero but fixed fraction of authigenic carbonates, then increasing β can in fact increase f_{org} contrary to what was described above. This is true even if the ocean isotope gradient is zero. The reason for this behavior is that there is no large change in the apparent carbonate record, $\delta^{13}C_{carb}^{AP}$, over Earth history. Hence as the OCC fraction is increased, $\delta^{13}C_{carb}$

must increase to maintain the equality in equation (5.2) in the main text. In other words holding the authigenic fraction fixed whilst decreasing OCC implies the ratio of authigenic carbon to allogenic carbonates is changing, which in turn leads to an increase in f_{org}. A similar counterintuitive result arises if OCC is fixed at some non-zero constant and the authigenic fraction is decreasing (it is possible to get a decrease in f_{org}). Whether such changes in fractional carbonate burial are physically plausible is unclear, but they demonstrate the possible ranges in behavior if carbon cycle parameters are unconstrained. They also help explain some of the counterintuitive results in the sensitivity analysis (table 4, main text). For instance the increase in f_{org} over Earth history is larger in row 5 than row 6 despite the only change being that the decrease in β is larger for row 6. This seemingly backwards result can be explained by the considerations above.

Appendix IV - Curriculum Vitae

Joshua Krissansen-Totton
Department of Earth and Space Sciences/Astrobiology Program
University of Washington, Seattle, WA
joshkt@uw.edu

Education and Qualifications

- **University of Washington, Seattle, WA**. PhD candidate, Department of Earth and Space Sciences / Astrobiology Program, September 2013 – present.
- **The University of Auckland, New Zealand**. BSc(Hons) in physics, awarded with First Class Honours, March 2012 - November 2012.
- **The University of Auckland, New Zealand.** BSc in physics and mathematics, BA in economics, March 2008 – November 2011.

Peer-Reviewed Publications and Book Chapters

- **Krissansen-Totton, J.**, R. Garland, P. Irwin & D. C. Catling (2018). Detectability of biosignatures in anoxic atmospheres with the James Webb Space Telescope: A TRAPPIST-1e case study, *The Astronomical Journal*, 156, 3, DOI:10.3847/1538-3881/aad564.

- **Krissansen-Totton, J.**, G. Arney, D. C Catling (2018). Constraining the climate and ocean pH of the early Earth with a geological carbon cycle model, *Proceedings of the National Academy of Sciences USA*, DOI:10.1073/pnas.1721296115.

- Sholes, S., **J. Krissansen-Totton**, D. C. Catling (2018). A Maximum Subsurface Biomass on Mars from Untapped Free Energy: Carbon Monoxide as an Anti-biosignature, *Astrobiology,* DOI: 10.1089/ast.2018.1835.

- **Krissansen-Totton, J.**, S. Olson, D. C Catling (2018). Disequilibrium biosignatures over Earth history and implications for detecting exoplanet life, *Science Advances*, 4, eaao5747. DOI:10.1126/sciadv.aao5747.

- Catling, D. C., **J. Krissansen-Totton**, N. Y. Kiang, D. Crisp, T. D. Robinson, S. DasSarma, A. Rushby, A. Del Genio, W. Bains, S. Domagal-Goldman (2018). Exoplanet biosignatures: A framework for their assessment, *Astrobiology*, 18, 709-738, 2018. DOI:10.1089/ast.2017.1737

- **Krissansen-Totton, J.** and D. C. Catling (2017). Constraining climate sensitivity and continental versus seafloor weathering using an inverse geological carbon cycle model, *Nature Communications,* DOI:10.1038/NCOMMS15423.

- **Krissansen-Totton, J.** and D. C. Catling (2017), The Search for another Earth and life elsewhere. In *What is Life? On Earth and Beyond* (Ed. A. Losch), Cambridge Univ. Press. E-print available here.

- **Krissansen-Totton, J.**, E. W. Schwieterman, B. Charnay, G. Arney, T. D. Robinson, V. Meadows, D. C. Catling (2016). Is the Pale Blue Dot unique? Optimized photometric bands for identifying Earth-like exoplanets. *The Astrophysical Journal* 817 (1), 31.

- **Krissansen-Totton, J.,** D. Bergsman, D. C. Catling (2016), On detecting biospheres from chemical thermodynamic disequilibrium in planetary atmospheres, *Astrobiology*, 16, 39-67.

- **Krissansen-Totton, J.**, R. Buick, D. C. Catling (2015). A statistical analysis of the carbon isotope record from the Archean to Phanerozoic and implications for the rise of oxygen, *American Journal of Science*, 315 (4), 275-316.

- Misra, A., **J. Krissansen-Totton**, M. C. Koehler, S. Sholes (2015). Transient sulfate aerosols as a signature of exoplanet volcanism, *Astrobiology*, 15(6), 462-477.

- **Krissansen-Totton, J.**, and R. Davies (2013), Investigation of cosmic ray–cloud connections using MISR, *Geophys. Res. Lett*., 40, 5240–5245.

White papers

- **Krissansen-Totton, J.**, Arney, G.N., Catling, D.C., Felton, R., Fortney, J., Garland, R., Irwin, P., Kopparapu, R., Lehmer, O., Lustig-Yaeger, J., Meadows, V., Molaverdikhani, K., Olson, S., Schwieterman, E., Taylor, J. (2019) Atmospheric disequilibrium as an exoplanet biosignature: Opportunities for next generation telescopes. *White Paper submitted to the National Academies of Sciences Astronomy and Astrophysics 2020 Decadal Survey*.

- Berdyugina S. V., Kuhn, J.R., Langlois, M., Moretto, G., **Krissansen-Totton, J.**, Grenfell, L., Catling, D., Santl-Temkiv, T., Finster, K., Tarter, J., Shostak, S., Marchis, F., Hargitai, H., Apai, D. (2018) The Exo-Life Finder (ELF) Telescope: New Strategies for Exoplanet Direct Detection, Biosignatures and Technosignatures, SPIE, Proceedings Volume 10700. Ground-based and Airborne Telescopes VII; 107004I.

Conference proceedings and talks

- Krissansen-Totton, J. (February 2019). Disequilibrium biosignatures in exoplanet atmospheres: early Earth analogs, detectability with next generation telescopes, and implications for instrument design. *NASA Goddard Large UV, Optical, InfraRed Surveyor (LUVOIR) Telescope Seminar* (invited talk).

- Catling, D.C. and Krissansen-Totton, J. (February 2019). Finding life on exoplanets from its imprint on atmospheric composition. *University of Washington, Department of Atmospheric Sciences Seminar* (invited talk).

- Krissansen-Totton, J. (December 2018). Disequilibrium biosignatures in exoplanet atmospheres and their detectability with the James Webb Space Telescope. *University of California, Santa Cruz, Other Worlds Laboratory, Planetary Lunch Seminar* (invited talk).

- Krissansen-Totton, J. (November 2018). The search for life elsewhere: Leveraging chemical disequilibrium metrics and Earth system science to anticipate exoplanet biosignatures. *University of Chicago, Department of Geophysical Sciences Seminar* (invited talk).

- Krissansen-Totton, J. (August 2018). Novel approaches to exoplanet life detection: Disequilibrium biosignatures and their detectability with the James Webb Space Telescope. *International Astronomical Union 30th General Assembly.* Vienna, Austria (talk).

- Krissansen-Totton, J., S. Olson, R. Garland, P. Irwin and D. C. Catling (August 2018). Disequilibrium biosignatures on the early Earth and their detectability with the James Webb

Space. *Goldschmidt*, Boston, MA (talk).

- Krissansen-Totton, J. (July 2018). Disequilibrium biosignatures in exoplanet atmospheres and their detectability with the James Webb Space Telescope. *Exoplanets 2 Conference*, Cambridge, UK (talk).

- Krissansen-Totton, J. (April 2018). Disequilibrium biosignatures in exoplanet atmospheres and their detectability with the James Webb Space Telescope. *Space Telescope Science Institute* Exoplanets, Star and Planet Formation Seminar Series (invited talk).

- Krissansen-Totton, J., S. Olson, R. Garland, P. Irwin and D. C. Catling (October 2017). New prospects for finding life on exoplanets: Disequilibrium biosignature metrics and their detectability with the James Webb Space Telescope. *Astrophysics Departmental Seminar, University of Exeter* (invited talk)

- Krissansen-Totton, J., G. Arney and D. C. Catling (September 2017). Robust constraints on the climate and ocean pH of the early Earth using a geological carbon cycle model. *EGU Galileo Conference*, Sao Miguel Island, Portugal (talk).

- Krissansen-Totton, J., S. Olson and D. C. Catling (April 2017). Atmospheric Disequilibrium Biosignatures on Earth through time, *Astrobiology Science Conference*, Mesa, Arizona (talk).

- Krissansen-Totton, J. and D. C. Catling (December 2016). Continental and Seafloor Weathering in the Global Carbon Cycle: Inverse Modeling and Implications for the Precambrian. *AGU*, San Francisco (talk).

- Krissansen-Totton, J. and D. C. Catling (July 2016). A model of ocean pH over Earth history. *Goldschmidt*, Yokohama, Japan (talk).

- Krissansen-Totton, J., D. Bergsman and D. C. Catling (October 2015). On detecting biospheres from thermodynamic disequilibrium in planetary atmospheres, *exoplanetary atmospheres and habitability conference*, Nice, France (talk).

- Krissansen-Totton, J. and D. C. Catling (June 2015). Do Pale Blue Dots have unique atmospheric disequilibrium and photometric color, NASA GSFC, Maryland (invited talk).

- Krissansen-Totton, J., D. Bergsman and D. C. Catling (April 2015). On detecting biospheres from thermodynamic disequilibrium in planetary atmospheres, *Astrobiology Science Conference*, Chicago, Illinois (talk).

- Krissansen-Totton, J. and D.C. Catling (July, 2014). The carbon isotope record and the rise of oxygen, *AbGradCon*, Troy, NY (talk).

- Krissansen-Totton, J. and D. C. Catling (June, 2014). A statistical analysis of the carbon isotope record from the Archean to Phanerozoic and implications for atmospheric oxygen, *Goldschmidt,* Sacramento, CA (poster).

- Krissansen-Totton, J. and D. C. Catling (May, 2014). What carbon isotopes can tell us about organic burial and the rise of oxygen, online seminar for *NSF Frontiers in Earth System Dynamics* research group (talk).

Selected Press

- Our *Science Advances* paper on disequilibrium biosignatures on the early Earth generated significant media attention around the world. It was featured in Scientific American, The LA Times, and The Verge.
- Our *PNAS* paper on constraining the climate and ocean pH of the early Earth was featured on Space.com.
- Our AJ paper on detecting life with the James Webb Space Telescope was featured on BBC News and EOS.
- UW Press Release – Weathering of rocks a poor regulator of global temperatures
- BBC Sky At Night - There's something in the air
- Astrobiology Magazine – Volcanoes light up atmospheres of small exoplanets
- Space.com – Could Earth's light blue color be a signature of life?

Academic Awards and Scholarships

- NASA Sagan Fellowship (beginning September 2019)
- Harvard-Smithsonian Center for Astrophysics Clay Fellowship 2019 (declined)
- NASA Postdoctoral Program Fellowship 2019 (declined)
- 51 Pegasi b Fellowship 2019 (declined)
- NASA Earth and Space Sciences Fellowship (Planetary Science), 2015-2018
- David A. Johnston Award for Research Excellence, 2018: Departmental award for research excellence, selected from 80 graduate students.
- College of the Environment Graduate Dean's Medalist, 2018: Awarded for outstanding academic achievement, leadership, and service, and selected from seven departments within the College.
- NASA Early Career Collaboration Award, 2015
- Outstanding Astrobiology Scholar Fellowship (UW), 2013
- Fulbright Science and Innovation Graduate Award, 2012
- Senior Scholar Award - Bachelor of Science and Bachelor of Arts (UoA), 2012
- University of Auckland Honours Scholarship, 2012
- University of Auckland Scholarship, 2008-2010

Teaching Experience and Outreach

- Teaching Assistant for Earth and Space Sciences 102: Space and Space Travel, 2018.
- Teen Science Café Presenter, *What can ancient rocks teach us about looking for life on other planets?* Hosted by the Pacific Science Center, 2018.
- Astronomy on Tap (Seattle) presenter. *How can billion-year-old rocks help the search for life among the stars?* Peddler Brewing Company, 2018.
- Presented astrobiology/astronomy talks to 90 11th Graders at Sammamish High School, 2018.
- Presented intro to astrobiology talks at Eatonville Middle School to 140 6th Graders, 2017.
- Pacific Science Center, Science Communication Fellow, 2017-
- Issaquah Middle School – taught introduction to astrobiology classes to around 300 7th Graders over 2 days.
- Issaquah Middle School Meet a Scientist for Career Day, 2017
- Science Café Presenter, *The Search for Life Beyond Earth*, hosted by the Pacific Science Center,

The Swiss Restaurant and Bar, Tacoma, 2016.

- Guest lecturer ESS 495 – NASA Space Grant Seminar, 2016.
- Presented astrobiology and cosmology talks as Roosevelt high school, 2015
- Presented Intro to Astrobiology talks at Lister Elementary and Harbor middle school, 2014.
- Telescope operator at Stardome Observatory, Auckland, New Zealand, March 2010-2013.
- Lab demonstrator and tutor in undergraduate physics, 2009-2010.
- Secretary of University of Auckland Reason and Science Society, 2010-2011.

Service

- Reviewer for *Nature Communications, American Journal of Science*, *Astrobiology, Frontiers in Earth Science, ACS Earth and Space Chemistry*
- University of Washington Astrobiology Program Student Representative, 2016-2017
- Geological Society of America Annual Meeting 2017, session organizing committee: The co-evolution of life and its environment during the Precambrian
- UW Astrobiology Journal Club, founder and co-organizer 2017-
- Earth and Space Sciences Research Gala organizing committee, 2017

Technical Skills

- Python, Matlab, Fortran, and R.
- Proficient with NEMESIS radiative transfer code.
- Experience with satellite data e.g. HDF files, CDF files.